High frequency ultrasonic imaging of targeted microbubble contrast agents under controlled shear stress

Mairéad B. Butler

A thesis submitted for the degree of Doctor of Philosophy

The University of Edinburgh

2005

Declaration

I declare that this thesis has been written by myself and that the work contained within is my own. Where work has been in collaboration with others, an acknowledgement has been made. This work has not been submitted for any other degree or professional qualification.

Mairéad B. Butler
July 2005

Acknowledgements

I would like to thank my project supervisors, Prof Norman McDicken and Dr Carmel Moran, for their hard work and patience over the past four years and for all their help during the writing of this thesis, it wouldn't be here otherwise. There are many other people who have also helped me throughout the course of this thesis. Many thanks go to: Tom Anderson for invaluable help with experimental set-ups especially with the work described in Chapter 4 and for providing the first flow chamber, Bill Easson for his help and expertise in laser Doppler anemometry and for the use of the LDA system. Jim Ross for bubble design and Carrie Cunningham, for making and sticking many batches of bubbles, Scott Inglis, for tissue mimic material advice, for help with the SAM system and for the loan of a microtome and Steve Pye for IVUS characterisation help. Paul Stansell for running the simulations described in Appendix 2. Also thanks to everyone else in Medical Physics at the University of Edinburgh who have helped in one way or another! Many thanks go to all the Cath Lab staff at the Royal Infirmary for allowing use of the IVUS scanner. My departmental mentor, Mark Bastin, and Irene Craig for making sure we're all alright. Thanks to all at the Chancellor's Building library for countless library book renewals and inter-library loans.

Thanks to BMUS and the Moray Endowment Fund for grants which allowed the purchase of the lens used in experimental work in Chapter 5. And thanks to Carmel for applying for said grants.

I'd like to thank the all students in the Medical Physics Student Group past and present for the support they provide, especially Jude for sharing her office and computer at the beginning and for being on the same wavelength as me, Michael and Katherine for being an email away, Jila for the rude comments and Kate and James for introducing cake-day.

Also, thanks to Karen and Toby for putting up with me as a flatmate for two years, Chris for proof reading and keeping me supplied with library books and EUWB for being a welcome distraction. Finally, thanks go to mum and Patricia for keeping me busy when at home and supplied with socks!

Abstract

Microbubble agents are used to enhance image-contrast and therapy using ultrasound. Current developments of these agents include the targeting of microbubbles to attach to specific markers expressed on certain diseased cells. Inflamed areas of atherosclerosis associated with unstable plaque in arteries have been shown to express specific inter-cell adhesion molecules such as ICAM-1. In order to distinguish between areas of stable and unstable plaque an ultrasonic contrast agent has been developed in-house for imaging with high frequency intravascular ultrasound (IVUS). The contrast agent has been imaged with IVUS at 40 MHz at different stages during development.

To assess in vivo applicability of the in-house agent it was necessary to image it attached to surfaces and under flow conditions. To image microbubbles at surfaces, work was undertaken on contrast agents at agar-based boundaries. Contrast agent was attached to agar-based material using the avidin and biotin interaction. The attached microbubbles were imaged with high frequency ultrasound, from 7 – 40 MHz. A flow chamber was developed for use with IVUS. The attached microbubbles were imaged under flow conditions. The microbubbles were found to remain echogenic and attached to the agar at a range of flow rates from 75 – 480 ml min^{-1} through a flow area of 9 mm^2. The peak negative acoustic pressures for a selection of high frequency transducers were determined in order to define the ultrasound imaging field.

Laser Doppler anemometry (LDA), a non-invasive high resolution technique for measuring flow velocities in liquids and gases was used to determine the flow profile within the flow chamber at the surface of the agar sample. The shear stress on the agar was calculated from the profile. Attached contrast agent was found to remain attached to agar under wall shear stresses of up to 3.4 Pa compared to a mean in-vivo arterial wall shear stress of 1.5 Pa. Free flowing in-house agent was shown to attach to prepared agar under low flow rates.

In this thesis the in-house contrast agent has been shown: to be echogenic at high frequencies, to be echogenic when attached to agar, to remain attached under physiological wall shear stresses and to attach to avidin coated agar when subjected to flow. An LDA system has been designed which can be used to assess the binding of agents as they are developed.

Table of Contents

Declaration ii
Acknowledgements iii
Abstract iv
List of Figures viii
List of Tables xiv
Abbreviations xv
Symbols xvi

Chapter 1 18
Introduction 18
1.1 Motivation 18
1.2 Aims and Objectives 19
1.3 Overview of Work 20
1.4 Outline of thesis 20

Chapter 2 22
Background 22
2.1 Cardiovascular Disease 22
2.1.1 The Cardiovascular System 22
2.1.2 Cardiovascular Disease 25
2.1.3 Vulnerable Plaques 25
2.1.4 Statistics 26
2.1.5 Current Methods of Detection and Treatment 26
2.2 Ultrasonic Contrast Agents 29
2.2.1 Theory 30
2.2.2 Applications of contrast agents with ultrasound 34
2.2.3 Available Contrast Agents 35
2.2.4 Targeting of contrast agents 35
2.3 Microbubbles and Flow 40
2.3.1 Introduction 40
2.3.2 Wall shear stress in arteries 40
2.3.3 Attachment and Detachment of Microbubbles 41
2.3.4 Flow chambers 42
2.4 Chapter 2 summary 43

Chapter 3 44
Ultrasonic Imaging of Microbubbles against Surfaces 44
3.1 Introduction 44
3.2 Materials 45
3.2.1 Ultrasound Scanners 45
3.2.2 Contrast Agents 45
3.3 Initial Work 46
3.3.1 Transcutaneous transducer 46
3.3.2 Intravascular transducer 47
3.3.3 Discussion 49
3.4 Development of new agent 50

3.4.1 Manufacture of the in-house agent 50
3.4.2 Initial Work 51
3.4.3 Data Capture 52
3.4.4 Comparison to different agents 53
3.4.5 Frequency tests 54
3.4.6 Timed and Gas Tests 55
3.4.7 Targeting in-house agent 57
3.4.8 Size distribution of the in-house contrast agent 57
3.4.9 Summary 58
3.5 Tissue Mimicking Material 59
3.5.1 Tissue mimicking materials 59
3.5.2 Recipes and Methods 59
3.5.3 Acoustic Impedance 61
3.5.4 Materials and Methods 61
3.5.5 Results 63
3.5.6 Discussion 64
3.6 Imaging bubbles attached to TMM 65
3.6.1 Methods 65
3.6.2 Results 67
3.6.3 Discussion 73
3.7 Imaging bubbles under flow 74
3.7.1 Materials and Methods 74
3.7.2 Discussion 80
3.8 Chapter 3 summary 81

Chapter 4 83
Characterisation of High Frequency Transducers 83
4.1 Introduction 83
4.2 Materials and Methods 84
4.3 Experimental procedure 87
4.3.1 Transcutaneous transducer characterisation 87
4.3.2 IVUS transducer characterisation 91
4.4 Results and Discussion 92
4.4.1 Transcutaneous transducers 92
4.5 Chapter 4 summary 105

Chapter 5 106
Measuring flow velocities in a chamber 106
5.1 Introduction 106
5.2 Velocity measurement techniques 106
5.2.1 Doppler wire 106
5.2.2 Particle image velocimetry 107
5.2.3 Laser Doppler anemometry 107
5.2.4 Which technique to use 108
5.3 Laser Doppler Anemometry as a method for determining flow profiles in the flow channel 109
5.3.1 Dual Beam LDA 110
5.3.2 Materials 111
5.3.3 Experimental Procedure 112

5.3.4 Initial results and Discussion 116
5.3.5 Discussion and further development 120
5.4 Final flow chamber design 122
5.5 Final results 124
5.6 Discussion 128
5.6.1 Reliability 132
5.6.2 Physiological Wall Shear Stresses 133
5.7 Chapter 5 summary 134

Chapter 6 135
Imaging attached bubbles under controlled shear stresses 135
6.1 Introduction 135
6.2 Methods 136
6.2.1 RF data analysis 139
6.3 Results 140
6.3.1 IVUS Images 140
6.3.2 Mean Backscattered Power 144
6.4 Discussion 147
6.5 Chapter 6 summary 151

Chapter 7 152
Attachment of targeted microbubbles under shear stress 152
7.1 Introduction 152
7.2 Methods 153
7.2.1 Timed Attachment 153
7.2.2 Flow Experiments 153
7.3 Results 155
7.3.1 Timed attachment 155
7.3.2 Flow experiments 156
7.4 Further Attachment Experiments 158
7.4.1 Results 158
7.5 Discussion 159
7.5.1 Methods of improving attachment 163
7.5.2 Effect of pump on circulating contrast agent 164
7.6 Chapter 7 summary 165

Chapter 8 167
Summary and Conclusions 167
8.1 Summary 167
8.2 Future Work 169

Appendix 1 172
Development of in-house contrast agent 172
Appendix 2 175
Hydrodynamic forces to which attached microbubbles are subjected 175
Appendix 3 181
Conferences and Publications 181
References 182

List of Figures

Figure 2.1: Basic diagram of the cardiovascular system..... 23
Figure 2.2: Diagram of the human heart. Printed by permission ©Current Medicine LLC. & Current Science Inc. 23
Figure 2.3: Anatomy of coronary arteries. Printed by permission ©Current Medicine LLC. & Current Science Inc. 24
Figure 2.4: Diagram of cross-section of a coronary artery. 25
Figure 2.5: IVUS catheter transducer for imaging the internal morphology of arteries. 28
Figure 2.6: IVUS images of arteries: a) normal section of artery b) section of artery with plaque. 28
Figure 2.7:a) angiograph showing 'normal' coronary artery b) corresponding IVUS image showing area of plaque. Printed by permission ©Current Medicine LLC. & Current Science Inc. 29
Figure 2.8: Use of avidin and biotin to attach an antibody to surface of microbubbles. 37
Figure 2.9: Variables involved in wall shear stress calculations. 41

Figure 3.1: Experimental set-up using Diasus scanner to image bubbles rising to an agar surface. 46
Figure 3.2: Agar containing aluminium scatterers, used as a boundary to rising bubbles, a) agar water interface prior to addition of Definity, b) Definity microbubbles 8 minutes after being added to the water. Some bubbles have risen to the interface enhancing the boundary between the agar and the water, c) Definity microbubbles suspended in the water after agitation of the whole solution. 47
Figure 3.3: Experimental set-up of microbubbles rising to an agar boundary, imaged using a 30 MHz IVUS catheter with the ClearView Ultra scanner. 48
Figure 3.4: a) IVUS image of agar supported in water with no contrast agent added, note the echo from the agar-water interface b) The same agar-water interface after contrast agent was added to the water and allowed to rise to the boundary. 48
Figure 3.5: IVUS images of Definity bubbles rising up to an agar-water interface over approximately one minute..... 49
Figure 3.6: Images printed from the scanner, a) saline with no agent, b) the in-house agent of 75 ml of liposomal powder per ml saline, c) the in-house agent diluted to a 1:4 concentration with saline..... 52
Figure 3.7: Reconstructed IVUS image from RF data showing the position of line 0 and line 90 at a distance corresponding to 660. 53
Figure 3.8: Graph showing the mean backscatter power with concentration for four contrast agents. These are compared to the mean backscatter power for the in-house contrast agent. (Courtesy of Dr C.M. Moran)..... 54
Figure 3.9: Power spectra from a perfect reflector a) 30 MHz Disco Ultra Transducer, b) 40 MHz Atlantis Transducer..... 55
Figure 3.10: a) in-house agent at time =11.00, b) in-house agent day 2 at time= 11.00, c) in-house agent day 3 at time= 10.00. The samples were inverted prior

to imaging each time to ensure the microbubbles were suspended in the saline. 56
Figure 3.11: Size distribution of in-house contrast agent containing 1% biotin. Measured using a Malvern Mastersizer 2000. 58
Figure 3.12: Diagram of scanning acoustic macroscope for determining the speed of sound through the agar based samples. 62
Figure 3.13: Acoustic impedance calculated for each agar sample where 0% contains no scatterers and 100% contains 100% of the scatterers needed for tissue mimicking material. 64
Figure 3.14: TMM block with wedge area cut-out to allow IVUS imaging of microbubbles attached to 0% scatterer agar. The TMM block and agar sample were submerged in water. 66
Figure 3.15: IVUS images of 0% scatterer samples. a) sample with nothing on, b) sample coated with streptavidin. 67
Figure 3.16: Agar based, 0% scatter samples: a) no bubbles attached, b) bubbles attached, c) sample with bubbles attached – inverted (edge with bubbles attached closest to transducer). 68
Figure 3.17: Agar samples containing 10% scatterers, a) no bubbles attached, b) bubbles attached. 69
Figure 3.18: Agar sample containing 0% scatterers, with no microbubbles attached imaged with a L5-10 MHz transducer. 70
Figure 3.19: 0% scatterer agar samples with in-house microbubbles attached. Imaged with 5-10 MHz linear array transducer. 70
Figure 3.20: Transducer L16-28 MHz a) agar sample with no bubbles attached b) original microbubbles attached to agar, c) microbubbles, with an increased amount of PE in the shell, attached to agar. 72
Figure 3.21: Schematic diagram of the flow chamber. 75
Figure 3.22: Picture of original flow chamber. 75
Figure 3.23: Variation of volume flow rate with height of IV-bag. Each point is the mean of three flow rates and the error bars are one standard deviation. 76
Figure 3.24: Picture of experimental set-up for IVUS imaging attached contrast agent under flow conditions. 77
Figure 3.25: a) agar with 0% scatterers with no microbubbles attached b) 0% scatterer agar with in-house microbubbles attached. No flow is present in either situation. 78
Figure 3.26: 0% scatterer agar sample with bubbles attached in flow chamber. Attached bubbles were subject to flow at 100 ml min^{-1} 78
Figure 3.27: Microbubbles attached under different flow rates. a) sample with no bubbles, b) 80 ml min^{-1}, c) 80 ml min^{-1} after 4 minutes of flow, d) 100 ml min^{-1}, e) 100 ml min^{-1} after 4 minutes of flow, f) 135 ml min^{-1}, g) 135 ml min^{-1} after 8 minutes of flow. 79

Figure 4.1: Sensitivity of the membrane hydrophone. (Data from calibration certificate). 84
Figure 4.2: Picture of circuitry used to selected 64th line pulse. 85
Figure 4.3: A schematic diagram of the rig and water tank for holding hydrophone and transducer in place. 86
Figure 4.4: Picture of rig to hold hydrophone and transducer. 86

Figure 4.5: Picture of the set-up for characterising transcutaneous transducers..... 88
Figure 4.6: Diagram showing orientation of x and y planes with respect to the transducer. The beam profiles in the x-plane were along the width of the line and the beam profiles in the y-plane were along the length of the line. 89
Figure 4.7: Pictures of set-up for IVUS catheter characterisation. 92
Figure 4.8: Beam profiles for each transducer, a, c, e, g are profiles in the x direction across the transducer face and b, d, f, h are in the y direction across the transducer face. 93
Figure 4.9: Example set of signals obtained for one beam profile at 0.1 mm intervals as the L8-16 MHz transducer moves across the sensitive element of the hydrophone. The corresponding beam profile is shown in Figure 4.8c. The y-axis on each plot is the measured voltage in mV and x-axis is time in μs..... 94
Figure 4.10: Peak negative acoustic pressures with distance between transducer and hydrophone at increasing transmit powers for four frequencies..... 96
Figure 4.11: Peak negative pressures for increasing transmit power. Focal point on scanner set to number 1. Transducers: L10-22 MHz and L 8-16 MHz. 97
Figure 4.12: Signal with increasing transmit power (10% - 96%) for the 8-16 MHz transducer at increasing hydrophone depths. For a depth of 0.5 cm the plots corresponding to each power output are labelled, this labelling also applies to the other plots in the figure. The y-axis on each plot is the measured voltage and the x-axis on each is time. The depth each data set was recorded at is indicated on the left-hand side of the figure. 98
Figure 4.13: Signals with and without the flow chamber lid between the transducer and the hydrophone. L10-22 MHz transducer. 101
Figure 4.14: Images from Diasus scanner of hydrophone. a) Transducer is at 90° to the hydrophone, b) Transducer is at 93° to the hydrophone. 102
Figure 4.15: Image from Diasus scanner, measurements on screen showing distance of transducer from hydrophone..... 103
Figure 4.16: Variation of peak acoustic pressure with depth for a sheathed IVUS transducer running at 40 MHz. 104
Figure 4.17: Example signal detected by hydrophone from 40 MHz IVUS transducer. The distance between transducer and hydrophone was 2 mm. Y-axis: 4 mV per division, x-axis: 41.3 ns per division. 104

Figure 5.1: Diagram of the first LDA experimental set-up (reference beam system). 109
Figure 5.2: Schematic diagram of LDA set up for measurement of velocity in one dimension. For 2D LDA another laser pair is added in the plane perpendicular to the first pair. 110
Figure 5. 3: Photographs of the LDA experimental set-up. a) The traverse system with probe holders and mounted flow chamber. b) Mounted flow chamber with the laser probe volume positioned at the front left corner of the flow chamber, this point was taken as (0,0,0) and used as a reference point when positioning the probe volume in the flow area..... 112
Figure 5.4: Orientation of probe volume in the flow area above the sample..... 113
Figure 5.5: LDA data of velocities in the flow chamber with no IVUS channel and gelatin based samples. There are three different flow rates, 80, 90 and 100 ml min^{-1}. 116

Figure 5.6: LDA profiles at increased flow velocities. A pump system was used in the set-up. The profiles are the mean of three sets of data and the error bars are the standard deviation. 118
Figure 5.7: LDA velocity profile across flow channel, (6 mm wide). The resolution of profile was 45 μm and the flow rate was 90 ml min^{-1}. 119
Figure 5.8: Schematic diagram showing flow channel shape for flow chamber versions 1 and 2, a) version 1 b) version 2..... 121
Figure 5.9: Diagram of the sections of the flow chamber. Enlarged is the area of sample holder. 123
Figure 5.10: Orientation of the probe volume in the flow channel with respect to the surface of the sample..... 124
Figure 5.11: LDA velocity profiles from the surface of an agar sample in the flow chamber, for flow rates of 110, 195, 300 and 385 ml min^{-1}. The error bars are one standard deviation. The x-axis is the distance from the front edge of the flow chamber i.e. from z = 0. 125
Figure 5.12: Plot of the end of the profile at surface of the agar sample with linear regression to find the line of best fit. Error bars are one standard deviation of the mean velocity. 126
Figure 5.13: Wall shear stress as a function of flow volume in the flow chamber. The error was calculated using the standard error in each gradient. (R^2=0.9837).. 127
Figure 5.14: Plot of point velocities horizontally perpendicular to flow direction for flow at 110 ml min^{-1} and 385 ml min^{-1}. 128
Figure 5.15: Flow profiles in the flow chamber with a flow rate of 295 ml min-1. Three profiles taken at three different times. 133

Figure 6.1: IVUS images at 40 MHz of agar samples with no microbubbles attached placed in both sample wells of the flow chamber. 137
Figure 6.2: Variation in mean backscatter power and mean contrast agent size for sonicated and unsonicated in-house microbubbles. (Courtesy of Dr C.M. Moran)..... 138
Figure 6.3: Image of microbubbles attached to agar placed in flow chamber. Image is reconstructed from the RF data collected from the IVUS scanner. The three positions where the RF data was collected are shown and marked 1, 2 and 3, each region of interest was 9 lines of RF data, the span of these lines are indicated by the blue, pink and green lines. 140
Figure 6.4: IVUS image of agar sample with no microbubbles attached in the flow chamber. Flow rate of 195 ml min^{-1}..... 141
Figure 6.5: IVUS images of agar samples with original recipe microbubbles attached, a) flow rate 110 ml min^{-1}, b) flow rate 380 ml min^{-1}. 142
Figure 6.6: IVUS images of microbubbles made with increased amounts of PE, attached to agar samples placed in the flow chamber. Flow rate of 195 ml min^{-1}. 143
Figure 6.7: IVUS images of microbubbles made with increased PE, sonicated for 30 seconds attached to agar samples. Flow rate through flow chamber was 195 ml min^{-1}. 143
Figure 6.8: Mean backscatter power across the surface of the agar sample with increasing flow rate. The data is the mean backscatter power across the surface of the agar sample for each flow rate in Figure 6.9. Mean backscatter power

from original recipe microbubbles and samples without microbubbles attached are shown. 145
Figure 6.9: Mean backscattered power for original recipe microbubbles attached to agar samples. The x-axis is labelled 1, 2 and 3 which represents the positions across the surface of the sample, with 1 being the centre and 2 and 3 being left and right of the centre. The mean backscatter power at each point for each flow rate is shown..... 145
Figure 6.10: Comparison of mean backscatter power across the surface of the agar sample for normal microbubbles, microbubbles with increased PE and microbubbles with increased PE which have been sonicated with increasing flow rate. Also displayed is the mean backscatter power across the surface of the agar sample with no microbubbles attached. 146
Figure 6.11: Mean backscatter power at each position across the sample surface. Data for original recipe microbubbles, increased PE microbubbles, increased PE and sonicated microbubbles and agar samples with no microbubbles attached. The error bars are one standard deviation of the mean. 147

Figure 7.1: Marks on the flow chamber allowing positioning and repositioning of the IVUS catheter..... 155
Figure 7.2: Mean backscatter power as a function of time of contact between biotinylated contrast agent and streptavidin coated agar. Under no-flow conditions. 155
Figure 7.3: Streptavidin coated agar sample in flow chamber a) initial image, before saline is circulated, b) image after saline has been circulated for 2 hours (flow chamber version 1). 156
Figure 7.4: Streptavidin coated agar samples in flow chamber, a) initial image before circulation of unbiotinylated contrast agent, b) after saline with unbiotinylated contrast agent has been circulated for 2 ½ hours (flow chamber version 2).... 156
Figure 7.5: Streptavidin coated agar samples in flow chamber a) initial image before biotinylated contrast is circulated, b) after biotinylated contrast has been circulated for 2 ½ hours (flow chamber version 1). 156
Figure 7.6: Mean backscatter power for streptavidin coated agar samples before and after being subjected to flow containing biotinylated in-house contrast agent, non-biotinylated in-house contrast agent, and saline only a) Flow chamber version 1 (V1), b) flow chamber version 2 (V2) error bars are one standard deviation. 157
Figure 7.7: IVUS images showing microbubbles containing 3 and 5% biotin after circulating for 2 ½ hours, a) before contrast, b) after 3% biotin-bubbles are circulated, c) before contrast, d) after 5% biotin-bubbles are circulated. 158
Figure 7.8: Mean backscatter power for 3% and 5% biotin microbubbles before and after circulation of microbubbles, error bars are one standard deviation..... 159
Figure 7.9: Diagram showing area of agar sample being imaged in flow chamber version 1 and version 2. A larger proportion of the sample surface was imaged in version one of the chambers..... 161
Figure 7.10: IVUS images from a) version 1 and b) version 2 of the flow chamber. 161
Figure 7.11: Cross-section through an IVUS catheter, showing potential use for delivery of targeted contrast agents. 164

Figure 7.12: Malvern Mastersizer size distribution of in-house agent before and after being pumped for 30 minutes (green line: before being circulated red line: after being circulated)..... 164

Figure 8.1: IVUS image of the in-house microbubble circulating in ex-vivo sheep aorta. Courtesy of Dr C.M Moran..... 169
Figure 8. 2:Sheep aorta mounted on slab of tissue mimicking material. Both images obtained scanner transmitting with a L8-16 probe and receiving using L10-22 probe. a) vessel prior to injection of contrast, b) vessel post injection of 1ml of in-house contrast agent..... 171

Figure Ap2.1 Forces on an attached bubble under flow conditions..... 176
Figure Ap2.2Forces experiences as the separation between cylinders increases, drag, lift and torque forces. Printed by permission, Dr Paul Stansell 179
Figure Ap2.3 Forces on each cylinder as the separation increases, drag, lift and torque forces. Printed by permission, Dr Paul Stansell..... 180

List of Tables

Table 2.1: Resonant frequency for different air bubbles and contrast agents of varying diameters (de Jong et al 2002). 34
Table 2.2: Ultrasound contrast agents currently available and under development (Miller and Nanda 2004). 35

Table 3.1: -6 dB bandwidth and centre frequency, determined using a perfect reflector, for the 30 MHz and 40 MHz IVUS transducers used with the ClearView Ultra scanner. 55
Table 3.2: Mean backscatter power from in-house agent over three days. 56
Table 3.3: Mean backscatter power from-house microbubble made using no gas, nitrogen and helium 57
Table 3.4: Ingredients for tissue mimicking material. 60
Table 3.5: Attenuation, speed of sound and acoustic impedance values for the TMM samples. The errors in the speed of sound values are one standard deviation of the mean speed of sound. 63
Table 3.6: Measured acoustic impedance in agar samples with difference concentrations of scatterers compared to published values of acoustic impedance of different lesion types (Goss et al 1978). 65
Table 3.7: Speed of sound values from SAM data for agar samples with 0% and 100% scatterers, with and without streptavidin. The errors in the speed of sound are one standard deviation of the mean. 68

Table 4.1: Depths of focal points 1 and 7 for each transducer. 90
Table 4.2: MI for each probe of the Diasus Scanner with increasing transmit power. 90
Table 4.3:Peak negative pressures (MPa) measured for each transducer where fp is the focal-point number for which the data was captured and the depth corresponds to the distance between the transducer and the hydrophone. 99

Table 5.1: Wall shear stresses calculated for each profile in Figure 5.5 117
Table 5.2: Wall shear stresses corresponding to the profiles in Figure 5.6. 118
Table 5.3: Measured peak velocities using LDA and calculated wall shear stress for each flow rate. 126
Table 5.4: Comparison of wall shear stress obtained from LDA data and calculated wall shear stress from Equation 2.3. 131
Table 5.5: Comparison of estimated and measured mean velocities through the flow chamber. 132

Table 6.1: Mean and standard deviation in mean backscatter power across surface of agar sample with no bubbles, original recipe bubbles, increased PE bubbles and sonicated bubbles attached. 150

Table 7.1: Mean and standard deviation in mean backscatter power across surface of agar sample with no bubbles, original recipe bubbles, increased PE bubbles and sonicated bubbles attached. 150

Table Ap1.1: Summary of tests completed on agent described in Chapter 3..... 173
Table Ap1.2: Summary of tests completed on agent in parallel to work competed in this thesis. The work described in this table was performed by Dr C M Moran. 174
Table Ap1.3: Description of bubble types used for targeting. 174

Abbreviations

BHF	British Heart Foundation
BMF	Blood mimicking fluid
CAD	Coronary Artery Disease
CVS	Cardiovascular system
ICAM-1	Intercellular adhesion molecule 1
IV	Intravenous
IVUS	Intravascular ultrasound
LDA	Laser Doppler anemometry
MI	Mechanical index
PIV	Particle image velocimetry
RF	Radio frequency
ROI	Region of interest
SAM	Scanning acoustic macroscope
TMM	Tissue mimicking material

f_0	resonance frequency
π	pi
R	bubble radius
R_0	initial bubble radius
γ	adiabatic ideal gas constant
ρ_0	density of fluid surrounding bubble
P_0	pressure surrounding bubble
S_c	shell elasticity parameter
p_v	vapour pressure
σ	surface tension
δ_τ	damping coefficient
ω	angular frequency
$p_{ac}(t)$	time varying acoustic pressure
τ	wall shear stress
μ	fluid viscosity
u	flow velocity
x	distance from vessel wall
Q	volume flow rate
w	flow chamber width
h	flow chamber height
Z	acoustic impedance
c	speed of sound
P	peak acoustic pressure
V	voltage
M	hydrophone sensitivity
δ_f	distance between fringes
λ	wavelength
θ	angle between laser beams
f_D	Doppler frequency
Re	Reynolds number
L_e	entrance length

Chapter 1

Introduction

1.1 Motivation

Microbubble contrast agents have successfully been used to enhance the backscatter of ultrasound leading to new and developing methods for diagnosis and therapy (Ophir and Parker 1989, Unger et al 2001a). A recent development of contrast agents has been the tagging of them to target specific sites of interest within the body such as areas of inflammation. Contrast microbubbles have the potential to be used to highlight specific areas within the body. Targeting of microbubbles to a specific marker expressed at certain areas could potentially be used for the enhancement of images and drug or gene delivery (Unger et al 2002, Unger and Sweitzer 2003).

Contrast agents have been predominantly developed for use with ultrasound of frequencies of 1-10 MHz. However, there is potential for the use of targeted contrast agents at the higher intravascular frequencies of 20-40 MHz. In order to do this, microbubbles specifically developed for use with frequencies greater than 10 MHz need to be developed. Another reason for the need for development of new contrast agents for targeting is the difficulty in modifying currently available contrast agents due to commercial sensitivity regarding their composition. Modification of the contrast agents is necessary to enable the shell to be adapted for targeting. To this

end, a microbubble is being developed in Edinburgh for use with high frequency ultrasound which will have the potential to be targeted to markers expressed on areas of atherosclerotic plaque (Moran et al 2003b, Moran et al 2004).

Areas of inflammation within the body are known to express certain molecules. Inflammation and hence these markers are found at areas of vulnerable plaque. Vulnerable plaque is a cause of myocardial infarction however; it does not always cause major blockages within the artery. Currently, intravascular ultrasound can be used along with angiography for the detection of plaque in arteries, however, determining whether the plaque is stable or unstable (vulnerable) is not presently possible. A contrast microbubble targeted to markers at areas of vulnerable arterial plaque could potentially be used to distinguish between stable and unstable plaque, leading to treatment prior to any episode of myocardial infarction.

1.2 Aims and Objectives

The title of this thesis is 'High frequency ultrasonic imaging of targeted microbubble contrast agents under controlled shear stress'

The aims and objectives of this thesis are to:

- Aid in the development of a targeted ultrasonic contrast agent for use with intravascular ultrasound.
- Use high frequency ultrasound to image contrast agents against surfaces and attached to surfaces.
- Image attached ultrasonic contrast agents under flow conditions.
- Determine the wall shear stresses to which the attached contrast agents are subjected.
- Investigate the wall shear stresses under which the contrast agents remain attached and under which they form an attachment.

1.3 Overview of Work

To pursue these aims, an ultrasonic contrast agent was developed in-house which could be imaged at intravascular frequencies. Initial optimisation of this agent was undertaken along with imaging of microbubbles against surfaces. It can be difficult to distinguish the backscattered signal from attached microbubbles from the signal from the vessel wall. Initial work on imaging attached microbubbles was completed against a surface of low echogenicity as this increased the ease of detection of the microbubbles. The in-house microbubble could be attached to agar and was imaged under flow conditions at increased flow rates. The shear rate to which the attached microbubbles were subjected was determined and used to calculate the shear rate under which the microbubbles remained attached.

1.4 Outline of thesis

This thesis follows the following format:

Chapter 1

Introduction to the thesis, motivation for the project and outline of thesis.

Chapter 2

Summary of the current literature on contrast agents and their applications. There is also an introduction to cardiovascular disease, an application for targeted contrast agents.

Chapter 3

Summary of work completed on imaging microbubbles against surfaces. Work on the development of a new contrast agent and imaging it attached to agar based samples with high frequency ultrasound. There is also work on imaging the attached microbubble in-vitro, under flow conditions.

Chapter 4

Summary of work completed on characterising high frequency ultrasound fields from intravascular and transcutaneous transducers which have been used to image attached microbubbles.

Chapter 5

Summary of methods for measuring flow velocities and flow profiles in the flow chamber in order to calculate the wall shear stress experienced by the microbubbles at increasing flow rates. Experimental work using laser Doppler anemometry to find flow profiles within the flow chamber is described. Along with the determination of the wall shear stresses to which the microbubbles were subjected.

Chapter 6

Summary of experimental work on imaging the microbubbles at increasing wall shear stresses with high frequency intravascular ultrasound. Also experimental work on imaging microbubbles with different shell constituents attached to agar.

Chapter 7

Summary of preliminary experimental work on attachment of the in-house agent in-vitro under flow conditions.

Chapter 8

Summary of this thesis, conclusions and future work.

Chapter 2

Background

2.1 Cardiovascular Disease

2.1.1 The Cardiovascular System

The major components of the cardiovascular system (CVS) are the heart, blood vessels and blood, the principal function of this system is the transport of oxygen, glucose, amino acids, other nutrients and drugs to and from tissues throughout the body, as well as the transport of waste products. The CVS is also involved with the control of hormones and the regulation of body temperature (Levick 2003, Seeley et al 1996)

A diagram of the cardiovascular system is shown in Figure 2.1. The heart consists of left and right ventricles which act as pumps. The right ventricle pumps deoxygenated blood to the lungs while the left side of the heart receives the oxygenated blood from the lungs and the left ventricle pumps it to the rest of the body via the aorta. The right side of the heart receives the deoxygenated blood from the body via the inferior and superior vena cava. A diagram of the heart is shown in Figure 2.2.

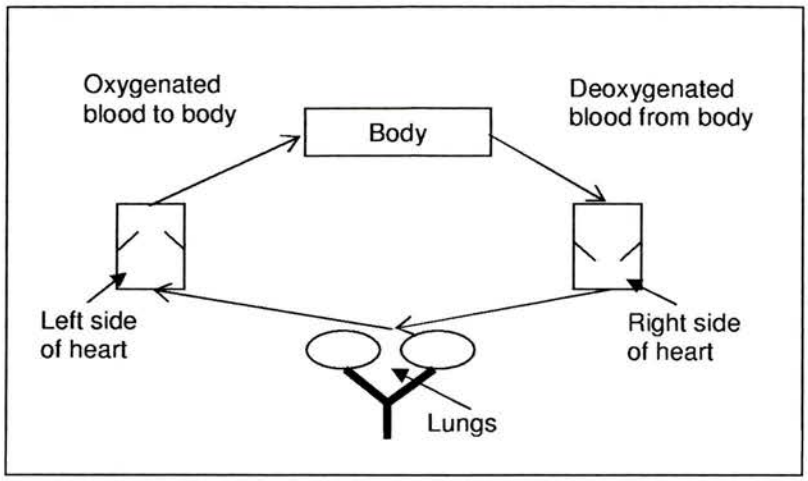

Figure 2.1: Basic diagram of the cardiovascular system.

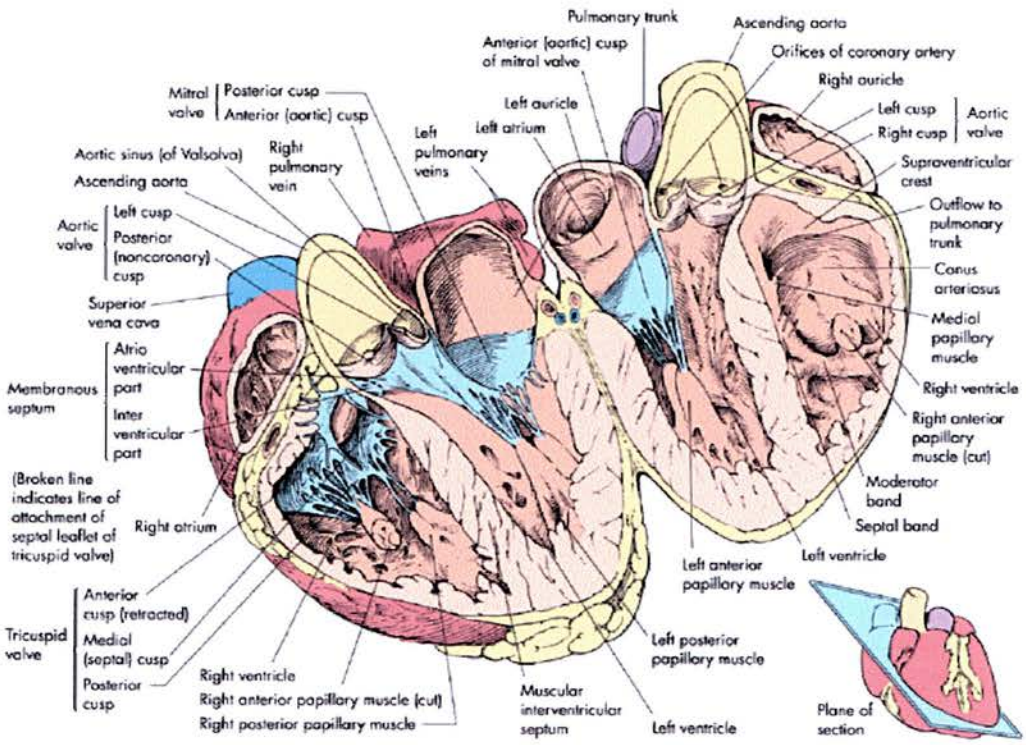

Figure 2.2: Diagram of the human heart. Printed by permission ©Current Medicine LLC. & Current Science Inc.

The coronary arteries supply oxygen rich blood to the tissues of the heart (Berne and Levy 1997), typically the aorta splits into two coronary arteries, the right and left, which form branches around the heart. Typically, the left coronary artery splits to form the left anterior descending artery (LAD) usually 100-130 mm in length and the left circumflex artery (LC) which is 60-80 mm in length. The right coronary artery is 120-140 mm long and gives rise to the posterior descending artery. Smaller arterial branches extend from the left and right coronary arteries to surround the heart. The aorta can be up to 25 mm in diameter and the coronary arteries approximately 4 mm in diameter (Levick 2003). The anatomy of the coronary arteries is shown in Figure 2.3, they surround the heart supplying blood to the tissue. A diagram showing the layers within a typical cross-section through a coronary artery is shown in Figure 2.4. There are three layers which make up the vessel wall, the adventia on the outside, followed by the medial and intima. Lining the inside of the vessel is the endothelium which consists of thin flat endothelial cells. These cells form a smooth surface within the vessel to aid blood flow and help prevent the formation of plaque.

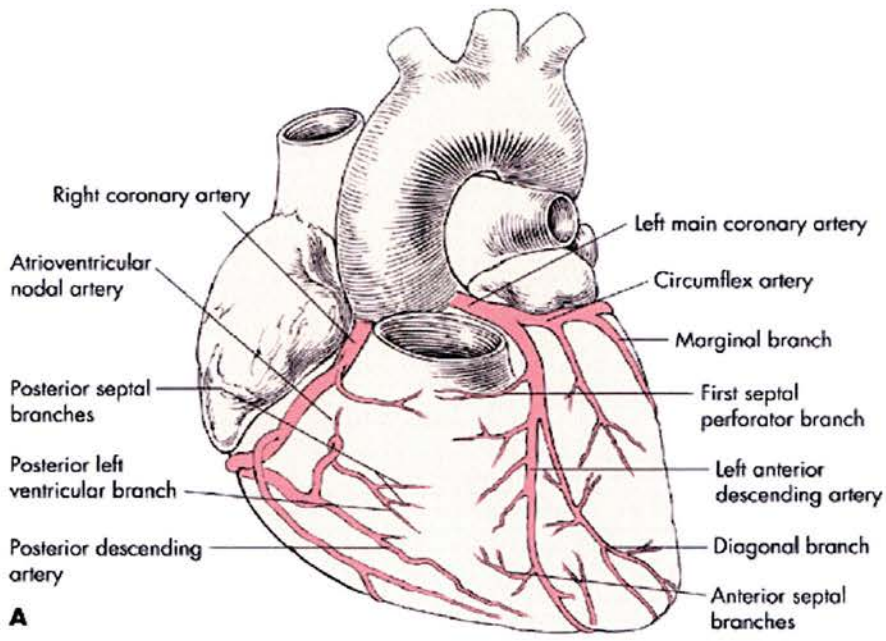

Figure 2.3: Anatomy of coronary arteries. Printed by permission ©Current Medicine LLC. & Current Science Inc.

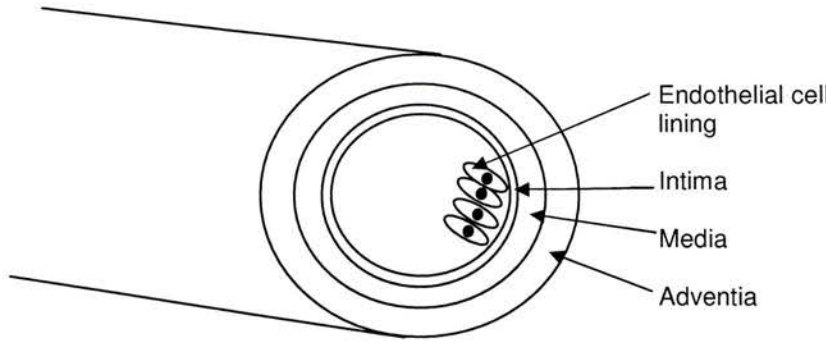

Figure 2.4: Diagram of cross-section of a coronary artery.

2.1.2 Cardiovascular Disease

Atherosclerosis is the build up of deposits of fatty substances (lipids), calcium, cholesterol or fibrous material in the lining of an artery. Arteries of the brain, heart, kidneys and other vital organs can be affected. In the heart, narrowing of the coronary arteries due to build up of plaque can lead to limited blood flow; thus reducing the level of oxygen to the heart muscle during times of stress. This can cause damage to the heart or cause the heart to malfunction. The first symptom of coronary artery disease (CAD) is commonly chest pain, known as angina. Atherosclerosis can cause damage by gradually or suddenly, during rupture, blocking the arteries or weakening the walls of the arteries. A thrombosis may form at the plaque which may lead to a myocardial infarction (heart attack).

2.1.3 Vulnerable Plaques

It is known that the plaques which cause unstable angina and myocardial infarction do not always cause severe stenoses in the coronary arteries (Libby 2004). This can make them difficult to detect by angiography as they are not seen as blockages in the arteries. The components of a plaque can affect the likelihood of rupture. Hard plaques with small amounts of lipids can be stable while soft plaques, with soft lipid centres and thin fibrous caps, are unstable and vulnerable (Schroeder and Falk 1995). These plaques can easily rupture leading to a myocardial infarction.

Inflammation is an important process involved with the development of atherosclerosis (Libby 1995). Animal models of atherosclerosis have shown that inflammation and build up of lipid in the artery wall develop at the same time (Libby et al 2002).

2.1.4 Statistics

Cardiovascular disease is the most common cause of death in the UK. Approximately 2.56 million people in the UK have CAD and nearly 50% of these have had a heart attack. The cost of CAD to the UK healthcare system in 1999 was £1.7 billion with the total annual cost to the UK economy being £7 billion after informal care and productivity losses were included, this is greater than the cost of any other single disease (NHS report 2003, Petersen et al 2004). About four in ten of all deaths are due to cardiovascular disease. Approximately 50% of deaths from cardiovascular disease are due to coronary heart disease. In Europe cardiovascular disease causes 4 million deaths each year. About 60% of all myocardial infarctions are caused by the rupture of a vulnerable plaque (Casscells et al 2003).

2.1.5 Current Methods of Detection and Treatment

Coronary artery disease can often be controlled solely with drugs which can reduce symptoms and risk factors associated with the disease. Drugs can be used to help lower blood pressure, help reduce cholesterol levels and inhibit or prevent blood clotting. However, if the blood vessels have become very narrowed or if drug treatment alone is not controlling the symptoms, surgery can be necessary to open up arteries or replace the blocked sections. Invasive treatments for coronary heart disease include: coronary angioplasty and coronary bypass surgery.

Over 20,000 angioplasties are performed in the UK each year. This treatment involves a catheter passing through a large artery in the groin or arm until it reaches the blockage. A stent is placed between the blocked walls with a balloon inside the stent being slowly inflated to expand the stent, flattening the blockage against the artery wall. The balloon is then deflated and removed, leaving the stent helping to

hold the vessel open. Coronary bypass surgery takes segments of blood vessels from other parts of the body e.g. legs and arms, which are grafted between the aorta and coronary arteries to bypass obstructions.

Prior to both treatments, the extent of narrowing within arteries needs to be assessed. Angiograms are used to view arteries by injecting dye into the bloodstream through a catheter. X-rays of the heart and coronary arteries are then taken, showing any reduction in vessel diameter due to an obstruction. The best treatment is decided after examination of the angiogram. There are however limitations to angiographies, some studies suggest angiograms underestimate the amount of atherosclerosis present in an artery (Nissen 2001, Nissen 2002). Also, vulnerable plaques can be invisible on angiographies since they do not necessarily cause severe narrowing (stenosis).

An intravascular ultrasound (IVUS) catheter transducer is shown in Figure 2.5, IVUS can be used to show the internal morphology of arteries (Figure 2.6) to complement angiography. The image obtained using IVUS is a full, cross-sectional image, whereas in angiography a planar, longitudinal image is seen. As well as imaging the artery and plaque morphology, IVUS can be used to image the position and expansion of stents which have previously been placed in arteries (Chong 1996). Figure 2.7a shows an angiograph showing a 'normal' coronary artery while the corresponding IVUS scan, Figure 2.7b, shows a substantial area of plaque within the artery showing how angiography can lead to misleading diagnosis.

Analysis of the raw ultrasound data (RF data) obtained from IVUS can be used to broadly determine the composition of plaque. 86% of plaques in excised coronary arteries were correctly determined to be composed of mixed fibrous tissue, a lipid pool or calcified plaque (Watson et al 2000). This work was subsequently performed in-vivo where plaques in patients with stable coronary artery disease were studied. Plaque composition in remodelled arterial segments was found to be mainly fibrous (McLeod et al 2004).

Unstable, vulnerable plaques cannot currently be routinely distinguished from stable plaques and neither analysis of the radio frequency (RF) data nor study of IVUS images give indication of biological markers expressed at areas of vulnerable plaque. Effective methods of diagnosing vulnerable plaques are necessary to obtain early detection and hence early treatment of the patient (Rudd et al 2005).

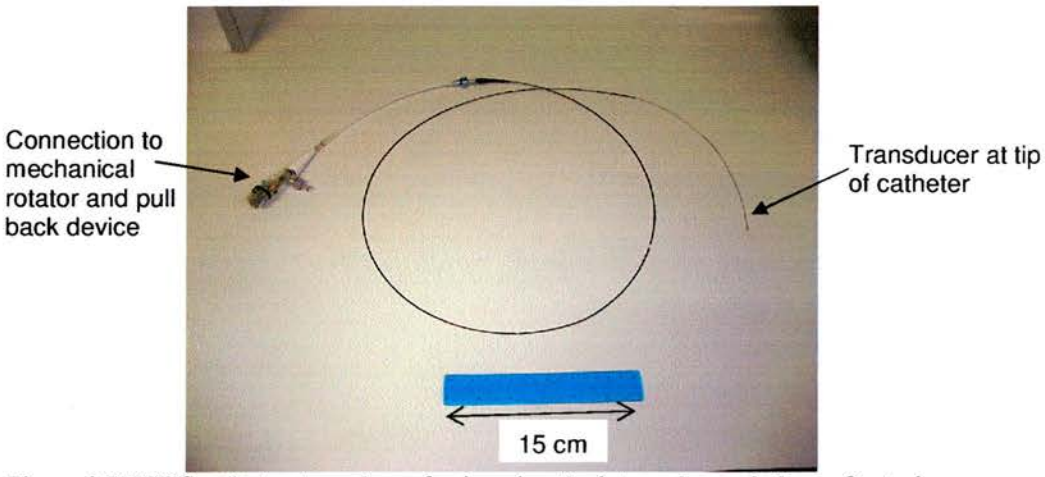

Figure 2.5: IVUS catheter transducer for imaging the internal morphology of arteries.

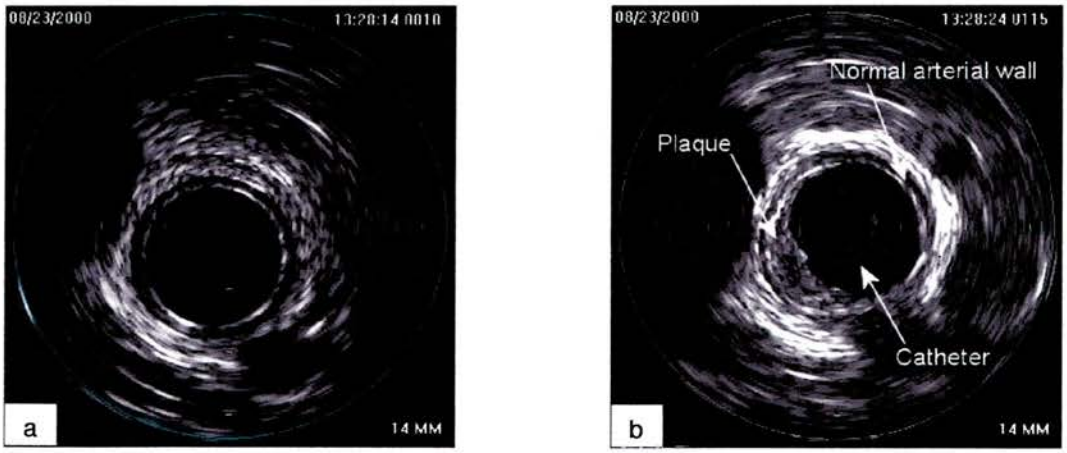

Figure 2.6: IVUS images of arteries: a) normal section of artery b) section of artery with plaque.

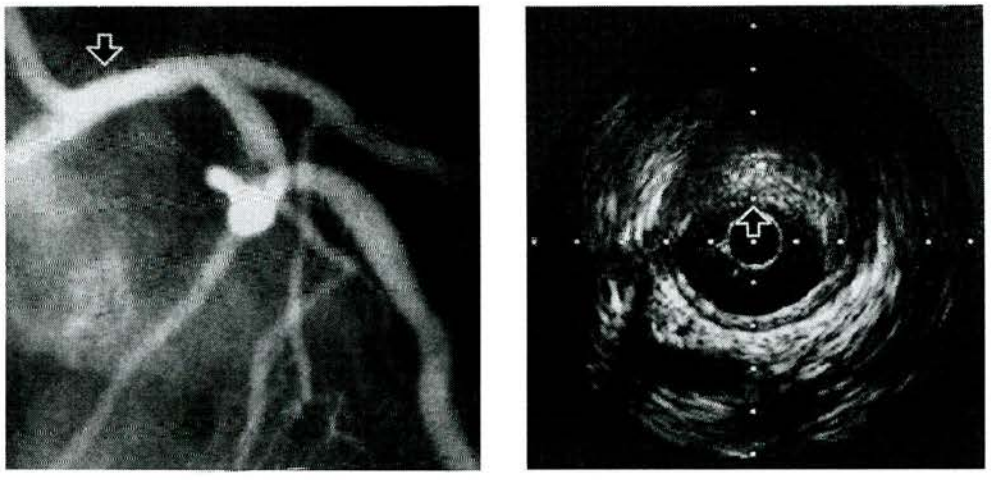

Figure 2.7:a) angiograph showing 'normal' coronary artery b) corresponding IVUS image showing area of plaque. Printed by permission ©Current Medicine LLC. & Current Science Inc.

In addition to IVUS, other methods being researched for the detection of plaques include, electron-beam computed tomography (EBCT), magnetic resonance imaging (MRI) and optical coherence tomography (Nissen 2004, Regar et al 2003).

IVUS elastography is an alternative technique which is being developed for identification of plaque where mechanical properties of plaque are determined by deformation of the tissue. The strain values for fibrous and fatty plaques have been found to be significantly different and could potentially be used to determine the nature of a plaque (de Korte and van der Steen 2002).

2.2 Ultrasonic Contrast Agents

The application of contrast agents in ultrasound was first seen by Joyner and reported by Gramiak and Shah in 1967. Initially injections of saline were used to identify the aortic root (Gramiak 1997, Gramiak and Shah 1968). Later a study using saline, indocyanine green, 5% dextrose and water and blood as contrast agents allowed the identification of cardiac structures with ultrasound (Gramiak et al 1969). The enhancement was attributed to microbubbles of air present in the solutions.

Free gas microbubbles have a short lifetime (~few seconds) in the body as the gas quickly dissolves or is filtered out by the lungs. To create more stable and long lasting microbubbles, air was encapsulated by gelatin shells increasing the lifetime of the bubbles (Carroll et al 1980). Further development led to encapsulated microbubbles small enough to pass through the heart and pulmonary vasculature which could provide enhancement of 1-10 minutes. Albumin was sonicated to form small microbubbles which could be visualised in the left side of the heart (Feinstein et al 1984). Since then ultrasonic contrast agents have developed to become a large field of medical ultrasound which is constantly expanding (Dijkmans et al 2004, Stride and Saffari 2003)

2.2.1 Theory

Ultrasonic contrast agents are gas-filled microbubbles approximately 6 μm or less in diameter, making them comparable in size to a red blood cell. If a bubble is present in a system the increased acoustic impedance mismatch between the gas and the blood or tissue interface increases the intensity of the backscattered ultrasound signal. The microbubbles can travel within the body to areas where the blood travels. A larger proportion of the incident ultrasound is scattered from the blood-microbubble interface than would be scattered from a blood cell, hence areas where the blood travels can be highlighted by the contrast agent.

When a microbubble is subjected to an oscillating acoustic signal, the microbubble, which is compressible, will oscillate. The resonant frequency, f_0 of an encapsulated gas bubble is given by (Forsberg 1997),

$$f_0 = \frac{1}{2\pi R}\sqrt{\frac{3\gamma}{\rho_0}\left(P_0 + \frac{\pi}{3}\frac{S_c}{\gamma R}\right)} \qquad (2.1)$$

where, R is the bubble radius, γ is the adiabatic ideal gas constant, P_0 and ρ_0 are the fluid pressure and density of the surrounding fluid respectively and S_c is a shell

elasticity parameter which accounts for the effect of the bubble shell. The response of an encapsulated microbubble to ultrasound is dependent on the shell properties.

2.2.1.1 Theoretical behaviour of contrast microbubbles

The resonant oscillations of a microbubble cause the increased backscatter of ultrasound. The larger the amplitude of oscillation the larger the scattered signal. Models describing the behaviour of free bubbles have previously been developed for applications such as underwater acoustics. The first account of the theoretical behaviour of bubbles when exposed to an external pressure was by Rayleigh (Rayleigh 1917). Free bubble models have thus provided a basis for developing models which describe the behaviour of encapsulated microbubble agents. A comparison of three free gas bubble models was given by Vokurka (1986) in which, the Rayleigh, Herring and Gilmore models were described (Vokurka 1986). The Rayleigh model, developed to become the Rayleigh, Plesset, Noltingk, Neppiras and Poritsky model (RPNNP) (Lauterborn 1976) describes the spherical oscillations of the ideal gas bubble. The liquid surrounding the bubble is assumed to be incompressible with the velocity of sound through the liquid infinite. The Herring model assumes a compressible liquid with a constant velocity of sound, which becomes the Rayleigh model for high sound velocities. The Gilmore model assumes the velocity of sound varies with pressure in the liquid. Other models for free gas bubbles exist, but are thought to behave in a similar way to the Herring model.

Gas bubble models have been further developed to describe encapsulated contrast agents by including terms which account for the presence of the encapsulating shell. The RPNNP equation was modified to account for factors associated with the presence of the microbubble shell and is given in Equation 2.2 (de Jong et al 1994).

$$\rho R\ddot{R} + \frac{3}{2}\rho\dot{R}^2 = p_{g0}\left(\frac{R}{R_0}\right)^{3\Gamma} + p_v - p_0 - \frac{2\sigma}{R} - S_c\left(\frac{1}{R_0} - \frac{1}{R}\right) - \delta_t \omega \rho R\dot{R} - p_{ac}(t) \qquad (2.2)$$

Gas pressure

Surface tension

Shell elasticity

Damping due to viscosity, heat conduction and re-radiation

where R is the bubble radius, R_0 is the initial bubble radius, ρ is the fluid density, p_{g0} is the initial gas pressure within the bubble, p_v and p_0 are the vapour and ambient pressure respectively, σ is the surface tension, Γ is the polytropic exponent of the gas which is equal to γ (the ratio of specific heats C_p/C_v), δ_t is a damping coefficient which is the sum of damping due to re-radiation, viscosity of the surrounding liquid and heat conduction and $p_{ac}(t)$ is a time varying acoustic pressure. The damping coefficients account for energy losses within the bubble shell due to re-radiation of sound, thermal radiation and viscous losses.

The behaviour of an insonated microbubble is dependant upon the incident acoustic pressure on the bubble. For low acoustic pressures (<50 kPa) the bubble oscillates linearly, with the frequency of the scattered wave matching that of the incident one (de Jong et al 2002, Deng and Lizzi 2002)[1]. As the incident acoustic pressure increases (50 kPa-200 kPa) the bubble oscillations become more non-linear and can contain harmonics allowing scattering due to the microbubble to be distinguished from surrounding tissue. Finally, higher pressures (>200 kPa) can cause the bubble to become disrupted. The increased non-linear oscillations can cause the bubble shell to fragment releasing free gas into the blood-pool. The free gas bubbles in the blood-pool provide an increased backscattered signal as there is no bubble shell which dampens the bubble oscillations.

Studies have been completed predicting the response of a microbubble to medical ultrasound (Chin and Burns 2000, Hilgenfeldt et al 1998) and also on observing the response of contrast microbubbles to different acoustic pressures and comparing the results to theoretical predictions (Sboros et al 2002). High speed cameras have been used to observe microbubbles when insonated (Dayton et al 1997, Dayton et al 1999b, de Jong et al 2000). More recently, the behaviour of individual microbubbles has been studied (Sboros et al 2003).

[1] The majority of current literature describing the response of microbubbles to ultrasound considers lower clinical frequencies (~3 MHz) where bubbles resonate and are currently used. When insonated at the higher frequencies used with IVUS (40 MHz) different bubble behaviours maybe observed. Morgan et al (1996) found that for 5 MHz insonation contrast agents were broken under low intensities, but for 38 MHz insonation the contrast agents remained intact under pressures of up to 2 MPa (Morgan et al 1996).

2.2.1.2 High Frequency Ultrasound and Contrast Agents

As the frequency of incident ultrasound on contrast microbubbles increases, the radius of microbubble which will be at resonance decreases. Commercial microbubbles are best detected by ultrasound at frequencies of 2-3 MHz. As the resonant frequency of a free bubble increases and the bubble diameter decreases, the damping coefficient due to viscosity increases (Miller 1998), (de Jong et al 2002). Church (1995) compared the effect of the damping coefficients for encapsulated bubbles to those for free bubbles previously obtained by Prosperetti et al (1988) (Church 1995, Prosperetti et al 1988). The main difference between the two is that for encapsulated bubbles viscous damping is due to the bubble shell as well as the surrounding liquid. It has been shown that although shell viscosity is the dominating damping mechanism at frequencies less than 10 MHz, as frequency increases acoustic damping (energy losses due to re-radiation of sound) becomes more important. Hoff et al (2000) have shown for a polymer shell microbubble acoustic damping becomes the dominant damping mechanism for a 4 micron bubble at frequencies greater than 40 MHz while viscous damping remains constant (Hoff et al 2000).

The resonant frequency of different microbubbles is shown in Table 2.1 (a more detailed table of commercial contrast agents is given in Table 2.2). Compared to a free gas air bubble the resonant frequencies of the encapsulated bubbles are greater. The difference between the resonant frequencies of the encapsulated bubbles is due to the shell properties, Quantison has a thick albumin shell making it a strong bubble, this accounts for the increased resonant frequency compared to the lipid shelled Sonovue and albumin shelled Albunex. As the microbubble diameter increases, the effect of the shell on the resonant frequency decreases as shown by the reduction in difference between the resonant frequencies of the 10 μm encapsulated agents in Table 2.1.

Diameter (μm)	Air bubble (MHz)	Sonovue (MHz)	Albunex (MHz)	Quantison (MHz)
1	9.4	21	57	127
2	3.8	7.7	20	45
5	1.3	2.2	5.2	11
10	0.6	0.9	1.9	4.0

Table 2.1: Resonant frequency for different air bubbles and contrast agents of varying diameters (de Jong et al 2002).

Intravascular ultrasound utilises frequencies of 20-40 MHz, which is higher than the resonant frequency of soft microbubbles such as Sonovue. For optimum imaging of microbubbles with high frequency ultrasound, bubbles with diameters less than 1μm are required, currently little is known about the resonant behaviour of submicron contrast microbubbles. There is little work published on the use of contrast microbubbles and their behaviour with high frequency ultrasound.

Commercially available ultrasonic contrast agents have been demonstrated to be echogenic at intravascular frequencies. Four intravenous contrast agents have been characterised using IVUS at 30 MHz (Moran et al 2002). Non-linear imaging of contrast agents at high frequencies of up to 30 MHz has been demonstrated (Goertz et al 2005a). Later, in section 2.2.4.2 work using high frequency ultrasound to image targeted contrast microbubbles is described.

2.2.2 Applications of contrast agents with ultrasound

Contrast Echocardiography was the first clinical application of ultrasonic contrast agents. The agents were used to image structures within the heart (Roelandt 1982). More recent developments of the use of contrast agents in echocardiography have included stress echocardiography, myocardial perfusion and the determination of valvular stenosis and regurgitation (Cheng et al 1998, Kaul 2001). Lesions within the liver have been enhanced using contrast agent with pulse inversion imaging allowing the detection of lesions less than a centimetre in width (Harvey et al 2000). The detection of tumours by studying tumour vasculature is a further application which

can make use of ultrasonic contrast agents (Cosgrove and Blomley 1997, Schirner et al 2004).

2.2.3 Available Contrast Agents

A list of ultrasonic contrast agents is shown in Table 2.2. Three of the agents listed (Optison, Definity and Imagent) have approval in the USA and are commercially available. Other agents also shown in Table 2.2 have approval in Europe and Canada and there are more continually being developed (Frinking et al 2000, Miller and Nanda 2004).

Agent Name	Manufacturer	Encapsulated gas	Shell type	Status
Levovist	Schering	Air	Galactose/Palmic acid	EU & Canada approved
Optison	Amersham Health	Octafluropropane	Albumin	USA, EU & Canada approved
Definity	Bristol-Myers Squib	Perfluropropane	Lipid	USA & Canada approved
Imagent	IMCOR Pharmaceuticals INC	Perflurohexane/ nitrogen	Lipid	USA approved
Sonovue	Bracco	Sulpher-hexafluoride	Lipid	EU approved
CardioSphere	Point Biomedical	Nitrogen	Albumin	Development
PB127				
AI-700	Acusphere	Perflurocarbon	Polymer	Development
Sonazoid	Nycomed	Perflurobutane	Lipid	Submitted in the USA

Table 2.2: Ultrasound contrast agents currently available and under development (Miller and Nanda 2004).

2.2.4 Targeting of contrast agents

An alternative to using contrast agents as blood pool enhancers is to attach them to specific sites enhancing the area of interest (Dayton and Ferrara 2002, Klibanov et al 1997, Lanza et al 2000). Microbubbles can be targeted to attach to specific cells which are found at certain points within the body, for instance, areas of inflammation or angiogenesis (Alessi et al 2004, Lanza and Wickline 2003). Expressed at these areas are antigens specific to the disease or condition which can be targeted. The relevant antibody can be attached to the shell of the microbubble. The antibody-antigen reaction is a well known receptor-ligand bond with a dissociation constant

ranging between 10^{-7} and 10^{-11} M, where M is Molar. The dissociation constant (K_d) is used to describe the affinity between receptors and ligands. It is an equilibrium constant for the dissociation of a molecule into its constituent components. The smaller the dissociation constant, the stronger the binding.

Ideally contrast agents would be tagged to target areas of plaque within the coronary arteries. It is hoped that vulnerable inflamed plaque which cause myocardial infarctions can be distinguished from other plaques. This would improve the understanding of the processes involved with inflamed plaques and lead to the possibility of a quick, accurate and relatively easy diagnosis and so early treatment.

2.2.4.1 Avidin-Biotin

The avidin-biotin interaction is used throughout research for binding purposes in areas such as immunology, histochemistry and affinity chromatography. Streptavidin and avidin are proteins which will bind to biotin. The bond between the two is known to be strong with a dissociation constant of 10^{-15} M, indicating a high affinity and very stable binding.

The avidin-biotin interaction can be utilised with contrast agents for attaching the microbubbles to surfaces. Biotin can be incorporated into the microbubble shell. An avidin link can be used to bridge the gap between the microbubble and an antibody, the antibody is specific to a certain antigen. The microbubbles can then be attached to areas of interest which express the specific antigen. Targeting using avidin and biotin is shown schematically in Figure 2.8.

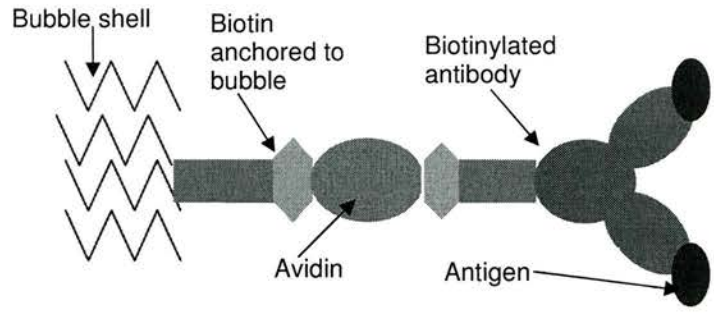

Figure 2.8: Use of avidin and biotin to attach an antibody to surface of microbubbles.

2.2.4.2 Targeted microbubbles for plaque

The targeting of ultrasonic contrast agents is an active field of research, which is constantly developing. Targeting contrast agents for diagnosis of thrombus and inflamed plaques is a technique which is possible due to endothelial cell adhesion molecules present at areas of inflammation. These molecules are present in higher concentrations at areas of plaque than at normal areas within blood vessels (O'Brian et al 1996). Certain cell adhesion molecules have been connected to areas of advanced atherosclerosis such as the intercellular adhesion molecule 1 (ICAM-1) (Lindner 2002).

Albumin based contrast agents were shown to attach to activated endothelial cells in-vitro(Villanueva et al 1997). Lipid shelled contrast agents have been modified to allow targeting to activated sites of inflammation (Lindner et al 2000a, Lindner et al 2000b, Lindner et al 2000c). Ultrasonic imaging of inflammation with site-specific targeted microbubbles has been shown to be a feasible technique (Klibanov et al 1997, Lanza et al 2000, Lanza 1996, Unger et al 1998, Villanueva et al 1998).

Targeting microbubbles to ICAM-1 was demonstrated when microbubbles targeted with a monoclonal antibody were found to attach to endothelial cells which were made to over-express ICAM-1 (Villanueva et al 1998). This work was further developed with microbubbles containing different densities of surface antibodies being exposed to normal and activated endothelial cells at different shear rates. It

was concluded that the density of shell antibody and the wall shear rate were critical bubble adhesion parameters (Weller et al 2002).

Contrast agents have been attached to porcine fibrin clots using the avidin-biotin interaction (Lanza 1996). A biotinylated ligand was targeted to attach to the fibrous tissue, avidin was then added which bound to the biotin. Finally the biotinylated agent was introduced to the system, the biotin sites bound to the avidin on the clot, attaching the contrast agent to the clot. Microbubbles, which have successfully been attached in this way, have been imaged using ultrasound. The attached bubbles were imaged at 7.5 MHz with a linear array transducer.

Microbubbles can be classified as liposomes when they are made from lipids and are multi-lamellar. Liposomes are made of layers of phospholipids and have been targeted to active endothelial cells at atherosclerosis in porcine carotid and femoral arteries (Demos et al 1999). The targeted liposomes appeared to attach to the activated areas within the arteries. The attached liposomes were imaged with 20 MHz IVUS and 7.5 and 3.5 MHz ultrasound. Enhancement in the ultrasound image due to the liposomes was seen and the level of enhancement was determined using grey scale levels (Hamilton et al 2002, Hamilton et al 2004).

2.2.4.3 Other Applications of Targeted Microbubbles

In addition to diagnostic applications for detection of inflammation at areas of plaque, targeted contrast agents also have the potential to target areas of angiogenesis and to be used to aid drug and gene delivery to specific sites (Alessi et al 2004, Blomley et al 2001, Scheirner et al 2004, Unger et al 2002).

There are a number of markers specific to angiogenesis in tumours which are currently being investigated and developed; a review of these is given in Alessi et al (2004). One group of these markers, α_v-integrins, have been targeted with microbubbles (Ellegala et al 2003, Leong-Poi et al 2003). The targeted microbubbles were found to detect early angiogenesis in tumours which could potentially be used with other biological factors such as changes in blood velocity and blood volume for

studying angiogenesis and for diagnostic purposes. It has also been shown that ultrasound contrast agents can be feasible for targeting active lymph nodes in mice and dogs (Hauff et al 2004).

This diagnostic application of ultrasound microbubbles can be further developed for therapeutic applications. If the microbubbles are made to contain a drug and targeted to a region of interest, the microbubble shell can be disrupted and the drug delivered directly to the site. Alternatively, the drug could be attached to the surface of the microbubble or contained within the fluid surrounding the microbubbles (Klibanov 1999, Lindner and Kaul 2001, Unger et al 2001b, Unger et al 2004). Gene therapy is also a feasible therapeutic application of targeted microbubbles (Unger et al 2001a). Albumin microbubbles have been successfully used to delivery genetic material to the myocardium in rats when insonated with ultrasound (Shohet et al 2000).

Targeted imaging and therapy with ultrasound and contrast agent microbubbles is an advancing field with applications in many different areas of medicine. However, development of these agents for targeting is difficult due to the lack of available information regarding the manufacture and content of the microbubbles. In order to study targeting of contrast agents in Edinburgh, we have found it necessary to develop ultrasonic contrast agents which can be manipulated as required. Targeted contrast agents capable of being imaged with high frequency ultrasound could potentially be used with IVUS to aid the detection of vulnerable plaques (Lindner 2002). The avidin-biotin reaction has been used to target perfluorocarbon filled, lipid shelled, microbubbles, to thrombus which can be imaged with high frequency ultrasound (Lanza et al 1997). Work described in part 2.2.4.2 of this chapter has used IVUS at 20 MHz to image liposomes conjugated to anti-ICAM1 and other markers expressed at areas of atherosclerosis in-vivo (Demos et al 1999, Hamilton et al 2004).

2.3 Microbubbles and Flow

2.3.1 Introduction

While there is great potential for the use of targeted microbubbles in vivo, in order to determine the feasibility of this application it is necessary to know the forces attached microbubbles can withstand. It is essential to know that when subjected to physiological wall shear stresses that the attached microbubble will remain in place. It is also necessary to know that the agent can be attached under flow conditions to ensure in vivo attachment is feasible. In larger blood vessels, attachment of targeted microbubbles to the wall under flow conditions is reduced since the microbubbles are distributed across the whole vessel, so only a proportion will come in to contact with the wall (Rychak et al 2004). The flow rate through a vessel also affects the attachment of microbubbles. At higher flow rates, the microbubbles are less likely to make prolonged contact with the vessel wall, hence reducing the number which attach. The following section of Chapter 2 describes wall shear stress in arteries and work by others on imaging targeted microbubbles under controlled shear rates.

2.3.2 Wall shear stress in arteries

Wall shear stress is the effect of the force on a vessel wall due to the viscosity of the fluid flowing through it, and is calculated by (Nichols and O'Rourke 1990),

$$\tau = \mu\left(\frac{du}{dx}\right) \tag{2. 3}$$

where, τ is the wall shear stress, μ is the viscosity of the fluid, u is the velocity of the fluid and x is the distance from the surface perpendicular to the flow, hence du/dx is the shear rate at the wall (Figure 2.9). In arteries the level of low wall shear stress has been associated with the development of atherosclerosis (Krams et al 1997, Malek et al 1999). It was thought that areas of high wall shear stress caused damage to the endothelial cell layer within vessels thus initiating areas of disease. More recently it has been shown that areas of low wall shear stress can cause an increase in the risk of arterial disease. At areas of low wall shear stresses the endothelial cells have a random alignment in the flow. The low wall shear stress promotes the expression of

molecules which aid in the development of atherosclerosis and also means there is an increase in the time for uptake of atherogenic particles from the blood; increasing the risk of disease development. Higher wall shear stresses have been shown to increase production of nitric oxide and other factors which inhibit coagulation and help protect against atherosclerosis (Shaaban and Duerinckx 2000).

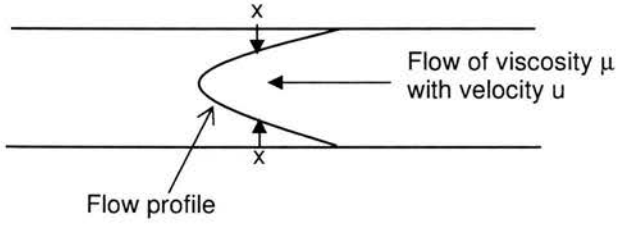

Figure 2.9: Variables involved in wall shear stress calculations.

The determination of wall shear stress in vivo is highly dependent on the measurement technique used. The main difficulty is in measuring the shear rate close to the vessel wall. The calculated wall shear stress can vary depending on the line fitting used with the profiles obtained. A linear fit to three data points closest to the wall has been used to determine the shear rate in vitro where the velocity profiles were found using pulsed Doppler ultrasound (Hughes and How 1993). Ultrasound techniques have been developed for the measurement of shear rates in vivo by determining the velocity profile (Brands et al 1995, Hoeks et al 1995). The wall shear stress is the product of the fluid viscosity and the wall shear rate. Reported wall shear stress in normal arteries ranges from 1-7 Pa (10 – 70 dynes cm^{-2}), with a mean arterial wall shear stress over the cardiac cycle of 1.5-2.0 Pa (15 – 20 dynes cm^{-2}). Atherosclerosis is predominant in areas of mean wall shear stress less than 0.5 Pa (5 dynes cm^{-2}) (Malek et al 1999).

2.3.3 Attachment and Detachment of Microbubbles

Attached microbubbles have been imaged in-vitro under flow conditions (Klibanov et al 1999). Recent attachment and detachment studies have been undertaken on microbubbles targeted to P-selectin (Takalkar et al 2004). A parallel plate flow

chamber was coated with P-selectin and the targeted microbubbles drawn through the chamber. Attachment and detachment studies at increasing wall shear stresses were completed. The maximum number of microbubbles was found to attach to the chamber surface at wall shear stresses of 0.06 Pa (0.6 dynes cm^{-2}) and 50% of the bubbles had detached by the time the wall shear stress was increased to 3.4 Pa (34 dynes cm^{-2}).

In larger blood vessels with high flow rates, the attachment rate of contrast agents can be reduced due to the fact that fewer microbubbles make contact with the vessel wall. The ultrasonic radiation force has been investigated as a method of increasing the number of microbubbles which come into contact with the wall, hence increasing the attachment rate (Dayton et al 1999a, Rychak et al 2004, Rychak et al 2005). Dayton et al (1999a) confirmed that acoustic radiation forces were able to displace contrast agents from the centre of a vessel. Rychak et al (2005) have investigated contrast microbubble targeted to P-selectin in vitro. Enhanced attachment of contrast agent was noted for acoustic pressures of up to 122 kPa.

2.3.4 Flow chambers

Parallel plate flow chambers are commercially available for observing cell interactions under flow conditions, these flow chambers have been developed for studying the attachment of microbubbles. In these chambers it is assumed that fully developed flow has been achieved at the area of interest and that the wall shear stress across the region of interest is approximately constant. For parallel plate flow chambers the wall shear stress can be calculated using (van Kooten et al 1992),

$$\tau = \frac{6Q\mu}{wh^2} \qquad (2.4)$$

where Q is the volume flow rate, μ the fluid viscosity, and w and h the width and height of the flow channel. However, it has been shown for parallel plate chambers that the wall shear stress calculated using Equation 2.4 can vary by 80% across the length of the area of interest, consequently the area of interest does not experience a constant wall shear stress (Chung et al 2003). This potentially means that in studies with parallel plate chambers where attached microbubbles are studied, the wall shear

stress the attached microbubbles experience can be 80% less than calculated. This can have implications for targeted contrast agents in-vivo. Attached contrast agents have to be able to withstand physiological wall shear stresses to allow in vivo imaging. For attachment of targeted contrast agents contact between the agent's shell and the vessel wall is necessary. In wide vessels and at high flow rates it can be difficult to ensure the microbubble and wall make contact; attachment of contrast agents to the area of interest needs to be feasible under physiological wall shear stresses.

2.4 Chapter 2 summary

Cardiovascular disease is the most common cause of death in the UK. Arterial plaque has been found to have a variety of characteristics with some forms of plaque more likely to cause myocardial infarctions. Vulnerable plaques have soft lipid cores with a thin cap which are more likely to erupt. It is difficult to diagnose vulnerable plaque in arteries as a severe arterial blockage is not always seen.

Contrast agents are gas filled microbubbles which enhance the backscatter of ultrasound. They have been shown to be echogenic at intravascular ultrasound frequencies. One development is the targeting of contrast agents to bind to markers expressed at certain sites such as areas of inflammation where inter-cell adhesion molecules (ICAM-1) are expressed. ICAM-1 molecules have been shown to be expressed at areas of vulnerable plaque. Targeted contrast agents have the potential to target these areas of inflammation to identify and hence aid in the diagnosis of vulnerable plaque.

The following chapters describe the development of an ultrasonic contrast agent for use with high frequency ultrasound and work completed on imaging attached contrast agent under static and flow conditions.

Chapter 3

Ultrasonic Imaging of Microbubbles against Surfaces

3.1 Introduction

Ultrasonic contrast agents are gas-filled microbubbles approximately 6 μm or less in diameter, making them comparable in size to a red blood cell. If a bubble is present in a system the increased acoustic impedance mismatch between the gas and the blood or tissue interface increases the intensity of the backscattered ultrasound signal. However, a problem can arise when the bubbles are next to surfaces. The boundary of the surface can have a bright echo due the acoustic impedance mismatch between the surface and the surrounding medium, making the bubbles difficult to detect. The contrast microbubble is small compared to the size of the surface to which it is attached. The returned signal from the microbubble can be difficult to determine from the surface echo.

Ultrasound contrast agents are generally used at diagnostic frequencies of 1 – 10 MHz. As described in Chapter 2 microbubbles of the size normally manufactured are known to resonate at these frequencies thus dramatically improving the contrast in ultrasound images. Higher frequency ultrasound gives better spatial resolution in images and frequencies up to 40 MHz can be used for intravascular imaging as reduced penetration associated with high frequency is not generally detrimental to the images obtained. Commercial agents which are used at lower frequencies have

been found to be echogenic at intravascular frequencies (Moran et al 2002). A potential use of microbubbles with high frequency intravascular ultrasound (IVUS) as described in Chapter 2 is the targeting of microbubbles to attach to areas of vulnerable plaque (Unger et al 2004). High frequency ultrasound is also used for applications such as musculoskeletal imaging, carotid artery imaging and mouse imaging (Foster et al 2002). Targeted contrast agents could potentially be used with these applications for imaging near-surface internal structures.

With a view to being able to image microbubbles attached to surfaces with high frequency ultrasound, initial work on imaging microbubbles at boundaries was completed. This work is described in the following section.

3.2 Materials

3.2.1 Ultrasound Scanners

Ultrasound scanners available for imaging work included the Dynamic Imaging Diasus scanner (Dynamic Imaging, Livingston, Scotland) with linear array probes of 5-10 MHz, 8-16 MHz, 10-22 MHz and 16-28 MHz. An intravascular ultrasound scanner, the Boston Scientific ClearView Ultra scanner (Boston Scientific, Natick, USA) was also available initially with 30 MHz Disco Ultra catheter transducers and later with the 40 MHz Atlantis catheter transducer.

3.2.2 Contrast Agents

Contrast agents available for use within the department were Definity (Bristol-Myers Squibb Medical Imaging Inc, N. Billerica, USA), Optison (Amersham Health, Amersham Place, Bucks, UK) and Sonovue (Bracco International B.V, Amsterdam, The Netherlands) which were described in Chapter 2. Definity and Sonovue microbubbles are lipid shelled while the Optison shell is made from albumin. Optison and Definity both contain fluorocarbon gases while Sonovue microbubbles contain sulphur-hexafluoride.

3.3 Initial Work

3.3.1 Transcutaneous transducer

Initial work was completed on imaging microbubbles against surfaces with high frequency ultrasound. The bubbles were imaged as they floated up to and rested against a boundary. The high frequency Dynamic Imaging Diasus scanner, with a 10-22 MHz probe was used to image Definity microbubbles through agar based samples. The initial experimental set up is shown in Figure 3.1.

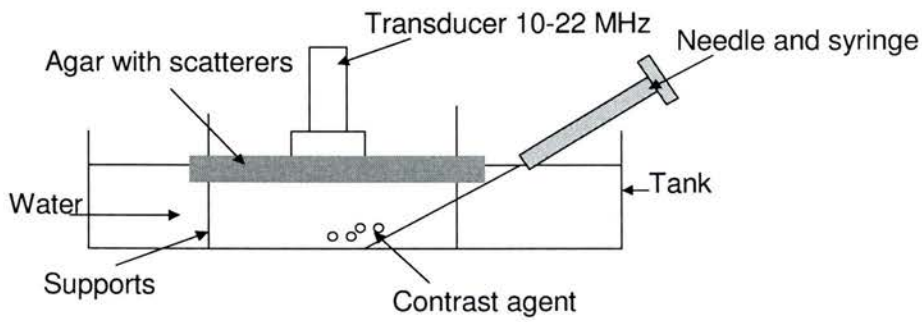

Figure 3.1: Experimental set-up using Diasus scanner to image bubbles rising to an agar surface.

Still images were saved as bitmaps on to the hard drive of the scanner and transferred to a PC. The images obtained using this set-up are shown in Figure 3.2. The agar used was based on a standard TMM recipe described in section 3.5 with a reduced number of scatterers. Figure 3.2a shows the agar with no Definity in the water, Figure 3.2b is 8 minutes after the Definity was added, echoes can be seen from the interface between the agar and water, the bubbles can also be seen in water. Figure 3.2c is 16 minutes after the Definity had been added and after minor agitation to re-suspend the bubbles which had settled against the surface of the agar. The microbubbles were seen again, rising towards the boundary. However, while it was possible to image the bubbles in the water and the agar-water boundary was enhanced, it was difficult to determine the microbubble location on the agar surface thus showing the difficulty in imaging microbubbles when against surfaces.

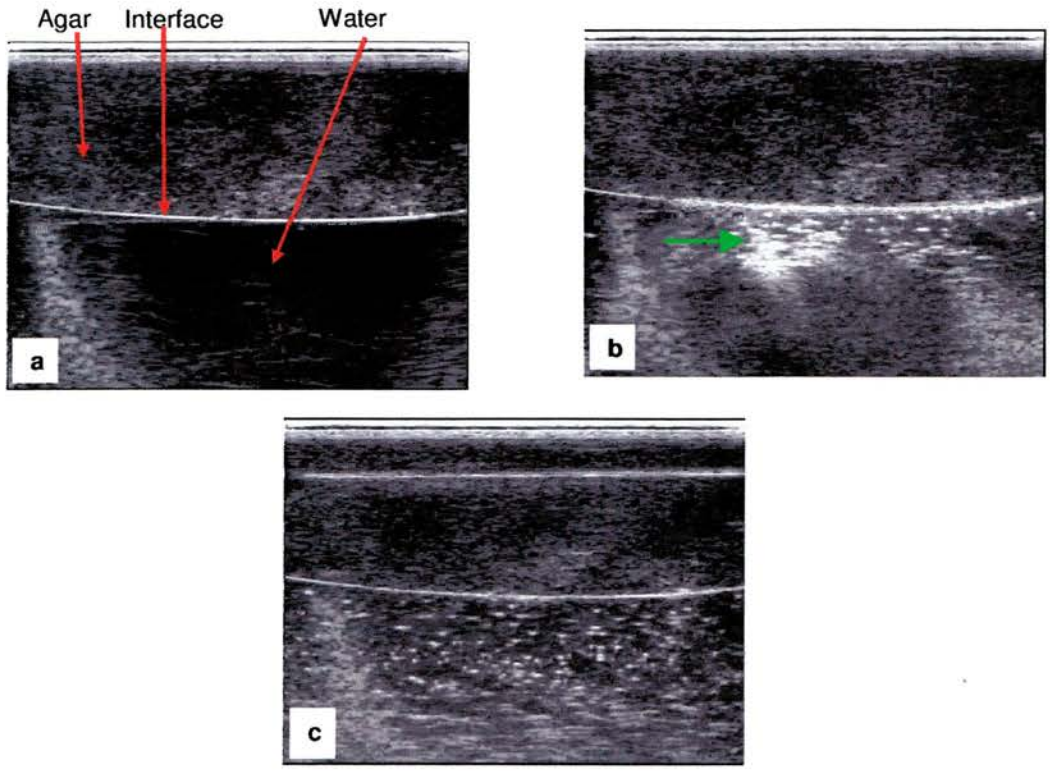

Figure 3.2: Agar containing aluminium scatterers, used as a boundary to rising bubbles, a) agar water interface prior to addition of Definity, b) Definity microbubbles 8 minutes after being added to the water. Some bubbles have risen to the interface enhancing the boundary between the agar and the water, c) Definity microbubbles suspended in the water after agitation of the whole solution.

3.3.2 Intravascular transducer

Imaging Definity against boundaries was repeated with IVUS. The Boston Scientific ClearView Ultra IVUS scanner with a 30 MHz Disco Ultra catheter was used. The experimental set-up is shown in Figure 3.3. The agar sample was cut to size and placed on a plastic support.

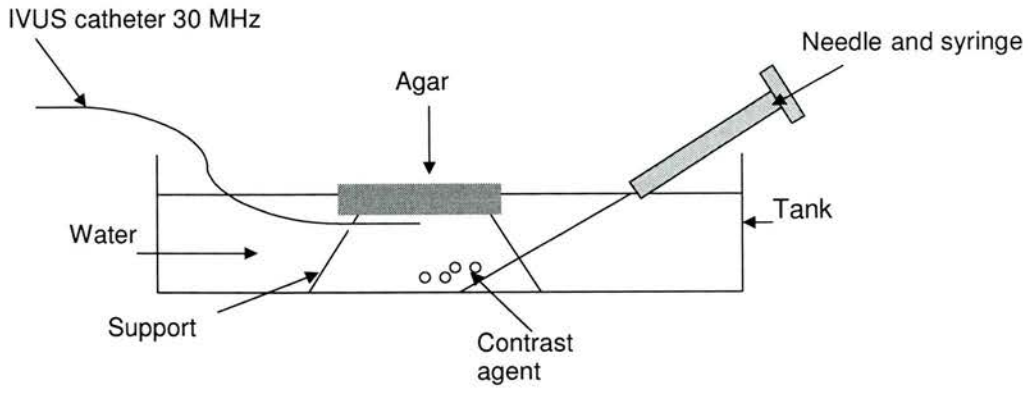

Figure 3.3: Experimental set-up of microbubbles rising to an agar boundary, imaged using a 30 MHz IVUS catheter with the ClearView Ultra scanner.

Initially, agar with no scatterers was used in place of TMM as agar was both optically and ultrasonically transparent. This significantly reduced the bright echo at the water-sample interface; allowing the bubbles at the boundary to be clearly seen. Images captured using this set-up are shown in Figure 3.4 and Figure 3.5. The images were printed from the IVUS scanner on a thermal printer and scanned on to a PC.

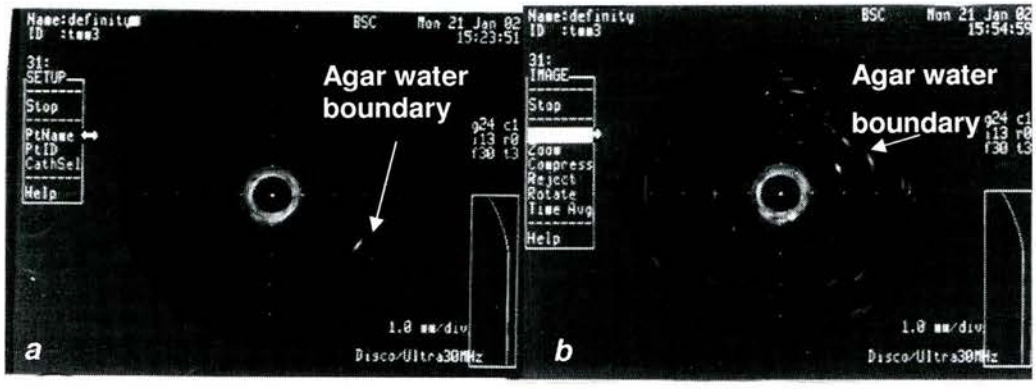

Figure 3.4: a) IVUS image of agar supported in water with no contrast agent added, note the echo from the agar-water interface b) The same agar-water interface after contrast agent was added to the water and allowed to rise to the boundary.

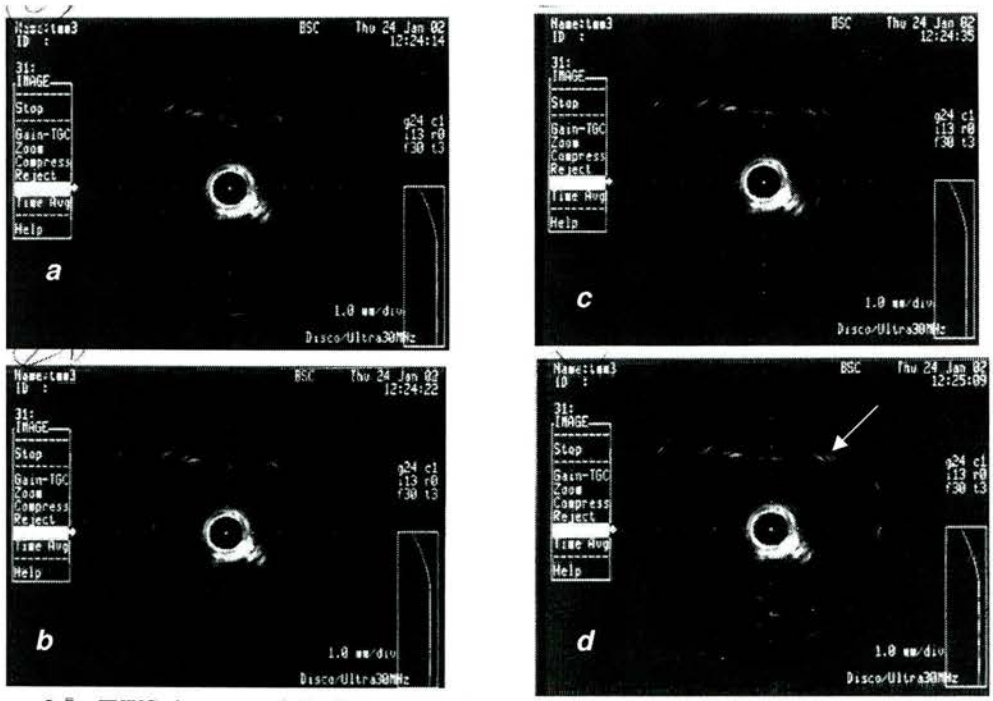

Figure 3.5: IVUS images of Definity bubbles rising up to an agar-water interface over approximately one minute.

The images in Figure 3.5 a-d show bubbles as they rise to the surface of the agar and show how the echo from the boundary changes over 55 seconds. Towards the right of the interface in Figure 3.5d (arrowed), a row of echoes are seen, this is not present in the previous three images. Echoes on the screen could be followed as they rose to the agar boundary although this is not clear in the images obtained.

3.3.3 Discussion

When plain, transparent agar was used in place of the agar with scatterers, the Definity bubbles could be clearly seen once they had reached the boundary. While watching the screen on the scanner it was possible to visually track individual bubbles and observe them come to rest at the interface. However, it was difficult to follow the bubbles the whole way as they drifted in and out of the field of the transducer. When agar with scatterers was used the stronger echo from the boundary was not enhanced by the bubbles. It was difficult to observe if there were bubbles at the boundary or not.

This initial work showed that it was possible to image microbubbles at agar surfaces using IVUS, provided the echo from the surface-water interface was minimised.

3.4 Development of new agent

Work funded by a British Heart Foundation (BHF) grant (Grant PG/03/061 Optimisation of a targeted antibody linked microbubble for ultrasonic imaging of arterial plaque) has involved the in-house development of a new microbubble temporarily named the in-house agent for the purpose of this work. The in-house agent is currently being developed with a view to targeting markers expressed on vulnerable plaques in coronary arteries. It is hoped that 'hot', vulnerable plaques, which are likely to rupture and cause a heart attack can be identified. Although some preliminary work was performed using commercial agents, the development of an in-house microbubble was necessary due to the commercial sensitivity which surrounds currently available ultrasonic contrast agents. The in-house microbubble was manufactured within the Tissue Injury and Repair Group, University of Edinburgh, who were collaborators on the BHF grant mentioned previously.

3.4.1 Manufacture of the in-house agent

The protocol for bubble manufacture was as follows. The lipid constituents of the microbubbles, Phosphatidyl Choline (PC), Cholesterol, Phosphatidylethanolamine (PE) and Phosphatidyl Glycerol (PG) (Sigma Aldrich Company Ltd, Dorset, UK) were dissolved in chloroform. Nitrogen gas was fed into the mixture causing evaporation which left a lipid residue on the sides and bottom of the container. The residue was reconstituted with cyclohexane and placed in dry ice in preparation for freezing. The mixture was left to freeze overnight and the remaining white powder reconstituted in saline when needed (Moran et al 2004).

3.4.2 Initial Work

The first stage in the development of the bubble was determining the optimal bubble composition. Appendix 1 contains a review of the optimisation tests on the agent described in this chapter, and also describes the various agent compositions tested in-order to produce a contrast agent echogenic at 40 MHz. The shell constituents were phospholipids which included cholesterol. Different concentrations of cholesterol in the shell were tested. The different proportions were studied to identify the concentration of cholesterol which gave the most echogenic microbubble. Solutions of 2.5, 5 and 15 mg of liposomal powder per ml of saline were used to determine the variation in echogenicity with concentration. Nitrogen (N_2) and Helium (He) were used during the preparation of the agent. N_2 and He were bubbled through the agent by placing the gas tube at the bottom of the container, allowing the gas to be bubbled into the mixture. N_2 and He were also incorporated by agitation of the agent with the gas tube being placed at the surface of the mixture. Using this method the gas was incorporated during the agitation of the agent. After ultrasonic imaging of the bubbles containing different gases, it was determined that the N_2 bubbled on top of the solution gave the most echogenic microbubble so was used for future bubble construction. More concentrated samples of 75 and 100 mg of liposomal powder per 1 ml saline were also tested. Examples of the IVUS images obtained from the agent are shown in Figure 3.6. An image showing saline only (Figure 3.6a) and the undiluted agent (Figure 3.6b) are shown along with an image for the agent in a 1:4 saline solution (Figure 3.6c).

In order to obtain quantitative information about the echogenicity of the agent, a data capture card was added to the PC. This allowed the radio-frequency (RF) signals to be captured and digitised and values for the mean backscatter power to be obtained.

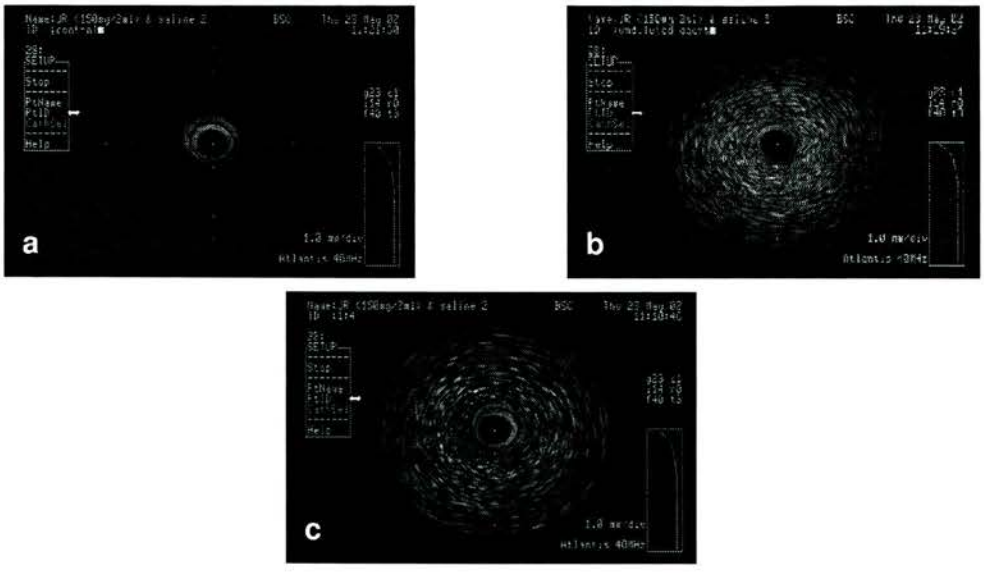

Figure 3.6: Images printed from the scanner, a) saline with no agent, b) the in-house agent of 75 ml of liposomal powder per ml saline, c) the in-house agent diluted to a 1:4 concentration with saline.

3.4.3 Data Capture

The digitising card (Gage Applied CS8500, Gage Applied Technologies, Lachine, Canada) was used to collect RF data for each experiment with the in-house contrast agent. The RF data was used in conjunction with the IVUS images to determine the variation in echogenicity of the in house microbubble during the various stages of characterisation. The data capture card which could digitise up to 500 Msamples per second was used to digitise the data to 8 bits at 250 Msamples per second. Programs had been previously written in IDL by Dr Robin Watson, Medical Physics, University of Edinburgh, for the analysis of contrast data, these were used in analysis of the captured data. A region of interest was chosen at the same point in each sample. Each region of interest contained 9 ultrasound lines of data with 128 points per line. The chosen region was centred about line 90 at a distance of 660, where 660 corresponded to 2mm from the centre of the transducer. Figure 3.7 shows a selected region of interest showing the area containing the 9 lines of data.

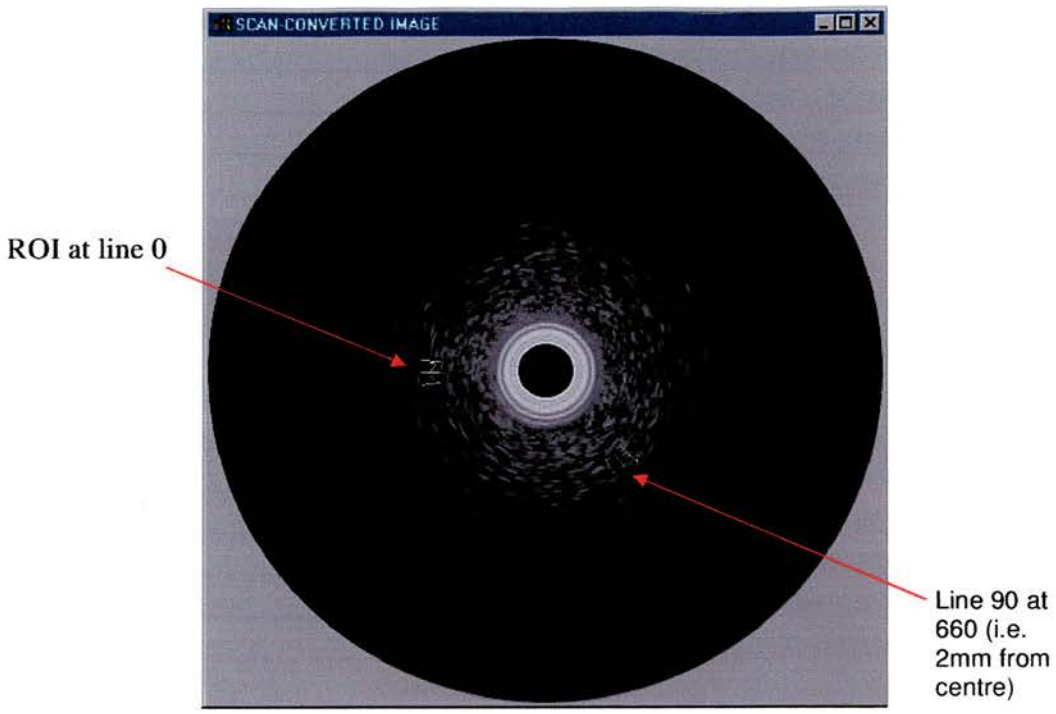

Figure 3.7: Reconstructed IVUS image from RF data showing the position of line 0 and line 90 at a distance corresponding to 660.

The perfect reflector data was determined using an air-water interface. The echo was maximised at a distance of 2 mm from the catheter and the RF data captured. The mean backscatter power over the region of interest was then calculated and plotted for each concentration. Data was also collected for the undiluted agent and the dilutant.

3.4.4 Comparison to different agents

The data capture card was used in experimental work to compare the in-house agent to present commercial contrast agents at high frequencies. The variation in mean backscatter power for each commercial agent is shown in Figure 3.8. The point representing the in-house agent was at the same concentration as the commercial agents and compares well.

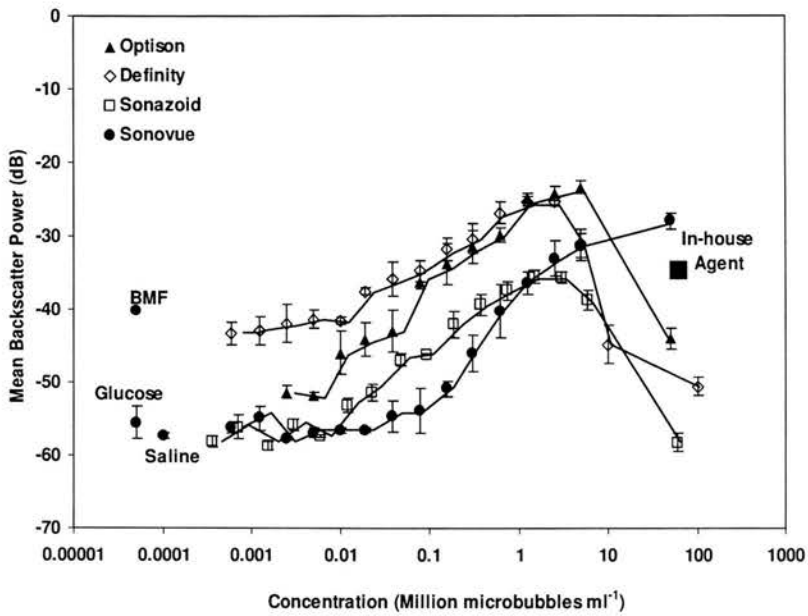

Figure 3.8: Graph showing the mean backscatter power with concentration for four contrast agents. These are compared to the mean backscatter power for the in-house contrast agent. (Courtesy of Dr C.M. Moran)

3.4.5 Frequency tests

During the experimental work the ClearView Ultra scanner was upgraded to run at 40 MHz for use with the Atlantis 40 MHz catheter (Boston Scientific, Natick, USA). Previously a 30 MHz Disco Ultra catheter transducer had been used, after the upgrade of the scanner Atlantis 40 MHz transducers were used. Comparisons were made between the Atlantis catheter and the Disco Ultra catheter to see how the power spectrum for each transducer varied. Examples of the power spectra from a perfect reflector at each frequency are shown in Figure 3.9. An air-water interface was used as a perfect reflector.

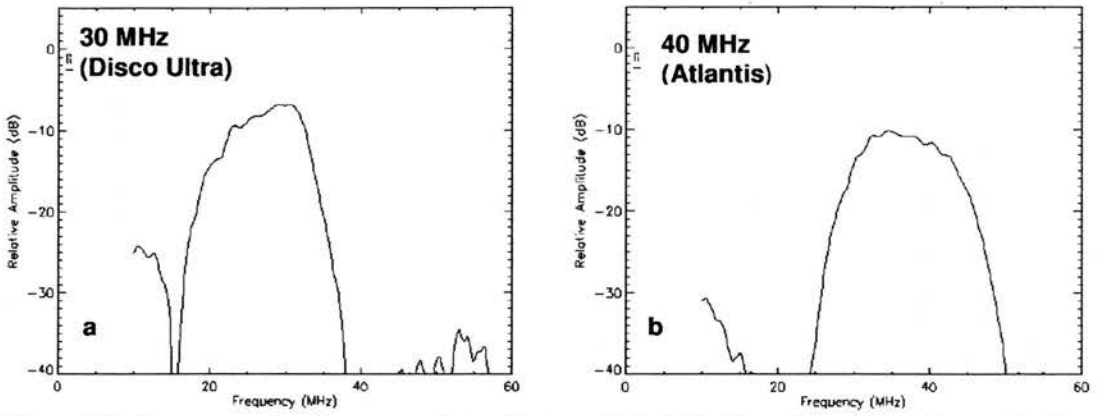

Figure 3.9: Power spectra from a perfect reflector a) 30 MHz Disco Ultra Transducer, b) 40 MHz Atlantis Transducer.

The bandwidths at -6 dB for each frequency are shown in Table 3.1[2]. The centre frequency for each transducer is also given. For 40 MHz, the centre is 35 MHz and for 30 MHz it is 27 MHz. The increase in centre frequency was 8 MHz.

	40 MHz	30 MHz
-6 dB Bandwidth (MHz)	30-46	20-35
Centre Frequency (MHz)	35	27

Table 3.1: -6 dB bandwidth and centre frequency, determined using a perfect reflector, for the 30 MHz and 40 MHz IVUS transducers used with the ClearView Ultra scanner.

3.4.6 Timed and Gas Tests

To investigate the change in echogenicity with time, images of an undiluted sample were captured every 30 minutes. The sample was then imaged after 24 and 47 hours with images and RF data being captured. Before imaging, the sample was gently inverted to re-suspend the microbubbles in the saline. Figure 3.10 shows that the bubbles remained significantly echogenic with time. The mean backscatter power is given in Table 3.2. The error shown is the standard deviation in three measurements. There was no significant variation in the mean backscatter power over the three days for which the sample was tested.

[2] The -6 dB bandwidth was taken instead of the -3 dB bandwidth as the IVUS transducers were both transmitter and receiver.

RF data was also captured for microbubbles made using Nitrogen and Helium, the mean backscatter powers are given in Table 3.3. There was no significant difference between the mean backscatter for the two types, although there was a larger standard deviation associated with the microbubbles containing helium. It was thought that air may be incorporated into the microbubble during manufacture, the sample made with no extra gas confirms this as the mean backscatter power was not significantly different from that of the sample containing helium and nitrogen.

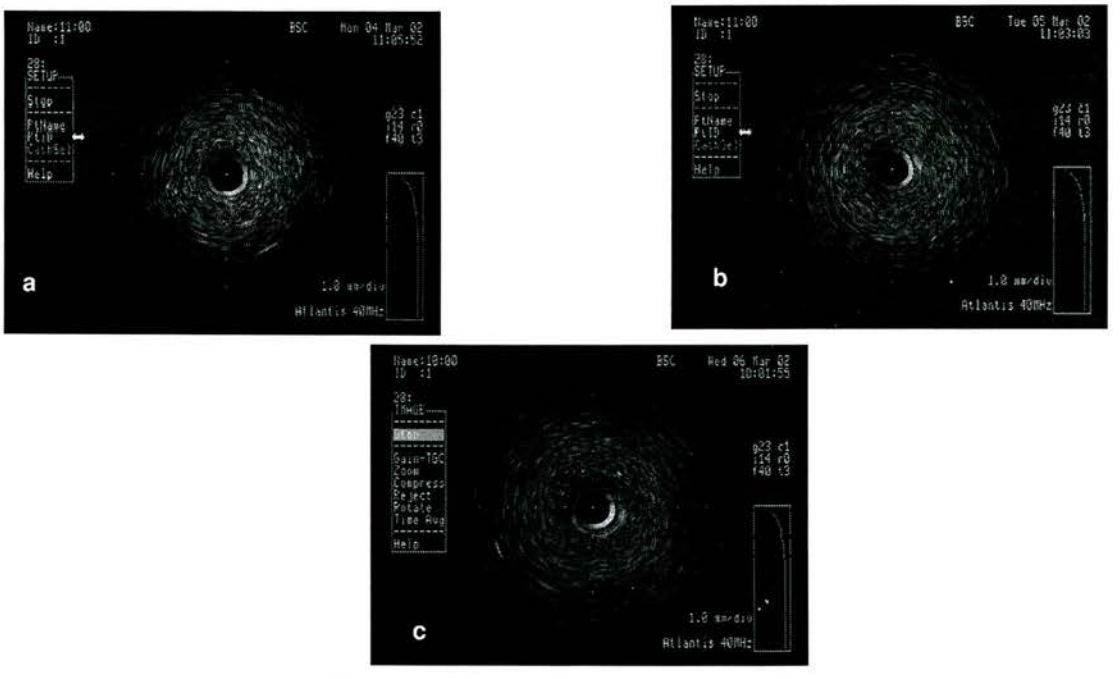

Figure 3.10: a) in-house agent at time =11.00, b) in-house agent day 2 at time= 11.00, c) in-house agent day 3 at time= 10.00. The samples were inverted prior to imaging each time to ensure the microbubbles were suspended in the saline.

Time	Mean backscatter power (dB)
1 (0)	-30 ± 2
2 (+24 hours)	-31 ± 1
3 (+47 hours)	-32 ± 1

Table 3.2: Mean backscatter power from in-house agent over three days.

Gas used in microbubble manufacture	Mean backscatter power (dB)
No gas (air)	-30.9 ± 0.4
Nitrogen	-31.5 ± 0.8
Helium	-31 ± 4

Table 3.3: Mean backscatter power from-house microbubble made using no gas, nitrogen and helium.

3.4.7 Targeting in-house agent

Since the motivation for developing the microbubble was to target it to bind to specific sites, work was completed on incorporating biotin into the bubble shell. Biotin could be used with avidin for attachment of the in-house microbubble as described in section 2.2.4.1. Biotin was added as 1% of the mixture at the initial lipid mixing stage of the manufacture process described in part 3.4.1 of this chapter.

Prior to the attachment of the microbubbles, the echogenicity of the biotinylated microbubbles was investigated. IVUS was used to image microbubbles with biotin incorporated into the shell. The backscattered power was determined as described previously. The addition of biotin to the shell was found not to affect the echogenicity of the microbubbles. For in-vivo use streptavidin could be used to bind the biotin in the microbubble shell to a biotinylated antibody which, in turn could bind to an antigen.

3.4.8 Size distribution of the in-house contrast agent

In order to determine the size distribution of the in-house contrast agent a Malvern Mastersizer 2000 (Malvern Instruments Ltd, Enigma Business Park, Malvern, UK) was used. The Mastersizer was used during the development of the in-house contrast agent to assess the change in size distribution of the agent when subjected to different manufacture techniques and when made with variations in the proportion of constituent ingredients. This is discussed further in Chapter 6. Figure 3.11 shows the size distribution of the in-house contrast agent when made containing biotin, the d(0.5) (diameter for which 50% of the particles measured are less than) is 1.229 μm.

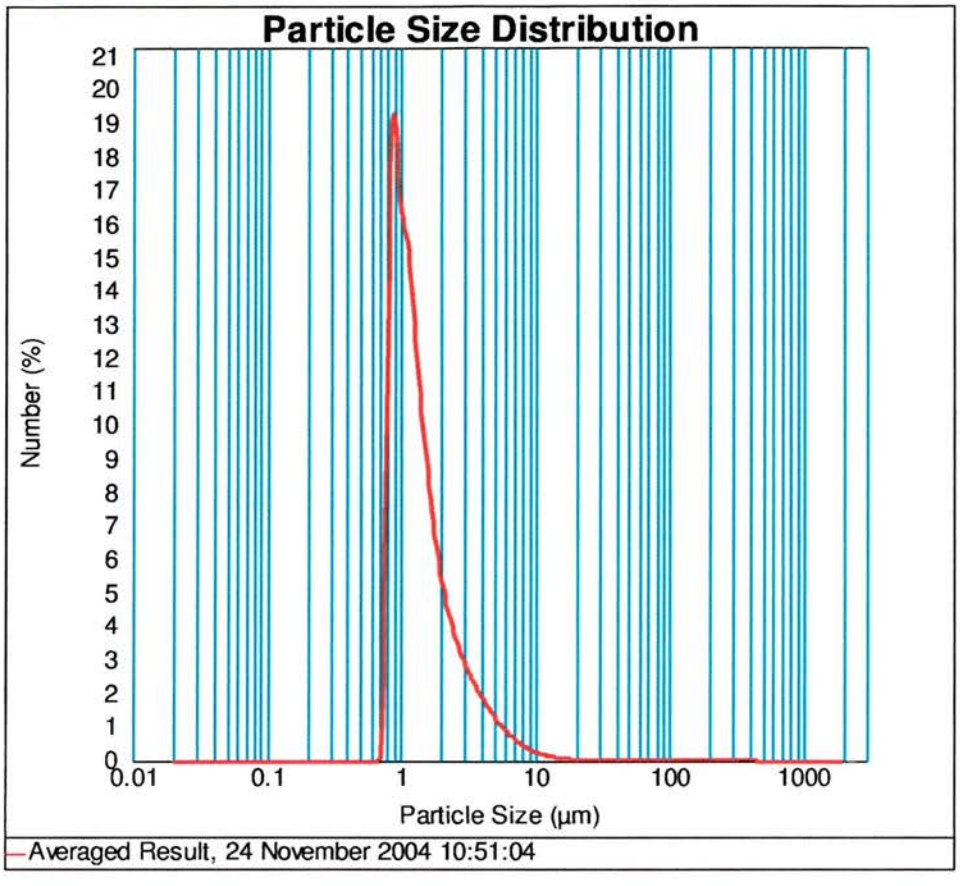

Figure 3.11: Size distribution of in-house contrast agent containing 1% biotin. Measured using a Malvern Mastersizer 2000.

3.4.9 Summary

The microbubble being developed was tested and was shown to be long-lasting, echogenic for up to 47 hours and echogenic at intravascular frequencies of 30 and 40 MHz.

The microbubble was adapted for targeting. Biotin was incorporated into the shell; the echogenicity of the bubble was unaffected. Since the bubble could potentially be targeted to bind to specific sites, work commenced on developing surfaces to which microbubbles could be attached, and which would be suitable for ultrasonic imaging.

3.5 Tissue Mimicking Material

3.5.1 Tissue mimicking materials

Previous work in this chapter has shown that it was easier to image microbubbles at boundaries when the material forming the boundary was not echogenic or had low echogenicity. Agar based tissue mimicking material (TMM) contains aluminium oxide (Al_2O_3) (size: 0.3 μm and 3 μm) and silicon carbide (SiC) (400 grain). These particles act as scatterers and the combination of all of the scatterers, the agar and glycerol produces a material which has the acoustic properties of soft tissue (Teirlinck et al 1998). It was thought that making the TMM recipe with less aluminium oxide scatterers would reduce the echogenicity of the sample and hence make microbubbles at the interface easier to image with ultrasound. This was confirmed when using the plain agar with IVUS shown in Figure 3.4 and Figure 3.5. The bubbles could be clearly seen against the agar-water interface. The acoustic properties of plain agar however are not ultrasonically the same as tissue, as the speed of sound is not the same due to the lack of glycerol in the recipe and the echogenicity is reduced due to the lack of scatterers.

In order to find an agar based sample which would be practical for ultrasonic imaging of attached microbubbles, agar samples based on a standard tissue mimic recipe, with different concentrations of scatterers were made. The acoustic impedance of each one was calculated for comparison with physiological values.

3.5.2 Recipes and Methods

The standard TMM recipe was followed but the concentration of particles was reduced. Agar samples containing 0%, 10%, 30%, 50% and 100% of particles of Al_2O_3 and SiC required for TMM were made using the following recipe.

3.5.2.1 TMM ingredients and recipe

The ingredients for standard TMM by percent of total mass are given in Table 3.4. To obtain the different agar samples of 0%, 10%, 30% and 50% scatterer concentration, the ingredients as in Table 3.4 were used but the percentage of SiC

and Al_2O_3 were varied according to the sample required (i.e. 0% contained no scatterers, 10% contained 10% of the mass of SiC and Al_2O_3 (the scatterers) shown in Table 3.4 and 100% contained 100% of the mass of the scatterers.)

Ingredient	% mass (%)
Water	79.04
Glycerol (99% solution)	11.32
Rodalon Benzalkoniumchloride (10% solution)	4.6
Silicon Carbide powder (SiC) (400 grain)	0.56
Aluminium oxide powder (Al_2O_3) (0.3 μm)	1.00
Aluminium oxide powder (Al_2O_3) (3 μm)	0.93
Agar	3.18

Table 3.4: Ingredients for tissue mimicking material.

3.5.2.2 Method

The dry and wet ingredients were weighed and mixed together separately. The water, glycerol and Rodalon were placed in a large heatproof beaker and secured in a temperature controlled water bath. A stirrer was placed in the solution and set to rotate to approximately 2.5 revolutions per second. The dry ingredients were slowly added to the solution ensuring that none remained on the inside of the beaker or the stirrer. This ensured that the particles were well mixed into the tissue mimic. A lid was kept on the beaker in the waterbath at all times during heating and cooling to minimise evaporation of water from the mixture.

The solution was heated to 96 °C using the water bath and left at this temperature for one hour. The mixture was continuously stirred during this time. After an hour, the mixture was cooled to 42 °C. Stirring was continued during this time to keep the particles homogenously distributed in the mixture. The TMM was poured into moulds once it had reached 42 °C since at this temperature the particles would not settle in the mixture as it set.

When the TMM was not in use, it was stored in a solution of 10% water-glycerol in an airtight container. This kept the concentration of glycerol in the samples constant. When stored in water, the glycerol eventually diffuses out; changing the acoustic properties of the samples (Hall et al 1997).

3.5.3 Acoustic Impedance

Since the number of scatterers in the agar based samples was reduced, the acoustic properties would be different to that of TMM. The attenuation and backscatter of the sample is dependent on the concentration of scatterers within the agar. The speed of sound is dependant on the concentration of glycerol which was not changed in the different samples hence the speed of sound in each sample should have remained the same.

Acoustic impedance is calculated using,

$$Z = \rho c \qquad (2.1)$$

Where Z is the acoustic impedance (kg m^{-2} s^{-1} or MRayl), ρ is the density of the material (kg m^{-3}) and c is the velocity of the sound (m s^{-1}). The size of the echo from a surface depends on the difference in acoustic impedances of the materials making up the interface.

To confirm that the speed of sound in the samples did not vary with different amounts of scatterers, and to allow the calculation of the acoustic impedance of each sample, the scanning acoustic macroscope (SAM) (Ultrasonic Sciences, Aldershot, Hants, UK) was used.

3.5.4 Materials and Methods

3.5.4.1 Scanning Acoustic Macroscope

A diagram of the scanning acoustic macroscope is shown in Figure 3.12. The SAM is formed by a single element focused transducer which operates in pulse echo mode. The measurements were made in a water bath which was kept at a constant temperature. The transducer was focused on the surface of a reflector and a reference dataset was collected. The transducer was then raster scanned over the sample surface. At each point the pulse from the transducer travels through the sample and a proportion of the incident signal is reflected back to the receiver. The received echo is digitised. Programs have been previously written in MATLAB (Version 6.5.0.1, The Mathworks Ltd, Cowley Park, Cambridge, UK) for the analysis of SAM data

(Inglis 1999, Ramnarine and Browne 1999). The speed of sound through the sample and the attenuation of the sample can be calculated. The difference between the peaks of the reference and sample data is used to calculate the speed of sound in the sample. For each set of data analysed the thickness of the sample and the reference speed of sound is required.

3.5.4.2 Experimental Methods

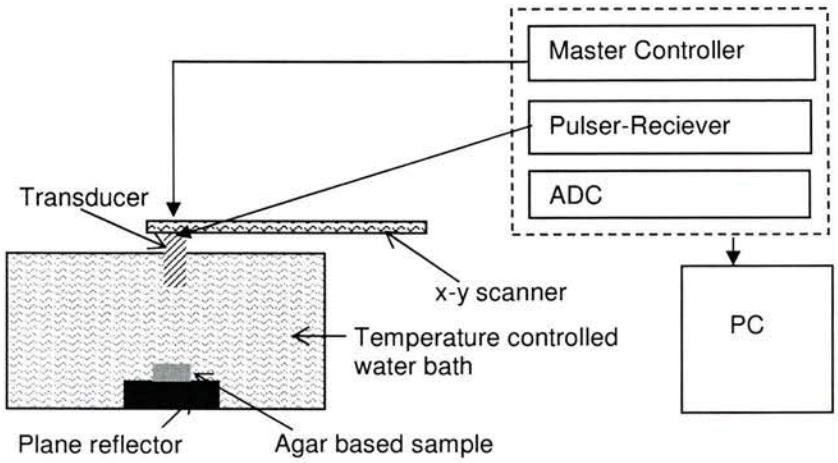

Figure 3.12: Diagram of scanning acoustic macroscope for determining the speed of sound through the agar based samples.

The agar samples, with different concentrations of particles, were cut to disks of 25 mm diameter and 5 mm depth. A water bath was filled prior to experiments and left to degas for a minimum of 24 hours.

A steel block acting as a plane reflector was placed in the base of the water bath. The temperature of the water was constantly monitored, the temperature of the water ranged from 20.0 to 20.8 °C. The reference speed of sound used in the analysis was 1482 m s^{-1}, which is the speed of sound in water at 20 °C. The SAM system running at 7 MHz was aligned over the steel reflector. The focal point for the transducer was 54 mm and the frequency range was 5.5 – 10.5 MHz. The signal was maximised and the transducer focused onto the reflector. The transducer was raster scanned over the surface, covering an area of 16 mm x 16 mm. Reference measurements were made at

the surface of the reflector. The transducer was then aligned over the sample and measurements of attenuation and speed of sound through it were made.

Two separate samples for each concentration of scatterers were measured. For analysis purposes the thickness of each sample was measured using a digital micrometer.

Each sample was then weighed and the volume calculated using the cross-sectional area and sample height. These values were used to calculate the density of the samples, which was in turn used in the calculation of acoustic impedance.

The SAM data was analysed using the pre-written in-house software. A map of attenuation across the sample was displayed during analysis. This enabled selection of data from a region of interest (ROI). Areas where the SAM scanned off the surface of the sample on to the reflector could be removed. The mean speed of sound and attenuation through each sample were then determined from the ROI.

3.5.5 Results

The speed of sound, attenuation and calculated acoustic impedance for each of the samples are shown in Table 3.5. The speed of sound values are the mean values of the speed of sound through the regions of interest in two different samples. The error associated with each value is the mean standard deviation for the ROIs. The variation of acoustic impedance with each sample is shown in Figure 3.13.

Sample (% mass of scatterers in agar)	Attenuation (dB cm^{-1} MHz^{-1})	Speed of sound (SAM) (m s^{-1})	Acoustic impedance (MRayl)
0	0.20 ± 0.01	1539 ± 2	1.570 ± 0.003
10	0.21 ± 0.01	1538 ± 4	1.629 ± 0.004
30	0.23 ± 0.08	1543 ± 4	1.666 ± 0.004
50	0.44 ± 0.09	1544 ± 4	1.675 ± 0.004
100	0.52 ± 0.01	1542 ± 4	1.680 ± 0.004

Table 3.5: Attenuation, speed of sound and acoustic impedance values for the TMM samples. The errors in the speed of sound values are one standard deviation of the mean speed of sound.

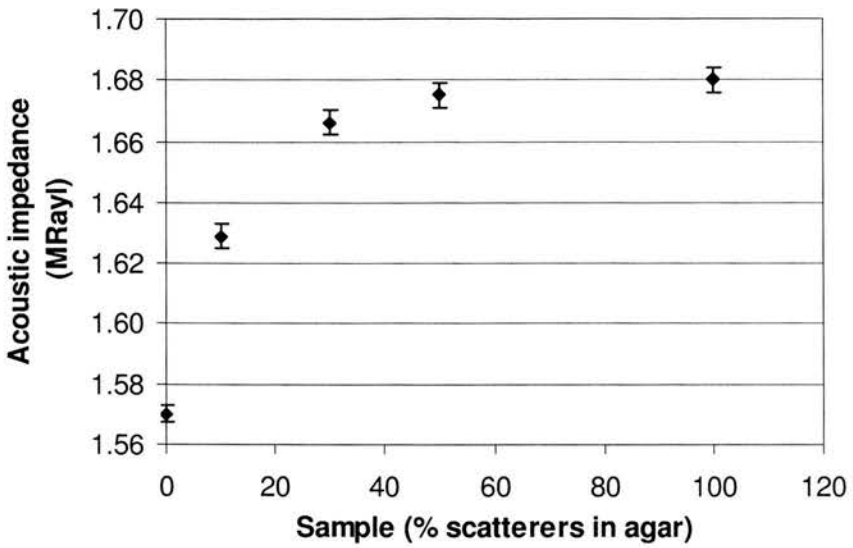

Figure 3.13: Acoustic impedance calculated for each agar sample where 0% contains no scatterers and 100% contains 100% of the scatterers needed for tissue mimicking material.

3.5.6 Discussion

The values of acoustic impedance for the different samples were compared to published values for the aortic wall and the aortic wall with different types of lesion (Goss et al 1978). The comparisons are shown in Table 3.6. The measured values are not the same as the aortic values but there were similarities and the recipes for the agar samples could potentially be modified to better mimic the acoustic impedance of different lesions if required.

Agar sample (% scatterers)	Acoustic Impedance (MRayl)	Structure	Acoustic Impedance (MRayl)
0%	1.570 ± 0.003	Aortic wall	1.56
10%	1.629 ± 0.004	Aortic wall/atherosclerotic ruptured lesion	1.60
30%	1.666 ± 0.004	Aortic wall/atherosclerotic fibrous lesion	1.65
50%	1.675 ± 0.004	Aortic wall/atherosclerotic fatty lesion	1.69
100%	1.680 ± 0.004	Aortic wall/atherosclerotic calcified lesion	1.76
Water at 20°C	1.48	Blood	1.67

Table 3.6: Measured acoustic impedance in agar samples with difference concentrations of scatterers compared to published values of acoustic impedance of different lesion types (Goss et al 1978).

3.6 Imaging bubbles attached to TMM

Once the microbubbles had been adapted for targeting and binding they were attached to the agar samples.

3.6.1 Methods

The agar containing 0% scatterers was used as this had the lowest impedance mismatch with water and so the echo from the agar surface was less echogenic than the other samples. The lipid-based, biotinylated bubbles were made and attached to 0% scatterer agar in-house. To attach the microbubbles, agar samples were coated with 1 ml of streptavidin (a form of avidin) in a coating buffer (0.5 ml streptavidin per 6 ml buffer) and left for 20-24 hours. They were then washed with saline and 1 ml of blocking buffer (saline and 1% BSA) was added and left for 2 hours. The samples were washed again with saline, and 200 µl of the in-house microbubble was added, at a concentration of 30 mg per 2 ml saline, and left for a further 2 hours. Finally the samples were washed with saline again to remove any excess unattached microbubbles.

To investigate how the speed of sound through the samples was affected by the use of streptavidin, agar samples with and without streptavidin were tested in the SAM system using the methods described previously. Samples with 0% and 100% scatterers were tested. Two different samples of each were used.

The samples with microbubbles attached were then imaged with IVUS at 40 MHz. Initially an agar sample before and after the addition of streptavidin was imaged. This was to determine if there were any changes in the ultrasound image due to the streptavidin.

3.6.1.1 IVUS imaging of attached contrast agent

Following this a block of TMM with a wedge cut-out as shown in Figure 3.14 was used as a support for the samples to sit on. The block and sample were submerged in water. The IVUS transducer was placed underneath the sample in the wedge and the attached microbubbles were imaged through the sample. The sample was then inverted and imaged again. Images were printed from the IVUS scanner and also saved to PC using image capture software (Matrox Intellicam software, Matrox VITE Ltd, Bucks, UK). This was repeated with agar samples made containing 10% scatterers.

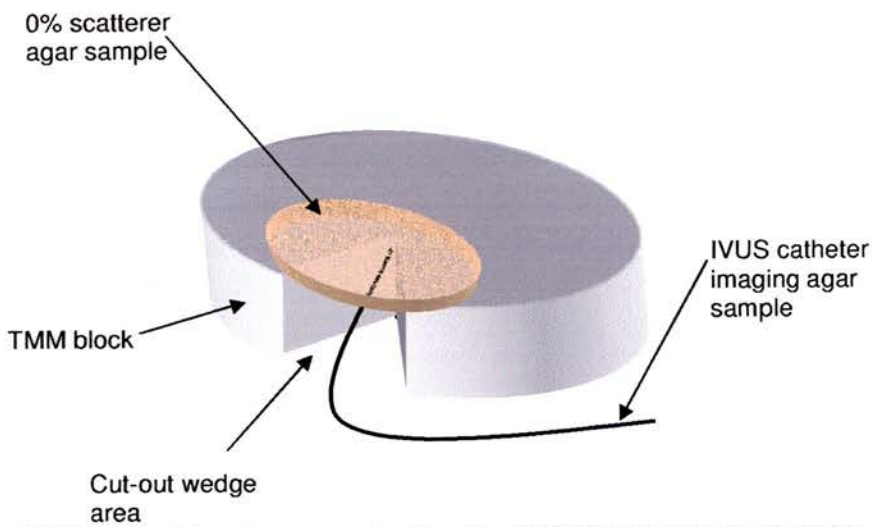

Figure 3.14: TMM block with wedge area cut-out to allow IVUS imaging of microbubbles attached to 0% scatterer agar. The TMM block and agar sample were submerged in water.

3.6.1.2 Imaging attached contrast agent with transcutaneous transducers

A similar set-up as previously described was used with the transcutaneous transducers. Microbubbles were attached to the agar samples using streptavidin and biotin. The block of TMM with the wedge shape cut out was used to hold the agar samples. The samples were then imaged at a low middle and high power. Initially a sample without microbubbles attached was imaged. The images were saved on the scanner as bitmap files. The characterisation of these transducers is described in Chapter 4 where the peak negative acoustic pressures were determined.

3.6.2 Results

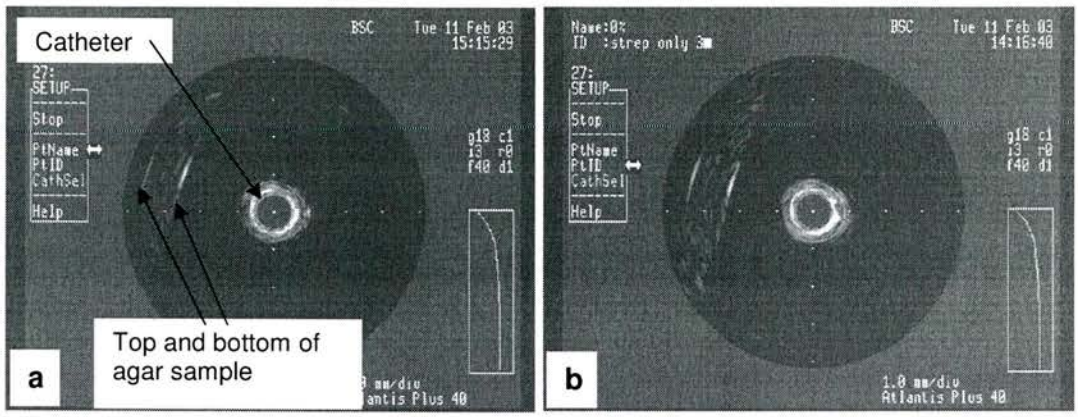

Figure 3.15: IVUS images of 0% scatterer samples. a) sample with nothing on, b) sample coated with streptavidin.

3.6.2.1 IVUS

IVUS images of the unaltered samples and samples coated in streptavidin are shown in Figure 3.15. There is little visual difference between the two images. The speed of sound through samples with 0% and 100% scatterers is shown in Table 3.7. The errors are one standard deviation of the mean.

Agar sample (% scatterer content)	Speed of sound (m s^{-1})
0% no streptavidin	1539 ± 3
0% with streptavidin	1542 ± 4
100% no streptavidin	1536 ± 3
100% with streptavidin	1536 ± 3

Table 3.7: Speed of sound values from SAM data for agar samples with 0% and 100% scatterers, with and without streptavidin. The errors in the speed of sound are one standard deviation of the mean.

Figure 3.16 shows 0% scatterer samples with no microbubbles attached (a) and 0% samples with microbubbles attached (b). The edge of the sample with bubbles attached is enhanced by the microbubbles. On inversion of the sample the line of bubbles can be seen again in (c). Before imaging, the samples were submerged in water to remove any bubbles which were not attached to the sample.

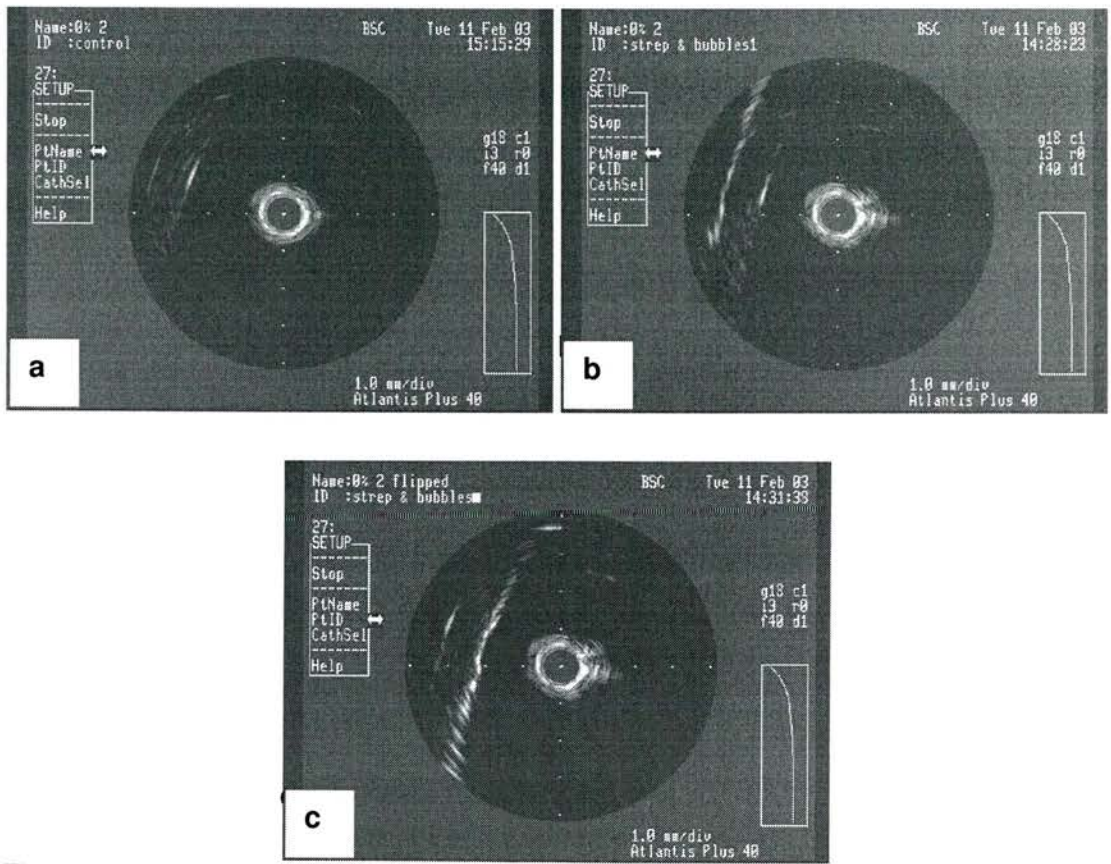

Figure 3.16: Agar based, 0% scatter samples: a) no bubbles attached, b) bubbles attached, c) sample with bubbles attached – inverted (edge with bubbles attached closest to transducer).

The bubbles attached to the agar samples containing 10% scatterers were more difficult to see in the IVUS images. Images of agar samples containing 10% scatterers with and without bubbles attached are shown in Figure 3.17. It is difficult to see any notable difference between the two samples meaning that if the microbubbles are targeted to tissue with an acoustic impedance of that of the agar with 10% scatterers, B-mode imaging of the microbubbles may not be possible. Other detection techniques may need to be employed.

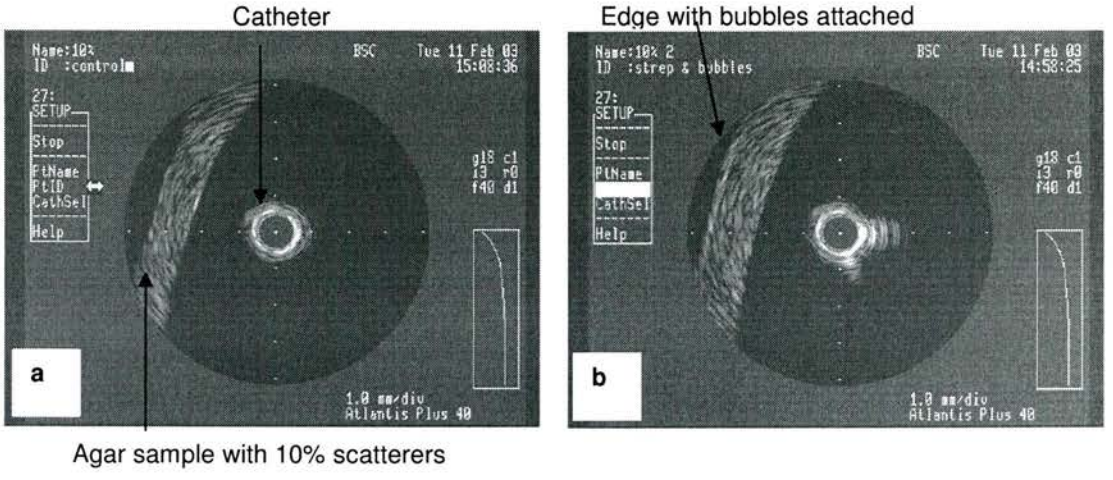

Figure 3.17: Agar samples containing 10% scatterers, a) no bubbles attached, b) bubbles attached.

3.6.2.2 Transcutaneous Transducers

An image of the 0% scatterer agar with no microbubbles attached is shown in Figure 3.18. The probe used was the L5-10 MHz. The sample with microbubbles attached is shown in Figure 3.19. Both images are taken for the same scanner settings and a low transmit power (11%).

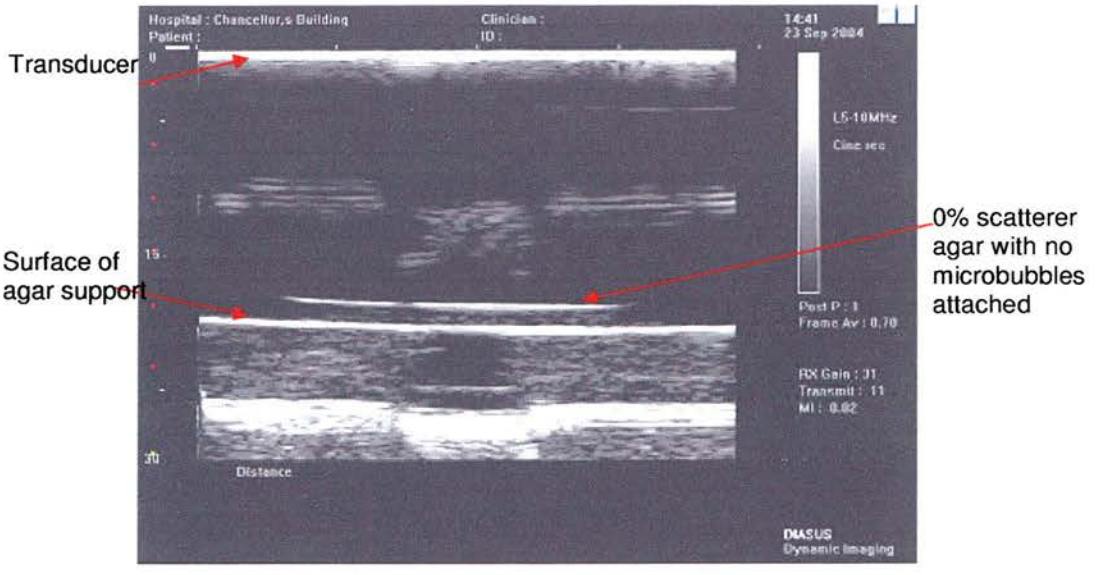

Figure 3.18: Agar sample containing 0% scatterers, with no microbubbles attached imaged with a L5-10 MHz transducer.

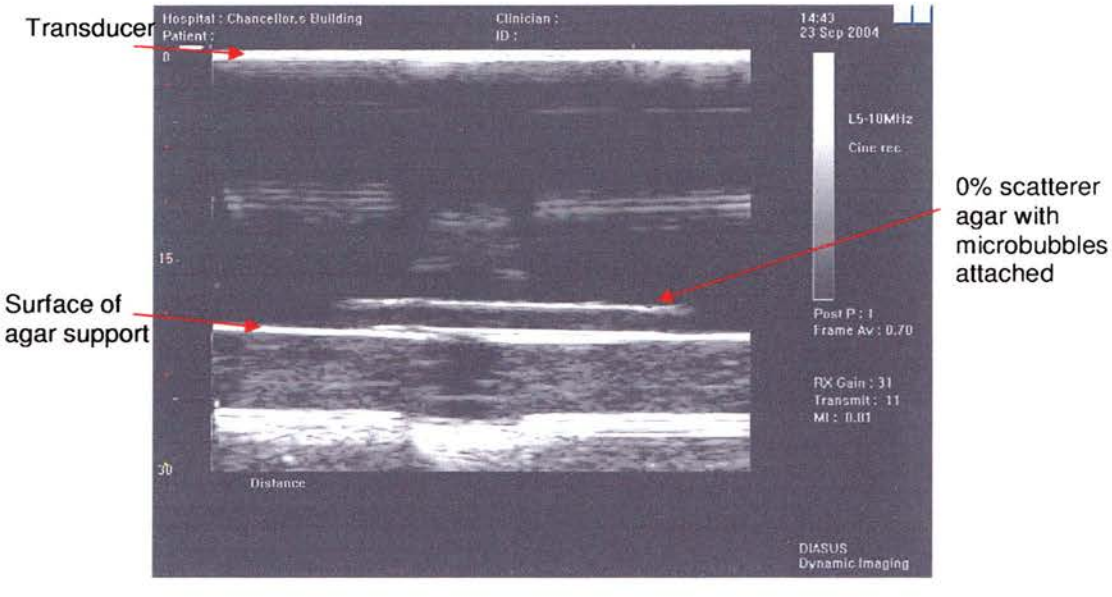

Figure 3.19: 0% scatterer agar samples with in-house microbubbles attached. Imaged with 5-10 MHz linear array transducer.

There was a slight difference in the images obtained with and without contrast agent attached as shown in Figure 3.18 and Figure 3.19, it was difficult to determine where the contrast agent was attached in Figure 3.19. On increasing the transmit power, the echo from the sample surface increased, but there was no obvious surface enhancement due to the attached contrast agent.

Imaging of the contrast agent attached to 0% scatterer agar was repeated with the L16-28 MHz transducer. Images obtained using this transducer are shown in Figure 3.20. Again the transmit power and the gain were the same in each image, the transmit power was at 10%. The microbubbles attached to agar in Figure 3.20c contained a higher percentage of PE (a phospholipid in the agent shell) than the original recipe. This is explained further in Chapter 7. In brief, during optimisation of the in-house microbubbles it was found that increasing the concentration of PE in the microbubble shell increased the backscatter power from the microbubble. In the images shown in Figure 3.20 the surface of the agar samples was enhanced when the microbubbles were attached. The enhancement was greater in the sample with increased levels of PE. On increasing the transmit power there were no observable effects on the microbubbles.

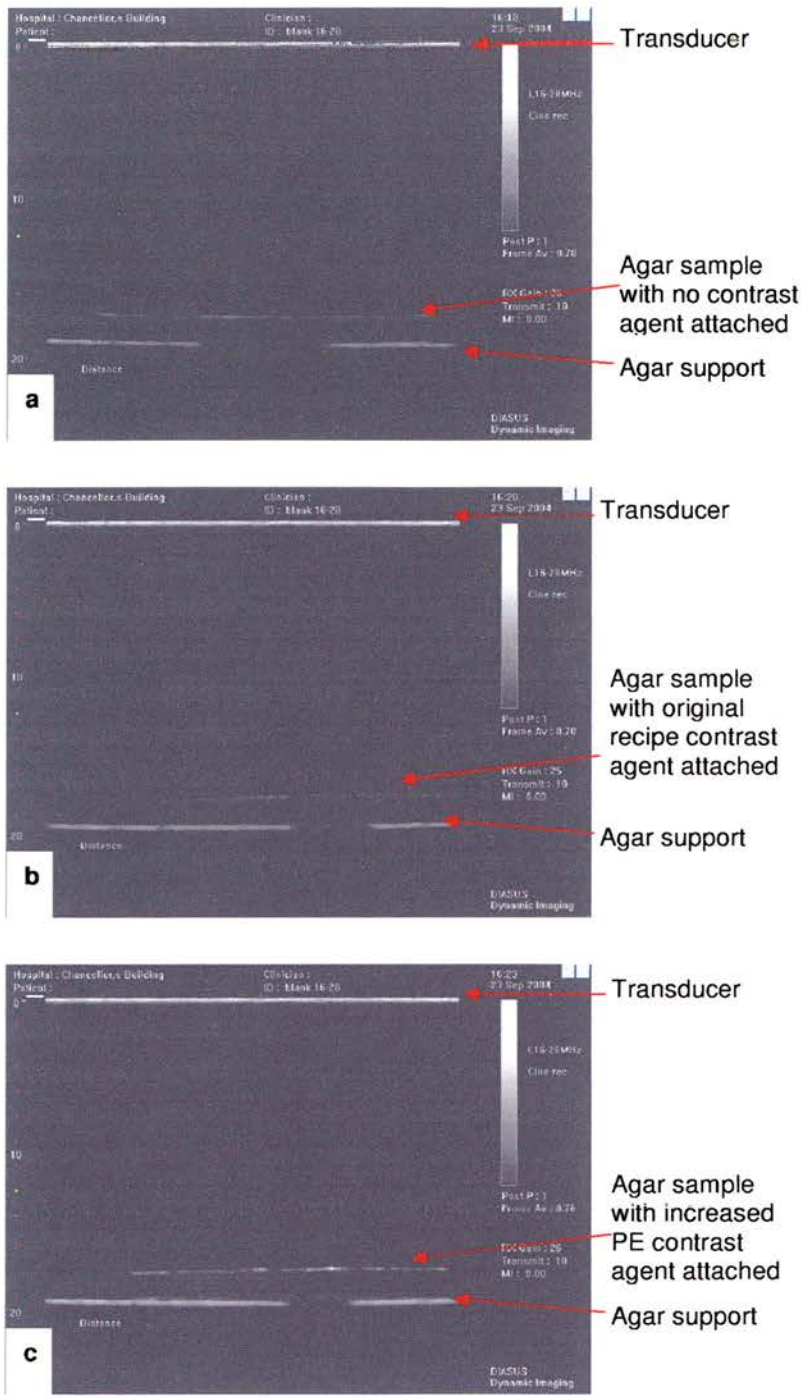

Figure 3.20: Transducer L16-28 MHz a) agar sample with no bubbles attached b) original microbubbles attached to agar, c) microbubbles, with an increased amount of PE in the shell, attached to agar.

3.6.3 Discussion

Agar based tissue mimicking materials have been made containing different concentrations of scatterers. This was in order to find a sample to which microbubbles could be attached and imaged effectively. The SAM system was used to measure the speed of sound through the samples and this was used to find the acoustic impedance of the different samples. The impedances for the samples tested compared well to measured values of acoustic impedance for different lesions on the aortic wall.

The 0% scatterer agar based samples were used as a surface to which the in-house bubbles could be attached. The bubbles were attached to the samples and imaged with IVUS. The microbubbles were also attached to the 10% scatterer agar samples but detection of the microbubbles proved more difficult. The next stage was to image the microbubbles under flow conditions.

When agar samples with microbubbles were imaged with the transcutaneous transducers the agar water boundary was enhanced when the higher frequency probe was utilised. This could have been due to the variation in bubble response with different incident peak negative pressures. The peak acoustic pressures to which the microbubbles were being subjected from the transducers were not known so the differences between the probes was unknown. It would be useful to know the peak pressures from the transducers when imaging microbubbles this would allow some control over the response of the bubbles to the ultrasound. As described in Chapter 7, during the optimisation of the in-house microbubble, increasing the amount of PE in the bubble shell was found to increase the mean backscatter power. When imaged with the L16-28 MHz transducer, the attached contrast agent, made with an increased amount of PE, was shown to increase the echo from the agar boundary as shown in Figure 3.20.

3.7 Imaging bubbles under flow

Once the process of attaching microbubbles to the agar based samples was reproducible and consistent, the attached bubbles were imaged under flow conditions. It was possible to repeatedly attach microbubbles to 0% scatterer agar based samples using streptavidin and biotin and to image the attached bubbles with high frequency ultrasound. A flow chamber had been previously designed in-house based on the work of Rainger et al (Rainger et al 2001) for the purpose of imaging microbubbles attached to agar. Rainger et al had designed a flow chamber which allowed the perfusion of leukocytes over endothelial cells in an effort to determine if stromal cells influenced the adhesion of leukocytes to endothelial cells. Their flow chamber allowed a coculture of endothelial and stromal cells allowing the adhesion of flowing leukocytes to be studied. The initial flow chamber for the study described here was designed by Mr Tom Anderson, Medical Physics, Edinburgh. The flow chamber was used and further developed as described throughout this thesis.

3.7.1 Materials and Methods

3.7.1.1 Flow Chamber

The flow chamber which had been designed and constructed was made of Perspex. A schematic diagram is shown in Figure 3.21 and a photograph of the flow chamber is shown in Figure 3.22. The overall dimensions of the flow chamber were 120 x 40 x 15 mm. In the centre of the chamber were two circular sample wells, 1 mm deep and 10 mm diameter. Below the sample wells was a channel for an IVUS catheter, 95 x 1.5 x 2 mm, above the samples was a flow channel. The flow channel was 1.5 mm high and had tapered ends. The main flow area over the samples was 6 mm wide and 55 mm long. Leur fittings were attached to the ends of the chamber to allow tubing to be secured for flow inlets and outlets. The chamber was in two main layers, the sample wells and IVUS channel within the base layer and the flow channel in the top layer. There were also 12 nuts recessed into the base and glued in place. Between the layers was a rubber lining which acted as a gasket. A small amount of silicon grease was applied to this and 12 screws were used to keep the layers together.

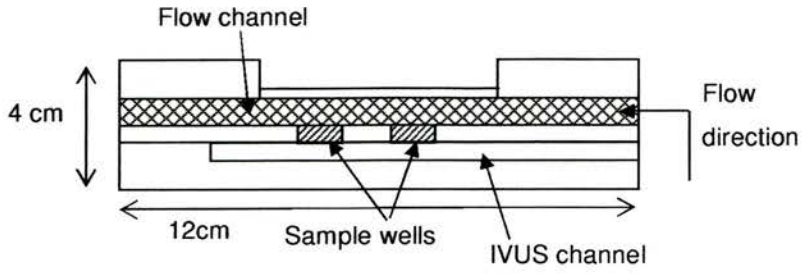

Figure 3.21: Schematic diagram of the flow chamber.

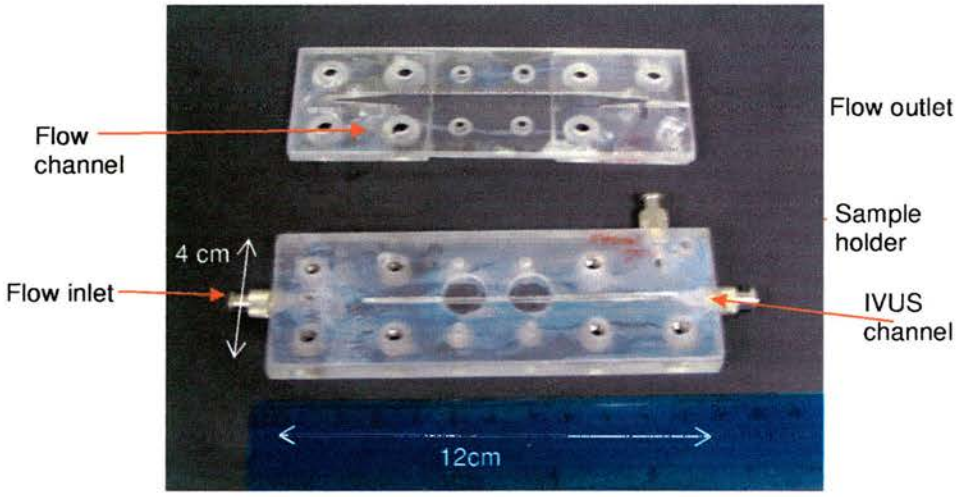

Figure 3.22: Picture of original flow chamber.

3.7.1.2 Methods

The agar samples were cut to the depth of the wells in the flow chamber. A microtome with blade was used to cut the agar to the correct depth for the sample holder. The microbubbles were attached using streptavidin as described earlier with the microbubbles containing 1% biotin. A circular cutter, made from Perspex, with internal diameter the same as the wells was used to cut the sample to the correct diameter for the wells. Agar samples with and without bubbles attached were placed in the chamber. Initially an IV-bag filled with degassed water was used to administer flow. Different flow rates were obtained by varying the height of the bag. The variation of flow rate with height of bag is shown in Figure 3.23. Each point is the

mean of three measurements and the error bars are one standard deviation of these points.

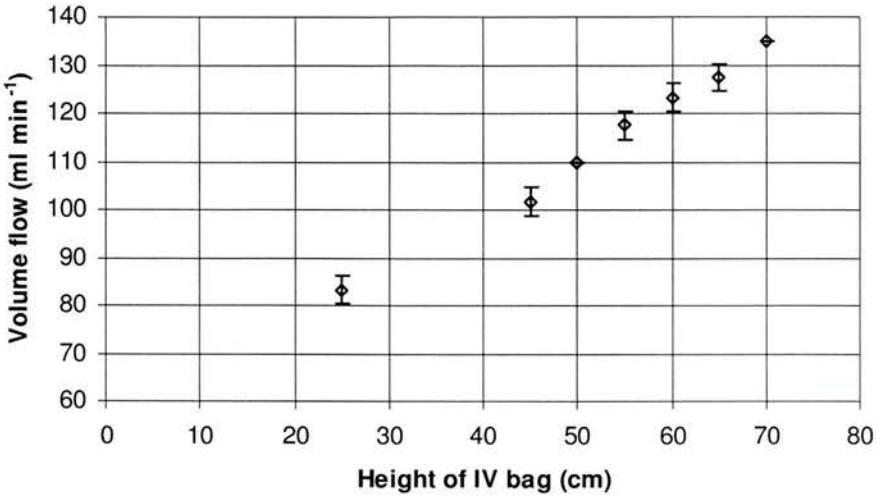

Figure 3.23: Variation of volume flow rate with height of IV-bag. Each point is the mean of three flow rates and the error bars are one standard deviation.

To ensure the microbubbles could be imaged before the chamber was sealed the samples were placed in the chamber, covered with water and imaged using IVUS. After being sealed watertight, flow was started and the microbubbles imaged. The flow rate was initially set to 100 ml min^{-1}.

Once it was established that the bubbles could be imaged in the flow chamber, a range of flow rates were investigated. The IV-bag was tested to ensure that a constant flow rate was delivered. The flow rate through the chamber at different bag heights was then determined. Ideally a pump system would have been used for this work but at the time the IV-bag was most suitable, when increased flow rates were required a pump system was used as described in Chapters 5 and 6.

Microbubbles were attached to 0% scatter agar samples as previously described in section 3.6.1. Samples with and without bubbles were then placed in the flow chamber. A picture of the set up is shown in Figure 3.24. The initial flow was 80 ml min^{-1}; images were saved after 2 and 4 minutes. The flow rate was then increased to

100 ml min^{-1} and images saved after 4 and 6 minutes, finally the flow rate was increased to 135 min^{-1} and the images saved after 2 and 8 minutes.

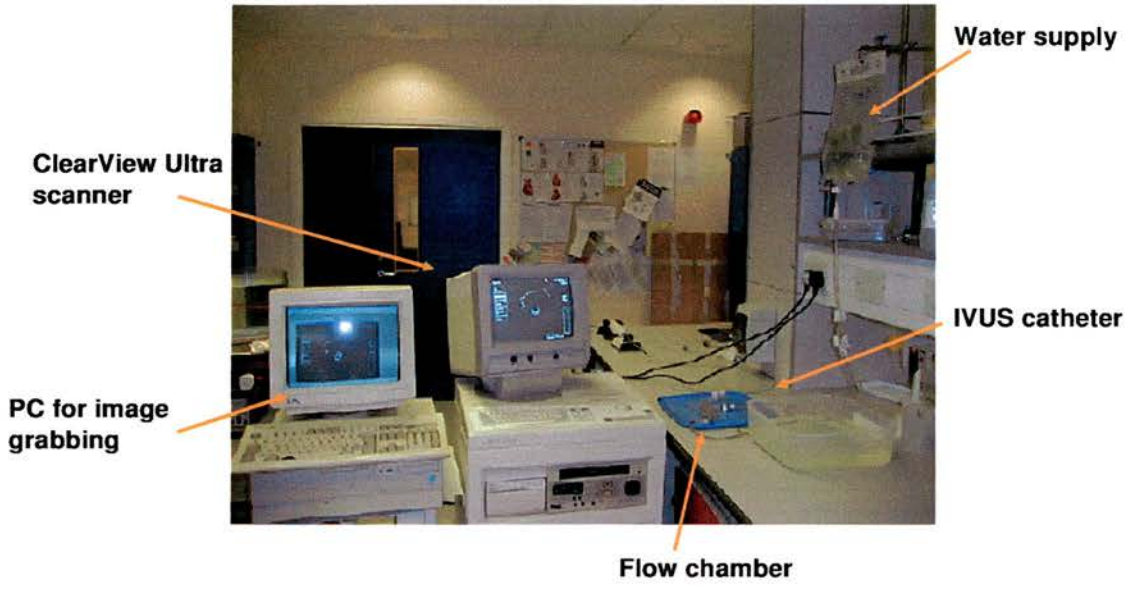

Figure 3.24: Picture of experimental set-up for IVUS imaging attached contrast agent under flow conditions.

3.7.1.3 Results

Figure 3.25 shows samples with and without microbubbles attached under no flow. The line of attached bubbles can be seen in Figure 3.25b. Figure 3.26 shows attached microbubbles when subjected to flow of 100 ml min^{-1}.

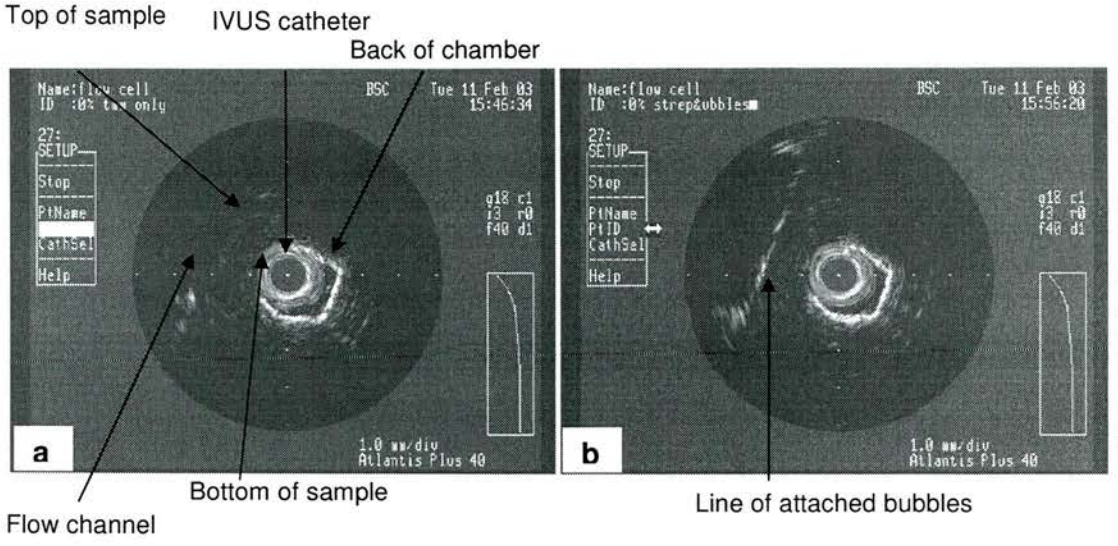

Figure 3.25: a) agar with 0% scatterers with no microbubbles attached b) 0% scatterer agar with in-house microbubbles attached. No flow is present in either situation.

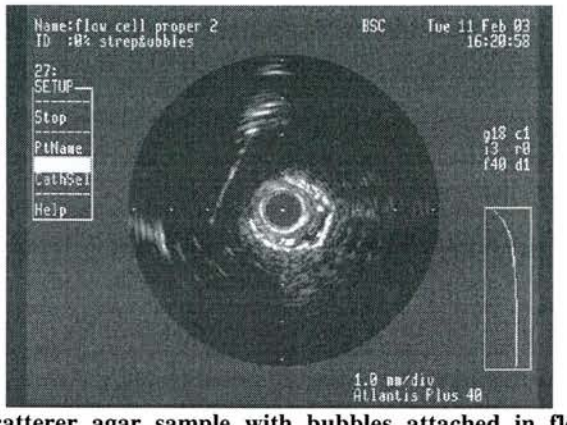

Figure 3.26: 0% scatterer agar sample with bubbles attached in flow chamber. Attached bubbles were subject to flow at 100 ml min^{-1}.

Figure 3.27 shows the attached microbubbles subjected to increasing flow rates. From observing the images, there was no difference in the image as the flow increased, suggesting that the microbubbles remained attached at these flow rates. The flow rate in the left anterior descending coronary artery is 80 – 130 ml min^{-1}, the in-house contrast agent remained attached to the agar under flow rates up to 135 ml min^{-1}.

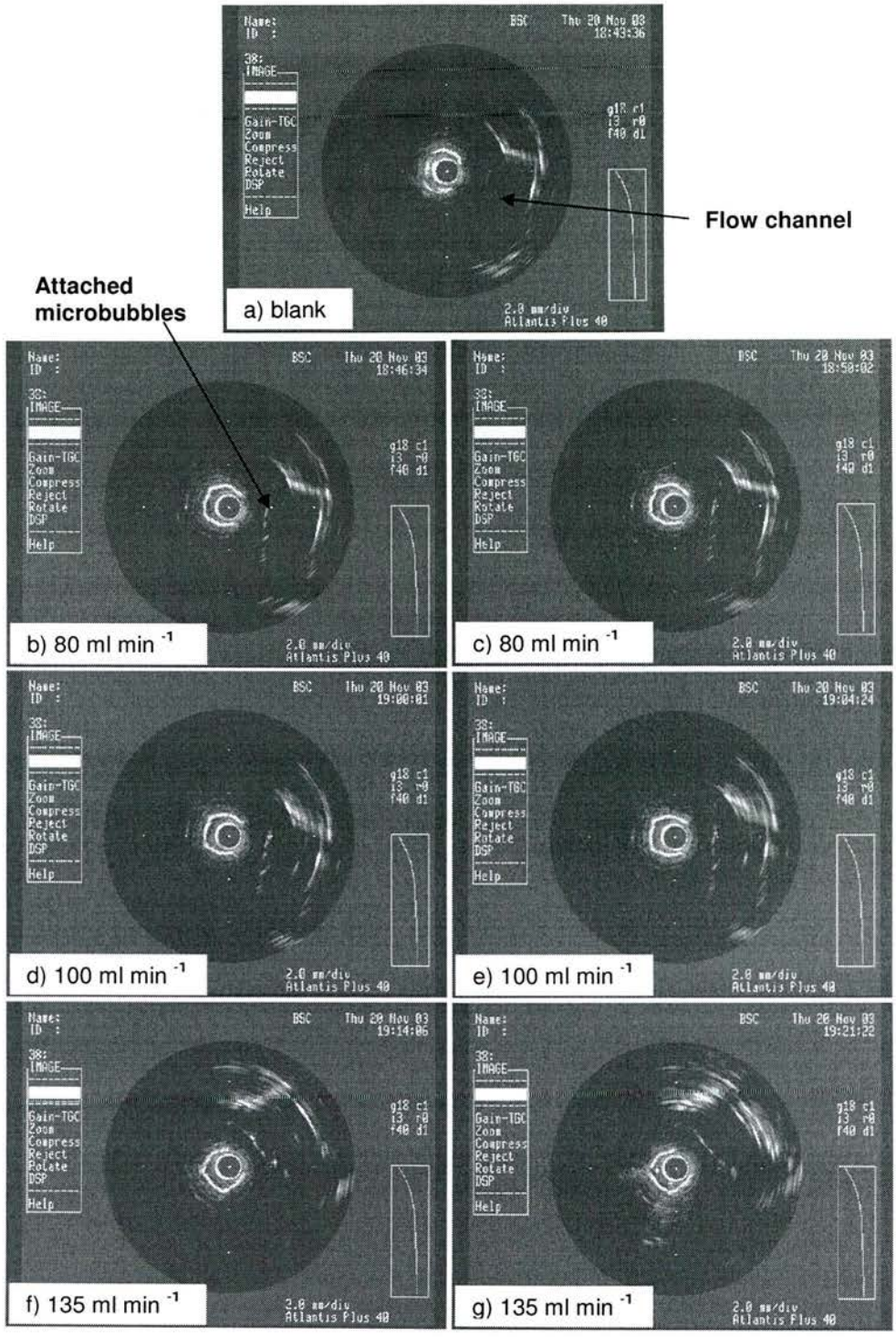

Figure 3.27: Microbubbles attached under different flow rates. a) sample with no bubbles, b) 80 ml min^{-1}, c) 80 ml min^{-1} after 4 minutes of flow, d) 100 ml min^{-1}, e) 100 ml min^{-1} after 4 minutes of flow, f) 135 ml min^{-1}, g) 135 ml min^{-1} after 8 minutes of flow.

3.7.2 Discussion

The microbubbles were attached to agar samples and imaged with IVUS at 40 MHz. A flow chamber was employed to hold the samples for imaging of the attached bubbles when subjected to flow rates of up to 135 ml min^{-1}. From observing the IVUS images the microbubbles remained attached to the agar samples at flow rates up to 135 ml min^{-1}.

As well as increased flow rates, the microbubbles were found to remain attached with time. The microbubbles could be seen in the IVUS images to remain attached to the 0% scatterer agar after being subjected to flow at 135 ml min^{-1} for at least 8 minutes.

The section of the agar to be placed in the flow chamber was taken from the edge of the sample, when attached contrast agent was imaged with IVUS under no flow conditions (as in Figure 3.16) the attached contrast agent was found at the edges of sample. While the IV bag provided a steady flow it had to be refilled regularly, also ensuring the correct height was sometimes difficult. The maximum flow rate through the chamber was limited by the height of the bag. Future work would be enhanced by the use of a pump system which would allow increased volume flow rates.

The bubbles remaining attached at increasing flow rates suggested that they would remain attached when attached in-vivo. Further work needed completion on determining the stresses to which the attached microbubbles were subjected in order to determine the feasibility of targeted agents for in-vivo use.

Imaging microbubbles through the lid of the flow chamber with the transcutaneous transducers was attempted. It was possible to distinguish the sample wells but not possible to see the microbubbles on the sample surfaces.

While the microbubbles could be imaged when subjected to increasing flow rates, the forces the attached bubbles were subjected to were unknown. It would be beneficial

to know the wall shear stresses the attached microbubbles could withstand to determine if they would remain attached at physiological wall shear stresses if used in-vivo.

3.8 Chapter 3 summary

The initial work described here shows how it was possible to ultrasonically image microbubbles which were against agar surfaces. The in-house contrast agent could be imaged with both IVUS and transcutaneous transducers at frequencies ranging from 10 to 40 MHz. When the echo from the water-sample interface was minimised the microbubbles were easier to distinguish from the boundary.

Agar samples based on a standard TMM recipe were made with different concentrations of scatterers and absorbers. The acoustic impedance of each of the agar based samples was calculated using speed of sound data acquired using a SAM and the density of the samples. These values were compared to published data of acoustic impedance of different types of aortic lesions.

The in-house bubble which was developed as part of a BHF grant was found to be long-lasting and echogenic. It could also be adapted to target specific sites. The microbubble could be attached to the agar based samples using biotin and streptavidin. When attached to the agar samples containing no scatterers (0% scatterer agar), which has an acoustic impedance comparable to that of the aortic wall) the microbubbles could be imaged with intravascular frequencies. The microbubbles could also be imaged with the linear array L16-28 transducer.

Samples with the bubbles attached were then placed in a flow chamber and imaged with IVUS under flow rates up to 135 ml min^{-1} through a flow area of 9 mm^2. The microbubbles were found to remain attached and echogenic with time.

While it was known that the microbubbles remained attached and echogenic with time, the flow velocities and wall shear stresses to which the microbubbles were

subjected were not. To assess the feasibility of using the agent in-vivo, it was necessary to ascertain the wall shear stresses attached contrast agent could withstand. Methods of measuring shear stresses are discussed further in Chapter 5. It is also helpful to know the acoustic pressures the microbubbles are subjected to when insonated. To do this, the transducers used for imaging needed to be characterised. Work detailing this is described in Chapter 4.

Chapter 4

Characterisation of High Frequency Transducers

4.1 Introduction

Contrast microbubbles expand and contract when insonated. The extent to which the bubble expands depends on the characteristics of the shell and also on the insonating peak negative pressure. As described in Chapter 2, increasing incident acoustic pressure affects the response of the microbubbles to ultrasound. It is essential to have knowledge of the pressures from the transducers used in experimental work so that the pressures to which the bubbles are subjected are known. This can aid in optimising the signal obtained when imaging the microbubbles and can be beneficial depending on the required bubble response e.g. bubble disruption.

Scanners used for the experimental work described in this chapter were the Diasus scanner and ClearView Ultra IVUS scanner which were introduced in Chapter 3. Diasus scanners are designed and built for musculoskeletal imaging, veterinary work and mouse imaging. The probes are wideband linear arrays and have frequency ranges of 5-10 MHz, 8-16 MHz, 10-22 MHz and 16-28 MHz. The IVUS scanner is used clinically for invasive imaging of arteries. A rotating 40 MHz transducer (Atlantis 40) was used with this scanner.

Currently the pressures produced by these transducers are not known for a range of distances from the transducer and for different scanner settings. Knowledge of the peak negative and peak positive pressures of the beam at different depths, transmit powers and focal points are needed for optimum imaging of ultrasonic contrast agents.

4.2 Materials and Methods

To characterise the transducers a hydrophone was set up to detect the output acoustic signal from the transducer and the peak pressures were then calculated. A Precision Acoustics, membrane hydrophone with active element of diameter 0.2 mm (Precision Acoustics Ltd, Dorchester, Dorset, UK) was used. The hydrophone calibration certificate containing values of sensitivity which were used in the pressure calculations was available. The hydrophone was calibrated at NPL (National Physical Laboratory, Teddington, Middlesex, UK) for 1 to 40 MHz (Date of calibration: February 2002). This assured that the hydrophone was sensitive enough for characterisation of the high frequency transducers. A plot of the hydrophone sensitivity with frequency is shown in Figure 4.1.

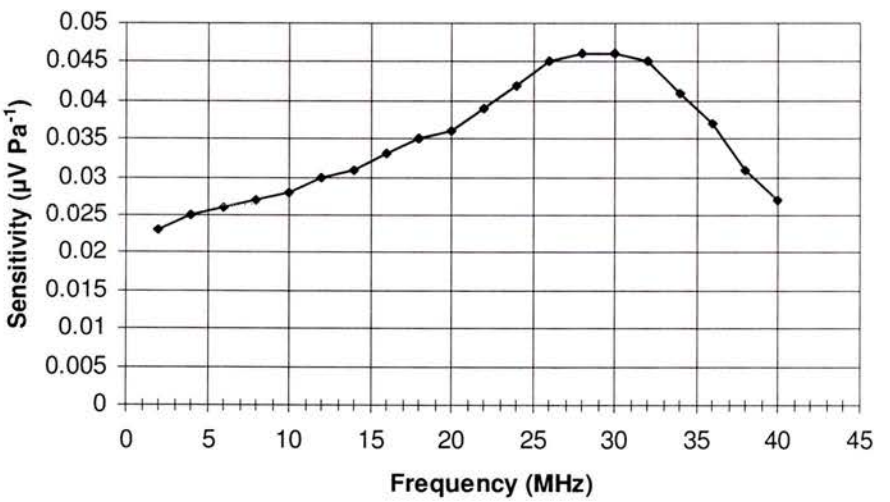

Figure 4.1: Sensitivity of the membrane hydrophone. (Data from calibration certificate).

Since the transducers for the Diasus scanner were wideband linear arrays, it was necessary to isolate the signal from the centre line so a single output signal could be detected. Circuitry was previously built in-house which allowed a line pulse from the 64^{th} line to be detected. A picture of the line pulse decimator is shown in Figure 4.2. There were two sets of switches incorporated into the circuitry. One set of switches allowed the line pulse to be selected and the second set allowed the number of lines of data to be selected. For the experimental work described here, one line of data at the 64^{th} line pulse was selected.

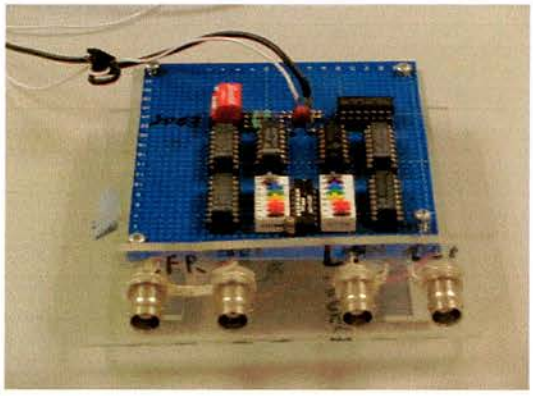

Figure 4.2: Picture of circuitry used to selected 64th line pulse.

A rig as shown in Figure 4.3 was available which could hold and move a hydrophone in a vertical direction and rotate it in the vertical plane. A device to attach the hydrophone to the holder was designed, made and secured into the holder. A transducer holder was incorporated into the rig, this held the transducer face perpendicular to the hydrophone.

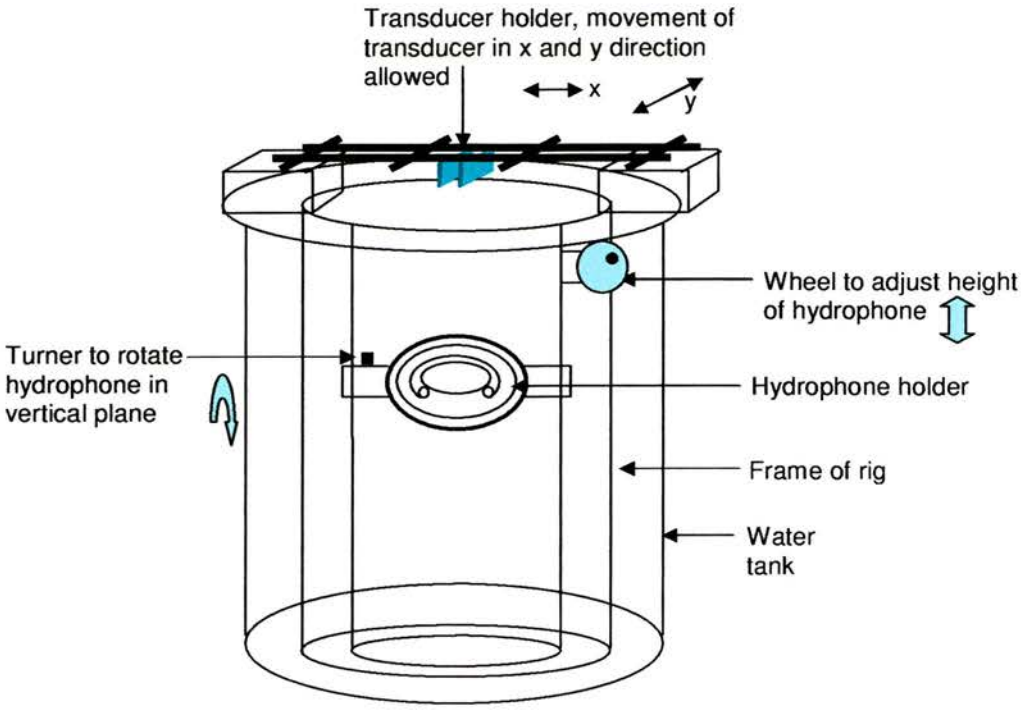

Figure 4.3: A schematic diagram of the rig and water tank for holding hydrophone and transducer in place.

A photograph of the actual rig used is shown in Figure 4.4. A micromanipulator with vernier scale was mounted on top and connected to the transducer holder which allowed fine movement of the transducer in both the x and y directions (see also Figure 4.6).

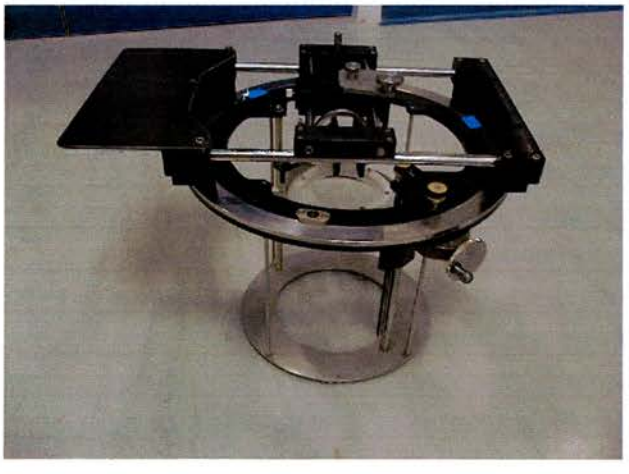

Figure 4.4: Picture of rig to hold hydrophone and transducer.

A KIKUSUS 100 MHz digital oscilloscope and Tektronix 2445b 150 MHz oscilloscope were used to view the signal detected by the hydrophone. The signal was captured using the data capture card described in Chapter 3. The data was saved at 500 megasamples per second in binary files. MATLAB was used to read in the binary data, find the peak positive and peak negative voltages and then calculate the peak positive and negative pressures. The captured voltages were converted to pressures using (Preston 1991),

$$P = V/M \qquad (4.1)$$

where P is the acoustic pressure (Pa),V is the measured voltage (V) and M is the sensitivity of the system ($\mu V\ Pa^{-1}$). The calibration certificate provided with the hydrophone was used to obtain the sensitivity of the system for different frequencies.

4.3 Experimental procedure

4.3.1 Transcutaneous transducer characterisation

A 21 litre cylindrical tank was filled with deionised water and left to degas for at least 24 hours before any experiments commenced. The hydrophone holder was secured to the rig and the whole set up was placed in the tank. The hydrophone was carefully placed in the holder ensuring no air bubbles were trapped underneath. A spirit level was used to ensure the hydrophone was flat. This was left to sit for at least 30 minutes to allow air bubbles to collect on the hydrophone. These were removed by gently flushing a syringe near the surface of the membrane. The hydrophone was connected to the oscilloscope with a 50 Ω terminator. The 50 Ω terminator was necessary for the calibration data to apply. A picture of the set-up is shown in Figure 4.5.

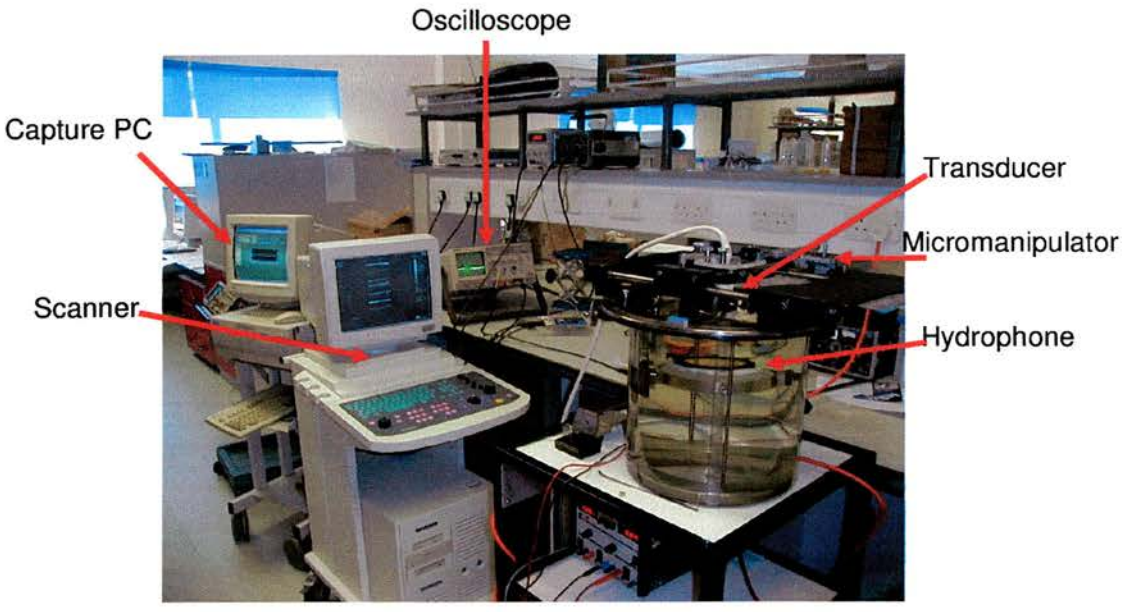

Figure 4.5: Picture of the set-up for characterising transcutaneous transducers.

The peak positive and negative voltages associated with the signals could be measured on the oscilloscope. The signal from the hydrophone was delayed using the oscilloscope so the pulse could be seen and measured easily. The output from the oscilloscope was saved as a binary file using the data capture card. This file was later used to calculate the peak positive and negative pressures for each dataset. This was a substitute to reading each measurement off the scope as it was less time consuming and gave an automatic electronic copy of the data collected. Intermittent data points were taken from the oscilloscope during each experiment to compare to the captured data to ensure the captured data was reliable.

The transducer was placed in the holder above and with its face perpendicular to the hydrophone. It was moved in the x and y planes until the hydrophone signal was detected on the scope, the micromanipulator was then secured to the transducer holder. The orientation of the transducer with respect to x and y is shown in Figure 4.6. The micromanipulator allowed fine movement of the transducer so the maximum signal could be identified. The image displayed on the scanner was used to ensure the transducer face was parallel to the hydrophone.

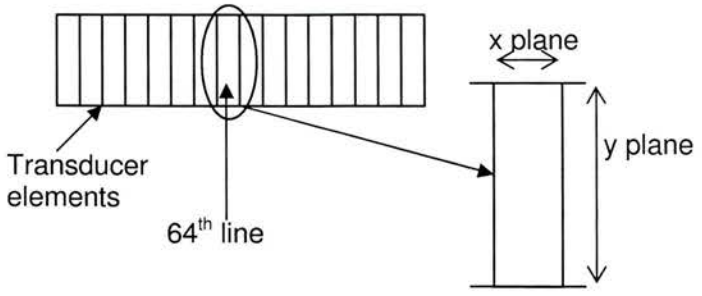

Figure 4.6: Diagram showing orientation of x and y planes with respect to the transducer. The beam profiles in the x-plane were along the width of the line and the beam profiles in the y-plane were along the length of the line.

4.3.1.1 Beam profile measurements

Beam profile measurements were collected for each of the transducers. The transducer was placed in the holder and the centre positioned over the sensitive element of the hydrophone. The peak signal was found and the transducer moved across the element to determine the boundary positions of the profile. The transmit power on the scanner was set to 50% of the maximum power and signals were captured as previously described. The transducer was moved in increments of 0.1 mm from the edge of the profile, through the peak and to the other edge. The focal point on the scanner was set to the 7^{th} point. The depths corresponding to focal points 1 and 7 for each transducer are shown in Table 4.1. The hydrophone was positioned as close as possible to the focal point on the scanner. The position was determined using the image displayed on the scanner.

4.3.1.2 Variation with power and depth

Signals were also captured at different transmit powers for different depths of hydrophone. Again the 7^{th} focal point was chosen. To obtain values for pressures at a focal point close to the transducer for two of the transducers, pressure data at increasing transmit powers were obtained for focal point 1.

Transducer	Depth of focal point 1 (mm)	Depth of focal point 7 (mm)
L 5-10 MHz	2.0	30
L 8-16 MHz	1.5	12
L 10-22 MHz	1.5	12
L 16-28 MHz	1.5	12

Table 4.1: Depths of focal points 1 and 7 for each transducer.

The transducer was placed in the holder, centred over the hydrophone and the signal maximised. Signals were captured for power settings in increments of 10, where 0 is 0% transmit power and 50 is 50% transmit power. The mechanical index (MI) of a scanner is given by,

$$MI = \frac{p_{neg}}{\sqrt{f}} \qquad (4.2)$$

where p_{neg} is the peak negative pressure of the acoustic field and f is the frequency. The MI is a safety index and is present on clinical scanners. The maximum available power from the scanner for the available probes was 96 - 98%; 100% output power was never achieved with the scanner used. The MI corresponding to increasing transmit power for each probe is given in Table 4.2. The values were calculated by the scanner and are relevant for tissue. While the experimental work described in this chapter was undertaken in water, the MI values were noted so the MI corresponding to each power setting was known .

Transmit Power (%)	MI L 5-10 MHz	MI L 8-16 MHz	MI L 10-22 MHz	MI L 16-28 MHz
10	0.01	0.01	0.00	0.00
20	0.05	0.03	0.01	0.01
30	0.10	0.06	0.02	0.02
40	0.18	0.11	0.03	0.03
50	0.26	0.16	0.05	0.05
60	0.37	0.23	0.07	0.07
70	0.50	0.30	0.10	0.10
80	0.65	0.39	0.12	0.12
90	0.82	0.50	0.16	0.16
Maximum (actual power)	0.96 (96%)	0.58 (98%)	0.19 (96%)	0.19 (96%)

Table 4.2: MI for each probe of the Diasus Scanner with increasing transmit power.

The depth of the hydrophone was altered and data captured for increasing transmit power was repeated. The hydrophone was moved from above the chosen focal point, through the focal point and past the focal point. The depth of the hydrophone was

dependent on the focal point chosen. The placement of the transducer was kept constant. To ensure the maximum signal was always captured the signal was maximised after the depth of the hydrophone was changed. This corrected any misalignment in the positioning of the transducer. The depth of the hydrophone was determined using the measurement callipers available on the scanner. Signals were captured at each point and the peak positive and negative pressures calculated.

4.3.1.3 Acoustic pressure through the flow chamber

To assess the change in acoustic peak pressure when imaging microbubbles through the flow chamber, the lid of the flow chamber was positioned between the transducer and the hydrophone. Peak voltages for the same scanner settings with and without the placement of the flow chamber lid were captured as described previously in part 4.3.1. The hydrophone was positioned 2 cm from the transducer. The flow chamber lid was secured at the face of the transducer. The transmit power was set to 40% (MI = 0.03). Signals were recorded at three different flow chamber positions: close to the transducer, close to the hydrophone and between the two. The L10-22 MHz transducer was used for this.

4.3.2 IVUS transducer characterisation

The tank of deionised water was prepared as described in section 4.3.1 and the hydrophone was held in the same holder set-up. A holder for the IVUS catheter was designed to be clamped to a micromanipulator thus allowing fine movement of the catheter in x, y and z planes. The experimental set-up is shown in Figure 4.7. The angle of the catheter could also be finely adjusted. The hydrophone was connected to the Tektronix oscilloscope. The signal was detected in a delayed mode and maximised. The peak positive and negative voltages were then measured from the scope. Measurements were taken at 1 mm intervals from 1 to 5 mm from the hydrophone. These depths were chosen as when working with IVUS on the optimisation of the in-house microbubble, RF data was collected at 2 mm from the centre of the catheter.

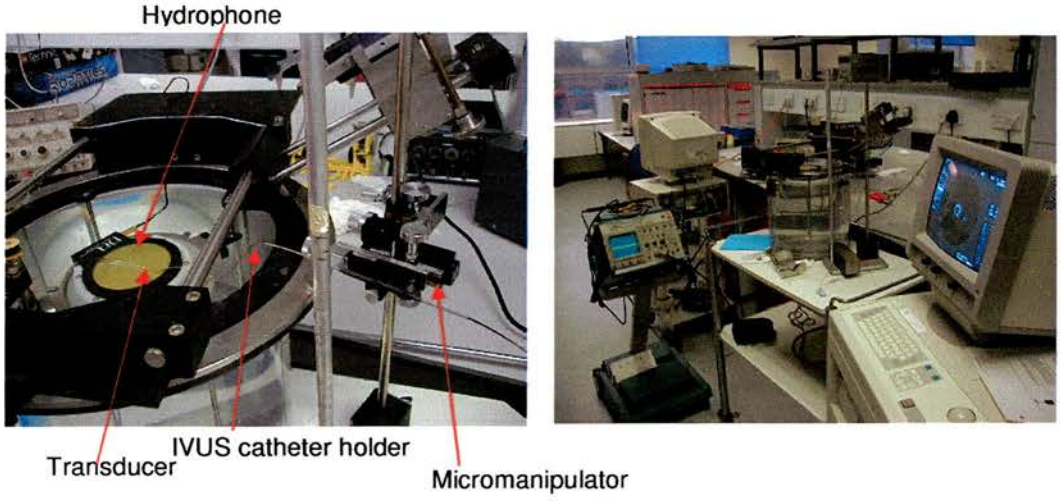

Figure 4.7: Pictures of set-up for IVUS catheter characterisation.

4.4 Results and Discussion

4.4.1 Transcutaneous transducers

4.4.1.1 Beam profiles

The beam profiles for each of the transcutaneous transducers are shown in Figure 4.8. The hydrophone was positioned as close as possible to the focal point. Figure 4.8 shows profiles in the x and y directions across the transducer face. As expected, as the frequency of the transducer increased the peak became narrower and smaller. The difference between the peak positive and peak negative values decreased from 3 MPa to 0.7 MPa as the frequency increased.

The resolution of the measurements was 0.1 mm and the maximum peak was initially found before any measurements were made. The end points of the profiles were then decided. This was to determine the end points of the measurements. As the end points for the profile were being determined, the signal was checked to ensure that the maximum signal was always being obtained. The signal was not maximised in the vertical direction. This would have ensured that the profile obtained was the maximum potential one and would have been a preferable method of choosing a

hydrophone depth. However, the hydrophone was placed as close as possible to the focal point set on the scanner.

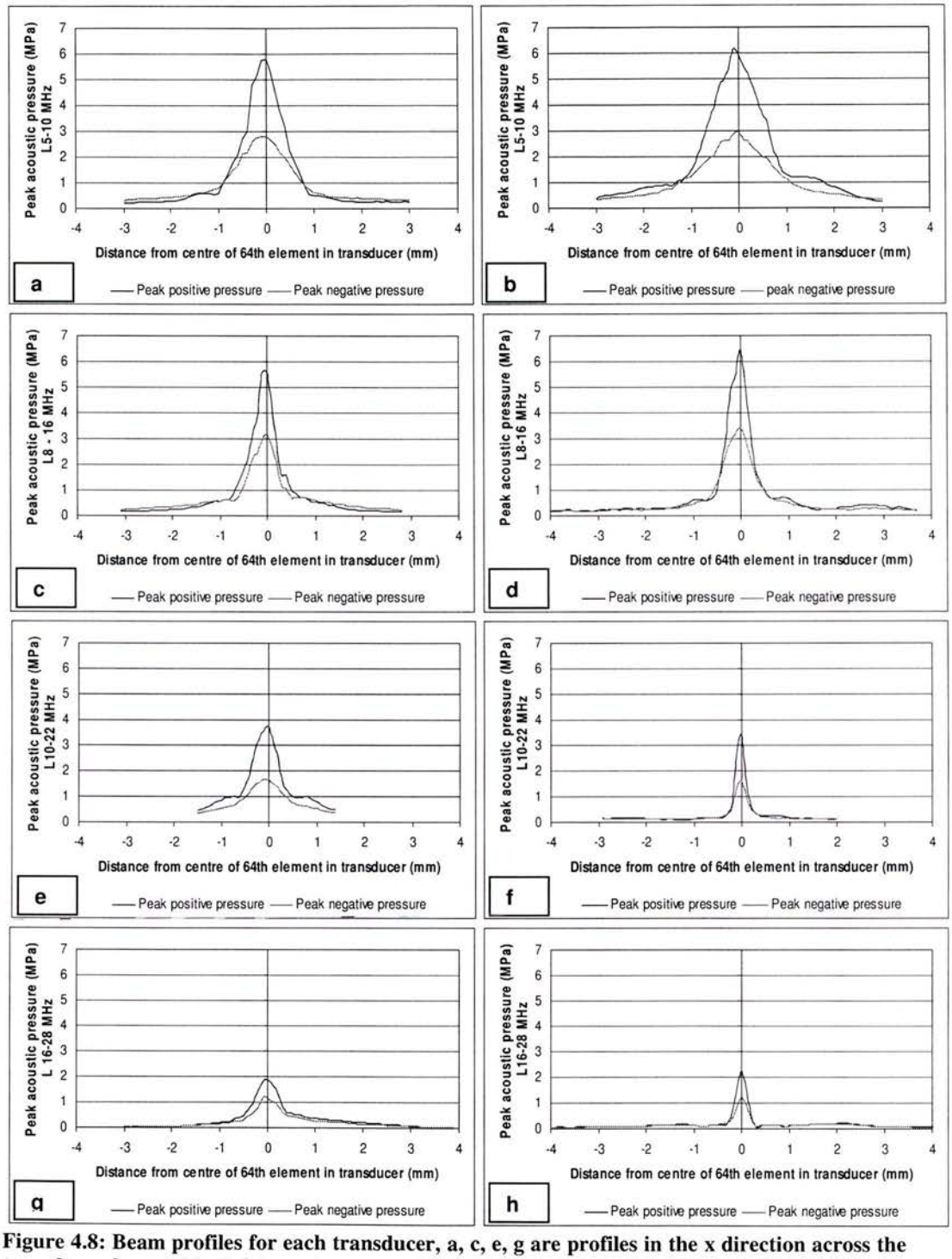

Figure 4.8: Beam profiles for each transducer, a, c, e, g are profiles in the x direction across the transducer face and b, d, f, h are in the y direction across the transducer face.

An example of how the signal changed for the beam profile shown in Figure 4.8c as the transducer was scanned across the sensitive element of the hydrophone is shown in Figure 4.9. The signal could be clearly seen to increase and decrease as the transducer moved across the sensitive element of the hydrophone. The plots numbered 1-20 show order of the signals in Figure 4.9. The y-axis was the measured voltage in mV for each position of the transducer. The y-axis scales on each plot vary as the peak voltages increase.

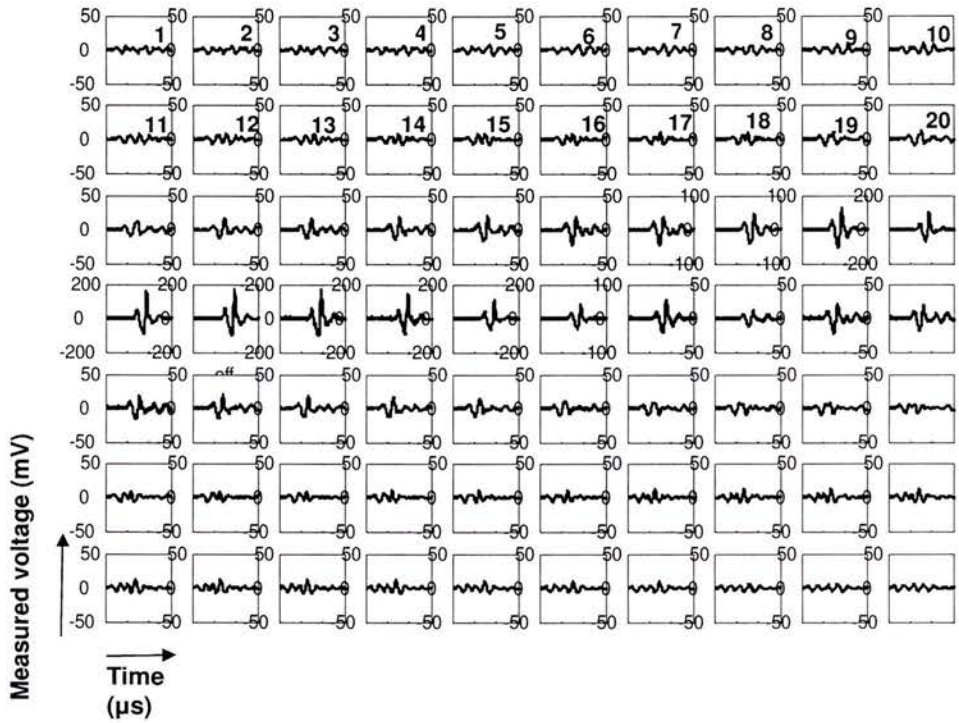

Figure 4.9: Example set of signals obtained for one beam profile at 0.1 mm intervals as the L8-16 MHz transducer moves across the sensitive element of the hydrophone. The corresponding beam profile is shown in Figure 4.8c. The y-axis on each plot is the measured voltage in mV and x-axis is time in μs.

4.4.1.2 Variation of pressure with depth

The peak negative pressures for each transducer with the hydrophone at a range of depths are shown in Figure 4.10. Pressures were calculated for increasing transmit power. The associated peak positive pressures were also calculated but for brevity and clarity are not shown here. In each of the plots, as the hydrophone passes through

the focal point of the transducer, the peak pressure recorded increased, peaked and then decreased. Again the signal was not maximised in the vertical plane which would have been preferable in order to find the maximum signal around the focal point. Although, for the 8-16 MHz and 16-28 MHz transducers, the hydrophone was moved in finer increments around the focal point.

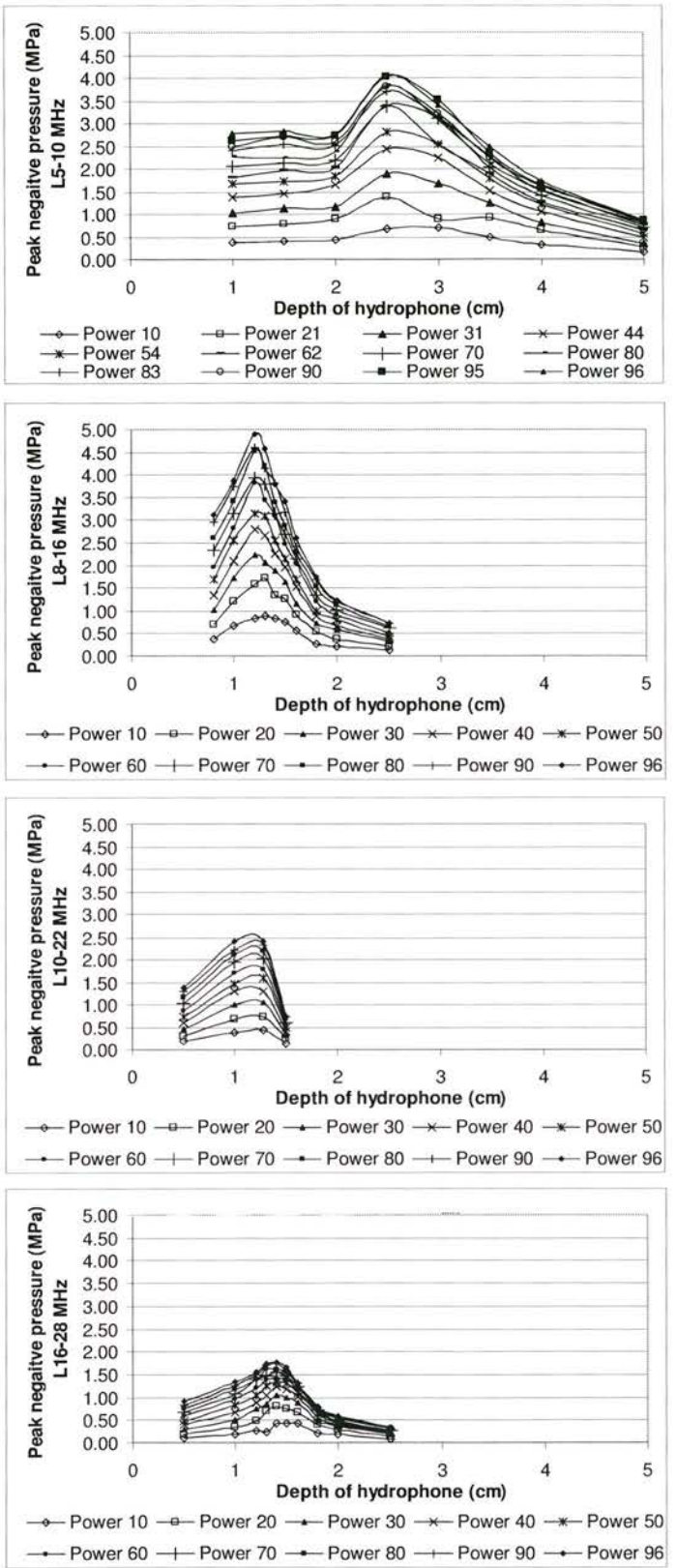

Figure 4.10: Peak negative acoustic pressures with distance between transducer and hydrophone at increasing transmit powers for four frequencies.

Peak negative acoustic pressures calculated for the L10-22 MHz and L8-16 MHz transducers, with the focal point set to 1, for increasing peak transmit powers are shown in Figure 4.11. This was not repeated for the other transducers as the maximum pressures for this focal point were very close to the transducer and it was difficult to manoeuvre the hydrophone in small increments to bring it close enough to the transducer to measure these.

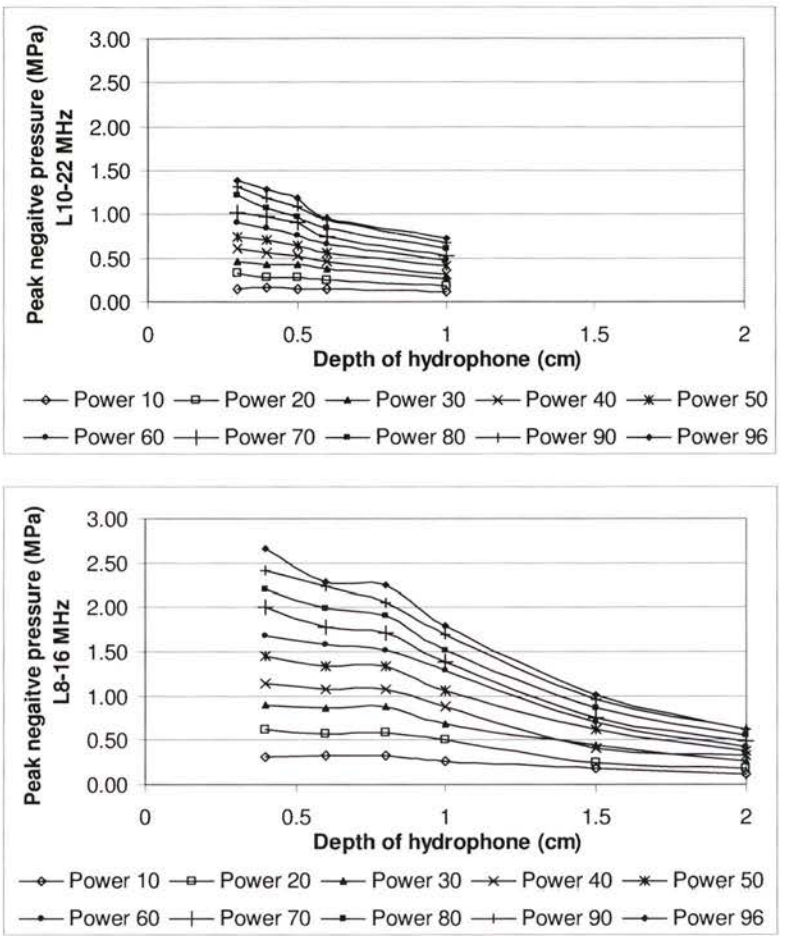

Figure 4.11: Peak negative pressures for increasing transmit power. Focal point on scanner set to number 1. Transducers: L10-22 MHz and L 8-16 MHz.

For the data shown in Figure 4.10 and Figure 4.11, repeat measurements were made. The data shown is typical of the captured data which was found to be consistently repeatable. An example of the change in signal with increasing power and change of depth is shown in Figure 4.12. There is a set of signals for 10 – 96% of the maximum transmit power at 5 different distances between the transducer and hydrophone. The

distances between transducer and hydrophone are 0.5, 1, 1.5, 2 and 2.5 cm. The focal point was at 1.2 cm. The peak for each set increases as the hydrophone approaches the focal point and reduces after the focal point has been passed.

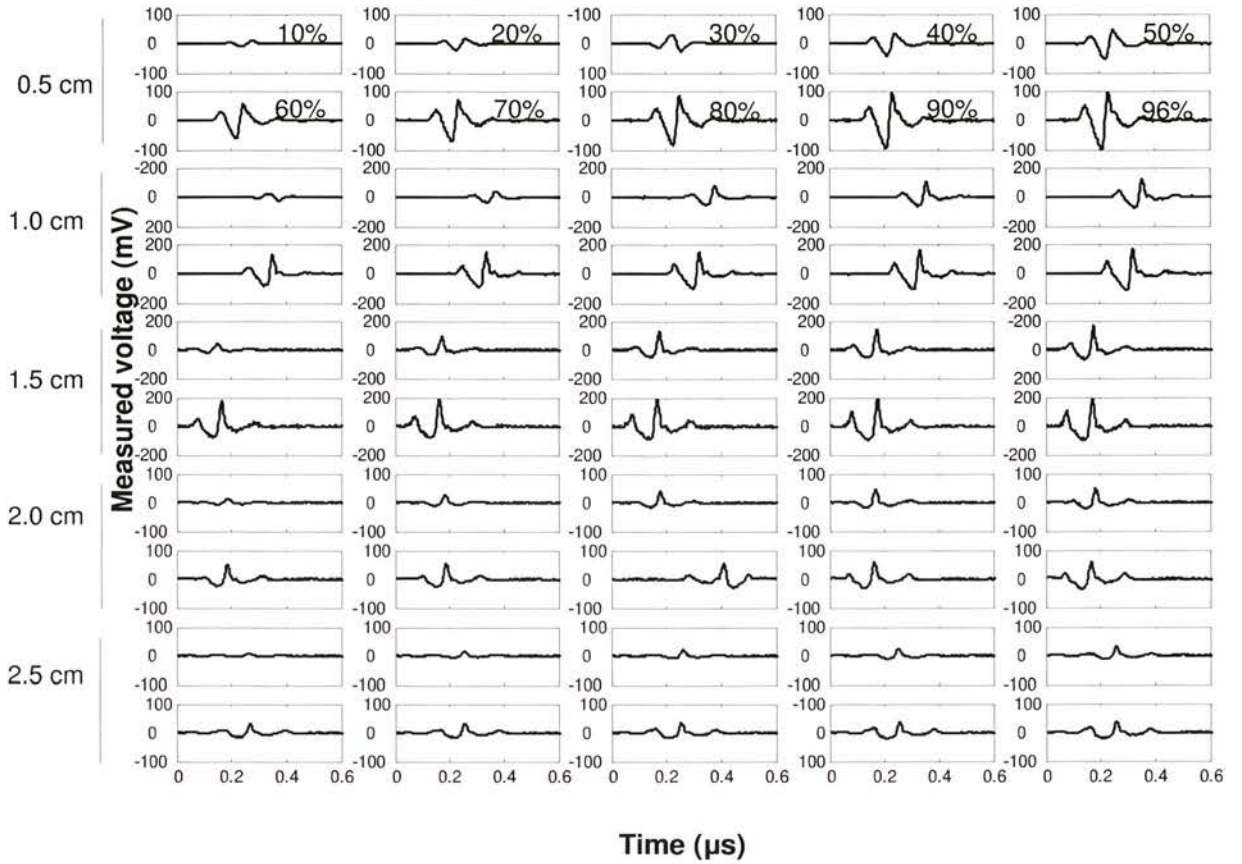

Figure 4.12: Signal with increasing transmit power (10% - 96%) for the 8-16 MHz transducer at increasing hydrophone depths. For a depth of 0.5 cm the plots corresponding to each power output are labelled, this labelling also applies to the other plots in the figure. The y-axis on each plot is the measured voltage and the x-axis on each is time. The depth each data set was recorded at is indicated on the left-hand side of the figure.

It is necessary to know the values of the pressures to which the microbubbles are subjected during contrast agent characterisation. Knowledge of microbubble behaviours at different acoustic pressures allows imaging techniques to be optimised depending on the application required. A summary of the peak negative pressure values calculated for each transducer at different transmit powers is given in Table 4.3.

power (diff intervals)	depth (cm)	fp	10	21	31	44	54	62	70	80	83	90	95	96
1: L 5-10 MHz SNo: 4DT1006	1	7	0.38	0.74	1.02	1.39	1.68	1.80	2.05	2.27	2.40	2.50	2.62	2.79
	1.5	7	0.41	0.80	1.14	1.47	1.72	1.98	2.13	2.24	2.55	2.70	2.72	2.84
depth of focal pt 7= 3.0 cm	2	7	0.44	0.88	1.15	1.64	1.85	2.04	2.20	2.38	2.50	2.59	2.72	2.76
	2.5	7	0.68	1.37	1.89	2.44	2.82	3.37	3.37	3.83	3.71	3.81	4.02	4.04
	3	7	0.71	0.88	1.67	2.24	2.53	2.53	3.11	3.07	3.15	3.21	3.53	3.41
	3.5	7	0.49	0.92	1.23	1.51	1.79	1.89	2.03	2.12	2.28	2.25	2.35	2.50
	4	7	0.33	0.64	0.81	1.05	1.22	1.28	1.41	1.55	1.50	1.61	1.66	1.72
	5	7	0.16	0.27	0.36	0.48	0.56	0.66	0.70	0.74	0.81	0.84	0.87	0.88

powers 10-100	depth (cm)	fp	10	20	30	40	50	60	70	80	90	96
2: L 10-22 MHz SNo: 4611005	0.5	7	0.19	0.31	0.45	0.59	0.72	0.87	1.03	1.16	1.29	1.37
	1	7	0.38	0.69	1.00	1.28	1.47	1.69	1.94	2.11	2.23	2.40
depth of focal pt 7= 1.2 cm	1.28	7	0.44	0.74	1.05	1.30	1.60	1.77	2.02	2.18	2.33	2.41
depth of focal pt 1= 0.15 cm	1.5	7	0.13	0.23	0.33	0.41	0.47	0.53	0.60	0.67	0.72	0.73
	0.3	1	0.15	0.33	0.47	0.61	0.74	0.91	1.02	1.22	1.31	1.38
	0.4	1	0.17	0.28	0.43	0.56	0.71	0.84	0.97	1.07	1.18	1.29
	0.5	1	0.14	0.28	0.43	0.52	0.64	0.76	0.90	0.98	1.08	1.18
	0.6	1	0.15	0.25	0.37	0.46	0.56	0.65	0.73	0.84	0.94	0.95
	1	1	0.11	0.19	0.27	0.32	0.41	0.47	0.53	0.61	0.68	0.72

powers 10-100	depth (cm)	fp	10	20	30	40	50	60	70	80	90	96
3: L 8-16 MHz SNo: 41W1012	0.8	7	0.38	0.70	1.01	1.35	1.70	1.96	2.34	2.60	2.96	3.12
	1	7	0.67	1.21	1.72	2.09	2.56	2.83	3.16	3.43	3.74	3.87
	1.2	7	0.83	1.57	2.24	2.80	3.16	3.83	3.92	4.52	4.60	4.89
depth of focal pt 7= 1.2 cm	1.3	7	0.89	1.72	2.06	2.66	3.09	3.44	3.78	4.18	4.14	4.58
depth of focal pt 1= 0.15 cm	1.4	7	0.83	1.35	1.88	2.25	2.56	3.10	3.15	3.39	3.81	3.78
	1.5	7	0.76	1.27	1.65	1.96	2.16	2.47	2.70	2.87	3.17	3.41
	1.6	7	0.55	0.91	1.17	1.53	1.69	2.05	2.15	2.29	2.41	2.62
	1.8	7	0.28	0.52	0.72	0.88	0.99	1.20	1.33	1.52	1.70	1.76
	2	7	0.22	0.38	0.58	0.68	0.80	0.91	1.02	1.14	1.22	1.24
	2.5	7	0.13	0.21	0.32	0.37	0.44	0.51	0.61	0.65	0.72	0.74
	0.4	1	0.32	0.61	0.90	1.14	1.45	1.68	2.00	2.19	2.41	2.66
	0.6	1	0.33	0.58	0.86	1.08	1.34	1.58	1.78	1.99	2.24	2.28
	0.8	1	0.33	0.59	0.88	1.07	1.33	1.52	1.71	1.90	2.06	2.25
	1	1	0.26	0.50	0.69	0.88	1.07	1.29	1.39	1.52	1.70	1.79
	1.5	1	0.17	0.24	0.45	0.41	0.62	0.70	0.75	0.86	0.95	1.01
	2	1	0.11	0.18	0.25	0.33	0.38	0.42	0.50	0.55	0.61	0.61

powers 10-100	depth (cm)	fp	10	20	30	40	50	60	70	80	90	96
4: L 16-28 MHz SNo:128W1002	0.5	7	0.10	0.19	0.29	0.40	0.49	0.58	0.66	0.75	0.82	0.90
	1	7	0.17	0.35	0.51	0.68	0.82	0.96	1.07	1.17	1.24	1.33
	1.2	7	0.26	0.49	0.74	0.88	1.05	1.21	1.40	1.39	1.49	1.55
depth of focal pt 7= 1.2 cm	1.3	7	0.25	0.68	0.87	1.05	1.25	1.39	1.48	1.64	1.70	1.74
depth of focal pt 1= 0.15 cm	1.4	7	0.42	0.79	1.03	1.24	1.35	1.43	1.56	1.62	1.73	1.76
	1.5	7	0.44	0.75	0.99	1.19	1.32	1.40	1.48	1.55	1.57	1.66
	1.6	7	0.42	0.68	0.87	1.01	1.09	1.15	1.23	1.28	1.32	1.32
	1.8	7	0.20	0.40	0.49	0.57	0.65	0.69	0.71	0.75	0.78	0.80
	2	7	0.17	0.30	0.37	0.40	0.42	0.47	0.49	0.54	0.57	0.60
	2.5	7	0.08	0.14	0.18	0.22	0.24	0.26	0.28	0.31	0.33	0.35

Table 4.3:Peak negative pressures (MPa) measured for each transducer where fp is the focal-point number for which the data was captured and the depth corresponds to the distance between the transducer and the hydrophone.

Microbubbles attached to agar have been imaged with two transcutaneous transducers (L5-10 MHz and L16-28 MHz) at 10%, 50% and 96% transmit powers. Selected images of these were shown in Chapter 3. These images were taken with the focal point at number 7. Table 4.3 can be used to find an approximate value for the peak negative pressures to which the attached microbubbles were subjected depending on the depth of the sample. From the images in Chapter 3, the surface of the agar sample was at approximately 1.8 cm. From Table 4.3 the peak negative pressures at 10% transmit power at the surface of the agar for each transducer was 0.44 MPa for the L5-10 MHz probe (taking the value for a depth of 2.0 cm) and 0.2 MPa for the L16-28 MHz probe. At the maximum transmit power, these values increased to 2.76 and 0.80 MPa respectively.

4.4.1.3 Acoustic pressure through the flow chamber wall

The acoustic signal with and without the flow chamber lid between the transducer and the hydrophone is shown in Figure 4.13. This was to investigate how the signal would be affected if the attached bubbles were imaged with the transcutaneous transducers through the flow chamber. The hydrophone was 2 cm from the transducer. As expected, there was no difference in the signals when the flow chamber lid was placed at different positions between the transducer and the hydrophone. On removal of the lid from between the hydrophone and transducer the peak value of the detected signal increased. The peak positive signal was three times higher when the flow chamber was not in place (32.57 mV reduced to 10.83 mV). The peak negative signal was 2.5 times larger when there was no flow chamber present (-16.65 mV reduced to -6.66 mV).

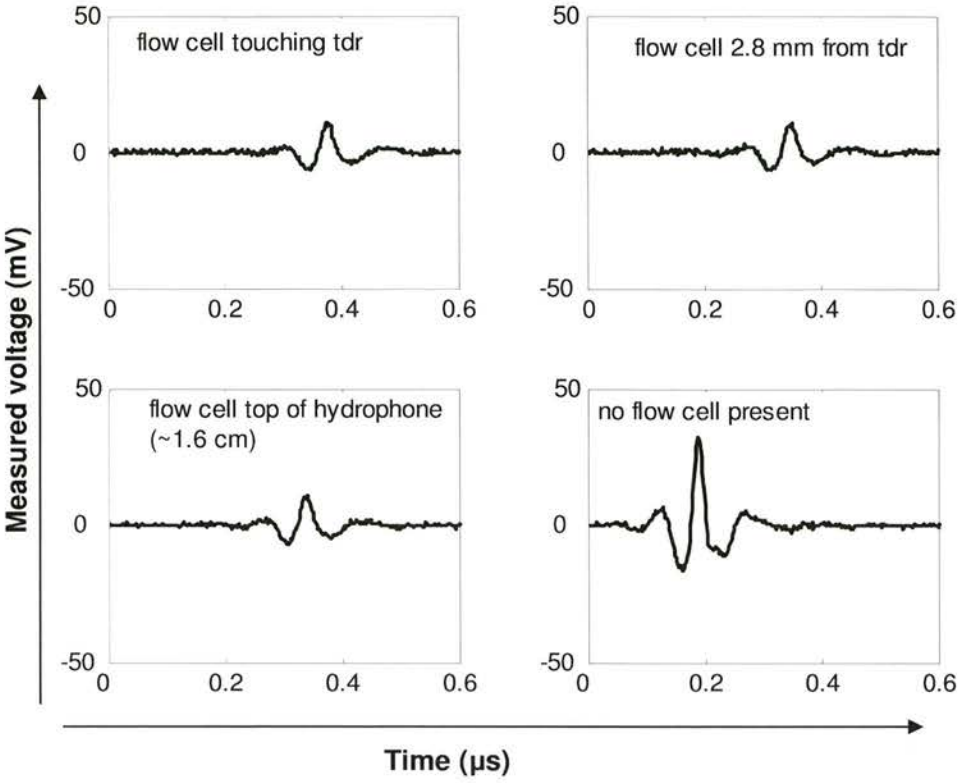

Figure 4.13: Signals with and without the flow chamber lid between the transducer and the hydrophone. L10-22 MHz transducer.

This experiment was only performed for one transducer since the flow chamber lid was very close to the membrane hydrophone so the total time performing the experiment was minimised to reduce the risk of accidental damage. Ideally, the decrease in signal for each transducer would have been determined. But the above data provided a guide on how the signal decreased. Since it was found that imaging the agar with these transducers through the flow chamber was difficult to perform, it was not deemed necessary to repeat for the remaining transducers.

4.4.1.4 Errors associated with placement of transducer in holder

The placement of the transducer was crucial to the size of the signal obtained. For maximum signal the transducer had to be perpendicular to the hydrophone. Images from the Diasus scanner are shown in Figure 4.14. Figure 4.14a shows the transducer

perpendicular to the hydrophone, the peak positive voltage measured from the oscilloscope was measured to be 139 mV and the peak negative voltage was measured to be -40 mV. Figure 4.14b, shows the transducer at an angle of 93° to the hydrophone.

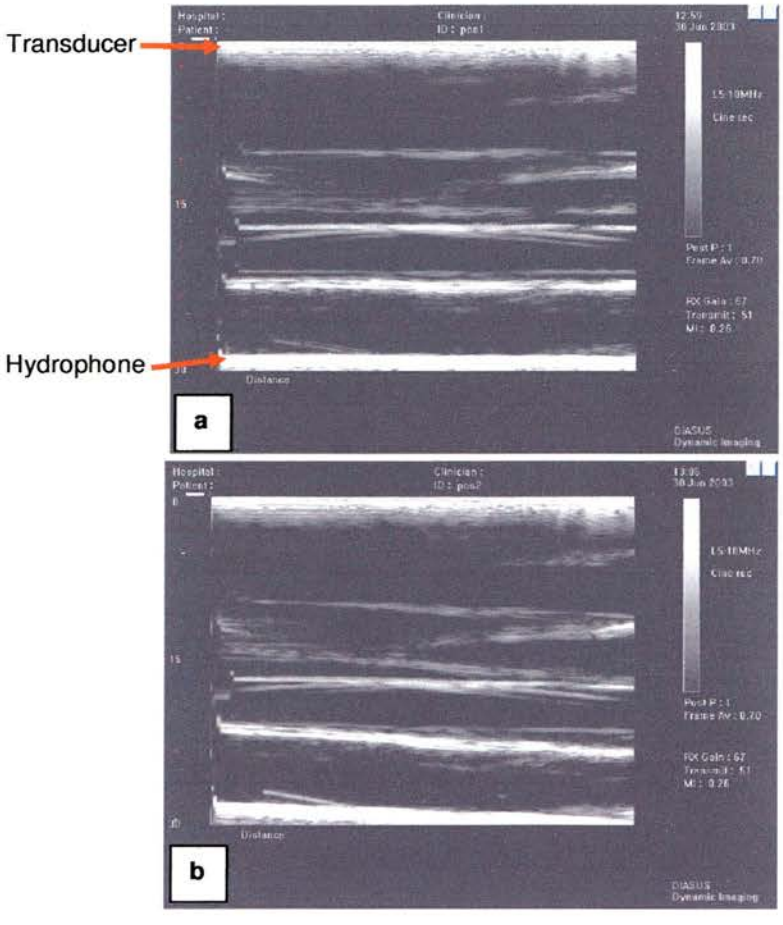

Figure 4.14: Images from Diasus scanner of hydrophone. a) Transducer is at 90° to the hydrophone, b) Transducer is at 93° to the hydrophone.

The peak voltages were measured to be 18.6 mV and -11.8 mV. This is a 120 mV difference in the peak positive voltages. There is a difference of 28 mV in the peak negative voltage.

To ensure that the transducer was perpendicular to the hydrophone during measurements, the distance from the hydrophone to transducer face was measured at each end of the transducer using the callipers on the ultrasound scanner. This was

completed each time experiments were started to ensure maximum signal was recorded. Figure 4.15 shows an example of an image with the scanner calliper measurements displayed.

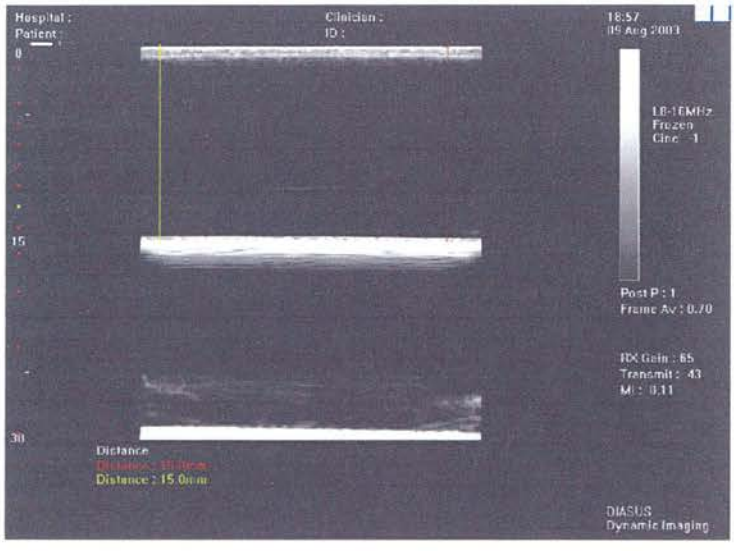

Figure 4.15: Image from Diasus scanner, measurements on screen showing distance of transducer from hydrophone.

IVUS transducer Figure 4.16 shows how the maximum peak acoustic pressure from the IVUS transducer varied with depth. The peak negative pressure ranged from 1.4 MPa at 1 mm to 0.55 MPa at 5 mm. At the working distance of 2 mm the peak negative pressure was 1.2 MPa. The transducer had the plastic catheter surrounding it which was also the case when using IVUS for imaging. When the IVUS transducer was used with the flow chamber, the attached microbubbles were imaged through the agar samples. It would have been useful to know the peak negative pressure through the agar samples but this would have been difficult to obtain due to the delicate nature of the work. It would have been difficult to mount the agar samples between the IVUS transducer and the hydrophone. An example signal detected by the hydrophone from the 40 MHz IVUS transducer is shown in Figure 4.17. The calibration of the hydrophone as shown in Figure 4.1 was only performed for frequencies of up to 40 MHz hence the IVUS was at the limit of this calibration. From Figure 3.9 the centre frequency for the 40 MHz Atlantis transducer was around 35 MHz. This is less than anticipated and will reduce the expected resolution of the

images obtained. There are difficulties in constructing transducers which work at high frequencies of 30 – 40 MHz, the transducers used in this thesis were the only ones available for use with the scanner to which there was access.

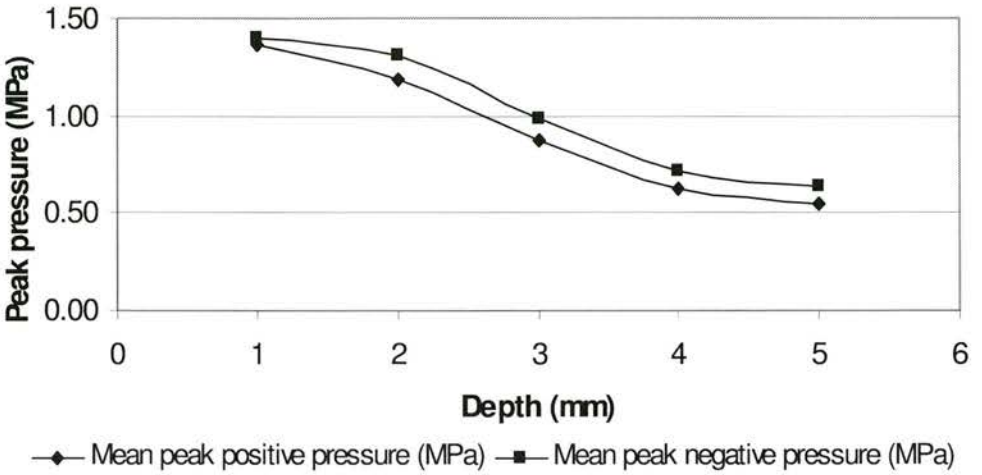

Figure 4.16: Variation of peak acoustic pressure with depth for a sheathed IVUS transducer running at 40 MHz.

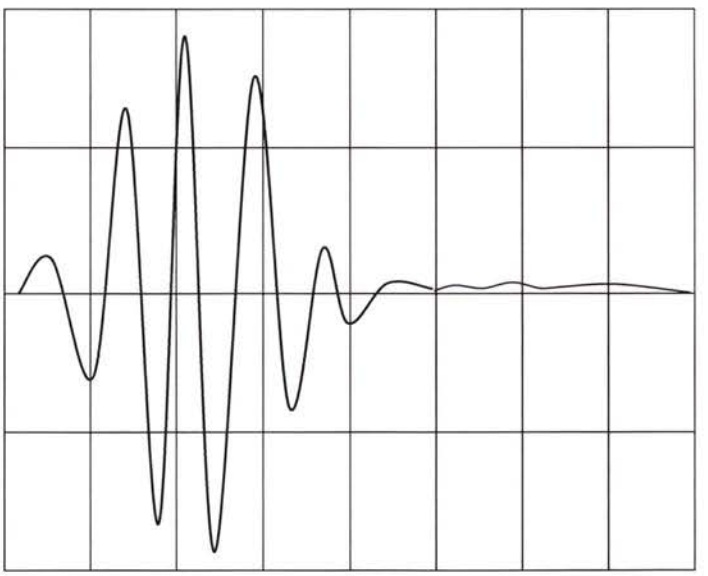

Figure 4.17: Example signal detected by hydrophone from 40 MHz IVUS transducer. The distance between transducer and hydrophone was 2 mm. Y-axis: 4 mV per division, x-axis: 41.3 ns per division.

4.5 Chapter 4 summary

The peak acoustic pressures for 4 different transcutaneous transducers were calculated for varying transmit powers and depths. Beam profiles for each transducer were also measured. When attached microbubbles are imaged with these transducers, the peak negative acoustic pressures which they are being subjected to will be known which may be useful for imaging. The peak acoustic pressures from the sheathed IVUS transducer were also measured at different depths. Transducer information will be useful to have during future characterisation and optimisation of the in-house microbubble and other contrast agents.

It is useful to have knowledge of the acoustic pressures the microbubbles may be subjected to depending on the response required from the microbubble. If bubble destruction is required, the pressure at which the bubble is destroyed needs to be known, if non-linear imaging is required, knowledge of the bubble response at different pressures is required.

Chapter 5

Measuring flow velocities in a chamber

5.1 Introduction

Chapter 3 showed IVUS images of microbubbles attached to agar subjected to flow. The microbubbles remained attached, with time, at flow rates of up to 480 ml min^{-1}. However, the flow velocities and wall shear stresses to which the microbubbles were subjected were unknown. To assess the feasibility of using the microbubbles in-vivo, it is necessary to determine the wall shear stresses to which they are subjected and to identify the wall shear stresses the attached microbubbles can withstand. It is also necessary to know how the attached microbubbles respond to ultrasound when subjected to increasing flow rates.

Wall shear stress was described in Chapter 2. It is calculated from Equation 2.3. To calculate the wall shear stress to which the in-house microbubbles were subjected, a detailed profile of the flow in the chamber was needed, more importantly, a well defined profile perpendicular to the surface of the agar sample.

5.2 Velocity measurement techniques

5.2.1 Doppler wire

There are various methods for obtaining flow velocities in vessels. Doppler catheter devices known as Doppler wires can be used to find the velocity of fluid flow.

However, it has been shown that the introduction of the Doppler wire into the flow can alter the flow profile, the extent to which depends on the measurement site, flow rate, degree of stenosis and dimension of the wire (Porenta et al 1999). The Doppler wire cannot be used to determine a detailed profile of flow, only a peak velocity. It has been shown computationally that peak velocities determined using Doppler wires can be subject to errors of up to 50% (Moraes and Evans 1995).

5.2.2 Particle image velocimetry

A method of measuring wall shear stresses in-vitro is the use of particle image velocimetry (PIV) to determine the velocity profile within the vessel. PIV is a non-invasive method of measuring the velocity of micron sized particles which are used to seed the flow. A sheet laser beam illuminates the seeding particles in the flow and a camera is used to record the positions of the particles with time. A velocity vector map across a section of the flow can be determined and hence the velocity profile within the model being studied (Prasad 2000). Flow patterns through carotid bifurcation models have been studied using PIV (Bale-Glickman et al 2003). The suitability of PIV for use with the flow chamber is discussed further in section 5.2.4.

5.2.3 Laser Doppler anemometry

Laser Doppler anemometry (LDA) provides an alternative method of measuring flow velocities and has been used to determine wall shear stress in-vitro. It is a well established, non-invasive technique of high resolution which measures point velocities in the flow. Velocities in 1, 2 and 3 dimensions can be determined. The flow is seeded with micron sized particles as with PIV. A laser pair is needed for each velocity component to be measured. The seeding particles in the flow scatter the laser light; there is a Doppler shift in the frequency of the scattered light due to the movement of the particles. The velocity of the particles can be determined from the Doppler frequency. LDA is described further in part 5.3. LDA has been used for the calculation of shear rate near walls under flow conditions (Fatemi and Rittgers 1994) and to validate numerically predicted results (Walsh et al 2003).

5.2.4 Which technique to use

A Doppler flow wire was used to determine flow velocities in the flow channel. However, it was difficult to obtain repeatable measurements of the flow rate and it was difficult to position the flow wire in the flow channel. Using the Doppler wire also meant it was not possible to obtain a detailed profile of the flow, only measurements at certain positions in the chamber. It was difficult to obtain repeat measurements at specific positions in the chamber. There were complications in positioning the wire in the centre of the flow, consequently it was not known if the peak velocity in the chamber was being measured. It was also often difficult to detect a signal from the wire due to difficulty orientating the wire correctly in the flow. In clinical practise it can be difficult to manipulate the wire to obtain the optimal signal (Gatzoulis et al 2003). Due to the size of the flow channel, the flow wire was often in contact with the edges of the channel making it difficult to position in the flow.

It was quickly determined that measurement of flow velocities using the Doppler wire would not provide data which could be used to calculate the shear stress on the surface of the samples.

In order to calculate the wall shear stress in the channel, PIV and LDA were investigated as methods of determining the flow profile. Practically, the size and design of the flow chamber described in Chapter 3 meant it was not ideal for PIV measurements. The area of the flow channel accessible for PIV was from the top, which would have allowed profiles across the width of the flow channel to be determined, however, profiles from the surface of the sample were required.

LDA was deemed to be more suitable than PIV since the probe volume could be moved through the flow channel, from the sample surface to the top of the flow channel, measuring the flow velocity at each increment. It was known there was potential for high resolution measurements of 45 μm and the current flow chamber design was thought to be suitable for use with the technique.

5.3 Laser Doppler Anemometry as a method for determining flow profiles in the flow channel

LDA is a well established technique allowing non-invasive, high resolution measurements of the velocities of liquids and gases. The first velocity measurements using LDA were made in 1964 (Yeh and Cummins 1964). This first set-up used an optical set-up referred to as a 'reference beam system' which is shown in Figure 5.1. A helium-neon laser whose output was split using a mirror was used with a polystyrene sphere-seeded flow. One beam was aligned along the flow tube through the flow, the light scattered by the spheres was collected through a port in the flow tube. The second laser beam, the reference beam, was frequency shifted, this beam corresponded to zero flow velocity. The scattered beam and reference beams were then compared and the flow velocity determined from the frequency of the scattered light. The LDA setup used for the work described in this thesis was a dual beam system described fuller in section 5.3.1. It was thought that LDA would be a feasible technique for determining the flow profile within the flow channel.

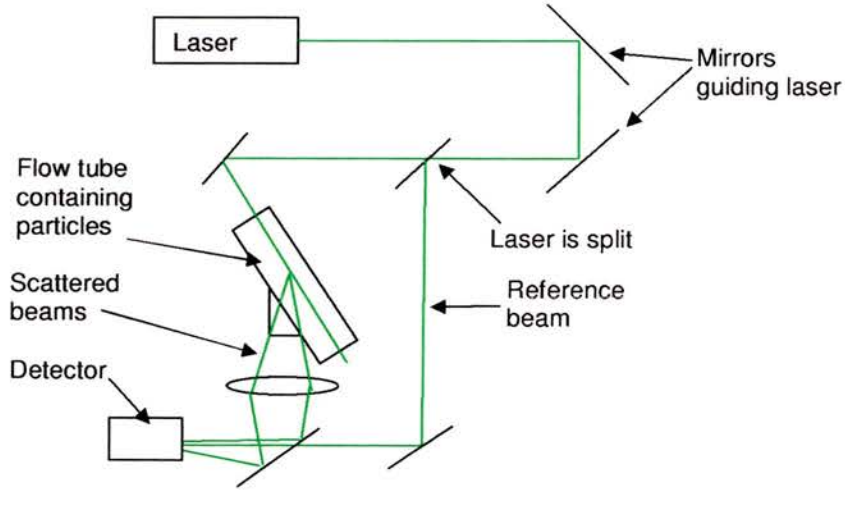

Figure 5.1: Diagram of the first LDA experimental set-up (reference beam system).

5.3.1 Dual Beam LDA

For dual beam LDA the original laser beam is split into pairs of parallel laser beams of different wavelengths (up to three pairs for 3D measurements). Figure 5.2 shows a diagram of a dual beam LDA set up for measurement of velocities in one direction. A laser beam pair is needed for each velocity component measured. Each pair of lasers is focused with lenses and the volume where the two intersect is known as the probe volume. The probe volume is positioned in the flow which contains micron-sized seeding particles. The seeding particles are assumed to move at the same velocity as the fluid, as they pass through the probe volume, they act as moving reflectors. There is a Doppler shift in the frequency of the scattered light due to the movement of the particles. The scattered light is received by a photodetector, the Doppler shift in the frequency of the scattered light is proportional to the velocity of the particle passing through the probe volume so the particle velocity and hence fluid velocity can be calculated using Equation 5.2.

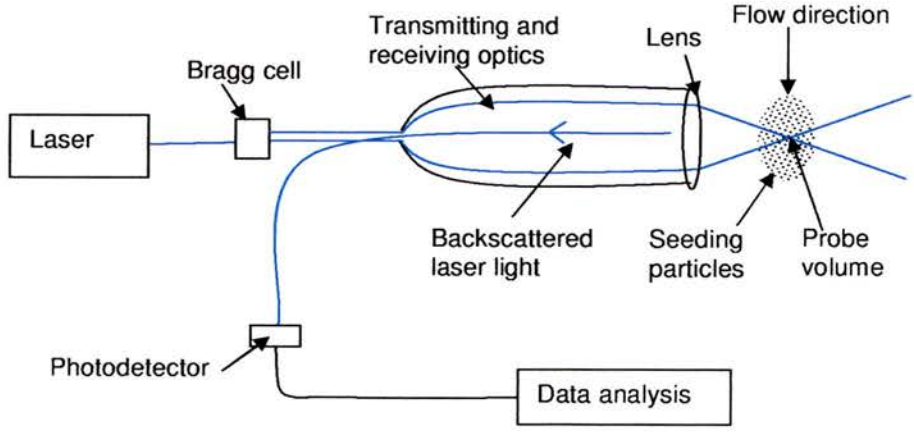

Figure 5.2: Schematic diagram of LDA set up for measurement of velocity in one dimension. For 2D LDA another laser pair is added in the plane perpendicular to the first pair.

5.3.1.1 The fringe model

The fringe model is often used to describe LDA (Watrasiewicz and Rudd 1976). At the intersection of the two coherent beams interference will occur producing parallel fringes of light. The distance between the fringes, δ_f, is:

$$\delta_f = \frac{\lambda}{2\sin(\theta/2)} \tag{5.1}$$

where λ is the wavelength of the laser light and θ is the angle between the incident beams. The fringes are orientated perpendicular to the flow direction hence the scattered light from the particles moving through the fringes varies at a frequency proportional to the velocity of the particle. Thus the velocity of the particles can be calculated using:

$$u = f_D \delta_f = \frac{f_D \lambda}{2\sin(\theta/2)} \tag{5.2}$$

where f_D is the Doppler frequency and u is the particle velocity.

5.3.2 Materials

A Dantec (Dantec Dynamics A/S, Skovlunde, Denmark) Dual Beam LDA system was available for use in the Mechanical Engineering Department of the University of Edinburgh. The system comprised of an Argon-ion, 5 W laser with a wavelength of 488 nm. There was a traverse system with two probes attached to it. The traverse system allowed movement of the probes in three perpendicular planes. Two pairs of laser beams (blue and green) were housed in one probe and a third pair was housed in the second probe. To focus the laser beams a 160 mm lens was purchased with funding from the British Medical Ultrasound society (BMUS) and The Moray Endowment Fund. This lens gave a probe volume of 45 x 45 x 200 μm, which allowed detailed profiles to be obtained. As only one 160 mm lens was available, this was placed on the probe with the two sets of laser beams thus enabling 2D LDA measurements.

5.3.2.1 Flow chamber design

The flow chamber described in Chapter 3 needed slight modification to enable use with LDA. A new chamber with the same flow area as the previous one was made. The main difference between the two chambers was that a microscope slide was incorporated into the lid of the chamber to allow a clear, scratch free window for the laser work. The microscope slide was added as the previous lid was made from Perspex which was easily scratched. The scratches would have caused the laser light to be diffracted and would have prevented reliable measurements from being made.

5.3.3 Experimental Procedure

The flow chamber was mounted on a tripod. A small spirit level was used to ensure the chamber and traverse system were parallel. The probe volume was positioned on the surface of the bottom left corner of the flow chamber. This was set to coordinates (0,0,0) and the probe was then moved relative to this position. The probe volume was scanned along the edge of the chamber to ensure the set-up was aligned correctly.

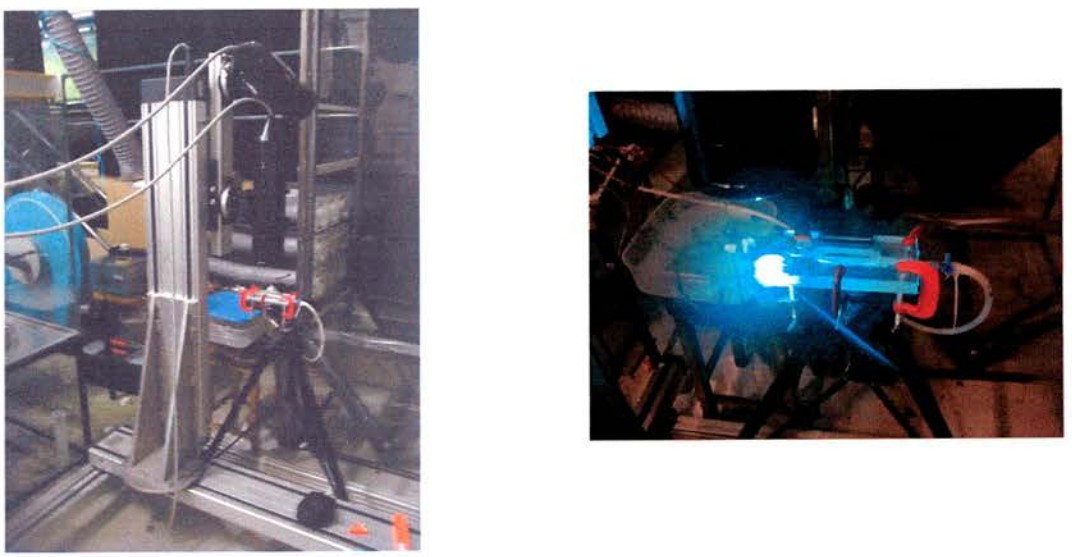

Figure 5.3: Photographs of the LDA experimental set-up. a) The traverse system with probe holders and mounted flow chamber. b) Mounted flow chamber with the laser probe volume positioned at the front left corner of the flow chamber, this point was taken as (0,0,0) and used as a reference point when positioning the probe volume in the flow area.

5.3.3.1 Optimisation of LDA technique

Flow was provided using an IV-bag filled with water. As in Chapter 3 the height of the bag was varied to give different flow rates.

Due to the design of the flow chamber, the orientation of the probe volume in the flow was as shown in Figure 5.4. The probe volume was incremented towards the agar sample in 200 µm intervals with the flow direction being parallel to the sample surface. This meant that the resolution of the profiles initially obtained during optimisation of the technique with the flow chamber were 200 µm and not the optimum resolution possible with the available lens of 45 µm.

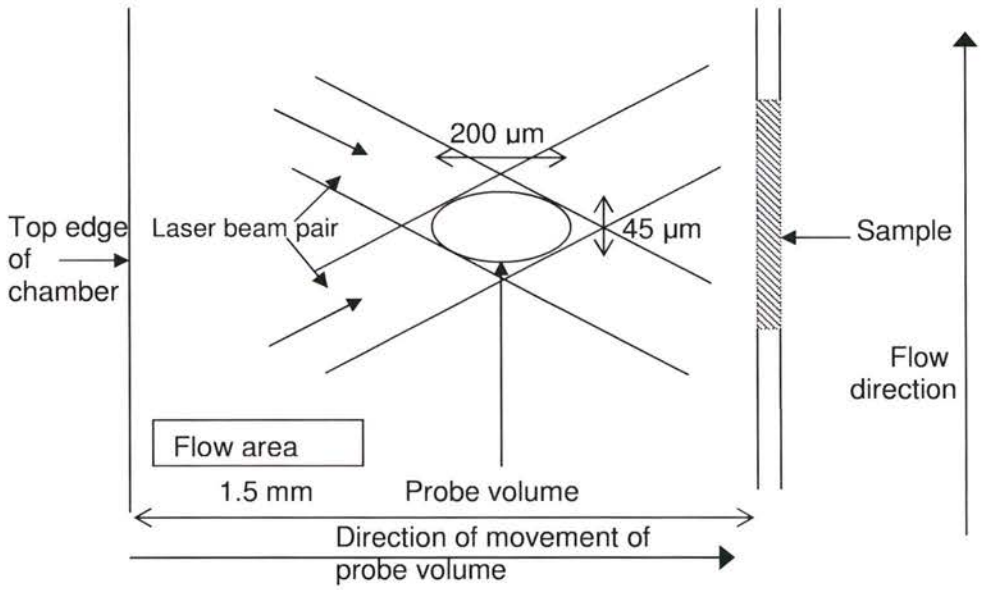

Figure 5.4: Orientation of probe volume in the flow area above the sample.

5.3.3.1.1 Initial Measurements

Agar samples, as described in Chapter 3 were placed in the sample wells in the chamber. The chamber was mounted in the LDA system. Water was used initially as it is known to often contain enough impurities to act as scatterers. The laser was run at 0.2 W. The probe volume was then moved to the middle of the flow chamber over the centre of one of the agar samples. The probe volume was incremented through

the flow channel towards the sample as shown in Figure 5.4. Point velocities of flow at 200 μm intervals were made. At each point, 10,000 measurements were made. The mean of these measurements was then recorded as the velocity at each point. After each increment of the traverse system, data collection was paused for 8 seconds allowing vibrations in the traverse system to disperse before making the next set of measurements.

5.3.3.1.2 Variation in laser power and seeding particle

The initial profiles obtained were not well defined, there was no distinct areas in the profiles which could be associated with the edges of the flow channel. To optimise the technique for use with the flow channel and to improve the definition of the profiles obtained, a series of runs were repeated with different experimental set-ups. Laser powers of 0.2, 0.5 and 1 W were used, as the power was increased, the profiles became more identifiable, but were still not what was predicted for the chamber. Milk was added to the water to act as seeding particles in the flow. This was an easy, inexpensive method of testing and further developing the system. The concentration of milk was varied to see if the poor profile was due to insufficient scatterers. As with the laser power, as the concentration of milk was increased, the profile was easier to identify but it was not as predicted for the flow in the chamber. The peak velocity was much lower than predicted and the profile shape was not a clear parabola as expected.

5.3.3.2 Further Development

5.3.3.2.1 Variation in flow chamber set-up

Reasons for the low measured flow velocity and undefined profile were thought to be backscatter from the agar sample and the IVUS channel. The chamber used was the same design as the first chamber described in Chapter 3 with the addition of a glass microscope slide. A consequence of this was that the IVUS channel was underneath the samples. The agar samples were not transparent which meant a large portion of

the laser light was backscattered to the receiver. The IVUS channel behind the samples could have also been affecting the amount of backscattered laser light.

To investigate the effect of the IVUS channel and the agar samples on the profiles obtained with LDA, a new chamber base of plain Perspex without the IVUS channel was made and the agar sample holder was removed. The lid was secured to the base and LDA measurements were made with no agar samples in the flow chamber.

The resulting profile was more defined and easier to identify as a flow profile. It also had a peak velocity which could be expected in the chamber. However, the areas of the profile at the surface of the sample and at the edge of the chamber were not well defined. It was difficult to identify points which could be used to calculate the shear rate at the sample surface.

The sample holder was then replaced and samples made from gelatin were used. The gelatin samples were made to a recipe for a tissue mimic (Hall et al 1997) but again without the addition of the scatterers. The gelatin samples were transparent whereas the agar samples, although they contained no scatterers, were not transparent. It was thought that if the profiles obtained with LDA were affected by the backscatter of laser light from the agar sample that a transparent sample may prevent this problem.

The experimental set-up was then altered slightly with the addition of a pump. This allowed increased flow rates and since the system would be re-circulating, an alternative seeding particle could be considered since there would be less wastage. The pump was controlled by a power supply. The flow rate through the flow chamber was measured for different pump speeds. The increase in flow rate corresponded to 1 Volt increments in the power supply to the pump. The pump was set to circulate steady flow.

5.3.4 Initial results and Discussion

The profiles in Figure 5.5 were from the chamber with no IVUS channel in the base but with the sample holder replaced. The gelatin based samples were used. Three different flow rates are shown in Figure 5.5, 80, 90 and 100 ml min^{-1}. This was within the limits of the IV-bag.

Again, although a profile could be seen in Figure 5.5 between -5 and -6.5 on the x-axis, the edges were not well defined and it was difficult to determine the ends of the profile. The edge of the chamber and the surface of the gelatin sample are indicated. The profiles from the surface of the sample were used in order to obtain an estimate of the wall shear stresses on the sample.

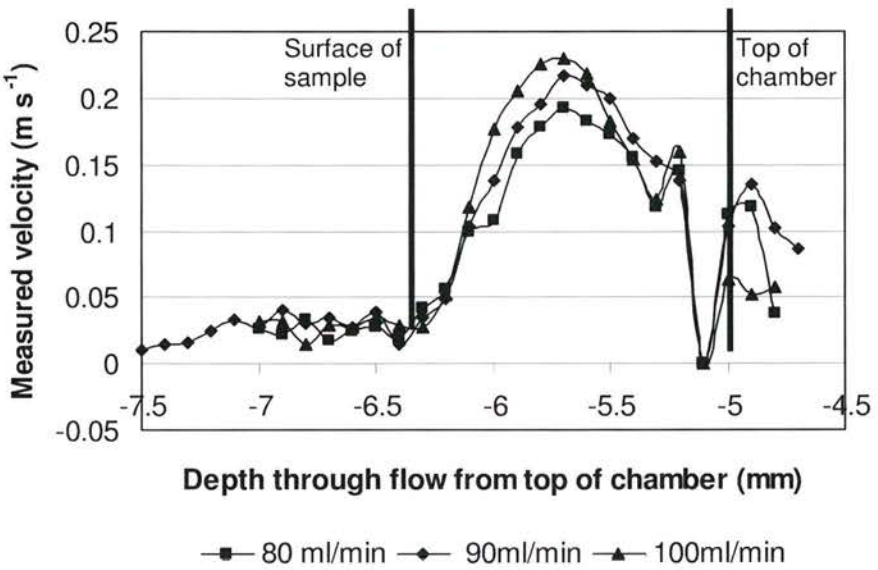

Figure 5.5: LDA data of velocities in the flow chamber with no IVUS channel and gelatin based samples. There are three different flow rates, 80, 90 and 100 ml min^{-1}.

The wall shear stresses calculated using Equation 2.3 for each profile are shown in Table 5.1. Although there was not a broad range of flow rates, and the profiles obtained were not well defined, the shear stress at the sample surface increased with flow rate. The value of viscosity taken for the calculation was 1.002 mPa s, the

viscosity of water at 20 °C (Weast et al 1988). The viscosity of the water with milk was measured using a size 75 calibrated Cannon-Fenske viscometer tube (Sigma-Aldrich) and was found to be comparable to that of water.

Flow Rate (ml min $^{-1}$)	Shear Stress (Pa)
80	0.29
90	0.35
100	0.45

Table 5.1: Wall shear stresses calculated for each profile in Figure 5.5.

Profiles obtained when using the pump to administer flow to the chamber are shown in Figure 5.6. The flow chamber set-up was without the IVUS channel and without the samples and sample holder (i.e. smooth Perspex base). The profile was much smoother than in Figure 5.5 but again the profile at the channel edges (between -7.5 and -8 and between -6.5 and -7 on the x-axis) are poorly defined. The profiles do not go to zero at the edges of the channel. There is the start of a 'phantom' profile which were thought to be caused by reflections in the Perspex base, this 'phantom' profile was not seen when gelatine samples were used. The flow rates ranged from 100 ml min^{-1} to 275 ml min^{-1}. Each run was repeated three times and the error bars are the standard deviation in each data set.

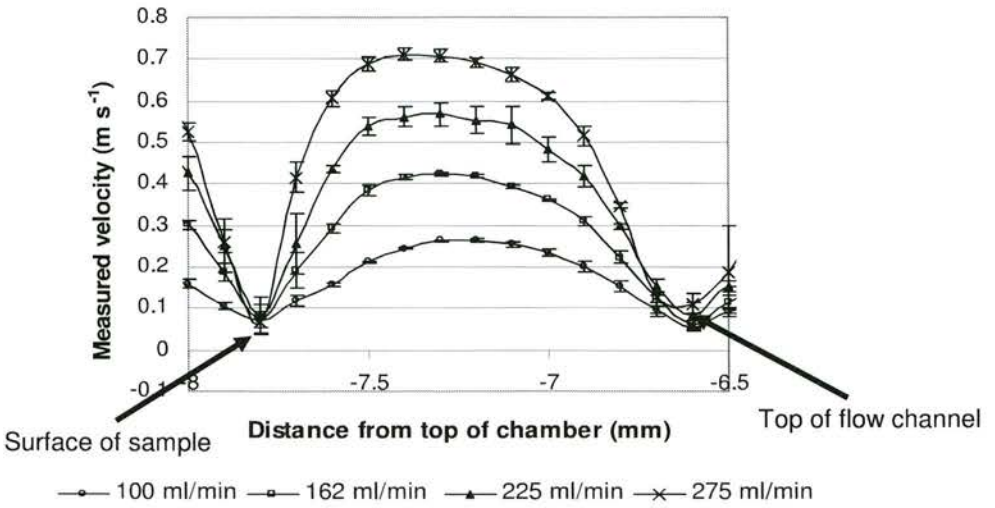

Figure 5.6: LDA profiles at increased flow velocities. A pump system was used in the set-up. The profiles are the mean of three sets of data and the error bars are the standard deviation.

Again, the shear rates at the chamber wall where the sample would be placed were calculated by performing a linear regression at the edge of the profile. For each dataset the last four points in the profile were used. The calculated wall shear stress values are shown in Table 5.2. While the profiles within the flow channel were well defined for each flow rate, at the edges of the flow channel the profiles were unclear (between x=-7.5 and -8 and between x=-6.5 and -7). The calculation of the wall shear rate and hence wall shear stress to which attached microbubbles would be subjected were subject to the interpretation of the edge of the profile at the surface of the agar sample.

Flow rate (ml min^{-1})	Shear Stress (Pa)
100	0.45
162	1.02
225	1.54
275	2.68

Table 5.2: Wall shear stresses corresponding to the profiles in Figure 5.6.

The value of wall shear stress for 100 ml min^{-1} in Table 5.2 is comparable to that for the corresponding profile at 100 ml min^{-1} in Table 5.1. For the previous profile (Figure 5.5) the wall shear stress at 100 ml min^{-1} was calculated to be 0.45 Pa where as in Table 5.2 the wall shear stress at 100 ml min^{-1} was 0.45 Pa.

In-order to investigate if better profiles could be obtained if data with 45 μm resolution was collected, the probe was incremented across the width of the flow channel (from side to side at a constant distance from the agar sample, as opposed to through the channel towards the agar sample) in 45 μm increments. This was to see if the profile obtained was better defined with the higher resolution measurements than the 200 μm profiles. If the profile was found to be more detailed and if the edges were better defined, it would be worth investing in re-designing the flow chamber to allow profiles with 45 μm resolution measurements to be made. The probe volume was scanned in 45 μm increments across the width of the flow channel. The profile obtained is shown in Figure 5.7. The profile is better defined at the edges of the flow channel than previous measurements. The profiles can be seen to go to zero which was not the case when incrementing the probe volume towards the agar samples. The chamber was 6 mm wide and the IV-bag was used to provide flow in this set-up. The data at the chamber edges was encouraging and well defined.

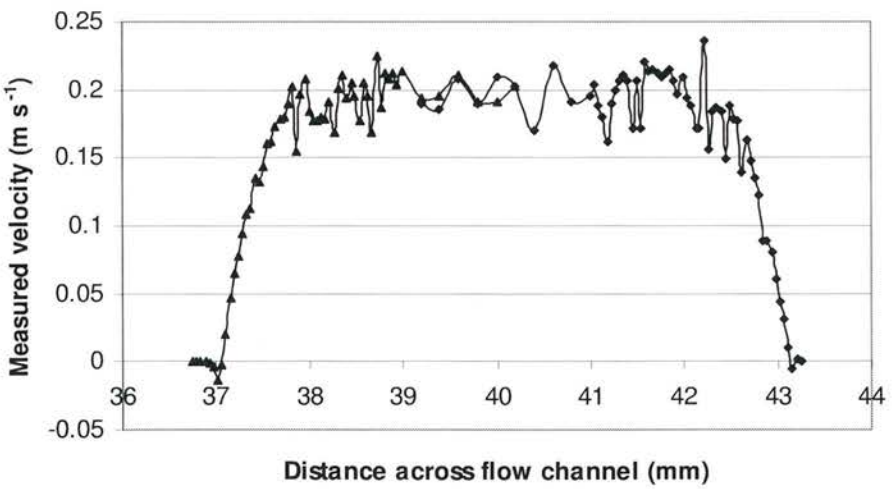

Figure 5.7: LDA velocity profile across flow channel, (6 mm wide). The resolution of profile was 45 μm and the flow rate was 90 ml min^{-1}.

The better defined profile at the edges of the chamber was thought to be due to the increased resolution of the measurements and to the orientation of the probe volume in the flow. The probe volume was incremented sideways across the channel from one edge to the other, so when close to the edge of the channel, the backscatter of the laser light was not affected as it was previously when the probe was incremented through the flow and into the Perspex base. As the probe became close to the edge of the chamber, a fraction of it was out of the flow and positioned in the Perspex, hence, reducing the accuracy of the measurements of the flow velocities. Using the alternative orientation of the probe volume, the whole probe volume was in the flow for a longer period of time and as it approached the edge of the channel, the backscatter from the base of the chamber remained relatively constant, since the depth of the probe volume in the flow was unchanged.

5.3.5 Discussion and further development

From Figure 5.5 and Figure 5.6 it was possible to broadly identify the flow profile through the flow channel. However, the boundaries of the channel were difficult to determine making it difficult to determine the shear stress at the surface of the sample. Since better profiles at the edges of the channel seemed to be possible to obtain when incrementing the probe volume in the 45 μm resolution direction, as shown in Figure 5.7. It was thought that more reliable data for the shear stress on the surface of the samples could be obtained.

As well as potentially obtaining better profiles, an improved flow chamber design would give more confidence of the flow path and of the flow profiles within the chamber. The initial channel design had tapered ends as shown in Figure 5.8a, which meant that the actual flow path was unknown. There could have been some meandering of the flow along the flow path due to the shape of the channel.

After discussion with Prof Bill Easson, a fluid dynamics expert from Mechanical Engineering at The University of Edinburgh, a new chamber design was proposed. The new channel shape is shown in Figure 5.8b. The new flow channel did not have

tapered ends and was 70 mm longer than the previous channel. This allowed the flow profile to develop as fluid travelled through the channel. The inlet and outlet reservoirs stabilised the flow as it entered and left the channel. The IVUS channel was behind the samples, not underneath, which permitted experimental work using IVUS to be undertaken using the same flow chamber and flow channel for which there would eventually be data on the wall shear stress. As with the previous version of the flow chamber, a glass slide was incorporated to allow a window for the laser. The cross-sectional flow area remained the same as that of the previous flow chamber (6 mm x 1.5 mm). Due to the new channel design, there was more confidence that the flow behaviour within the channel would be as predicted. The agar samples could be placed in a different orientation with respect to the probe volume which would allow measurements of 45 μm resolution from the surface of the samples to be made.

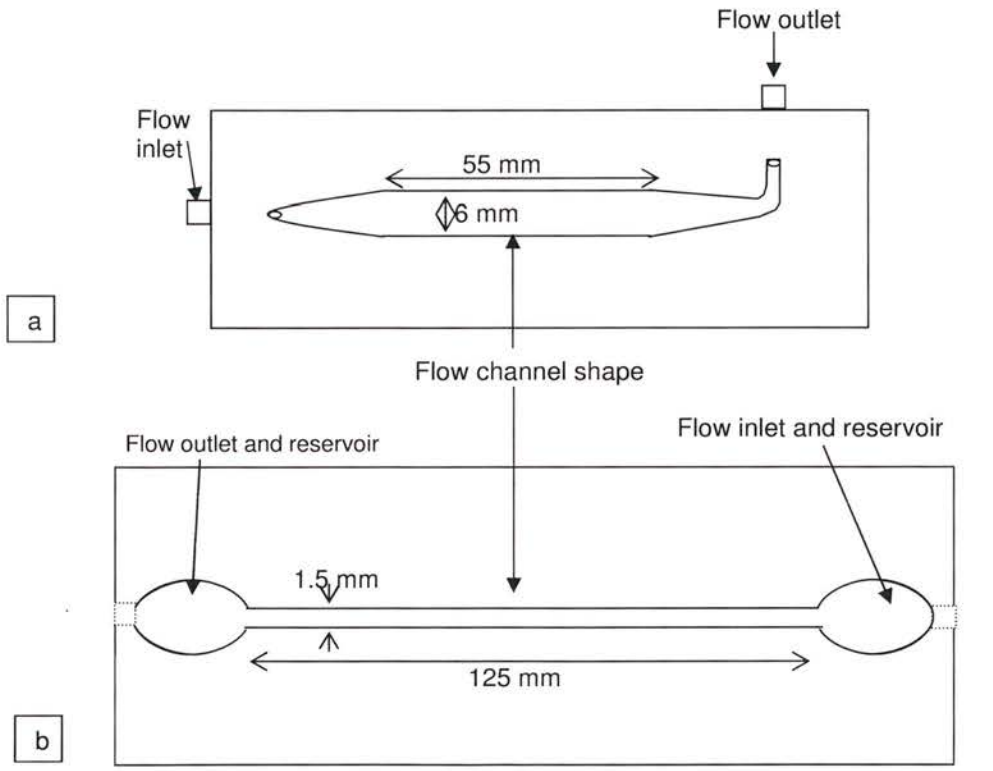

Figure 5.8: Schematic diagram showing flow channel shape for flow chamber versions 1 and 2, a) version 1 b) version 2.

5.4 Final flow chamber design

The final chamber design is shown in Figure 5.9. The chamber was made from 3 layers of Perspex. The overall dimensions were 160 mm x 80 mm, with each layer being 6 mm thick. The base layer was a plain Perspex rectangle. The centre layer had a channel with 2 wells for agar samples of dimensions 10 x 1.5 x 6 mm. The flow channel specification was 125 mm x 1.5 mm x 6 mm; at each end of the channel were two reservoirs which stabilised the flow before entering the flow channel. Fully developed flow at the sample surfaces was assumed. Luer fittings were attached to each end of the channel to allow tubing to be connected securely. In the same layer, behind the sample wells, was a channel for use with the high frequency IVUS transducer. The IVUS catheter could then be used to scan through the agar samples in the wells. The IVUS channel was 2 mm deep and 1.5 mm wide and was parallel to the flow channel as shown in Figure 5.9. A luer fitting was used at the end of the IVUS channel with a Y junction to secure the catheter in place. As with the previous flow chamber, a microscope slide was inserted into the centre of the top layer, with the bottom of the slide flush with the bottom of the Perspex. This was glued in place and made watertight. A second centre layer was also made without the IVUS channel lest there were any adverse effects on the profiles due to the IVUS channel. There were two 2 mm holes through each layer which were used with steel rods for alignment of the layers. The chamber was sealed using silicon grease between the sections and then clamped together. This provided a leak proof seal and was time saving when assembling the chamber. G-clamps were used to hold the layers together.

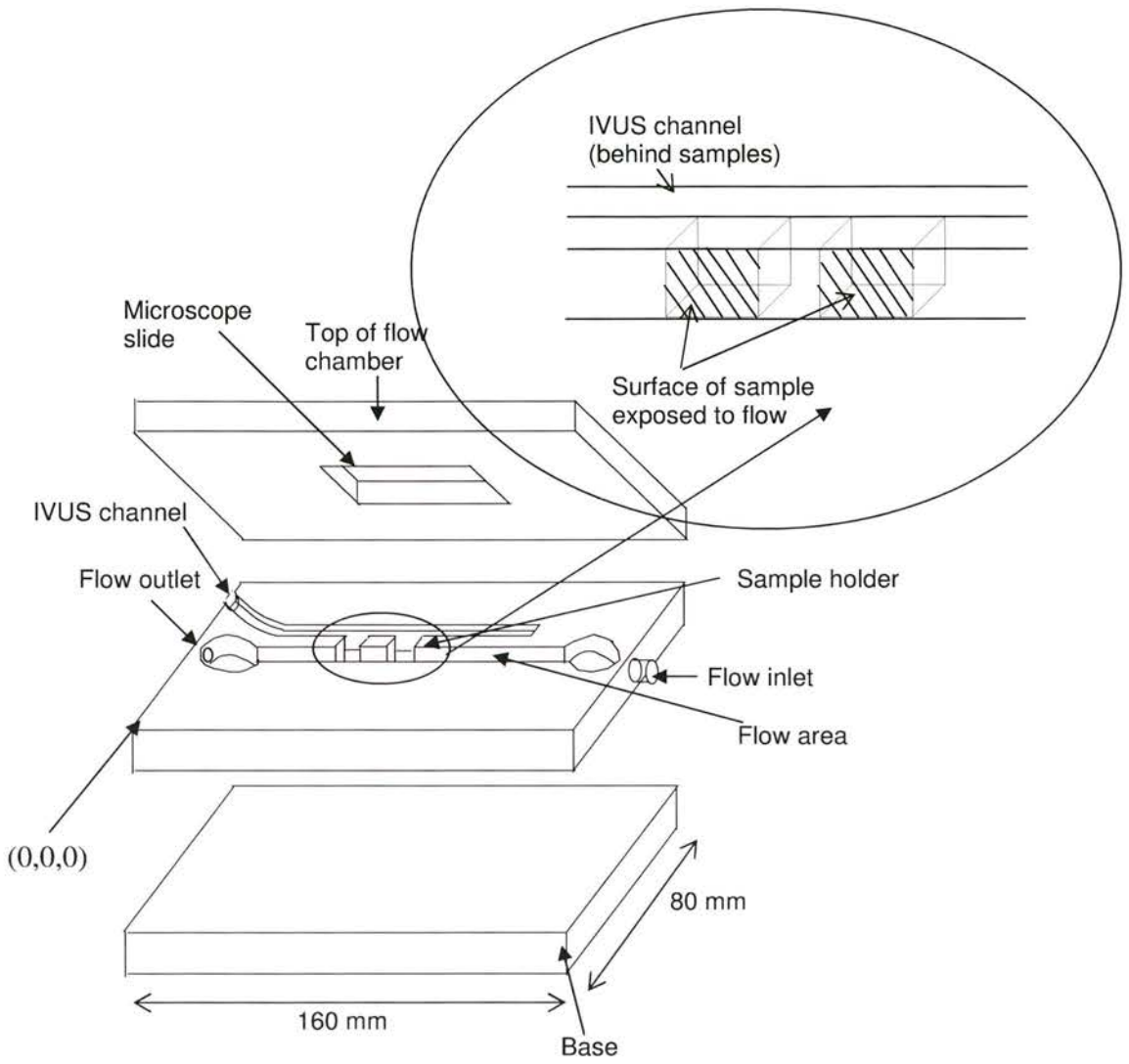

Figure 5.9: Diagram of the sections of the flow chamber. Enlarged is the area of sample holder.

As before the chamber was mounted in the LDA system. The pump system was used to administer steady flow. Flow rates of 110, 195, 300 and 385 ml min^{-1} were used. Flow profiles from the surface of the sample were measured. The new orientation of the probe volume in the flow channel is shown in Figure 5.10. The probe volume was incremented in 45 μm intervals towards the surface of the agar sample. Initially the probe volume was incremented through the channel from top to bottom in order

to locate the peak flow position. The flow profile from the surface of the agar sample was then found at this depth in the flow.

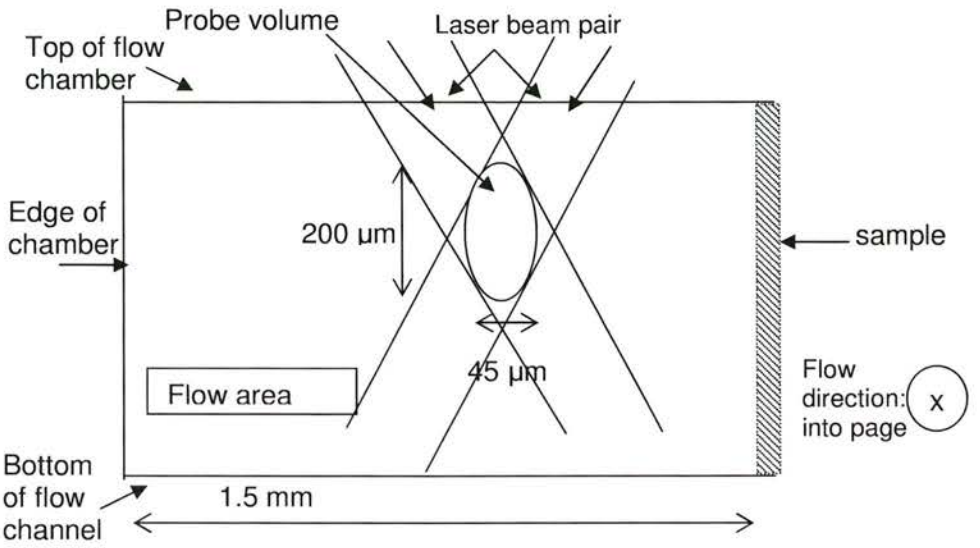

Figure 5.10: Orientation of the probe volume in the flow channel with respect to the surface of the sample.

5.5 Final results

Figure 5.11 shows the mean velocity profiles obtained using LDA, the error bars are one standard deviation. As expected, as the flow rate was increased, the peak velocity increased and hence the shear rate increased. The section of the profile between 38.4 and 38.6 mm on the x-axis is the profile at the sample surface, the area of the profile at about 37.4 mm is the profile at the edge of the chamber.

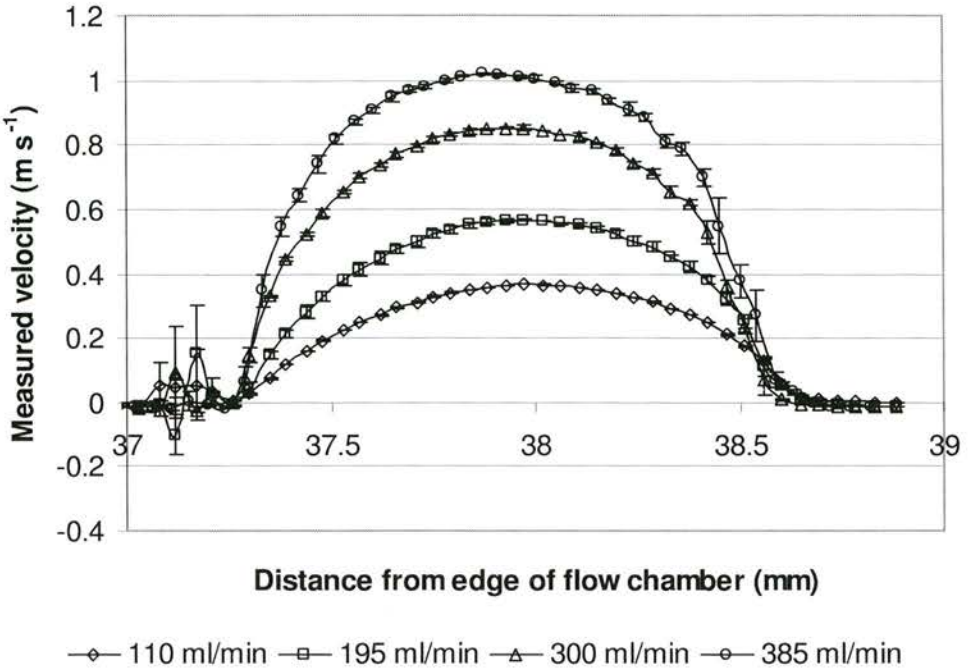

Figure 5.11: LDA velocity profiles from the surface of an agar sample in the flow chamber, for flow rates of 110, 195, 300 and 385 ml min^{-1}. The error bars are one standard deviation. The x-axis is the distance from the front edge of the flow chamber i.e. from z = 0.

To calculate the shear stress at the surface of the sample, a linear regression was performed in Excel (Microsoft Excel 2000). The points of the profiles at the surface of the samples were used. Figure 5.12 shows the profile close to the edge of the channel at the surface of the sample for a flow rate of 300 ml min^{-1}. The gradient of this line was the wall shear rate and was used to calculate the wall shear stress, the error bars are one standard deviation of the mean points as plotted in Figure 5.11. Four data points were used for each linear regression. Using a linear fit to the data close to the edge of the vessel of interest is a standard method of determining wall shear rate. A study of shear rate calculations from LDA measurements for steady and pulsatile flow (Fatemi and Rittgers 1994) found less than 10% error in wall shear stress measurements for steady flow when linear fits were used. Since the profiles shown in Figure 5.11 are not perfectly symmetrical it was thought that applying a linear fit to the data close to the edge would give the most reliable wall shear rates. To assess any variability in calculating the wall shear rate, the linear regression was

repeated with the last 5 data points in the profile, but no significant difference in the wall shear stress calculation was found, this was expected since the points were 45 μm apart. The wall shear stresses were calculated using Equation 2.3, where the viscosity of the fluid was again taken to be that of water at 20 °C. The wall shear rates and stresses calculated for each of the profiles in Figure 5.11 along with the standard error in calculating the gradient are shown in Table 5.3. These values are plotted in Figure 5.13 for each flow volume. There is a linear trend in the increase in wall shear stress with flow rate in the chamber (R^2= 0.98).

Flow rate (ml min^{-1})	Peak velocity (cm s^{-1})	Shear Stress (Pa)
110	36.54 ± 0.05	1.2 ± 0.1
195	56.63 ± 0.16	1.8 ± 0.4
300	85.19 ± 1.17	2.95 ± 0.02
385	101.72 ± 0.43	3.4 ± 0.2

Table 5.3: Measured peak velocities using LDA and calculated wall shear stress for each flow rate.

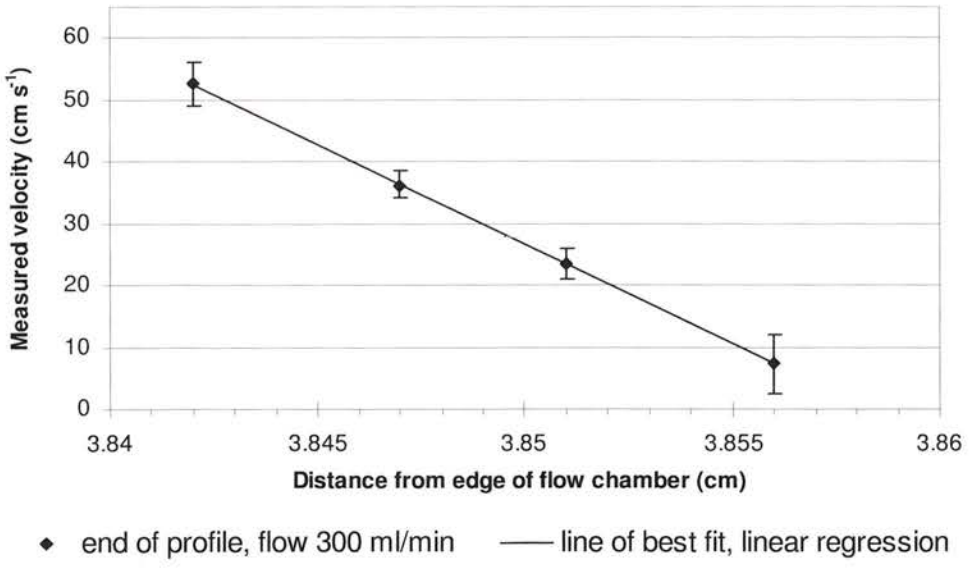

Figure 5.12: Plot of the end of the profile at surface of the agar sample with linear regression to find the line of best fit. Error bars are one standard deviation of the mean velocity.

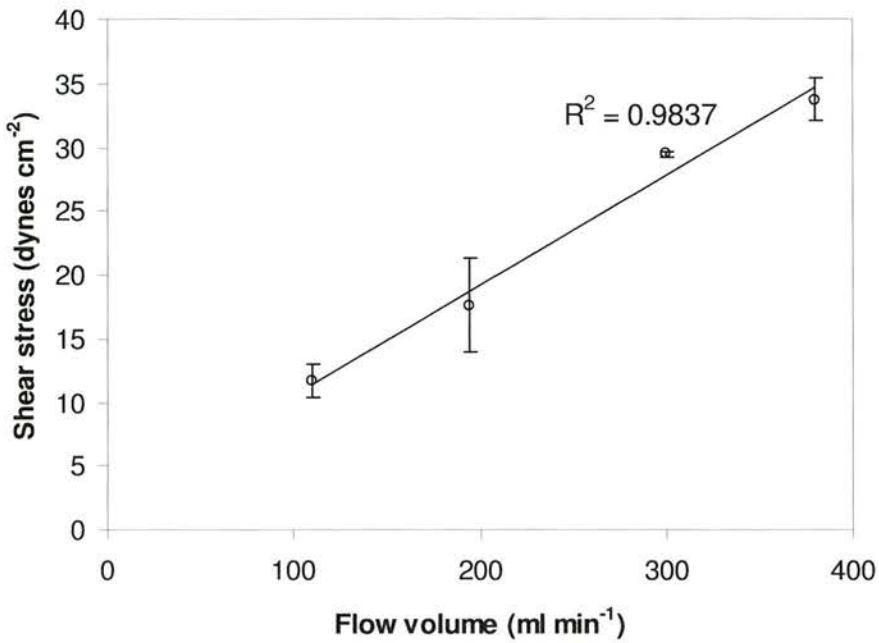

Figure 5.13: Wall shear stress as a function of flow volume in the flow chamber. The error was calculated using the standard error in each gradient. (R^2=0.9837).

The second laser beam pair measured the velocity component of off-axis flow in the z-direction, horizontally perpendicular to those in Figure 5.11. These were found to be approximately constant at zero in the flow region, examples of the distribution of point velocities for flow rates of 110 ml min^{-1} and 385 ml min^{-1} are shown in Figure 5.14.

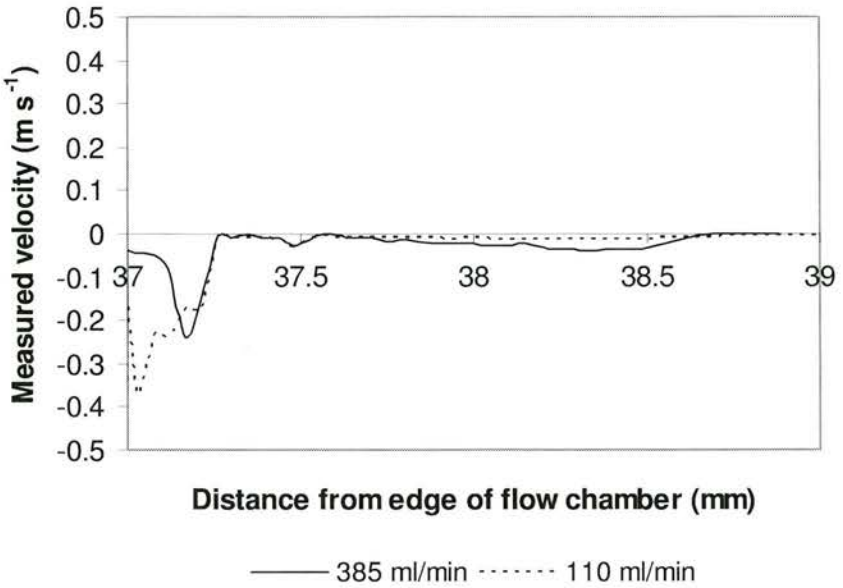

Figure 5.14: Plot of point velocities horizontally perpendicular to flow direction for flow at 110 ml min^{-1} and 385 ml min^{-1}.

5.6 Discussion

This chapter has described how Laser Doppler Anemometry (LDA) was used to determine flow profiles in a modified flow chamber which could be used for IVUS imaging of microbubbles attached to agar. LDA is a well-established technique allowing non-invasive, high resolution measurements of the velocities of liquids and gases. It has recently been used to validate numerically predicted wall shear stresses in arteries (Walsh et al 2003). Walsh et al used pulsatile flow in a model artery with LDA and calculated time-averaged velocity profiles. These profiles were then compared to profiles found using computational fluid dynamics (CFD). They concluded that for pulsatile flow LDA should be used for point velocity validations but large errors were found when experimentally determining the wall shear stress. The calculation of the shear rate from LDA data was highly dependent on the curve-fitting technique used. An earlier study of shear rate calculations from LDA measurements for steady and pulsatile flow (Fatemi and Rittgers 1994) found less

than 10% error in wall shear stress measurements for steady flow when linear fits were used.

Since steady flow was used in the set-up described in this study, the errors in the calculated wall shear stresses were small. The resolution of the data points was 45 μm, so the profile was detailed very close to the chamber wall. When the profile was extrapolated back to the wall at both ends of the profile, the distance between the profile edges was 1.38 $\pm$ 0.04 mm. On measuring the chamber width with a micrometer, at a position as close as possible to where the LDA measurements were taken, the width was found to be 1.43 $\pm$ 0.02 mm. The difference was due to errors in both methods of calculating the distance, but the values are comparable.

Linear regressions on the end of the profile at the agar surface were used to calculate the shear rate. When 5 data points were used instead of 4, there was no significant difference in the wall shear stresses calculated. The mean difference in wall shear stress value calculated using 5 data points was $\pm$ 0.08 Pa. No more than 5 points were used in the regression as the further from the wall the points were taken the less linear the profile became.

The profiles in Figure 5.11 are parabolic and for the lower flow rates symmetrical. As the flow rate increased, the profile in the channel became slightly asymmetrical. Also, the off axis flow (Figure 5.14) perpendicular to that in Figure 5.11 is not consistently at zero. This could have been due to the increased flow rate causing turbulence in the channel. To find the likelihood of the flow being turbulent, the Reynolds numbers for the minimum and maximum flow rates were calculated and found to be 540 and 1515. The Reynolds numbers (Re) were calculated from,

$$\mathrm{Re} = \frac{\rho v h}{\mu} \qquad \textbf{(5. 3)}$$

where, ρ is the fluid density, v is the fluid velocity, h is the characteristic distance (height of flow channel) and μ is the dynamic fluid viscosity. Both Reynolds numbers are suitably low enough to suggest that the flow in the channel should have been laminar. As the flow rate increased, fully developed flow would take longer to occur, which could be the cause of the deviation from symmetrical parabolic shape at increasing flow rates. The entrance length (Le) required for fully developed flow to be achieved can be calculated from:

$$Le = 0.06\,Re\,h \qquad \textbf{(5.4)}$$

Using the Reynolds numbers previously described the entrance lengths were calculated to be 5 cm for the lowest flow rate and 14 cm for the highest flow rate. The position within the flow chamber where the LDA measurements were made was 9.5 cm along the flow channel, hence as the flow rates were increased, fully developed flow was not achieved. Although, fully developed flow was not achieved, the shear rate for each flow rate was determined.

Current in-vitro work where the effect of wall shear stress on microbubbles is investigated can use supplier quoted values for the shear stress in the commercial flow chambers used. As introduced in Chapter 2, the wall shear stress within a parallel plate flow channel can be calculated using Equation 2.4 by assuming that throughout the region of interest the wall shear stress and volume flow rate are related. In parallel plate flow chambers the wall shear stress has been shown to vary across the chamber by as much as 80% (Chung et al 2003), so the exact shear stress at specific points within a chamber can be difficult to calculate. The supplier quoted values will not be applicable to the whole region of interest with in the flow chambers.

The flow chamber described here allows high frequency IVUS imaging of samples with microbubbles attached under flow conditions, the LDA data gives wall shear stress values for different flow rates at the surface of the sample being investigated, so the shear rate at the area of interest is known.

When the shear rate is calculated using Equation 2.4 for the flow rates used in Chapters 5, the values calculated are higher than those obtained from the LDA data. Table 5.4 shows a comparison of wall shear stresses obtained from the LDA data and those calculated using Equation 2.4. The calculated values are consistently higher than experimental values for work completed with flow chamber version 1 and lower for version 2.

Flow rate (ml min^{-1})	Calculated (Pa)	Measured (Pa)	% Difference
Flow chamber 1, with IV-bag			
80	0.59	0.29	51
90	0.67	0.35	48
100	0.74	0.45	39
Flow chamber 1, with pump			
100	0.74	0.45	39
162	1.20	1.02	15
225	1.67	1.54	8
275	2.04	2.68	-31
Flow chamber 2			
110	0.90	1.16	-29
195	1.59	1.76	-11
300	2.45	2.95	-20
385	3.14	3.37	-7

Table 5.4: Comparison of wall shear stress obtained from LDA data and calculated wall shear stress from Equation 2.3.

As the flow rate through flow chamber 1 increased the difference between experimental and theoretical wall shear stresses decreased. As mentioned before, the flow path and profile within the first flow chamber was difficult to predict due to the shape of the flow channel. The uncertainty in the flow profile and path meant the LDA data was essential for determining the wall shear stress within the flow chamber. However, since the profiles determined in this flow chamber were not well defined at the flow channel edges (Figure 5.6), the calculation of the wall shear stress was subject to the method used to calculate the shear rate.

The difference between calculated and measured wall shear stress in the second version of the flow chamber did not seem to follow a trend. The measured wall shear stress was consistently higher than the theoretical wall shear stress.

5.6.1 Reliability

To asses the reliability of the LDA data, the profiles in Figure 5.11 were used to calculate the mean velocity through the chamber for each flow rate. This could be compared to the estimated approximate mean flow velocity expected through a flow area of 9 mm^2 at each volume flow rate. The comparisons are shown in Table 5.5. The estimated velocities are similar to the measured mean velocities, confirming that the flow velocities obtained using LDA were comparable to the values which would be expected in the flow channel.

Flow rate (ml min^{-1})	Estimated mean velocity (cm s^{-1})	Measured mean velocity (cm s^{-1}) (LDA data)
110	20	25
195	36	39
300	56	54
385	71	64

Table 5.5: Comparison of estimated and measured mean velocities through the flow chamber.

Three flow profiles for a flow rate of 195 ml min^{-1} are shown in Figure 5.15. The profiles were measured over two days. There is little difference between the three profiles. The slight difference between the red profile and the other two is due to a small difference in the positioning of the probe volume. The mean velocity of each profile between the edges of the flow channel is 0.39 m s^{-1}.

It would have been beneficial to perform computational modelling of the flow through the flow channel. Computational fluid dynamics (CFD) would allow wall shear stress on the contrast agents to be determined and would potentially allow the study of a variety of flow conditions and flow rates. Unfortunately CFD was not performed for the flow chamber in this study.

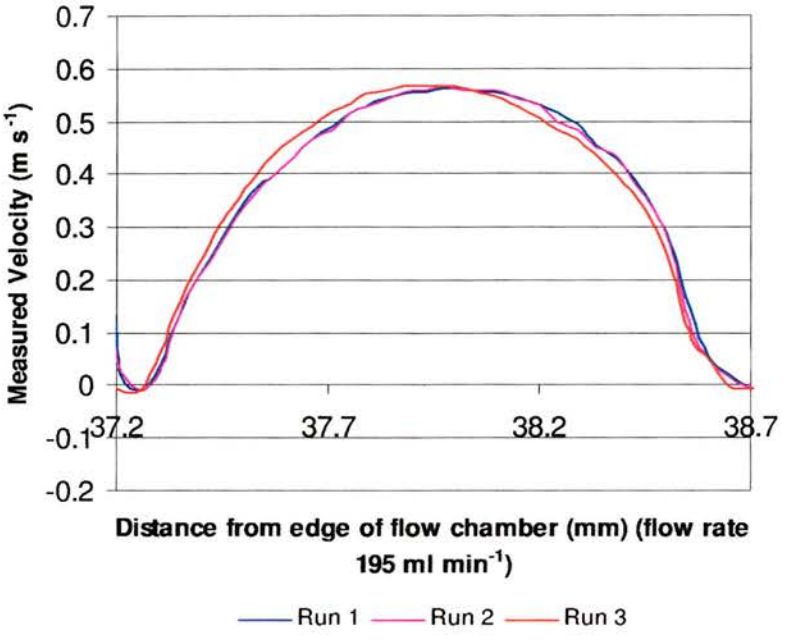

Figure 5.15: Flow profiles in the flow chamber with a flow rate of 295 ml min-1. Three profiles taken at three different times.

5.6.2 Physiological Wall Shear Stresses

The work in this study has been completed with steady flow. When subjected to pulsatile flow the attached microbubbles may respond in a different manner. However, the aim of this study is to investigate whether or not the microbubbles detach from the agar samples with increased wall shear stresses. When attached to disrupted plaque the microbubbles will not always experience shear stresses as if attached to an intact endothelial wall, since they may be contained within crevices or fissures in the wall.

Physiological flow rates in the coronary arteries range from 80 - 130 ml min^{-1} (Lupotti 2002) with a peak centre velocity of approximately 36 cm s^{-1}. The flow rates used in the present study were from 75 - 480 ml min^{-1} through a flow area of 9 mm^2.

The LDA data in Figure 5.11 shows that the peak velocities of flow to which the microbubbles were subjected in the flow channel ranged from 36 - 84 cm s^{-1}. At these velocities wall shear stresses of 1.16 to 3.37 Pa were calculated from the measured shear rates. Reported wall shear stresses experienced by artery walls are highly dependent on the measurement technique used. However, normal main arteries can experience wall shear stresses of up to 7.0 Pa with mean wall shear stresses of less than 1.5 Pa as described in Chapter 2 (Malek et al 1999).

5.7 Chapter 5 summary

LDA was used to determine the flow profiles within the flow chamber at different flow rates. The profiles were used to calculate the shear stress on the surface of agar samples. This was the shear stress to which microbubbles attached to the samples would be subjected. It is of use to know the wall shear stress under which microbubbles remain attached, so the potential for in vivo usage can be determined. It is also beneficial to know the shear rates under which the microbubbles will bind to surfaces. This is discussed further in Chapter 7. While the shear stresses experienced at the walls of the flow channel were known, the specific forces acting on the attached bubbles were not known. This is discussed briefly in Appendix 2.

The values of wall shear stress determined in the flow chamber can be used to determine the wall shear stresses under which the microbubbles remain attached to the agar. Chapter 6 describes how the flow chamber was used with IVUS to image microbubbles attached to agar samples when subjected to increasing wall shear stresses. LDA has the potential to benefit contrast microbubble research by allowing the study of targeted microbubbles with: different binding agents, different contrast agents, and different flow conditions.

Chapter 6

Imaging attached bubbles under controlled shear stresses

6.1 Introduction

In Chapter 3 it was shown that the in-house contrast agent could be attached to agar and imaged under flow conditions. Chapter 5 described in detail one method of determining the velocity flow profiles in a flow chamber. The chamber could also be used for IVUS imaging of contrast agent attached to agar samples. While in Chapter 3 it was shown that the contrast agent remained attached to the agar at flow rates of up to 135 ml min^{-1}, the wall shear stresses to which the attached microbubbles were subjected was unknown. The flow chamber used in Chapter 3 (flow chamber version 1) was redesigned for use with LDA. In order to assess how well the microbubbles were attached to the agar, the same flow chamber described in Chapter 5 (flow chamber version 2) was employed with IVUS and microbubbles attached to agar. This was to investigate the flow rates, and hence wall shear stresses, the microbubbles could be subjected while remaining echogenic and without detaching from the samples. As described in Chapter 2, part 2.2.4.1 the avidin-biotin interaction is strong with a dissociation constant of 10^{-15} M compared to antibody-antigen dissociation constants of 10^{-7}-10^{-11}, however, it is not known how strength of the

avidin-biotin bond relates to the wall shear stress within the flow chamber. Therefore it is not known how well the in-house microbubbles will be attached and for what flow rates they will remain attached.

6.2 Methods

Agar containing no scatterers was manufactured as described in Chapter 3. Samples were then cut to 1.5 $\pm$ 0.2 mm thick. The microbubbles were attached to the agar using streptavidin in an identical manner to that described in Chapter 3. Samples with and without microbubbles attached were prepared. The samples were carefully placed in the sample wells in the new flow chamber described in Chapter 5.

In the version 1 of the flow chamber, samples with and without microbubbles attached could be placed in the sample wells of the flow chamber and imaged under the same conditions thus allowing comparisons between agar samples in the flow chamber. In the new chamber, when two blank samples were placed in the two sample wells, different echoes were seen. An example of this is shown in Figure 6.1; the echo from the surface of the samples with no microbubbles attached is different in each well. A possible reason for the difference in the images is that as the IVUS catheter is inserted into the IVUS channel, there is a bend close to the first sample well. As the catheter is moved through the channel, the imaging angle between the transducer and the agar surface may change, accounting for the difference in received echo. At the agar sample in well 1 the transducer was at an angle of approximately 4^{o} whereas at well 2, the transducer was at approximately 2^{o}. While two samples in the chamber at the same time could not be compared, comparisons of samples placed in the same wells could be made.

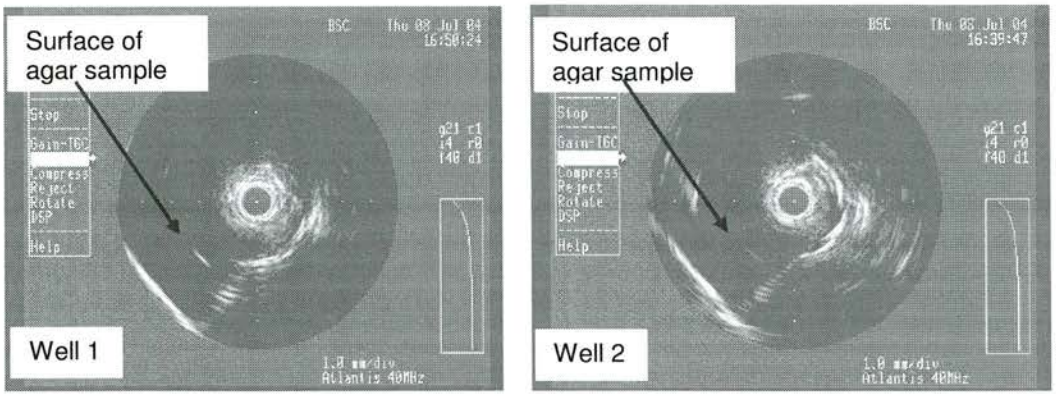

Figure 6.1: IVUS images at 40 MHz of agar samples with no microbubbles attached placed in both sample wells of the flow chamber.

Initially samples without microbubbles were imaged at increasing flow rates, following this samples with microbubbles attached were imaged. All samples were placed in the flow chamber. The same pump system as described in Chapter 5 was used. The samples were imaged at increasing flow rates from 75 ml min^{-1} to 385 ml min^{-1} (75, 110, 195, 300 and 385 ml min^{-1}) the same flow rates for which LDA data was collected were used. After each increase in flow rate the sample was left exposed to flow for at least 30 seconds before images were obtained, allowing the flow to stabilise at the increased flow rates and to ensure the agar surface was subjected to each flow rate for a considerable length of time. The images were captured using the image capture card and software described in Chapter 3. Later, the RF data for each sample was also captured using the method and data capture card described in Chapter 3. An air-water interface was used as the perfect reflector as described previously. However for the work described in this Chapter, the perfect reflector data was collected at 2.5 mm depth since the surface of the agar sample was 2.5 mm from the centre of the catheter when imaged with IVUS.

Samples with microbubbles attached were then placed in the flow chamber. Care was taken when placing the samples in the chamber as an accidental slip could cause the attached bubbles to be wiped off. As with the samples with no microbubbles attached, the samples with bubbles were imaged at increasing flow rates. The

samples were exposed to each flow rate for at least 30 seconds prior to image capture. Again, RF data was later captured for samples with microbubbles attached. While the work described so far was being undertaken, simultaneous work was being undertaken on optimisation of the in-house microbubble (Moran et al 2003a, Moran et al 2004). The bubble constituents and preparation technique were varied in order to optimise the ultrasonic backscatter and to reduce mean bubble size.

On finding that increasing the amount of PE in the microbubble shell increased the echogenicity, microbubbles containing an increased amount of PE were attached to the agar samples as previously described. Samples were placed in the flow chamber and imaged at increasing flow rates. Sonicating the contrast agent had been previously found to reduce the mean microbubble size and increase the mean backscattered power which is shown in Figure 6.2. There is a large difference in the mean microbubble size between no sonication and 30 seconds sonication. Sonicating for longer than 30 seconds did not have any increased effect. Sonicated bubbles with increased PE in the shell were also attached to the agar samples and imaged in the flow chamber at increasing flow rates. RF data from the attached microbubbles was captured for increasing flow rates.

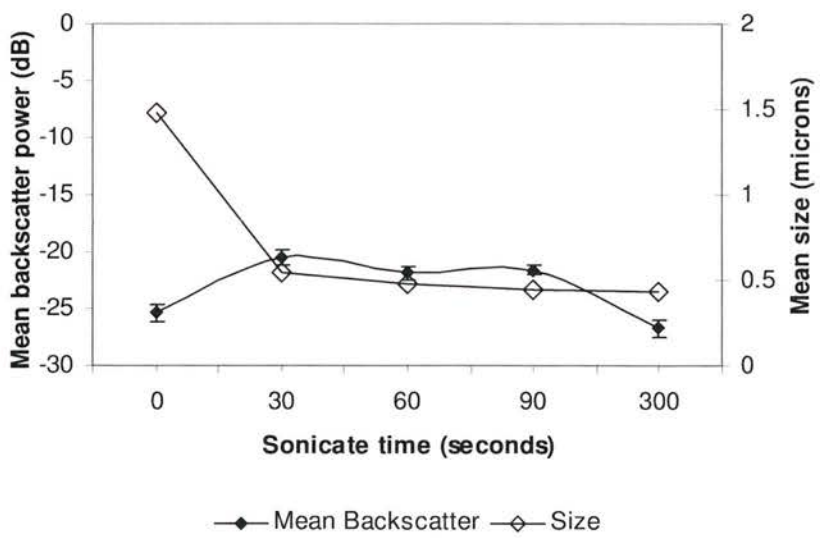

Figure 6.2: Variation in mean backscatter power and mean contrast agent size for sonicated and unsonicated in-house microbubbles. (Courtesy of Dr C.M. Moran)

6.2.1 RF data analysis

For the captured RF data, the mean backscatter power was calculated across the microbubble line and/or surface of the sample, depending on the sample being imaged. The software available for analysis of the data allowed specific areas to be selected. This could be by either selecting the required line of data and position on the line, or by selecting an area on the image via the mouse. Both methods were attempted. While using the line number and position on the line was good for repeatability, i.e. for choosing the depth in the image at the surface of the sample, each reconstructed image had a different orientation, so the line number was different each time. The line number for a particular area was roughly known, but to get the exact area, it was necessary to repeat the step until the correct part of the image was selected. When using the alternative method of selecting the required area, the mouse could be used to position the cursor on the region of interest. This made the process less time consuming.

Three regions of interest were chosen for each sample. These were taken across the surface of the agar exposed to flow. An image showing three regions of interest is shown in Figure 6.3. Each ROI contained 9 lines of RF data with the mean of these 9 lines giving the data for each section. The mean backscatter power at each site was then used to calculate the mean backscatter power for the surface of the sample. The mean backscatter power for samples with and without microbubbles attached was calculated. For the samples without microbubbles attached it was sometimes difficult to determine the surface of the sample, the thickness of the sample was known so this was used as a guide to find the surface. The position of the sample surface relative to other features in the flow chamber was also known, so this was also used as a guide.

Figure 6.3: Image of microbubbles attached to agar placed in flow chamber. Image is reconstructed from the RF data collected from the IVUS scanner. The three positions where the RF data was collected are shown and marked 1, 2 and 3, each region of interest was 9 lines of RF data, the span of these lines are indicated by the blue, pink and green lines.

6.3 Results

6.3.1 IVUS Images

An example of an IVUS image from an agar sample with no microbubbles attached is shown in Figure 6.4. The flow rate through the flow chamber was 195 ml min^{-1}. The surface of the agar sample exposed to flow is indicated.

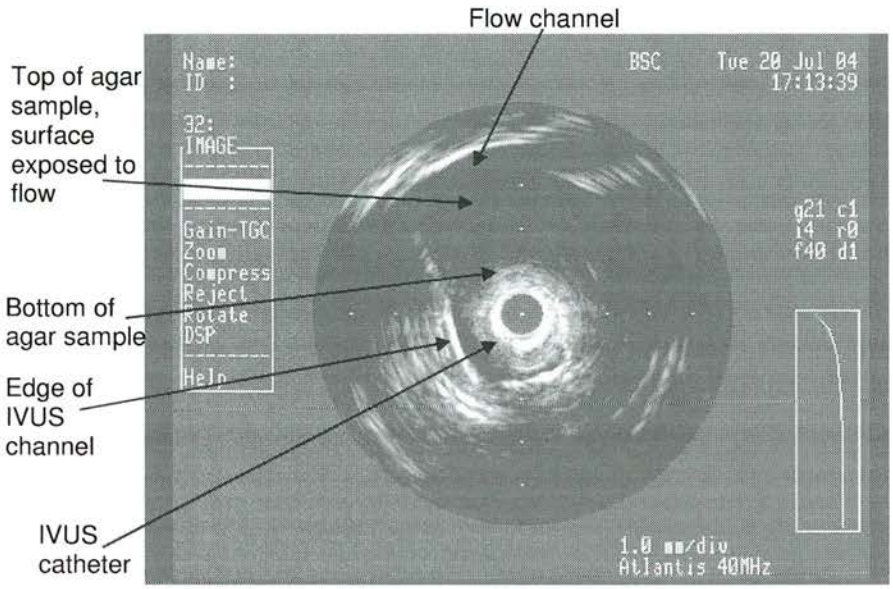

Figure 6.4: IVUS image of agar sample with no microbubbles attached in the flow chamber. Flow rate of 195 ml min^{-1}.

IVUS images of original recipe bubbles attached to agar in the flow chamber subjected to flow rates of 110 ml min^{-1} and 385 ml min^{-1} are shown in Figure 6.5a and b. There was no noticeable difference between the images suggesting that the microbubbles were not detached with increasing flow rate.

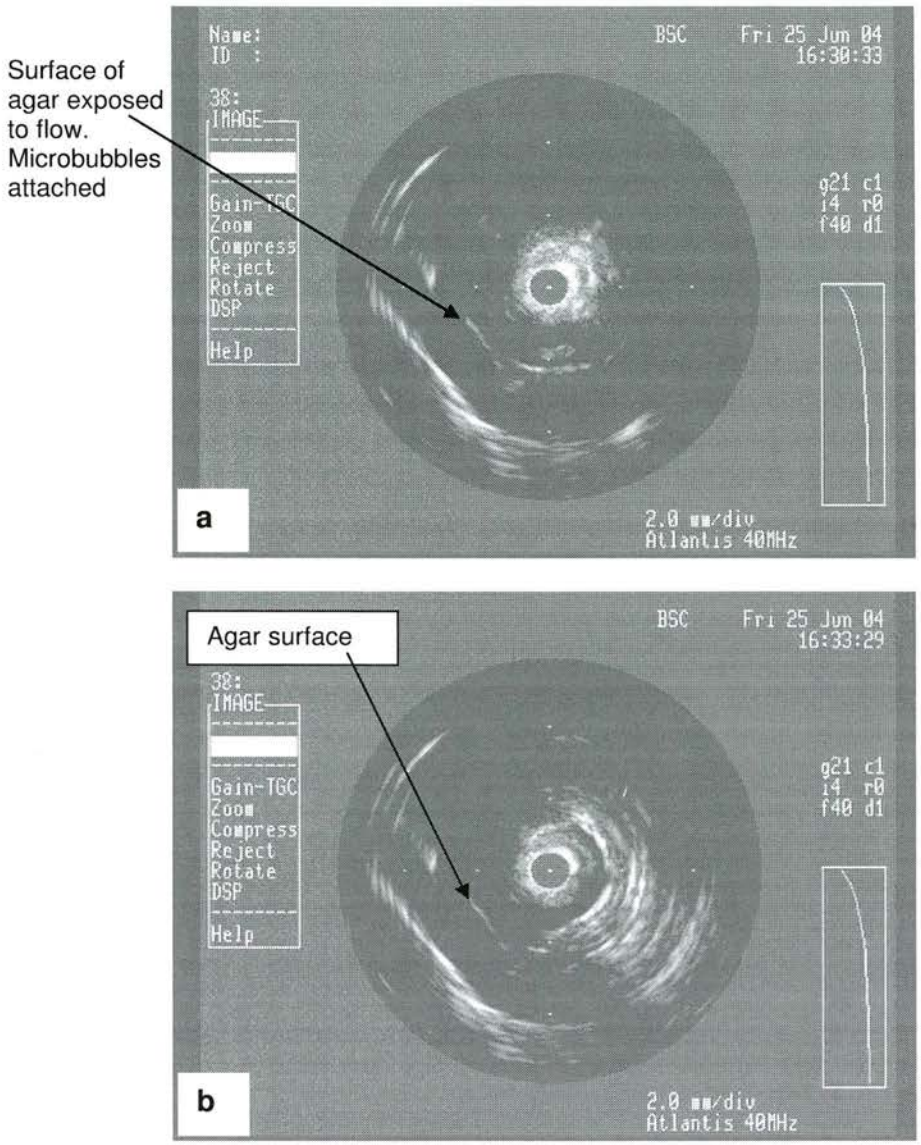

Figure 6.5: IVUS images of agar samples with original recipe microbubbles attached, a) flow rate 110 ml min^{-1}, b) flow rate 380 ml min^{-1}.

Figure 6.6 shows microbubbles made containing increased PE attached to agar and subjected to a flow rate of 195 ml min^{-1}. The echo from the bubble line is brighter than the echo in Figure 6.5. This suggests that the echo from the attached microbubbles increases with increased PE concentration, as it does when the microbubbles are in a suspension. This is also seen with the sonicated microbubbles in Figure 6.7. The microbubbles were sonicated for 30 seconds prior to being

attached to the agar. The echo from the bubble line was enhanced and there was increased coverage across the agar sample.

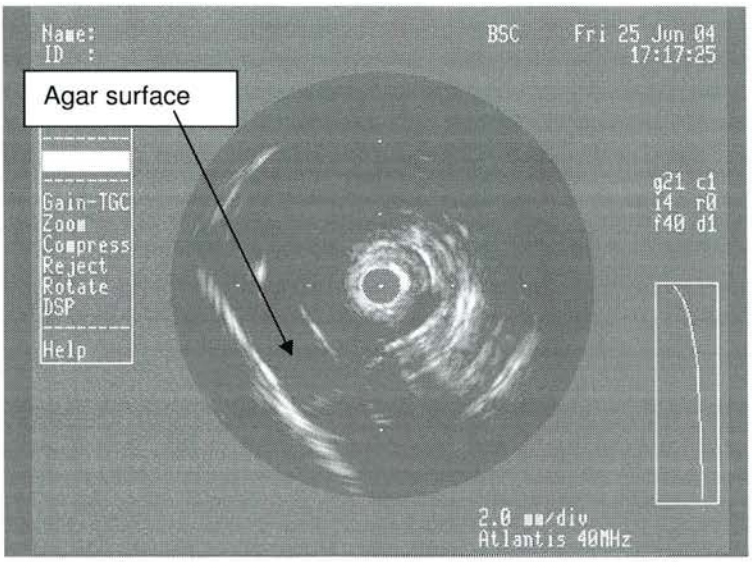

Figure 6.6: IVUS images of microbubbles made with increased amounts of PE, attached to agar samples placed in the flow chamber. Flow rate of 195 ml min^{-1}.

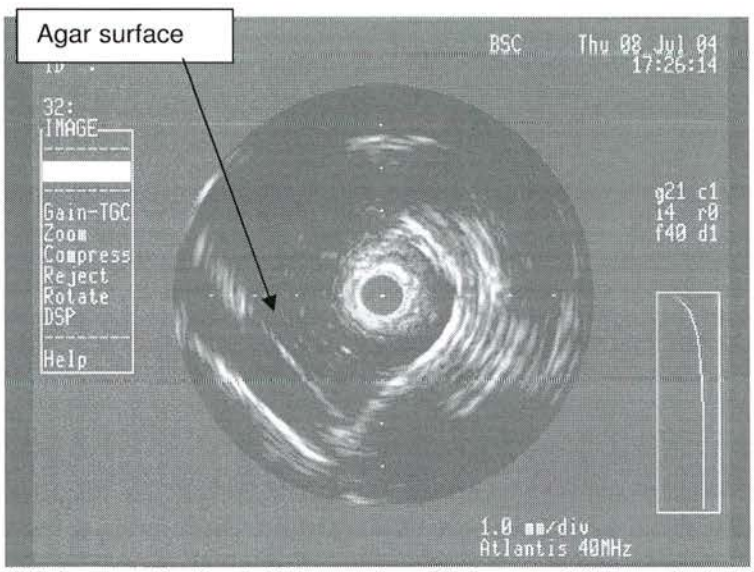

Figure 6.7: IVUS images of microbubbles made with increased PE, sonicated for 30 seconds attached to agar samples. Flow rate through flow chamber was 195 ml min^{-1}.

For each of the above sets of attached microbubbles, images were recorded at increasing flow rates. For each flow rate there was no visible difference in the image. After increasing the flow rate to 385 ml min^{-1} and reducing it again to 110 ml min^{-1},

the image did not appear different. This suggested that for each microbubble recipe the microbubbles were firmly attached and were not removed at increasing flow rates.

6.3.2 Mean Backscattered Power

In addition to the IVUS images and to investigate if the mean backscattered power from the attached microbubbles varied with increasing flow rate, the RF data collected at each flow rate was used to calculate the mean backscattered power at three points across the surface of the agar sample as described previously. The mean backscatter power from original recipe microbubbles attached to 0% scatterer agar, across the surface of the sample (i.e. the mean backscatter power from position 1, 2 and 3), with increasing flow rate is shown in Figure 6.8. Mean backscatter powers across agar samples without microbubbles attached are also shown. The mean backscatter power from the agar with microbubbles attached was approximately 12 dB greater than from the sample with no bubbles attached.

After the flow rate was increased to 385 ml min^{-1}, it was reduced to 110 ml min^{-1}. These points are represented by the filled data points in Figure 6.8. There was no significant difference between the mean backscattered power at 110 ml min^{-1} before and after the flow rate was increased.

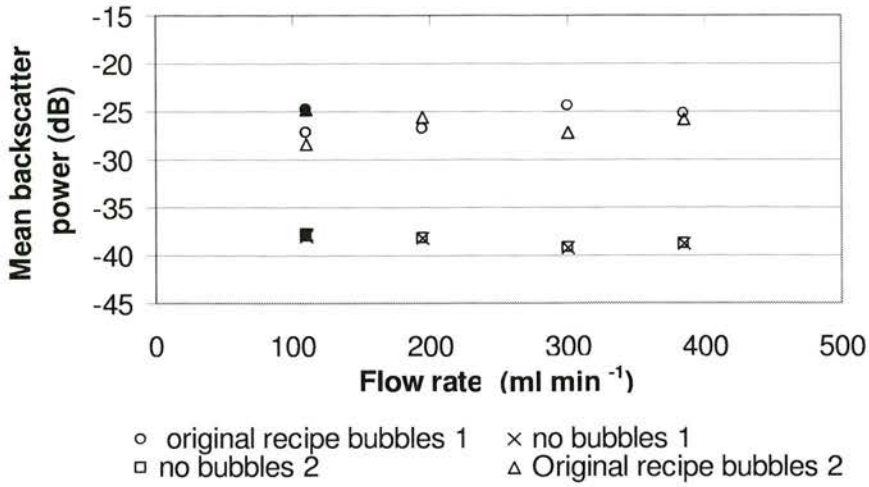

Figure 6.8: Mean backscatter power across the surface of the agar sample with increasing flow rate. The data is the mean backscatter power across the surface of the agar sample for each flow rate in Figure 6.9**. Mean backscatter power from original recipe microbubbles and samples without microbubbles attached are shown.**

The mean backscatter power at the three positions across the surface of the sample is shown in Figure 6.9. The first position was at the centre of the sample and positions 2 and 3 were on either side as shown previously in Figure 6.3.

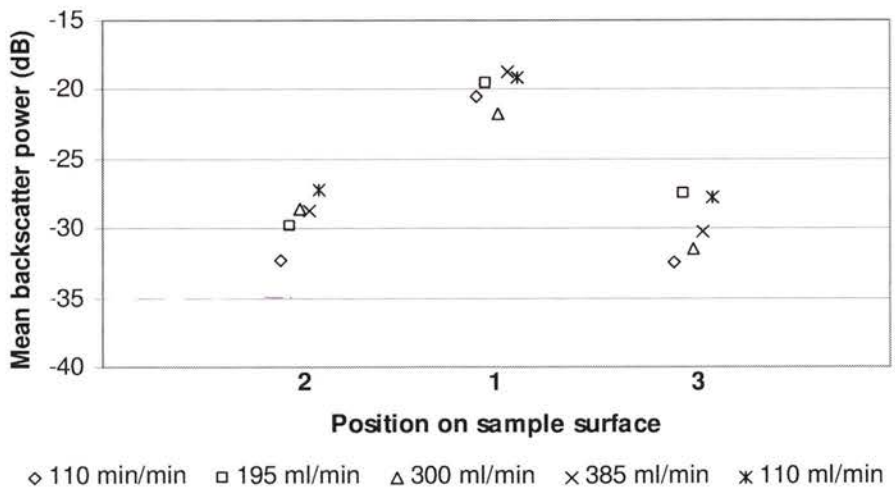

Figure 6.9: Mean backscattered power for original recipe microbubbles attached to agar samples. The x-axis is labelled 1, 2 and 3 which represents the positions across the surface of the sample, with 1 being the centre and 2 and 3 being left and right of the centre. The mean backscatter power at each point for each flow rate is shown.

The microbubbles did not attach evenly over the whole agar surface meaning the agar section chosen to be placed in the flow chamber was not necessarily covered completely, this is shown in Figure 6.9 where the mean backscatter power at position 1 gave the greatest mean backscatter power at each flow rate. The mean backscatter power reduced by approximately 10 dB at positions 2 and 3. The position of the sample in the ultrasound field was also thought to contribute to the reduction in the mean backscatter power at positions 2 and 3 and this is discussed further in section 6.4.

The mean backscatter power for microbubbles made with an increased amount of PE and microbubbles with increased PE which were sonicated prior to attaching are shown in Figure 6.10. Unattached microbubbles with increased PE have been shown in-house to have increased mean backscatter power with sonicated microbubbles having even greater backscatter. However, in Figure 6.10 there was no significant difference in the mean backscatter power for each bubble type.

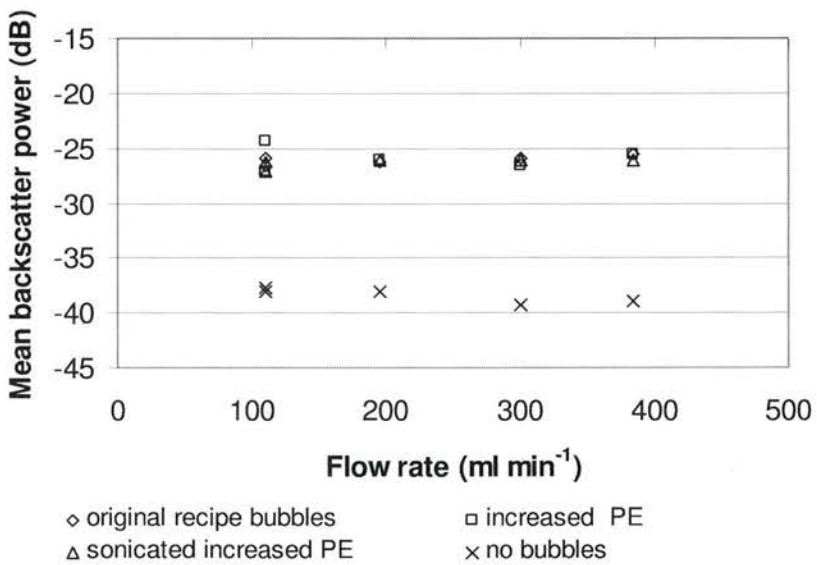

Figure 6.10: Comparison of mean backscatter power across the surface of the agar sample for normal microbubbles, microbubbles with increased PE and microbubbles with increased PE which have been sonicated with increasing flow rate. Also displayed is the mean backscatter power across the surface of the agar sample with no microbubbles attached.

The mean backscatter power from each position across the surface (region of interest 1, 2 and 3) for the data in Figure 6.10 is shown in Figure 6.11. Again there was no apparent trend in increased backscattered power with increased amounts of PE. There was no significant difference in the mean backscatter from different bubble types, however, the mean backscatter power for each bubble type is significantly higher than the mean backscatter from the samples with no microbubbles attached.

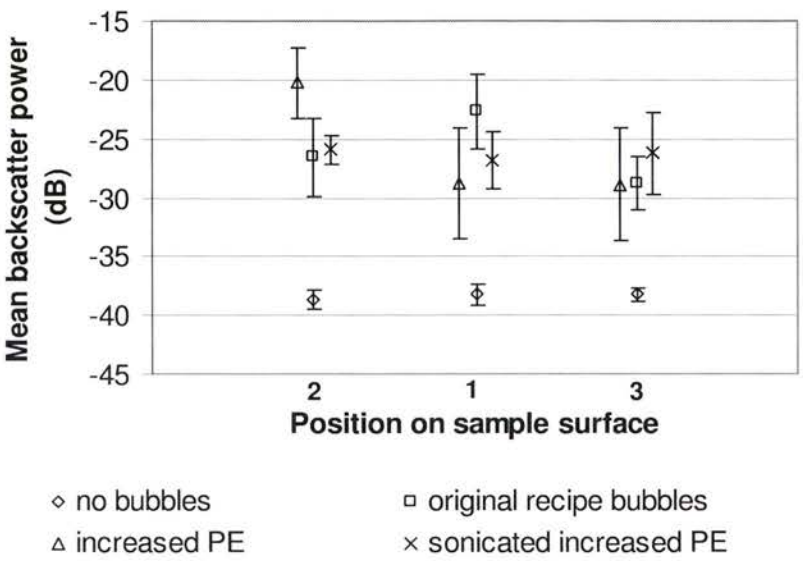

Figure 6.11: Mean backscatter power at each position across the sample surface. Data for original recipe microbubbles, increased PE microbubbles, increased PE and sonicated microbubbles and agar samples with no microbubbles attached. The error bars are one standard deviation of the mean.

6.4 Discussion

From the images obtained with IVUS, it appeared that the microbubbles remained attached to the agar samples when subjected to increasing flow rates. After increasing the flow rate and reducing it again, there was no observable difference in the IVUS images. This was confirmed when the mean backscattered power from the

sample surface was considered. There was no significant difference between the mean backscattered power before and after increasing the flow rate.

There was variation in the backscatter power at each position across the surface of the agar sample. Figure 6.9 shows the mean backscatter power from original recipe microbubbles at the three points across the surface for each flow rate. The highest backscatter power was from the centre of the samples while for samples with no microbubbles attached, the backscatter across the surfaces was more consistent. The difference across the surfaces of the samples with bubbles attached was possibly due to the distribution of contrast agent on the surface of the agar and the position of the sample in the ultrasound field. The centre of the sample was closest to the transducer, thus would experience maximum acoustic pressure.

There did not appear to be any trend with mean backscatter power and increasing flow rate. For Figure 6.8 the mean backscatter across the surface of the sample was taken to be the mean backscatter power. The mean backscatter power did not vary significantly with increasing flow rate. After the flow rate had been increased to 385 ml min^{-1} and then reduced to 110 ml min^{-1}, the mean backscatter power across the surface of the sample did not reduce. This was in agreement with the IVUS images which were not found to change with increasing flow rate.

From the data obtained previously, in Chapter 5, the shear stresses at the surface of the agar sample for increasing flow rates were known. From the RF and IVUS images, it was thought that the microbubbles remained attached to the agar at increasing flow rates. The maximum measured wall shear stress the microbubbles were subjected to was 3.4 Pa (34 dynes cm^{-2}). Although the wall shear stress for flow rates greater than 385 ml min^{-1} were not determined due to the increased pressure causing the flow chamber to leak, at flow rates above 385 ml min^{-1} the microbubbles were thought to remain attached to the agar as the images obtained did not appear to differ.

As described in Chapter 2 values of wall shear stress measured in-vivo are highly dependant on the measurement techniques used. In arteries the values of wall shear stress is less than 1.5 Pa, but can reach up to 7.0 Pa (Malek et al 1999). The microbubbles remained attached and echogenic when subjected to wall shear stresses of up to 3.4 Pa. In-vivo, the wall shear stress to which a microbubble would be subjected would be highly dependent on the site being investigated. The surface of a plaque in an artery may not be smooth and can contain fissures and crevices. The position of the microbubbles within the plaque would affect the wall shear stress experienced.

From the ongoing optimisation of the microbubble, it was found that increased levels of PE within the microbubble shell increased the mean backscattered power. When in solution, the increase in mean backscatter power was significant at higher levels of PE. An increase was not seen when the contrast agent with increased PE in the shell was attached to the agar.

From the IVUS images, the enhancement of the agar surface was more apparent when the microbubbles contained increased amounts of PE. However, when the RF data was analysed to calculate the mean backscatter power, there was no obvious trend between mean backscatter power and bubble composition as shown in Figure 6.10. The increased PE microbubbles which were sonicated prior to attachment while not constantly having the largest backscatter power, did have better coverage across the surface of the agar samples, this is shown in Figure 6.11 where the difference in mean backscatter power between positions 1, 2 and 3 is less for the sonicated contrast agent than it is for the unsonicated agents. The standard deviations of the mean backscatter power across the agar surface are shown in Table 6.1, this confirms that there was better coverage when the contrast agent was sonicated prior to attachment.

	No bubbles	Original bubbles	Increased PE bubbles	Sonicated bubbles
Mean backscatter power	-38.40	-26.02	-25.95	-26.33
Standard Deviation	0.24	3.09	4.98	0.48

Table 6.1: Mean and standard deviation in mean backscatter power across surface of agar sample with no bubbles, original recipe bubbles, increased PE bubbles and sonicated bubbles attached.

The standard deviation for the samples with no bubbles attached and with sonicated bubbles attached are both less than those for original and increased PE bubbles. While there was no difference in the mean backscatter power across the surface for the agar samples with contrast agent attached contrast agent with original levels of PE typically had enhanced sections across the surface, but not usually for the whole surface, as shown in Figure 6.7. It was thought that sonicating the microbubbles broke the shell of the outer microbubble which reformed and created smaller microbubbles. It was not known where the biotin was located within the microbubble shell. The breaking of the outer bubble shell potentially exposed more biotin from the layers within the microbubble to the streptavidin coated agar causing an increased number of microbubbles to bind and hence better coverage across the surface. As with the original recipe microbubbles those manufactured with increased amounts of PE in the shell remained attached at increased flow rates and wall shear stresses up to 3.4 Pa.

Since the backscatter varied across the surface in Figure 6.11 the mean backscatter power at each position across the surface of the agar samples was compared. Again there was no significant difference in the backscatter for the different bubble types.

While the IVUS images and mean backscatter power data suggested that the microbubbles remained attached to the agar samples at increasing flow rates, this was not confirmed optically. It was attempted to get optical images of the microbubbles attached to the agar samples but this was difficult due to the agar samples being opaque.

6.5 Chapter 6 summary

Microbubbles were attached to the agar samples. The samples were placed in the flow chamber described in Chapter 5. The attached microbubbles were imaged with IVUS at 40 MHz and subjected to the same flow rates for which flow profiles were determined in Chapter 5. The images obtained from IVUS suggested that the microbubbles remained attached at increasing flow rates. The mean backscatter power across the surface of the agar samples was calculated, there was no significant difference in the backscatter power at the low and high flow rates confirming that the microbubbles remained attached to the agar at the increased flow rates. The wall shear stresses obtained in Chapter 5 were applicable for the flow rates used in this work, so the wall shear stresses under which the microbubbles remained attached were known. The maximum shear rate to which the microbubbles were subjected was 3.4 Pa (34 dynes cm^{-2}). In-vivo the mean value of wall shear stress for pulsatile flow is around 1.5 Pa (15 dynes cm^{-2}). The wall shear stresses in the flow chamber obtain using LDA suggest that the in-house contrast agent could potentially remain attached in-vivo, once attachment has been achieved. However, attachment of microbubbles under flow conditions is also an active area of important research (Dayton et al 1999a, Rychak et al 2004, Takalkar et al 2004).

Chapter 7

Attachment of targeted microbubbles under shear stress

7.1 Introduction

It was shown in Chapters 3 and 6 that the in-house contrast agent could be attached to agar, imaged with high frequency ultrasound and that the microbubble remained attached under high shear rates. While it is important to know the forces which will detach targeted microbubbles, it is also of great importance to know that the contrast agent can be attached under flow conditions. Current work in the field of attaching contrast agent was introduced in Chapter 2. At low flow rates, targeted microbubbles have been able to attach in-vitro. This is suitable for low flow rates and for small vessels. For larger blood vessels and areas of high flow rates, it is difficult to ensure the microbubble comes into contact with the vessel wall which reduces the number of microbubbles which will attach. The radiation force has been used to push the microbubbles towards vessel walls increasing the number which make contact, hence increasing the number which will attach (Dayton et al 1999a, Rychak et al 2004).

Previously the in-house microbubble had been attached to the 0% scatterer agar plates as described in part 3.6.1 which involved placing the bubble solution on the prepared plates and allowing them to attach over two hours. This chapter describes preliminary work on attachment of the in-house contrast agent to 0% scatterer agar under flow conditions to further determine in-vivo applicability.

7.2 Methods

7.2.1 Timed Attachment

In order to determine the time for successful attachment of contrast agent to the 0% scatterer agar, the agar samples were prepared with streptavidin in the standard way described in Chapter 3. 0.5 ml of agent was added to a plate at half hour intervals. These were then all washed with saline after 1.5 hours. As well as assessing binding over hours, agar samples were also left with contrast agent on for 3, 5 and 12 minutes to determine if attachment was possible for shorter time periods.

After the samples were washed, each one was imaged using the technique described in Chapter 3, (part 3.6.1). The same block of agar with the wedge shape cut out (Figure 3.14) was used to image the microbubbles attached to the 0% scatterer agar. The IVUS catheter was placed in the cut out area and each agar sample placed over it in turn. For each, the RF data and image was captured.

7.2.2 Flow Experiments

The flow chambers described previously throughout this thesis were used. Both versions were utilised as there were benefits seen in using each chamber. For flow chamber version 1 it was easier to image samples with no microbubbles attached and samples with microbubbles attached during the same imaging session. Whereas for flow chamber version 2 the flow channel design meant there was more confidence that the flow profile obtained was parabolic.

It was not known if the microbubbles would attach to the samples under flow conditions. 0% scatterer agar samples prepared with a coating of streptavidin as described in Chapter 3 were placed in flow cell version 1. The same RF capture and image capture facilities were used to collect data throughout the experimental work. Prior to the circulation of the contrast agent, RF and image data for the coated agar was saved. Initially 3 ml of microbubbles in saline was added to 300 ml saline and circulated around version 2 of the flow chamber at a rate of 35 ml min^{-1}. The agent was allowed to circulate continuously. The IVUS scanner was used to monitor the echo from the surface of the samples. Images were saved and RF data captured after

1, 2 and 2.5 hours. These times were initially chosen since the timed attachment experiments suggested that the microbubble would bind to agar after at least 1.5 hours. Later attachment images were captured before agent was circulated and after approximately 2 hours of circulation. The pump system was used with flow chamber version 2 as there were practical difficulties using version 1 with the pump.

To allow achievement of flow rates slower than was possible with the pump system a syringe pump was also used. The syringe pump held a 60 ml syringe and allowed a maximum flow of 1.65 ml min^{-1}. When the syringe was emptied it was refilled with the same solution and the syringe pump restarted. 0.5 ml of bubbles in saline was used in the syringe with 50 ml of saline. The low flow rate was necessary to prolong the contact time of the bubbles with the agar surface, increasing the likelihood of attachment. This set-up was used with flow chamber version 1.

The above work was repeated with streptavidin coated agar samples with saline and with streptavidin coated agar samples with unbiotinylated in-house contrast agent as controls.

During each experimental run, the IVUS catheter was marked on the covering sheath at the point where it corresponded with the entry to the flow chamber. This was so measurements at the same position within the flow chamber could be taken before and after circulation of the contrast agent. As well as marking the catheter, the outsides of the flow chambers where the transducer could be seen through the Perspex were marked at the position of the transducer (see Figure 7.1). Initially it was found that there was difficulty in imaging the same area once the IVUS catheter had been moved. Each sample was imaged and data captured prior to circulation of contrast agent, the catheter was then left in position to image one sample continuously. The other samples were then imaged in the same place that the first measurements had been made (using the markers on the IVUS catheter and the flow chamber) after the contrast had been allowed to circulate for at least 2 hours.

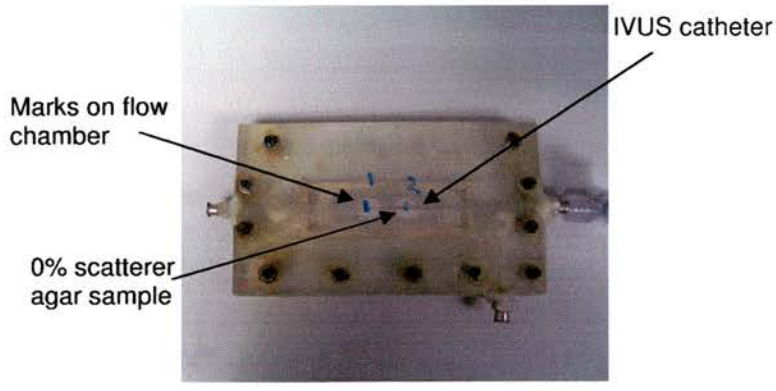

Figure 7.1: Marks on the flow chamber allowing positioning and repositioning of the IVUS catheter.

7.3 Results

7.3.1 Timed attachment

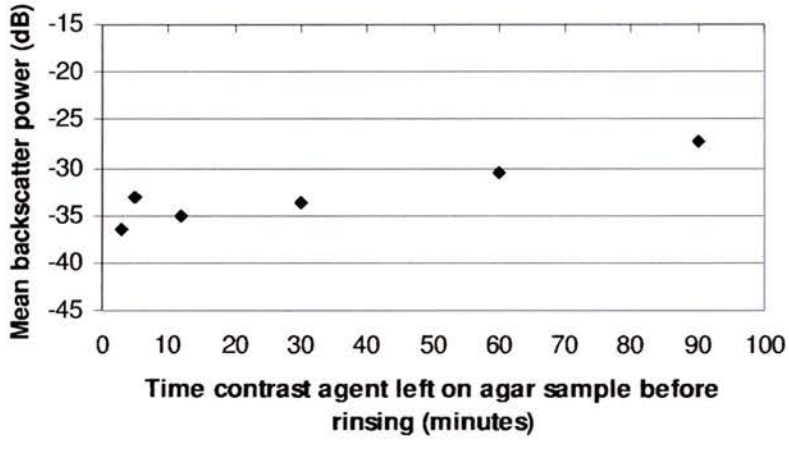

Figure 7.2: Mean backscatter power as a function of time of contact between biotinylated contrast agent and streptavidin coated agar. Under no-flow conditions.

Figure 7.2 shows how attachment of microbubbles under static conditions had increased significantly after the bubbles were left for at least 1 hour 30 minutes so when the contrast agent was circulating around the flow chamber, it was left for at least 2 hours to allow attachment.

7.3.2 Flow experiments

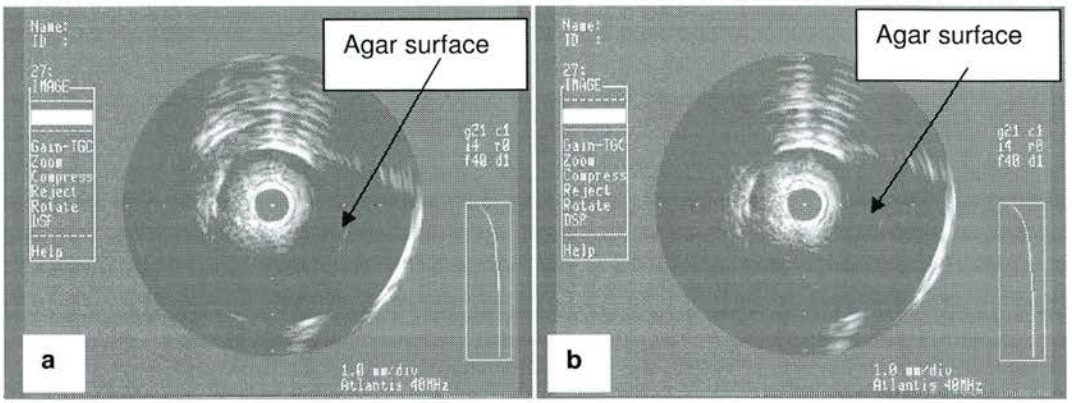

Figure 7.3: Streptavidin coated agar sample in flow chamber a) initial image, before saline is circulated, b) image after saline has been circulated for 2 hours (flow chamber version 1).

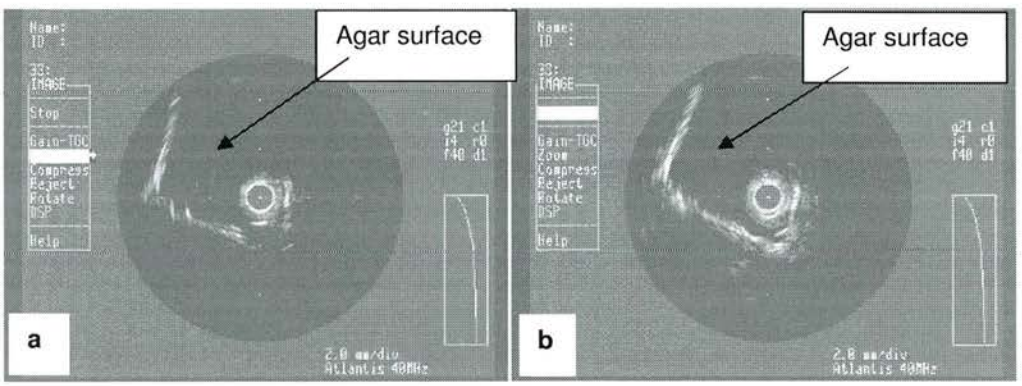

Figure 7.4: Streptavidin coated agar samples in flow chamber, a) initial image before circulation of unbiotinylated contrast agent, b) after saline with unbiotinylated contrast agent has been circulated for 2 ½ hours (flow chamber version 2).

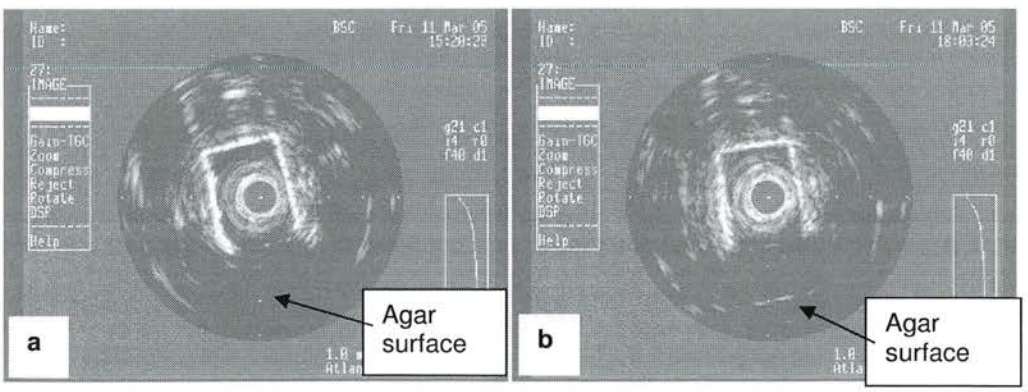

Figure 7.5: Streptavidin coated agar samples in flow chamber a) initial image before biotinylated contrast is circulated, b) after biotinylated contrast has been circulated for 2 ½ hours (flow chamber version 1).

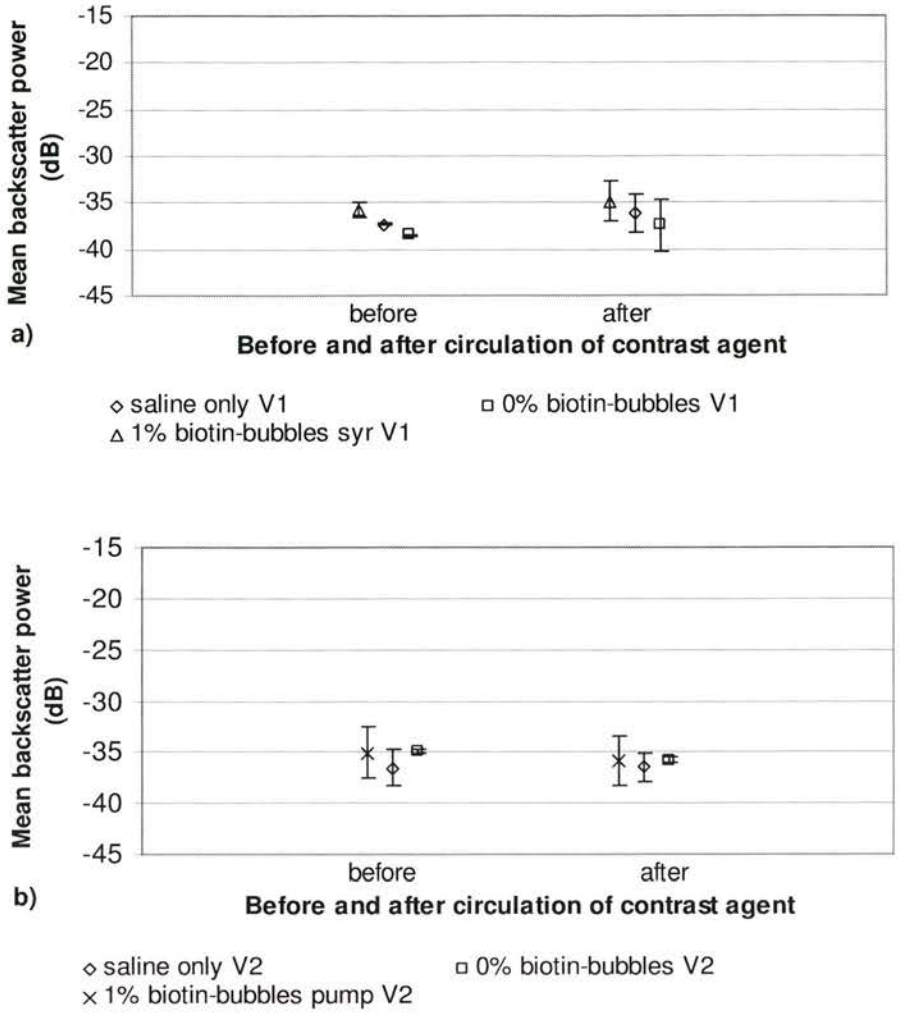

Figure 7.6: Mean backscatter power for streptavidin coated agar samples before and after being subjected to flow containing biotinylated in-house contrast agent, non-biotinylated in-house contrast agent, and saline only a) Flow chamber version 1 (V1), b) flow chamber version 2 (V2) error bars are one standard deviation.

Both chambers showed no enhancement of the agar surface when saline and non-biotinylated bubbles were circulated (Figure 7.3, Figure 7.4). The IVUS images shown in Figure 7.5 shows enhancement of the agar surface after biotinylated contrast agent had been circulated around flow chamber version 1. However, the mean backscatter power across the agar surface before and after circulation of contrast agent did not show a significant increase in the mean backscatter power in either flow chamber as shown in Figure 7.6.

7.4 Further Attachment Experiments

In order to determine if the microbubbles containing more biotin in the shell attached more readily than the original recipe contrast agent of 1% biotin, contrast agents containing 3% and 5% biotin in the shell were circulated through the flow chambers as described previously in section 7.2.2.

7.4.1 Results

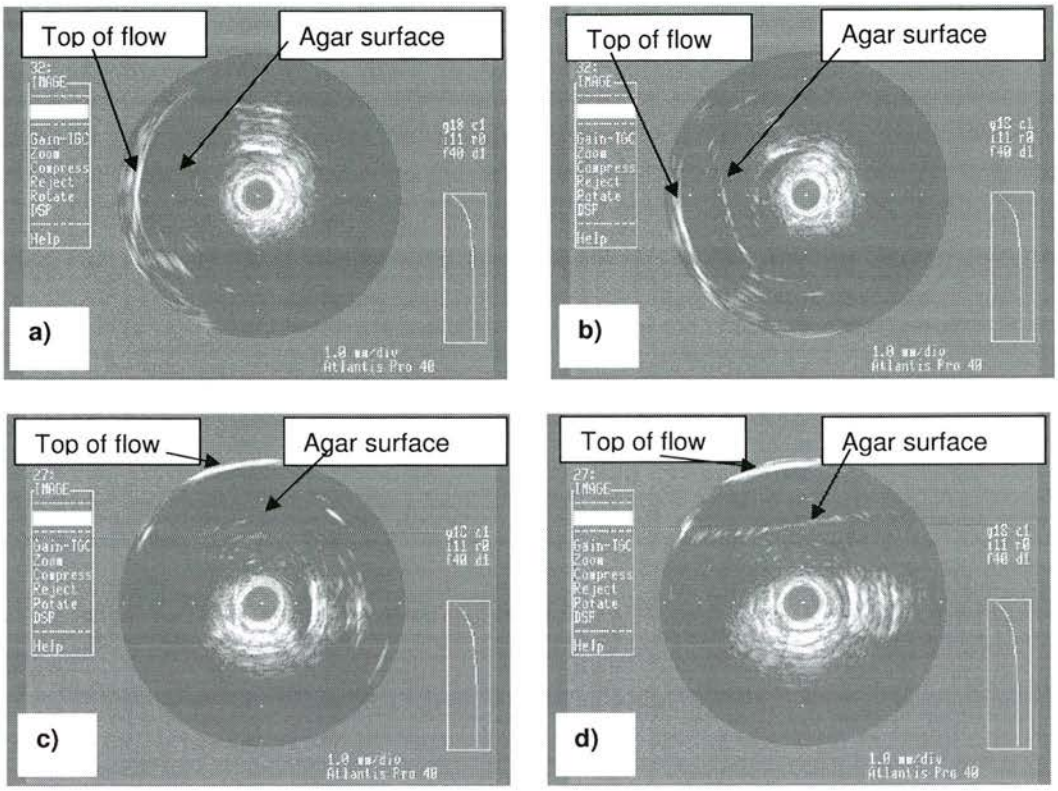

Figure 7.7: IVUS images showing microbubbles containing 3 and 5% biotin after circulating for 2 ½ hours, a) before contrast, b) after 3% biotin-bubbles are circulated, c) before contrast, d) after 5% biotin-bubbles are circulated.

Figure 7.7 shows enhancement of the agar surface after circulation of contrast agent containing both 3% and 5% biotin. Figure 7.7b and d show the line of attached contrast agent where Figure 7.7b shows 3% biotin contrast agent and Figure 7.7d shows 5% biotin contrast agent.

The mean backscattered powers shown in Figure 7.8 shows that in version 1 of the chamber there was some enhancement of the agar surface after circulation of the

contrast agent, with the mean increase in mean backscatter power over both chambers being 2 ± 2 dB. This value becomes a mean of 3 ± 2 dB when the value for the 3% biotin-bubble in chamber version 2 is not included. The omission of the mean value for 3% biotin for flow chamber version 2 was due to the significant difference between the mean backscatter power for the 3% biotin bubbles in chamber version 2 and the other mean backscatter powers after circulation of the 3% and 5% biotin bubbles shown in Figure 7.8. The reason for the difference was unknown but may have been due to an error in the experimental set-up for the 3% microbubbles. The 3% biotin bubbles used in both versions of the chamber were from the same batch so discrepancies between bubble batches are unlikely. By not including the mean backscatter power from the 3% biotin bubble in flow chamber version 2, the mean increase in mean backscatter power does not change significantly. The mean backscatter powers shown in Figure 7.8 are below those for bubbles attached under no-flow conditions, as was the mean backscatter power for 1% biotin bubbles.

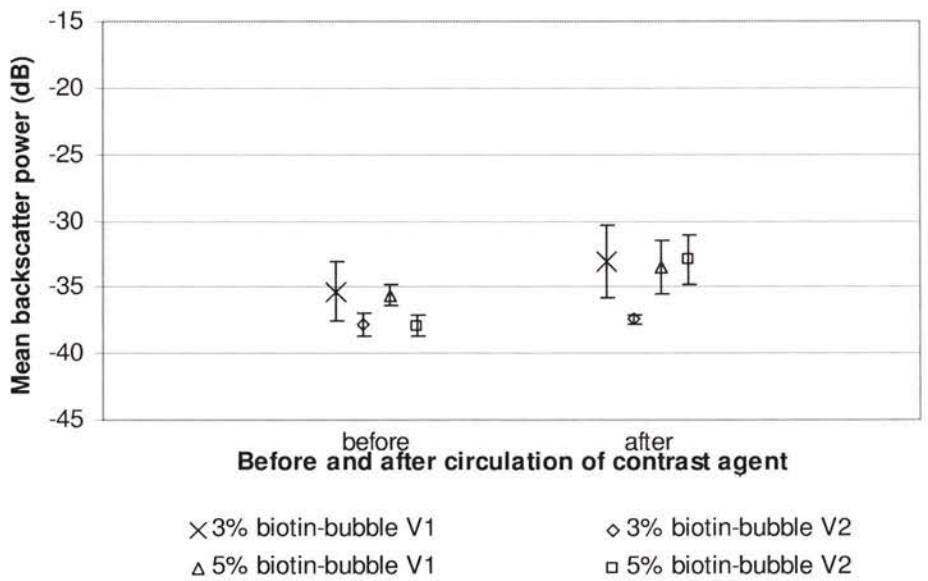

Figure 7.8: Mean backscatter power for 3% and 5% biotin microbubbles before and after circulation of microbubbles, error bars are one standard deviation.

7.5 Discussion

From the data presented here, biotinylated contrast agent attached to the streptavidin coated agar when circulated over time. There was enhancement of the agar boundary

after the contrast agent had been circulated for 2 hours as shown in Figure 7.5 and Figure 7.7. However, with the 1% biotin contrast agent, the mean backscatter power across the surface was not as high as seen when the contrast agent was attached under static conditions. Although unlike the mean backscatter powers shown in Figure 7.6, Figure 7.8 shows an increase in the mean backscatter power for the 3% and 5% biotin microbubbles.

Both versions of the flow chamber were used for the attachment experiments. Greater enhancement of the agar boundary was seen in version 1 of the chamber. It was thought that this was due to a number of factors. The syringe pump was used with version 1 of the flow chamber, this provided a flow rate of 1.65 ml min^{-1}, which was slower than the flow rate through version 2 of the flow chamber. A slower flow rate meant that potentially the microbubbles remained in contact with the agar for a longer period of time. In version 1 of the flow chamber, a larger area of the agar surface was imaged, this was due to the location of the IVUS channel with respect to the sample. The position of the IVUS catheter within the flow chambers is represented diagrammatically in Figure 7.9. The larger surface area being imaged in version 1 meant there was a greater chance that a section with bubbles attached would be imaged. However, the sample area over which the mean backscatter power was calculated was the same for both flow chambers, so the mean backscatter powers obtained were for the same amount of data in all cases.

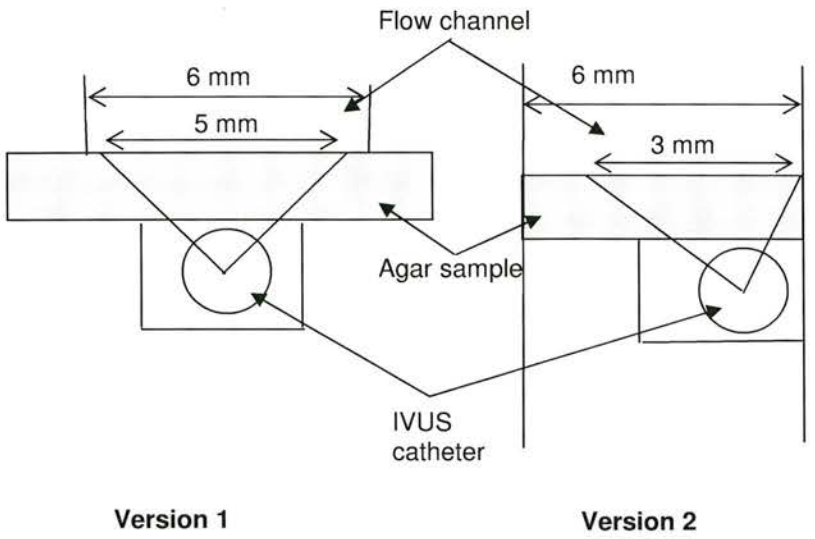

Figure 7.9: Diagram showing area of agar sample being imaged in flow chamber version 1 and version 2. A larger proportion of the sample surface was imaged in version one of the chambers.

As a comparison; images (with no microbubbles attached) from version 1 and 2 of the flow chambers are shown in Figure 7.10. The area over which the surface of the agar sample was imaged in flow chamber version 1 was approximately 5 mm whereas in version 2 it was approximately 3 mm.

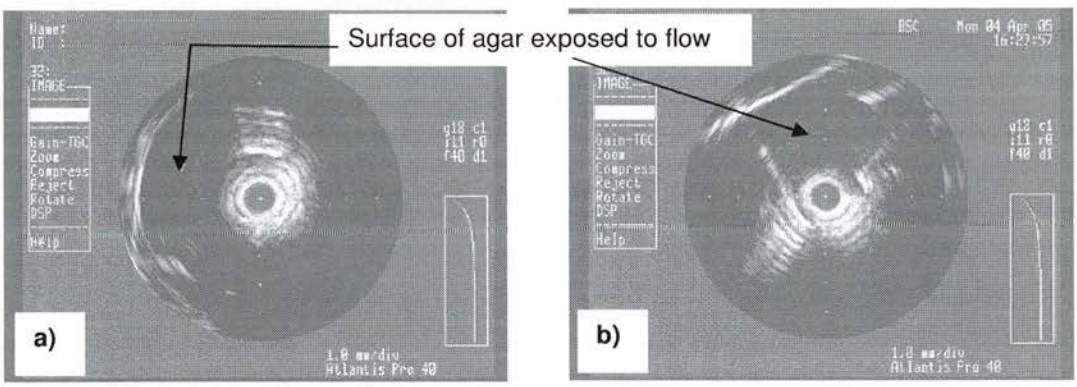

Figure 7.10: IVUS images from a) version 1 and b) version 2 of the flow chamber.

On varying the proportion of biotin in the contrast agent shell, it was thought that the number of attachment events may increase, as there would be a greater probability of biotin making contact with the streptavidin. From the images shown in Figure 7.7,

there was attachment of the contrast agent containing 3% and 5% biotin. The mean backscatter power was not significantly different between the 1%, 3% and 5% biotin bubbles. However, the IVUS images in Figure 7.7 show a brighter line of attached bubbles for the contrast agent containing 3% and 5% biotin than for the 1% biotin bubbles shown in Figure 7.5 suggesting that more binding events occurred when more biotin was incorporated into the microbubble shell.

Current research on attaching targeted microbubbles under flow conditions suggests that the radiation force could be used as a mechanism to push the microbubbles towards the vessel wall, increasing the numbers which make contact, hence, increasing the number of microbubbles which bind (Dayton et al 1999a). This is especially relevant in larger vessels of high flow rates as few microbubbles will make contact with the vessel wall. Dayton et al (1999a) have demonstrated the use of the radiation force to displace contrast microbubbles towards a vessel wall, in this instance, vessels of 200 μm and 50 μm were used. More recently the acoustic radiation force has been used to enhance adhesion of lipid shelled microbubbles which were targeted to P-selectin (a cell adhesion molecule) (Rychak et al 2004). Attachment studies of contrast agents have been completed under controlled shear rates (Takalkar et al 2004). Takalkar (2004) assessed the binding and detachment of lipid based contrast agent targeted to P-selectin where the targeted microbubbles were drawn through a P-selectin coated flow chamber which was 2.5 mm wide with a gasket thickness of 0.254 mm. Attachment and detachment at increasing shear rates were studied. The maximum number of microbubbles was found to attach to the chamber wall at a wall shear stress of 0.06 Pa and 50% of the bubbles had detached by the time the wall shear stress was increased to 3.4 Pa.

In this chapter the flow rates through both flow chambers were very low. Attachment at the increased flow rates was not attempted as when the microbubbles were circulated, they would need to remain in the flow channel above the agar samples long enough to make contact and bind. At the increased flow rates, the contrast agent was less likely to make contact with the flow chamber wall. Using Equation 2.4, described in Chapter 2 for determining the shear stress between parallel plates, the

wall shear stress for fully developed flow in both chambers was calculated and is shown in Table 7.1.

Flow chamber version	Flow rate (ml min^{-1})	Theoretical Shear stress (Pa)
Chamber version 1	1.65	0.01
Chamber version 2	35	0.30

Table 7.1: Calculated wall shear stresses for flow chambers version 1 and 2 for the flow rates used during attachment experiments.

The theoretical wall shear stress calculated using equation 2.4 for flow chamber version 1 and version 2 was 0.01 Pa and 0.30 Pa respectively. While these were not expected to be the exact wall shear stresses in the flow chamber, previously in Chapter 5 the theoretical and experimental wall shear stresses were shown to be in good agreement.

7.5.1 Methods of improving attachment

Methods of attaching contrast agents need to be improved. In the case described in this chapter, the radiation force could potentially be utilised to increase the number of microbubbles which make contact with the agar surface. The in-house microbubbles are currently being developed for the targeting of vulnerable plaque and are to be imaged with intravascular ultrasound. The ultrasound catheter itself could provide a mechanism for enhancing attachment of the targeted contrast agent as the microbubbles can be introduced to the flow system via the catheter. A diagram of an IVUS catheter is shown in Figure 7.11. If the contrast agent is introduced via the catheter, the microbubbles will go direct to the area of interest and are, potentially, more likely to bind to the area of interest, however, this method will only deliver the contrast agent to the appropriate area, it does not prolong the length of time the contrast agent will remain in contact with the area of interest. This technique was not feasible with the current flow chamber design as the IVUS catheter imaged the agar surface through the samples; the catheter was not positioned at the surface of the agar coated with streptavidin.

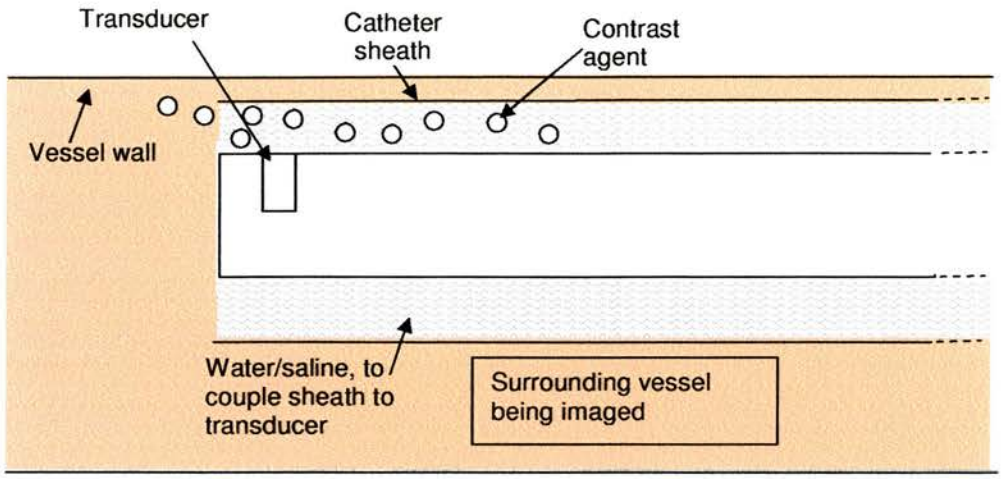

Figure 7.11: Cross-section through an IVUS catheter, showing potential use for delivery of targeted contrast agents.

Attachment work completed so far has been for steady flow. When pulsatile flow is considered, there may be a greater chance of the microbubbles binding during diastole when the flow rate reduces, thus increasing the length of time the microbubbles are in a certain position.

7.5.2 Effect of pump on circulating contrast agent

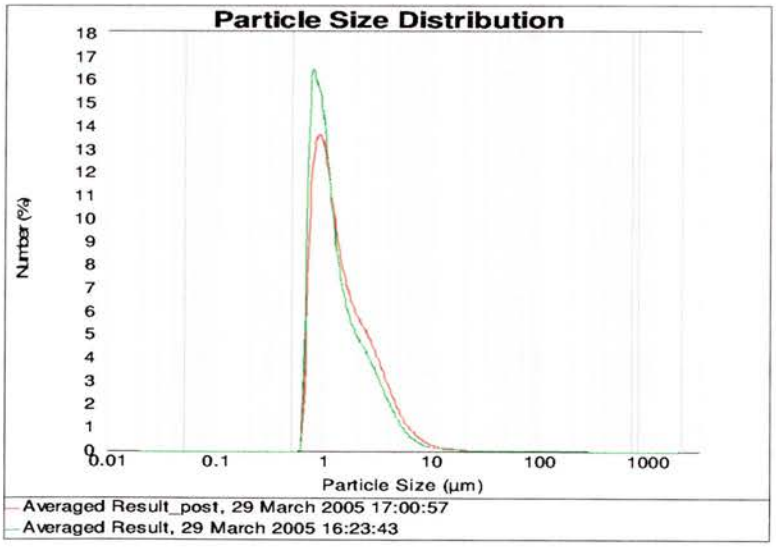

Figure 7.12: Malvern Mastersizer size distribution of in-house agent before and after being pumped for 30 minutes (green line: before being circulated red line: after being circulated).

In order to determine if the pump had an influence on the microbubbles being circulated, a sample of bubbles was sized using the Malvern Mastersizer 2000 before being pumped. The sample was then re-sized after being circulated through the pump for 30 minutes. Figure 7.12 shows the size distribution before and after the agent was circulated through the pump.

The d(0.5) value before the contrast agent was circulated (green line) was 1.132 μm and after being circulated was 1.283 μm meaning that the size of the microbubbles increased slightly after being pumped. This could be due to some smaller bubbles being destroyed, or the contrast agent could have reformed to make larger bubbles; the size distribution for the contrast agent which had been pumped was broader than the distribution for the un-pumped sample. While there were some affects of the pump on the microbubbles, the distribution remained largely unchanged so the pump system was not thought to affect the microbubbles significantly.

7.6 Chapter 7 summary

Preliminary attachment studies of the in-house agent were performed. Both versions of the flow chamber were used as they were both thought to have advantages and disadvantages. The contrast agent was circulated around the flow chambers for 2-2.5 hours. For flow rates of 1.65 ml min^{-1} in the first version of the flow chamber, the in house agent was found to attach to streptavidin coated agar. However, the mean backscatter power across the agar surface did not show significant enhancement of the agar surface. Microbubbles containing 1%, 3% and 5% biotin were used. The 3% and 5% biotin microbubbles appeared to give better coverage in the IVUS images; however, there was no significant difference in the mean backscatter power between the different bubble compositions. The attachment experiments performed in the second version of the flow chamber did not consistently show attachment of microbubbles when being circulated at a rate of 35 ml min^{-1}. Differences between the flow chambers and the flow channels were thought to account for the difference

in attachment success. The flow rate through each flow chamber was also thought to have an effect.

Attachment of the microbubbles under flow conditions is necessary for in-vivo applications. Small vessels and regions of low flow rates are more likely to allow contact between the vessel wall and the contrast agent; in larger vessels other techniques such as utilising the radiation force may be necessary. It is known that the microbubbles remain attached when subjected to flow, so optimising the attachment process is now necessary.

Chapter 8
Summary and Conclusions

8.1 Summary

The work presented throughout this thesis describes an in-house ultrasonic contrast agent which has been developed and continues to be developed to enable imaging of vulnerable plaque with intravascular ultrasound. The microbubble has been tested during initial development stages and continuously throughout development.

An advance in ultrasonic contrast imaging is the targeting of contrast agents to attach to specific markers expressed on cells at certain sites within the body. In order to develop techniques for imaging of attached contrast agents it is necessary to attach the agents in vitro. However, development of commercially available contrast agents for the purpose of targeting is difficult due to commercial sensitivity. Manufacturers of contrast agents are reluctant to divulge the contents of their microbubbles or the best method of modifying them, hence the need to develop a bubble in Edinburgh for targeting. The new in-house contrast agent has a lipid shell and has been found to be echogenic at intravascular frequencies of 30 and 40 MHz. The contrast agent is capable of being targeted to attach to specific sites of interest by modifying the shell constituents.

Of interest at the current time are cardiovascular applications for targeting vulnerable (unstable) plaque in arteries. Areas of inflammation are associated with areas of vulnerable plaque and are known to express specific markers; the microbubble can be modified to target these areas. As well as targeting vulnerable plaque, the in-house agent has the potential to be targeted to any site of interest if the relevant antibodies are utilised.

The in house contrast agent was biotinylated and attached to streptavidin coated agar. The attached contrast agent was imaged with high frequency intravascular and transcutaneous transducers and subjected to different peak acoustic pressures. When attached to agar containing no additional scatterers, the contrast agent could be imaged with high frequency ultrasound.

A new flow chamber was developed for imaging attached contrast agent under flow conditions. Attached microbubbles have been imaged at increasing flow rates and the microbubbles have been found to remain attached to agar at wall shear stresses comparable to those found in-vivo.

The flow chamber was modified for use with laser Doppler anemometry (LDA). LDA is a high resolution technique for the measurement of the velocities of fluids and gases. The flow profile in the new flow channel was found using LDA and used to calculate the shear stress on the surface of the agar samples. The microbubbles were found to remain attached under wall shear stresses of 3.4 Pa, mean arterial wall shear stress is 1.5 Pa. The technique of using LDA with the flow chamber has potential to be used for future contrast studies, different contrast agents, different binding mechanisms and flow conditions can be studied.

Initial work was completed on attachment of the contrast agent under flow conditions. Under slow flow rates contrast agents were found to attach to streptavidin coated agar. This is a continuing field of research with groups investigating methods of attaching contrast agent in-vivo when the vessels being studied can be large and the flow rates high.

8.2 Future Work

The in-house contrast agent is currently being further optimised and characterised for use with high frequency ultrasound. For use with IVUS, as described in this thesis, it is necessary to produce smaller microbubbles which will resonate at the higher acoustic frequencies (Moran et al 2006). The work described in this thesis has involved imaging the in-house agent in-vitro, more recent work has involved imaging the in-house agent and commercial contrast agent in excised sheep aorta as shown in Figure 8.1. It is possible to target the agent to target specific markers within the artery. Currently markers expressed at areas of unstable plaque are of interest, although the agent can be targeted for a variety of applications such as angiogenesis (Ellegala et al 2003, Leong-Poi et al 2003). In future development of the in-house agent applications other than targeting vulnerable plaque may be considered.

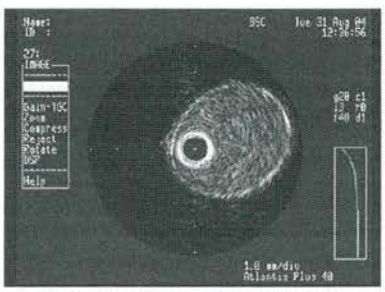

Figure 8.1: IVUS image of the Definity circulating in ex-vivo sheep aorta. (Image courtesy of Dr C.M Moran.)

Microbubble agents are also being developed for applications other than increasing contrast in ultrasound images and have great potential for the future developments (Unger et al 2004). In addition to diagnostic applications, the in-house agent can be developed further to allow drug delivery, the microbubble can be loaded with a drug, targeted to a specific site of interest and used to deliver the drug immediately to the affected area. The mechanism of drug delivery from microbubbles to cells is one which needs further work to understand and optimise the technique. As well as drug delivery, delivery of genetic material with the aid of ultrasound is also a feasible development (Newman et al 2001). The study of the transfer of material from contrast agents is on-going and current work in the department is investigating the transfer of materials from attached contrast agents as is the application of sonoporation to microbubbles and cells.

The behaviour of individual contrast agents when suspended in a solution has been previously studied (Sboros et al 2003), however, the behaviour of individual microbubbles when attached to a surface is unknown. It is of interest to know the behaviour when considering targeting applications of contrast agents.

The method used to manufacture the agent described in this thesis is solvent based which is time consuming and results in small quantities of agent. A non-solvent method of manufacturing the agent is currently being developed and this method will allow large quantities of the agent to be made. The new method is heat based and results it a solution containing fewer un-dissolved lipid crystals. Current work involves investigation of the size distribution and echogenicity of the agent and will determine if the new method produces smaller microbubbles which can be used with 40 MHz ultrasound.

Small animal imaging is a continually expanding field of interest. High frequency ultrasound can be used to obtain high resolution images. A consequence of the small size of a mouse (a few centimetres wide), a large depth of penetration is not required to image organs or vessels of interest so higher frequencies and hence higher resolution imaging can be used. A contrast agent which is echogenic at higher frequencies would allow contrast imaging and targeted imaging in small animals to be studied.

The flow chamber has been characterised for certain flow rates and LDA can be used to further characterise the wall shear stress for lower and higher flow rates. This will have use in future attachment and detachment studies where different microbubble compositions, and the effectiveness of different binding mechanisms under flow conditions can now be studied.

Harmonic imaging of the in-house agent when attached to agar could improve detection of the agent. Currently it is not possible to perform harmonic imaging using the available IVUS scanner however, a prototype IVUS catheter for performing

harmonic imaging is being developed elsewhere (Goertz et al 2005b). There are also alternative set-ups available which allow harmonic imaging. Work has begun on imaging the in-house agent using harmonic imaging at lower frequencies, an example image of sheep aorta imaged using a Diasus scanner transmitting with a L8-16 probe and receiving using L10-22 probe is shown in Figure 8.2, where the aorta before and after the addition of contrast agent is shown. Other methods of distinguishing the microbubble echoes from tissue echoes by using techniques such as pulse inversion have yet to be investigated with IVUS and could potentially enhance the images obtained from attached contrast agents.

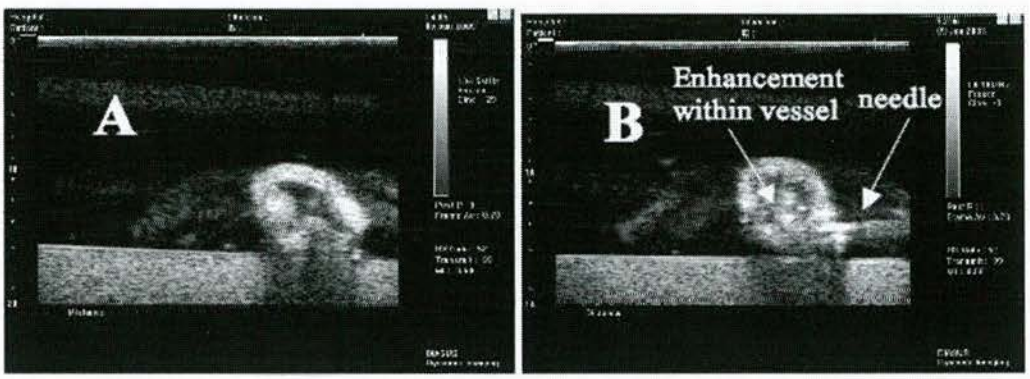

Figure 8.2:Sheep aorta mounted on slab of tissue mimicking material. Both images obtained scanner transmitting with a L8-16 probe and receiving using L10-22 probe. a) vessel prior to injection of contrast, b) vessel post injection of 1ml of in-house contrast agent (Image courtesy of Dr C.M Moran.)

The attachment of the agent under flow conditions is crucial for in vivo usage. A reliable method of attaching the bubbles under flow conditions, especially in areas of high flow is needed. The binding mechanism could be modified so as to use a mechanism which binds on contact. This combined with utilising the radiation force as a method for pushing the bubbles in flow towards the vessel wall would enhance the attachment of microbubbles to the area of interest. The radiation force has been shown to be a feasible technique for pushing bubbles towards vessel walls and will be most applicable in large vessels with high flow rates (Rychak et al 2005).

The field of ultrasound contrast agents is a very active area of current research and is continually expanding.

Appendix 1

Development of in-house contrast agent

Ap1.1 Introduction

Chapter 3 describes the development of in in-house contrast agent suitable for imaging with 40 MHz intravascular ultrasound and which was to be developed for targeted imaging of vulnerable plaque. This appendix provides a concise overview of the development and optimisation of the in-house agent.

Section 3.4.1 describes the general protocol for the manufacture of the in-house agent. The lipid constituents of the microbubbles: Phosphatidyl Choline (PC), Cholesterol, Phosphatidylethanolamine (PE) and Phosphatidyl Glycerol (PG) (Sigma Aldrich Company Ltd, Dorset, UK), were dissolved in chloroform, this allow the mixing of the constituents. Nitrogen gas was used to evaporate the chloroform off the mixture leaving a lipid residue in the container. The residue was re-dissolved in cyclohexane and placed in dry ice in preparation for freezing. The mixture was left to freeze dry overnight. The resulting white powder of the combined lipids could then be mixed with saline to form the contrast agent. When dissolved in saline the natural form the lipids take is in the form of multi-layer microbubbles, gas was then bubbled through the solution to incorporate the gas into the agent. The process is described more fully in (Moran et al 2004) and (Moran et al 2006)

The tests completed during initial optimisation of the in-house agent are described in Table Ap1.1. These tests are described in Chapter 3. The aim of agent optimisation

was to develop an agent which was echogenic at intravascular frequencies and which could be targeted to specific sites. Ideally the agent would be reduced in size to approach the bubble size which would be resonant at 40 MHz. Further work on optimisation of the in-house agent was completed in parallel to the work described in this thesis, various methods for reducing the size of the agent and increasing the mean backscatter power were tested and are described in Table Ap1.2. Table Ap1.3 describes the different agent compositions used for attachment in Chapters 6 and 7. The initial studies found that the amount of biotin in the agent shell was important for the attachment of the agent.

Variation tested	Method of testing	Result summary
Cholesterol content in agent shell	Agent containing 30-70% cholesterol was made. Each agent was imaged with IVUS and the images studied to determine any change in backscatter.	No significant change in mean backscatter power was found with change in cholesterol concentration.
Amount of mixture dissolved in saline to make up agent	Solutions from 5 mg agent per ml of saline to 100 mg per ml were imaged with IVUS to determine the optimum concentration of agent in saline.	25 mg per ml of saline was determined to be optimum.
Method of bubbling gas into agent	Helium and Nitrogen were bubbled through the agent solution (gas tube placed in bottom of the container and bubbled through) or bubbled on top of the solution (gas tube placed by top surface of solution and bubbled on top, agitating the solution). The resulting agent was image with IVUS.	From the images obtained from IVUS it was thought that Nitrogen gas bubbled on top of the solution gas the most echogenic bubbles.
To determine if the mean backscatter power from the agent varied with the gas used for bubbling on the solution.	Nitrogen and Helium were bubbled on top of the solutions. Each was imaged with IVUS and the mean backscatter power for each compared. Agent made with no extra gas being incorporated was also tested.	No significant difference in mean backscatter power for Nitrogen, Helium and no extra gas.
Lifetime of agent	The agent was imaged with IVUS and the mean backscatter power determined for the same samples over 48 hours.	There was no significant decrease in mean backscatter from the agent after 48 hours.
Targeting of agent	Biotin was incorporated into the agent shell. Streptavidin coated surfaces were used to determine if the agent could be attached successfully.	The agent containing biotin in the shell attached to streptavidin coated surfaces.

Table Ap1.1: Summary of tests completed on agent described in Chapter 3.

Variation tested	Method of testing	Result summary
Concentration of PE in the agent shell	The proportion of PE in the agent shell was varied from 10% to 90% and the mean backscatter power and mean agent size determined for each.	The mean backscatter power increased with increasing PE concentration.
Sonication of the agent	The agent, after being reconstituted in saline, was sonicated for increasing lengths of time from 30 seconds to 300 seconds and the change in mean backscatter power and agent size determined.	The mean backscatter power from the agent increased after being sonicated for 30 seconds. There was no change in mean backscatter power for increased lengths of sonication.

Table Ap1.2: Summary of tests completed on agent in parallel to work competed in this thesis. The work described in this table was performed by Dr C M Moran.

Variation tested	Method of testing	Result summary
Amount of biotin in shell	In attachment under flow conditions described in Chapter 8, agent containing 1%, 3% and 5% biotin was used	Generally, there was increased attachment with increased biotin.
Sonication of agent	The agent was sonicated for 30 seconds prior to being placed on the agar for attachment.	The was a increase in attachment when the agent was sonicated.
Variation of PE in shell	The agent was made with 34% more PE in the shell than the original recipe bubbles.	There was increase attachment with the increased PE.

Table Ap1.3: Description of bubble types used for targeting.

Currently the method of bubble manufacture is being modified with a new non-solvent method being used. This method allows the manufacture of larger quantities of agent. The new method has initially produced batches of contrast agent which contain fewer lipid crystals than the solvent method. Further investigation of the size distribution and echogenicity of the agent will determine if the new manufacture method produces smaller microbubbles. This work is currently ongoing.

Appendix 2

Hydrodynamic forces to which attached microbubbles are subjected

Ap2.1 Forces on bubbles at surfaces

While the experimental techniques and results presented in this thesis allowed the ultrasonic imaging of attached microbubbles under flow conditions and the determination of the wall shear stress to which the attached bubbles were subjected. The specific forces acting on the attached bubbles were not known. It is instructive to consider the forces present to increase understanding of the situation to avoid making any fundamentally flawed assumptions.

The forces on the bubble against the wall due to flow would comprise of drag, lift and torque forces shown in Figure Ap2.1. It is of interest to know the strength of the forces on the attached bubbles due to the flow to understand how the bubble may be affect by the flow.

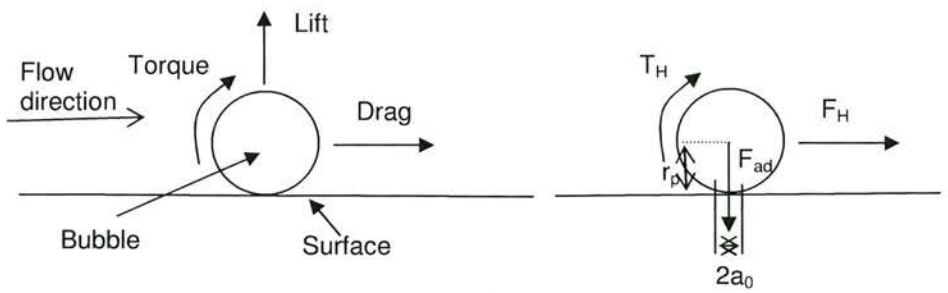

Figure Ap2.1 Forces on an attached bubble under flow conditions.

The hydrodynamic force (F_H) (drag) for a spherical particle in contact with a plane wall has been shown to be(O'Neil 1968),

$$F_H = 1.7009 \times 6\pi\mu r_p v(r_p) \qquad \textbf{(Ap2. 1)}$$

where, μ is the dynamic viscosity of the fluid, r_p is the radius of the particle and $v(rp)$ is the velocity of the fluid at a distance of r_p from the surface. The value 1.7009 is the dimensionless coefficient of force acting on the sphere. The fluid is assumed to be incompressible with a constant density and viscosity and the flow is assumed to be steady and laminar with low Reynolds numbers.

The torque acting on a spherical particle at a surface exposed to a shear flow has been calculated by (Hubbe 1984),

$$T_H = 1.38 \times F_H r_p \qquad \textbf{(Ap2. 2)}$$

where T_H is the hydrodynamic torque and can be used to calculate the adhesive force between the particle and surface since,

$$T_H = F_{ad} a_0 \qquad \textbf{(Ap2. 3)}$$

where F_{ad} is the adhesive force and $2a_0$ is the area of contact between the particle and surface. These equations have been previously used to study particle-membrane interactions under flow conditions (Elzo et al 1996).

Equation Ap2.1 can be used with the data obtained in Chapter 6 where the viscosity of the water was 1 mPa.s and the radius of the bubble was 1μm, the flow velocity at

1μm from the edge is taken to be 1 cm s^{-1}. The torque acting on the attached bubble can then be calculated using Equation Ap1.2, which can in turn be used to calculate the adhesive force between the bubble and agar surface by Equation Ap2.3.

Substituting the above values into equations Ap2.1, 2.2 and 2.3, the following values were obtained, F_H=3.2x10^{-10} N, T_H=4.4x10^{-16} N and F_{ad} 2.2x10^{-9} N.

The above equations are applicable for rigid spheres whereas contrast microbubbles are compressible, however, these calculations provide the basis for the calculation of the forces on the contrast agent due to the flow.

The calculated forces on the bubbles show that the adhesive force is orders of magnitude greater than the lift force and one order of magnitude greater than the drag force, this is dependent on the assumption for the value of at area of contact (0.2μm in this case). This however does not take account of the binding force between the avidin and biotin used to attach the bubbles.

Cells when attached to surfaces do not always form perfect spheres, thus varying in the area of contact at the surface. Cells when subjected to flow align and elongate in the direction of the flow, thus leading to non-spherical particles at the surface. Work has considered the effect of cell smoothing and cell surface on the forces experienced by the particles (Brooks and Tozeren 1996). The forces on cells subjected to flow were calculated. As a spherical cell aligned in the direction of the flow, the forces acting on the cell were found to decrease by 25%. When the cell modelled was given a rough surface, the forces on the cell were slightly smaller than for a smooth cell.

The attached contrast agents when subjected to flow may experience forces similar to those of rigid spheres, however, during insonation, the agents will experience forces due to the ultrasound which may also affect the net force experienced by the attached bubbles.

Initial Simulations

Initial 2D simulations studying the forces on attached bubbles were run by Dr Paul Stansell, Department of Physics, University of Edinburgh. Microbubbles were modelled as cylinders, against a surface. The drag, lift and torque forces experienced by single and multiple cylinders was considered. Figure Ap2.2 shows normalised drag, lift and torque forces against separation of the cylinders for a row of 10 cylinders. As the separation increases, the forces expressed on each of the cylinders tends towards that of a single cylinder. For smaller spacing between cylinders, the first experiences larger forces than the following cylinders. Figure Ap2.3 shows the forces experienced on each cylinder. For each force, the first cylinder in the row experiences a greater force than the following cylinders. For small spacing between cylinders, the last cylinder in the row experiences an increased drag and torque force but a decreased lift force. These initial simulations can be further developed for different flow conditions and for spheres to enhance the understanding of the forces experience by attached microbubbles.

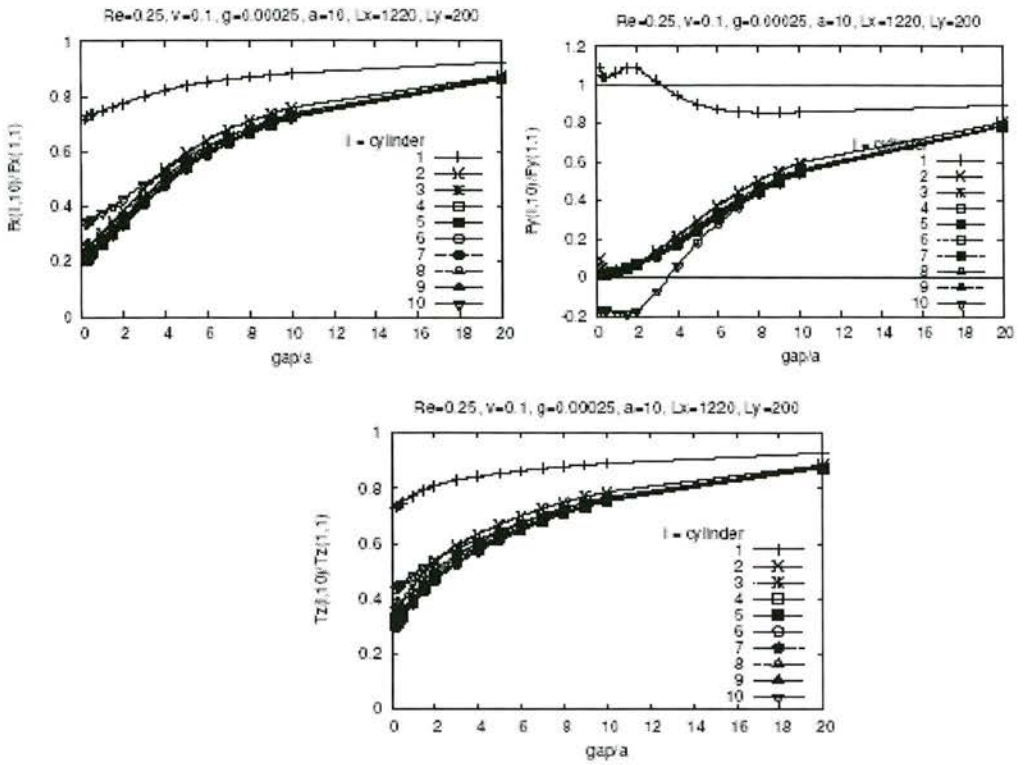

Figure Ap2.2Forces experiences as the separation between cylinders increases, drag, lift and torque forces. Printed by permission, Dr Paul Stansell

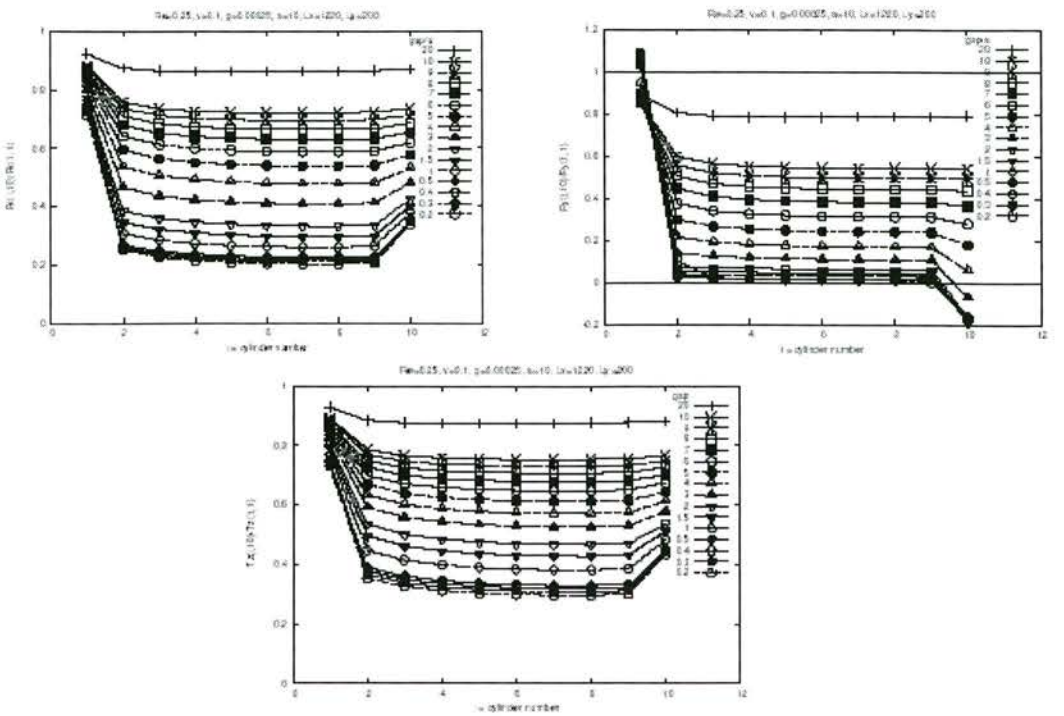

Figure Ap2.3 Forces on each cylinder as the separation increases, drag, lift and torque forces. Printed by permission, Dr Paul Stansell

Appendix 3

Conferences and Publications

Conference presentations and publications

Butler, M.B., Moran, C.M., Oliver, C., Ross, J.A., Ansell, I., Anderson, T., McDicken, W.N., High Frequency ultrasonic imaging of contrast agents attached to surfaces, *British Medical Ultrasound Society Annual Scientific Meeting*, Harrogate, UK, December 2003 (Oral presentation)

Butler, M.B., Moran, C.M., Anderson, T., Cunningham, C., Ross, J.A., Easson, W.J., Fox, K.A.A., McDicken, W.N., Shear Stresses on ultrasonic contrast microbubbles attached to arterial plaque – an in vitro model, *Scottish Society of Experimental Medicine*, Dundee, UK, June 2004 (Poster presentation)

Butler, M.B., Moran, C.M., Anderson, T., Cunningham, C., Ross, J.A., Easson, W.J., Fox, K.A.A., McDicken, W.N., (2004), Quantitative laser Doppler anemometry measurements of the shear stresses exerted on ultrasonic microbubbles attached to surfaces under physiological flow conditions, *IEEE Ultrasonics Symposium,* Montreal, Canada, August 2004 (Oral presentation) paper printed in: *Proceedings on the 2004 IEEE Ultrasonics Symposium,* pp 17-19

Butler, M.B., Passive and targeted microbubbles for ultrasound imaging, *British council, New imaging techniques in biology,* Nerja, Spain, March 2005 (Oral presentation)

Butler, M.B., Moran, C.M., Anderson, T., Cunningham, C., Ross, J.A., Easson, W.J., Fox, K.A.A., McDicken, W.N., Use of laser Doppler anemometry to determine the shear stress to which ultrasonic contrast agents attached to agar are subjected, Institute of Physics and Engineering in Medicine Biannual Physics and Technology of Ultrasound meeting, York, UK, March 2005 (Oral presentation by C.M. Moran)

Butler, M.B. Moran, C.M., Cunningham, C., Anderson, T., Ross, J.A., Fox, K.A.A., McDicken, W.N., (2005) High frequency ultrasonic imaging and attachments of contrast agents under flow conditions, *IEEE Ultrasonics Symposium*, Rotterdam 2005 (Poster presentation)

Refereed Publications

Butler, M.B., Moran, C.M., Anderson, T., Cunningham, C., Ross, J.A., Easson, W.J., Fox, K.A.A., McDicken, W.N., (2005) Laser Doppler anemometry measurements of the shear stresses on ultrasonic contrast agent microbubbles attached to agar, *Ultrasound in Medicine and Biology*, **31**, 4, pp 545-552

ELSEVIER

Ultrasound in Med. & Biol., Vol. 31, No. 4, pp. 545–552, 2005

0301-5629/05/$–see front matter

doi:10.1016/j.ultrasmedbio.2004.12.012

Original Contribution

LASER DOPPLER ANEMOMETRY MEASUREMENTS OF THE SHEAR STRESSES ON ULTRASONIC CONTRAST AGENT MICROBUBBLES ATTACHED TO AGAR

MAIREAD B. BUTLER,* CARMEL M. MORAN,* TOM ANDERSON,* CARRIE CUNNINGHAM,† JAMES A. ROSS,† WILLIAM J. EASSON,‡ KEITH A. A. FOX,§ and W. NORMAN MCDICKEN*

*Departments of Medical Physics, †TIRG, Center for Inflammation Research, ‡Mechanical Engineering and §Cardiovascular Research Unit, University of Edinburgh, Edinburgh, United Kingdom

(*Received* 5 *August* 2004; *revised* 6 *December* 2004; *in final form* 14 *December* 2004)

Abstract—Ultrasonic contrast agents are currently being developed to target and bind to specific areas of interest such as atheromous plaque. A microbubble has been developed in-house which can be targeted to attach to specific cell-lines. To assess the feasibility of using the microbubble *in vivo*, the shear stresses which the bound microbubbles can withstand need to be known. A flow chamber was developed for use with intravascular ultrasound (IVUS) and laser Doppler anemometry (LDA). Biotin was incorporated into the microbubble shells and streptavidin was used to attach them to agar. IVUS at 40 MHz was then used to image the attached microbubbles under steady flow at a range of flow rates from 75 to 480 mL min^{-1} through a flow area of 9 mm^2. LDA was employed to find high resolution velocity profiles of the flow in the chamber at a selection of these flow rates and the shear stresses on the bubbles were calculated. The bubbles were found to remain attached to the agar for shear stresses of up to 3.4 Pa. This compares with mean physiological arterial shear stresses of less than 1.5 Pa for pulsatile flow. (E-mail: M.Butler@ed.ac.uk) © **2005 World Federation for Ultrasound in Medicine & Biology.**

Key Words: **Ultrasound, Contrast agents, Microbubbles, Targeted, Shear stress, Laser Doppler Anemometry.**

INTRODUCTION

Ultrasonic contrast agents are gas-filled microbubbles approximately 5 μm in diameter. They are currently used diagnostically to enhance the backscatter of ultrasound in areas such as the liver and heart (Campani et al. 1998; Kaul 2001; Miller and Nanda 2004). Therapeutic applications are presently being developed to target and attach microbubbles to specific sites of interest within the body (Klibanov et al. 1997; Klibanov et al. 1999; Lanza 1996; Lindner 2004; Villanueva et al. 1998). This application has potential for gene and drug delivery, as well as detection of tumours (Ellegala et al. 2003) and vascular thrombus (Unger et al. 2002).

Angiograms are used to visualize blood flow in the cardiovascular system. However, it is not possible to say whether a narrowing in an artery is due to a stable or unstable (vulnerable) plaque. Intravascular ultrasound (IVUS) is used to image plaque and different types have been broadly distinguished using spectral analysis (Spencer et al. 1997; Watson et al. 2000; Nair et al. 2001). IVUS elastography is a technique also being investigated as a method of assessing plaques (de Korte et al. 1998). However, an accurate diagnosis of unstable plaque is still not possible. There is a real clinical need for optimising the diagnosis and hence treatment of vulnerable plaques.

With a view, to this a targeted lipid-based microbubble has been developed in-house (Moran et al. 2003a, Moran et al. 2004a). It is echogenic at intravascular frequencies. The microbubble has the potential to attach to markers expressed on the surface of plaques and hence to identify vulnerable plaques using IVUS. To assess the feasibility of using the microbubbles *in vivo*, it is necessary to know the shear stresses that they can withstand without detachment and how they behave at different flow rates.

Attached microbubbles under flow conditions have been imaged *in vitro* (Klibanov et al. 1999; Villanueva et al. 1998) and, more recently, they have been studied under controlled shear rates (Takalkar et al. 2004). Takalkar et al. (2004) assessed the binding and detachment of a contrast agent targeted to P-selectin. A flow chamber was coated with P-selectin and the targeted microbubbles were drawn through the chamber. Attachment and detachment studies at increasing shear stresses

Address correspondence to: Mairead Butler, Medical Physics and Medical Engineering, University of Edinburgh, The Chancellor's Building, 49 Little France Crescent, Edinburgh, EH16 4SB, UK. E-mail: M.Butler@ed.ac.uk

were completed. The maximum number of microbubbles was found to attach to the chamber surface at a shear stress of 0.06 Pa and 50% of the bubbles had detached by the time the shear stress was increased to 3.4 Pa. The density of antibody on the microbubble shell and wall shear rate have been found to be critical parameters for bubble adhesion (Weller et al. 2002).

A flow chamber has been designed which can be used for IVUS imaging of microbubbles attached to agar using avidin and biotin. The attached microbubbles can be imaged under a range of flow rates. In order to know the shear stress to which the attached microbubbles are subjected, a detailed profile of the flow is required. While it is important to know the shear stresses under which the microbubbles can attach to surfaces, it is also necessary to determine the shear stress which attached microbubbles can withstand.

Shear stress

Shear stress is calculated from Nichols and O'Rourke (1990),

$$\text{Shear stress} = \mu\left(\frac{du}{dx}\right) \quad (1)$$

where μ is the viscosity of the fluid, u is the velocity of the fluid and x is the distance from the surface, perpendicular to the flow. These variables are represented diagrammatically in Fig.1. A high-resolution flow profile near the surface of the wall is needed to calculate the shear stress on attached microbubbles.

Laser Doppler Anemometry

Laser Doppler Anemometry (LDA) is a well-established technique allowing noninvasive, high-resolution measurement of the velocities of liquids and gases (Durrani and Greated 1977). In LDA, the Doppler shift of laser light scattered by seeding particles in the flow is measured and the corresponding velocities in one, two or three dimensions are determined. This study describes how this technique has been used to determine the flow profile in the flow chamber.

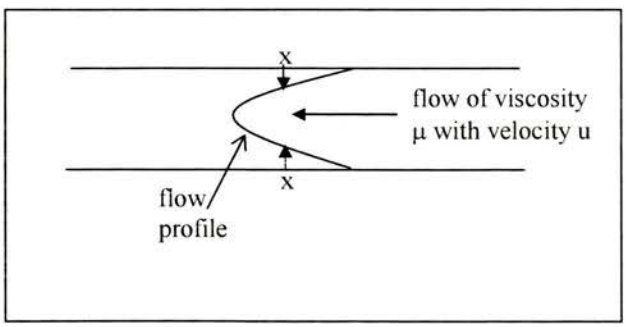

Fig. 1. Shear stress variables: x is the distance from the wall, μ is the viscosity of the fluid and v is the flow velocity of the fluid.

MATERIALS AND METHODS

Flow chamber

A flow chamber was developed to enable ultrasonic imaging of contrast agents attached to surfaces. The design was modified to allow LDA measurements. After initial experimental work with LDA (Butler et al. 2004), the design was modified to allow higher resolution velocity measurements to be made. The position of the samples in the flow was changed from the base of the chamber to the side, so the probe volume could be moved in 45 μm increments. A schematic diagram of the final version of the chamber is shown in Fig. 2. The chamber was made from three layers of perspex. The overall dimensions of the flow chamber were 160 × 80 mm; each layer was 6 mm thick. The base layer was a plain perspex rectangle. The center layer had a channel with two wells for agar samples, of dimensions 10 × 1.5 × 6 mm. The flow channel specification was 125 × 1.5 × 6 mm; at each end of the channel were two reservoirs. Luer fittings were connected to each end of the channel, to allow tubing to be attached securely. In the same layer, behind the sample wells, was a channel for use with a high frequency IVUS transducer. The IVUS catheter could then be used to scan through the agar samples in the wells. This channel was 2 mm deep and 1.5 mm wide and was parallel to the flow channel, as shown in Fig. 2. A luer fitting was used at the end of the IVUS channel, with a Y-junction to secure the catheter in place. The top layer had a microscope slide inserted into the center with the bottom of the slide flush with the bottom of the perspex. This was glued in place and made watertight. The microscope slide allowed a clear scratch-free window for the laser and was placed so that, when the chamber was assembled, it was positioned over the area of the sample wells. There were two 2 mm holes through each layer, which were used with steel rods for alignment of the layers.

The agar samples used for all of the work described here were made following a standard tissue-mimic recipe (Teirlinck et al. 1998) but without the addition of the scatterers. This reduced the backscatter from the water-sample interface, enabling the detection of microbubbles with IVUS. The speed of sound through the agar was determined using a scanning acoustic microscope; the acoustic impedance was then calculated and found to be 1.57 MRayl. Water was circulated through the flow chamber at a constant flow rate using a voltage controlled pump. The chamber was sealed using silicone grease between the sections and then clamped together. This provided a leak-proof seal and was time-saving when assembling the chamber.

Attaching the microbubbles

The lipid-based biotinylated bubbles were made in-house (Moran et al. 2003a; Moran et al. 2003b). Agar samples were coated with 1 mL of streptavidin in buffer

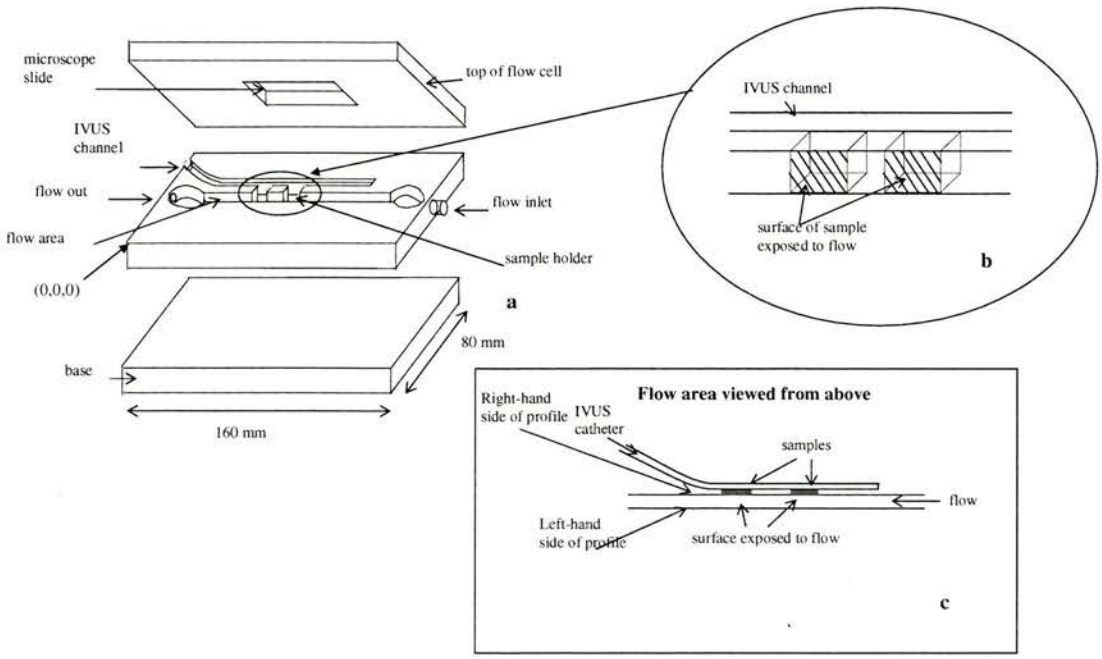

Fig. 2. Diagram of the sections of the flow chamber: (a) Sections of the chamber, (b) Enlargement of sample area and (c) View of flow area from above.

(0.5 mL streptavidin per 6 mL buffer) and left for 20 to 24 h. They were then washed with saline and 1 mL of blocking buffer (saline and 1% BSA) was added and left for 2 h. The samples were washed again with saline and 200 μL of the in-house microbubble was added and left for a further 2 h. Finally, the samples were washed with saline again to remove any excess microbubbles.

IVUS

A Boston Scientific ClearView Ultra IVUS scanner was used with a rotating Atlantis 40 MHz transducer (Boston Scientific, Natick, USA). The samples with and without bubbles attached were placed in the wells in the flow chamber. The chamber was sealed, the IVUS catheter was placed in the IVUS channel and both samples were imaged. The voltage controlling the speed of the pump was increased from 2 V to 15 V in 1 V increments; this corresponded to flow rates of 75 mL min^{-1} to 480 mL min^{-1}. Images of the sample with microbubbles attached were recorded at each flow rate after approximately 60 s; this was repeated for the sample with no bubbles attached. The images were recorded as single frames using Matrox Intellicam software (Matrox VITE Limited, Sefton Park, Buckinghamshire, UK).

To quantify any change in backscatter with increasing flow rate, a PC with a digitising card (Gage-Applied Technologies Inc, Lachine, Canada (CS8500 digitising card)) was used to capture the RF IVUS signal. For flow velocities of 110, 195, 300, 385 mL min^{-1} and again at 110 mL min^{-1}, one frame was acquired. Each RF frame consisted of 256 image lines and was digitized to 8 bits at rate of 250 Megasamples per second. Using prewritten analysis software in IDL, a region-of-interest (ROI) of 128 data points and nine ultrasonic lines was chosen at the point of the exposed surface of the agar. The ROI at a distance of 2.5 mm from the transducer was calculated to be 0.31 mm^3. For each flow rate, the same depth of ROI was chosen, although different depths were necessary for different samples due to slight differences in sample thickness. The mean backscattered power for three points across the surface of the sample was calculated. Consecutive lines of ultrasound were chosen. The data were normalized to an echo from an air-water interface with the depth between the probe and the water being the same as the depth between the probe and the sample surface in the flow chamber. Mean backscattered power from samples with and without bubbles attached for each flow rate was calculated.

LDA

A DANTEC LDA system based in Mechanical Engineering, University of Edinburgh, was used to measure the velocity profile in the chamber. The laser used was a 5 W argon ion laser with a wavelength of 488 nm. The beam was split and one probe housed the two pairs of beams used to measure 2D velocity data. A front lens with 160 mm focal depth was purchased for this work; this lens created a probe volume of 45 $\times$ 45 $\times$ 200 μm. The laser probe was mounted on a traverse system, which allowed fine mechanical movement of the probe in

x, y and z directions. The samples were cut to size and placed in the flow chamber. The flow chamber was mounted on a tripod and positioned perpendicular to the laser probe.

The laser was run at 0.2 W. Initially, the focal point was positioned at the surface of the flow chamber on the bottom left-hand corner. This was taken to be position (0, 0, 0) as shown in Fig. 2. The flow chamber inlet was connected to the pump and flow was started. At first, 6 mL milk per 2000 mL water was used to seed the flow. This proved to be an effective and economic method of getting the set-up running smoothly. Later, a fine powder, titanium dioxide (S. Black Ltd, Hertford, UK) suitable for LDA work, which had a size distribution of 3 to 10 μm, was used to seed the flow. Once flow was established, the LDA measurements were taken. The flow rates used were 110, 195, 300 and 385 mL min^{-1}.

Before determining the flow profile from the surface of the agar samples, the profile through the flow channel (from top to bottom) was found. This allowed the position of the peak velocity to be determined; the profile from the sample surface was taken at this point. The probe volume was then incremented in 45 μm intervals toward the surface of the agar sample. Flow velocities along the channel and across the channel width were determined simultaneously by 2D LDA. At each point, up to 10,000 velocity measurements were made. The maximum time for each set was 15 s. Between each increment, the traverse system was allowed to pause for 8 s, to allow vibrations in the system to disperse before velocity data were collected. The data were collected and processed using DANTEC LDA BSA software. Velocity measurements for each flow rate were made three times and the mean profile was calculated.

RESULTS

Figure 3 shows the mean velocity profiles obtained using LDA; the error bars are one standard deviation of the mean of three runs. As expected, as the flow rate is increased, the peak velocity increases and, hence, the shear rate increases. The right-hand side of the profile is the profile at the sample surface and the left-hand side is the profile at the edge of the chamber.

To calculate the shear stress at the surface of the sample, a linear regression was performed in Excel (Microsoft Excel 2000). The points of the profiles at the surface of the samples (between 38.5 and 38.7 on the x-axis in Fig. 3) were used. Figure 4 shows the profile close to the edge of the flow channel for a flow rate of 300 mL min^{-1}; the gradient of this line was the shear rate and was used to calculate the shear stress: the error bars are one standard deviation of the mean point of the three data sets. Four data points were used for each linear regression. Including an extra point in the linear regression found no significant difference in the shear stress

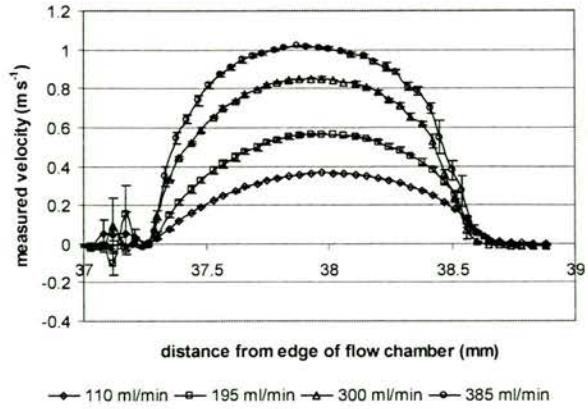

Fig. 3. LDA velocity profiles from the surface of an agar sample in the flow chamber, for flow rates of 110, 195 and 300 and 385 mL min^{-1}. The error bars are one standard deviation of the mean of the three runs. The x-axis is the distance from the front edge of the flow chamber. The region of the profile between 38.5 and 38.7 on the x-axis is the profile at the sample surface; the region of the profile between 37.3 and 37.5 on the x-axis is the profile at the edge of the flow channel.

calculated. The shear stresses were calculated using eqn 1, where the viscosity of the fluid was taken to be that of water at 20°C, *i.e.*, 1.002 Pa s (Weast et al. 1988). The shear rates and stresses calculated for each of the profiles in Fig. 3, along with the standard error in calculating the gradient, are shown in Table 1. These values are plotted in Fig. 5 for each flow volume. There is a linear trend in the increase in shear stress with flow rate in the chamber ($R^2 = 0.98$).

The second laser beam pair measured the velocity components of off-axis flow, horizontally perpendicular to those in Fig. 3. These were found to be approximately constant at zero in the flow region; examples of the distribution of point velocities for flow rates of 110 and 385 mL min^{-1} are shown in Figure 6.

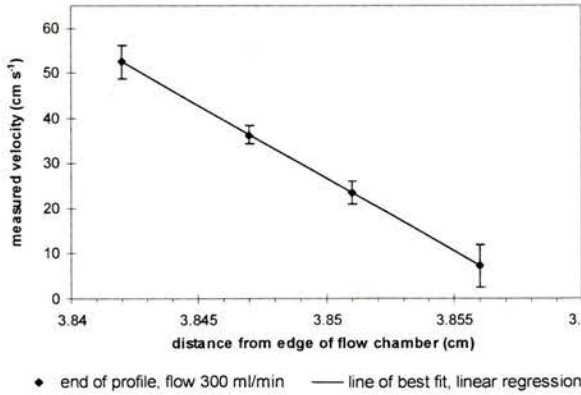

Fig. 4. Plot of the end of the profile at surface of the agar sample, with linear regression to find the line of best fit. Error bars are one standard deviation of the mean velocity from the three runs.

Table 1. Measured peak velocity and calculated sheer rates and shear stresses for varying flow rates

Flow rate (ml min^{-1})	Peak velocity (cm s^{-1})	Shear rate (s^{-1})	Shear stress (Pa)
110	36.54 ± 0.05	1162 ± 128	1.2 ± 0.1
195	56.64 ± 0.16	1756 ± 366	1.8 ± 0.4
300	85.00 ± 1.17	2947 ± 22	3.0 ± 0.02
385	101.72 ± 0.43	3373 ± 169	3.4 ± 0.2

IVUS images of microbubbles attached to the agar samples in the flow cell are shown in Fig. 7. Figure 7a shows a sample with no bubbles attached and Fig. 7b shows a sample with microbubbles attached. Images grabbed at increasing flow rates are shown in Fig. 8. As the flow rate increases, the IVUS images do not change. This suggests that the microbubbles remain bound to the agar samples under increasing flow rates. The RF data shown in Fig. 9 confirmed this. Figure 9a shows a plot of the mean backscattered power for agar samples with and without microbubbles attached at each position across the surface of the agar sample. The first position was at the center of the sample; the second and third points are on the left and right of the center. The data are the mean for two different samples, with the error bars being the standard deviation of the mean backscatter power. Figure 9b shows the mean backscatter power across the surface of the agar sample at increasing flow rates. After increasing the flow to 385 mL min^{-1}, it was reduced again to 110 mL min^{-1} and the backscatter data were collected again. The data collected after reducing the flow rate to 110 mL min^{-1} are also shown in Fig. 9b represented by filled-in data points. After the flow rate was increased to 385 mL min^{-1} and reduced

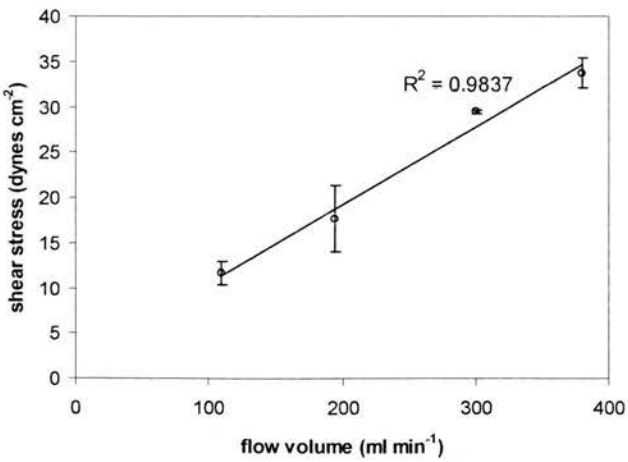

Fig. 5. Shear stress as a function of flow volume in the flow chamber. The error bars are the standard error which was calculated by Excel during the linear regression. The units of distance have been converted to cm for the shear rate calculation. (R^2 = 0.9837.)

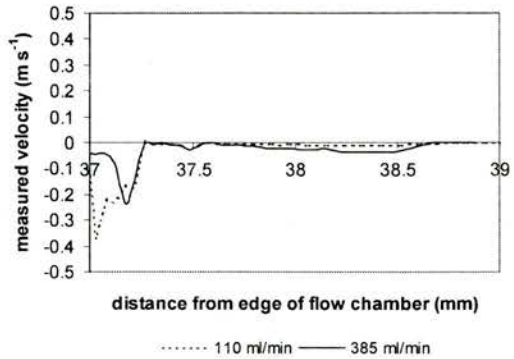

Fig. 6. Plot of point velocities horizontally perpendicular to flow direction, for flows at 110 mL min^{-1} and 385 mL min^{-1}.

to 110 mL min^{-1}, there was no obvious difference in the mean backscattered power from each section across the sample, suggesting that the microbubbles were not dislodged with increasing flow rates.

DISCUSSION

The data described here have shown that the in-house microbubbles remained attached to agar samples when subjected to increasing flow rates. The shear stress experienced by the attached microbubbles was determined using LDA. The use of LDA with the flow chamber enabled the shear stress at the point in the flow channel where the agar samples were positioned to be determined.

The flow rates used in the present study were from 75 to 480 mL min^{-1} through a flow area of 9 mm^2, with shear stresses in the flow channel being determined for 110, 195, 300 and 385 mL min^{-1}.

The LDA data in Fig. 3 show that the range of peak flow velocities to which the microbubbles were subjected was from 36 to 84 cm s^{-1}. These velocities corresponded to shear stresses of 1.2 to 3.4 Pa . Reported shear stresses experienced by artery walls are highly dependent on the measurement technique used. However, normal main arteries experience mean wall shear stresses of less than 1.5 Pa (Hoeks et al. 1995).

Laser Doppler anemometry (LDA) is a well-established technique allowing noninvasive high-resolution measurements of the velocities of liquids and gases. It has recently been used to validate numerically-predicted wall shear stresses in arteries (Walsh et al. 2003). In this study, pulsatile flow in a model artery was used with LDA and time-averaged velocity profiles were calculated. These profiles were then compared with profiles found using computational fluid dynamics (CFD). They concluded that, for pulsatile flow, LDA should be used for point velocity validations, but large errors were found when experimentally determining the wall shear stress. The calculation of the shear rate from LDA data were

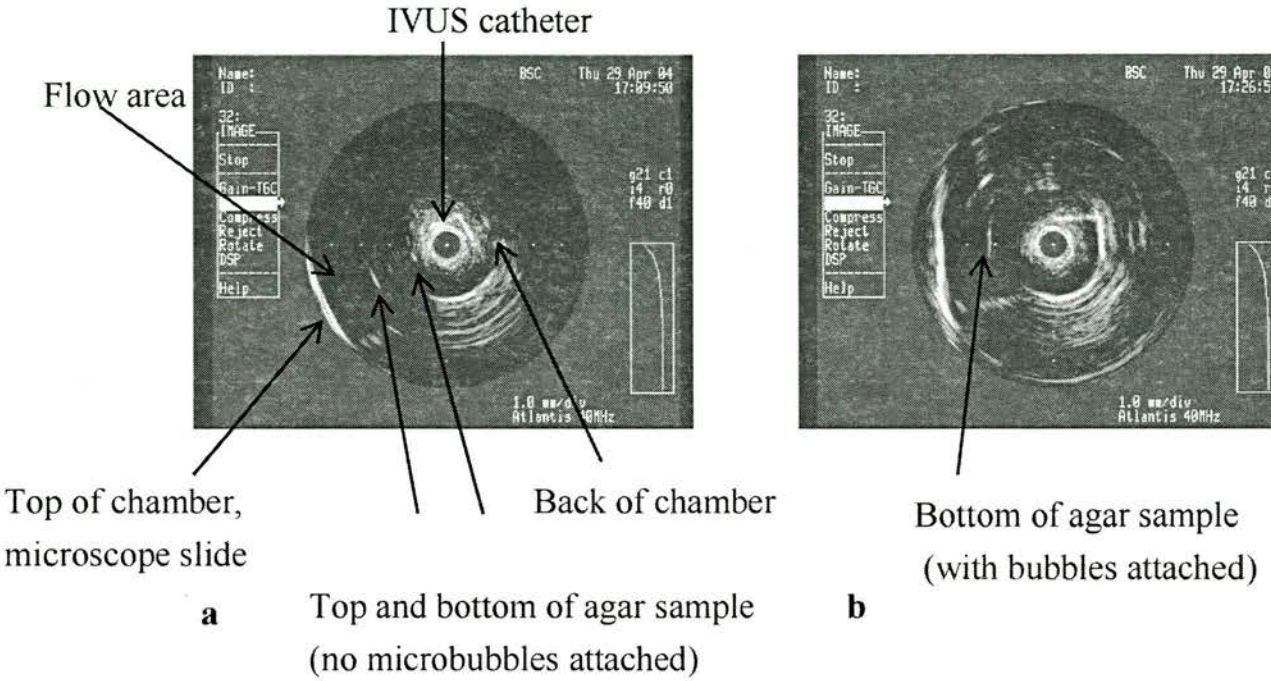

Fig. 7. (a) IVUS image from flow chamber with agar-based sample without microbubble attached, (b) IVUS image from flow chamber with agar based sample with microbubbles attached.

highly dependent on the curve-fitting technique used. An earlier study of shear rate calculations from LDA measurements for steady and pulsatile flow (Fatemi and Rittgers 1994) found less than 10% error in wall shear stress measurements for steady flow when linear fits were used.

Since steady flow was used in the set-up described in this study, the errors in the calculated shear stresses were small. The resolution of the data points was 45 μm, so the profile was detailed very close to the chamber wall. When the profile was extrapolated back to the wall at both sections of the profile at the edges of the flow channel, the distance between the edges was 1.38 $\pm$ 0.04 mm. On measuring the channel width with a micrometer, at a position as close as possible to where the LDA measurements were taken, the width was found to be 1.43 $\pm$ 0.02 mm. The difference was due to errors in both methods of calculating the distance, but the values are comparable.

Linear regressions on the section of the profile at the edge of the channel were used to calculate the shear rate at the surface of the samples. When five data points were used instead of four, there was no significant difference in the shear stresses calculated. The mean difference in shear stress value calculated using five data points was $\pm$0.08 Pa.

The profiles in Fig. 3 are parabolic and, for the lower flow rates, symmetrical. As the flow rate increased, the profile in the channel became slightly unsymmetrical. Also, the off-axis flow (Fig. 6) perpendicular to that in Fig. 3 was not consistently at zero. This could have been due to the increased flow rate causing turbulence in the channel. To find the likelihood of the flow being turbulent, the Reynolds numbers for the minimum and maximum flow rates were calculated and found to be 600 and 1500, respectively. These both suggest that the flow in the channel should have been laminar. As the flow rate increased, fully-developed flow would take longer to occur; this could also be the cause of the deviation from symmetrical parabolic shape at increasing flow rates.

Current *in-vitro* work, where the effect of shear stress on microbubbles is investigated, use supplier quoted values for the shear stress in the commercial flow chambers used. In flow chambers, the shear rate can vary across the chamber (Chung et al. 2003), so the exact shear stress at specific points in a chamber can be difficult to calculate. The flow chamber described in this paper allows high frequency IVUS imaging of samples with microbubbles attached under flow conditions; the LDA data give shear stress values for different flow rates, so there is a potential to use any shear rate required. The flow profile at different points in the chamber described here can be assessed so the shear stress throughout the chamber can be known.

The work in this study has been completed with steady flow. When subjected to pulsatile flow, the attached microbubbles may respond in a different manner. However, the aim of this study was to investigate whether or not the microbubbles detached from the agar samples with increased wall shear stresses. When attached to disrupted plaque, the microbubbles will not

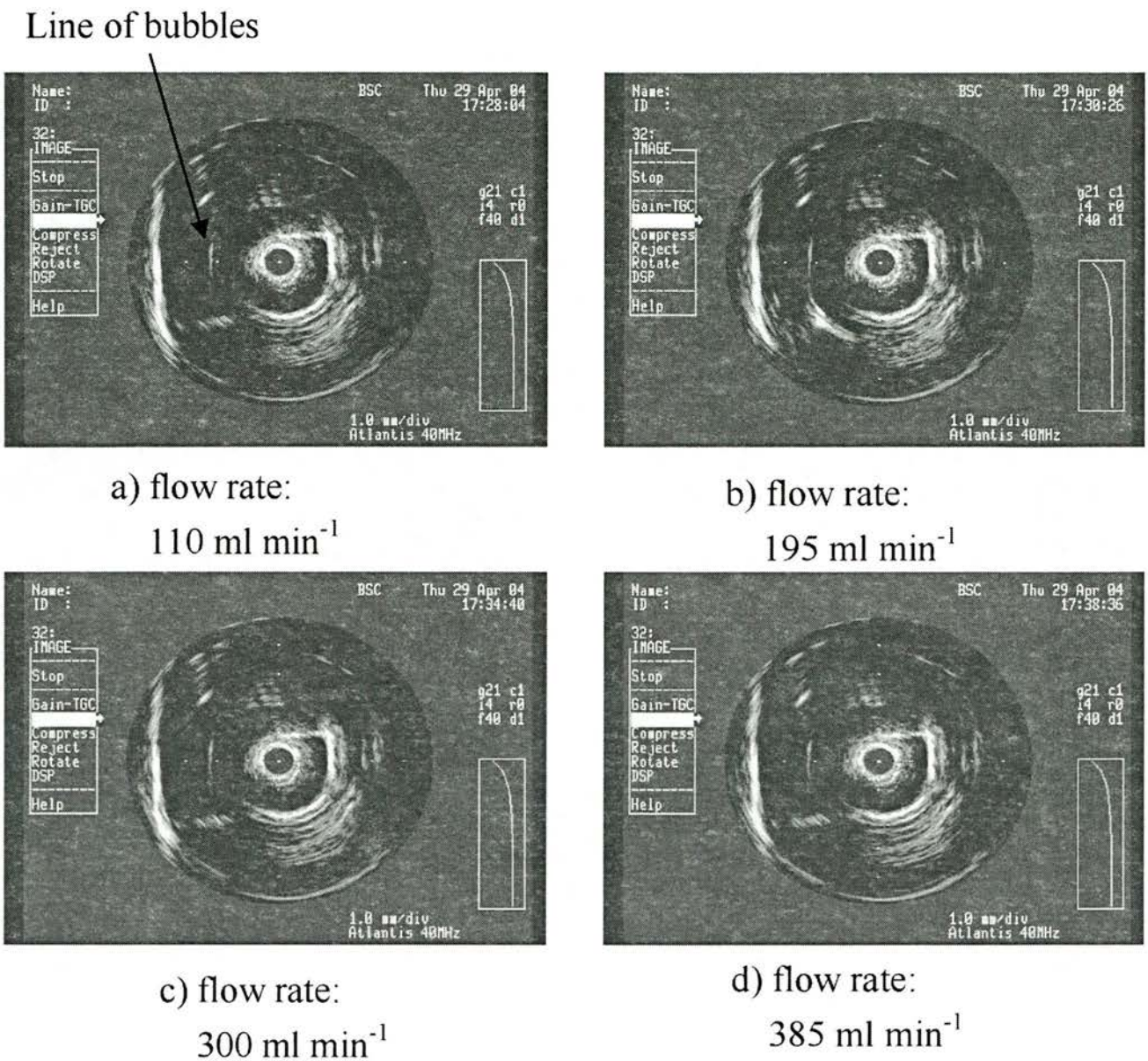

Fig. 8. IVUS images at 40 MHz of bubbles attached to agar-based samples subjected to different flow rates.

experience shear stresses as if attached to an intact endothelial wall, as they will be contained within crevices or fissures in the wall.

The microbubbles could be imaged with IVUS and remained attached and echogenic under increased flow rates. This was confirmed with the calculated mean backscatter power at the surface of the sample. Figure 9b shows that there was very little difference in the mean backscatter power after the flow rate had been increased.

CONCLUSIONS

A flow chamber has been designed for ultrasonic imaging of microbubbles attached to agar. Intravascular ultrasound was used to image attached microbubbles under steady flow conditions. The chamber was also used with laser Doppler anemometry to allow detailed profiles of the flow in the chamber to be found. These profiles were used to calculate the shear rate at the wall of the chamber and, hence, the shear stress to which the microbubbles were subjected. The microbubbles were found to remain attached and echogenic under flow rates higher than physiological rates and to withstand shear stresses of up to 3.4 Pa.

The shear stresses experienced at the surface of samples for different flow rates are known for the flow chamber. These values can be used when the microbubbles are

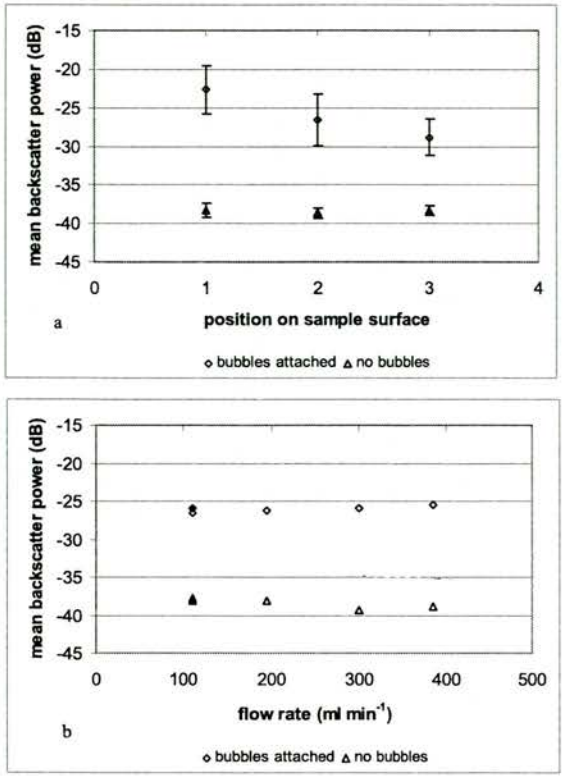

Fig. 9. (a) Mean backscatter power for each position across the surface of agar samples with and without microbubbles attached. Error bars are one standard deviation. (b) Backscattered power against flow rate for agar-based samples with and without microbubbles attached. The filled-in data points represent the mean backscattered power after the flow rate had been increased to 385 mL min^{-1} and decreased back to 100 mL min^{-1}.

attached to different samples or attached using different binding methods when other detachment studies are undertaken. The in-house microbubbles have been found to remain attached to agar samples under flow rates comparable with physiological rates; this information has the potential to be used in future characterization of the microbubble.

Acknowledgments—The authors would like to acknowledge the British Medical Ultrasound Society (BMUS) and the Moray Endowment Fund for grants that allowed the purchase of the lens used in this work. CMM and CC are funded by the British Heart Foundation. MB is funded by an EPSRC studentship.

REFERENCES

Butler MB, Moran CM, Anderson T, et al. Quantitative laser Doppler anemometry measurements of the shear-stresses exerted on ultrasonic microbubbles attached to surfaces under physiological flow conditions. Proceedings of the IEEE UFFC 2004, (in press).

Campani R, Calliada F, Bottinelli O, et al. Contrast enhancing agents in ultrasonography: Clinical applications. Eur J Radiol 1998;27:S161–S170.

Chung BJ, Robertson AM, Peters DG. The numerical design of a parallel plate flow chamber for investigation of endothelial cell response to shear stress. Comput. Struct 2003;81:535–546.

de Korte CL, van der Steen AFW, Cespedes EI, Pasterkamp G. Intravascular ultrasound elastography in human arteries: Initial experience *in vitro*. Ultrasound Med Biol 1998;24:401–408.

Durrani TS, Greated CA. Laser systems in flow measurment. New York: Plenum Publishing Corporation, 1977.

Ellegala DB, Leong-Poi H, Carpenter JE, et al. Imaging tumor angiogenesis with contrast ultrasound and microbubbles targeted to {α}v{β}3. Circulation 2003;108:336–341.

Fatemi RS, Rittgers SE. Derivation of shear rates from near-wall LDA measurements under steady and pulsatile flow conditions. J Biomech Eng 1994;116:361–368.

Hoeks APG, Samijo SK, Brands PJ, Reneman RS. Noninvasive determination of shear-rate distribution across the arterial lumen. Hypertension 1995;26:26–33.

Kaul S. Myocardial contrast echocardiography: Basic principles, I. Prog Cardiovasc Dis 2001;44:1–11.

Klibanov AL, Hughes MS, Marsh JN, et al. Targeting of ultrasound contrast material. An *in vitro* feasibility study. Acta Radiol Suppl 1997;412:113–120.

Klibanov AL, Hughes MS, Villanueva FS, et al. Targeting and ultrasound imaging of microbubble-based contrast agents. MAGMA 1999;8:177–184.

Lanza GM. A novel site-targeted ultrasonic contrast agent with broad biomedical application. Circulation 1996;94:3334–3340.

Lindner JR. Molecular imaging with contrast ultrasound and targeted microbubbles. I. J Nucl Cardiol 2004;11:215–221.

Miller AP, Nanda NC. Contrast echocardiography: New agents. Ultrasound Med Biol 2004;30:425–434.

Moran CM, Ross J, Ansell I, et al. Characterization of a newly developed ultrasonic contrast agent. Heart 2003a;89(Supp 3):iii40–iii42.

Moran CM, Ross J, Oliver C, Butler M, McDicken WN. *In vitro* 40 MHz characterization of in-house liposomal microbubble dispersions developed for targeting atherosclerotic plaque. Proceedings of the IEEE UFFC 2004a, (in press).

Moran CM, Ross J, Oliver C, et al. Ultrasonic characterization of a newly developed targeted ultrasonic contrast agent. Eur J Echocardiogr 2003b;4:S19.

Nair A, Kuban BD, Obuchowski N, Vince DG. Assessing spectral algorithms to predict atherosclerotic plaque composition with normalized and raw intravascular ultrasound data. Ultrasound Med Biol 2001;27:1319–1331.

Nichols WW, O'Rourke MF. McDonald's blood flow in arteries. London: Edward Arnold, 1990.

Spencer T, Ramo MP, Salter DM, et al. Characterization of atherosclerotic plaque by spectral analysis of intravascular ultrasound: An *in vitro* methodology. Ultrasound Med Biol 1997;23:191–203.

Takalkar AM, Klibanov AL, Rychak JJ, Lindner JR, Ley K. Binding and detachment dynamics of microbubbles targeted to P-selectin under controlled shear flow. J Control Release 2004;96:473–482.

Teirlinck CJPM, Bezemer RA, Kollmann C, et al. Development of an example flow test object and comparison of five of these test objects, constructed in various laboratories. Ultrasonics 1998;36:653–660.

Unger EC, Matsunaga TO, McCreery T, et al. Therapeutic applications of microbubbles. Eur J Radiol 2002;42:160–168.

Villanueva FS, Jankowski RJ, Klibanov S, et al. Microbubbles targeted to intercellular adhesion molecule-1 bind to activated coronary artery endothelial cells. Circulation 1998;98:1–5.

Walsh M, McGloughlin T, Liepsch DW, et al. On using experimentally estimated wall shear stresses to validate numerically predicted results. Proc Inst Mech Eng [H] 2003;217:77–90.

Watson RJ, McLean CC, Moore MP, et al. Classification of arterial plaque by spectral analysis of *in vitro* radio frequency intravascular ultrasound data. Ultrasound Med Biol 2000;26:73–80.

Weast RC, Astle MJ, Beyer WH. Handbook of chemistry and physics, 69th ed. Florida: CRC Press, 1988.

Weller GER, Villanueva FS, Klibanov AL, Wagner WR. Modulating targeted adhesion of an ultrasound contrast agent to dysfunctional endothelium. Ann Biomed Eng 2002;30:1012–1019.

Reference List

Alessi, P., Ebbinghaus, C., and Neri, D., Molecular targeting of angiogenesis, *Biochemica et Biophysica Acta*, 2004, **1654**, 39-49.

Bale-Glickman, J., Selby, K., Saloner, D., and Savas, O., Experimental flow studies in exact-replica phantoms of atherosclerotic carotid bifurcations under steady input conditions, *J Biomech Eng*, 2003, **125**, 38-48.

Berne, R. M. and Levy, M. N., Coronary circulation, Cardiovascular Physiology, Mosby, Missouri, 1997

Blomley, M. J. K., Cooke, J. C., Unger, E. C., Monaghan, M. J., and Cosgrove, D. O., Science, medicine, and the future - Microbubble contrast agents: a new era in ultrasound, *British Medical Journal*, 2001, **322**, 7296, 1222-1225.

Brands, P. J., Hoeks, A. P. G., Hofstra, L., and Reneman, R. S., A noninvasive method to estimate wall shear rate using ultrasound, *Ultrasound Med Biol*, 1995, **21**, 2, 171-185.

Brooks, S. B. and Tozeren, A., Flow past an array of cells that are adherent to the bottom plate of a flow channel, *Computers & Fluids*, 1996, **25**, 8, 741-757.

Carroll, B. A., Turner, R. J., Tickner, E. G., Boyle, D. B., and Young, S. W., Gelatin encapsulated nitrogen microbubbles as ultrasonic contrast agents, *Investigative Radiology*, 1980, **15**, 260-266.

Casscells, W., Naghavi, M., and Willerson, J. T., Vulnerable atherosclerotic plaque. A multifocal disease, *Circulation*, 2003, **107**, 16, 2072-2075.

Cheng, S. C., Dy, T. C., and Feinstein, S. B., Contrast echocardiography: review and future directions, *The American Journal of Cardiology*, 1998, **81**, 12, Supplement 1, 41G-48G.

Chin, C. T. and Burns, P. N., Predicting the acoustic response of a microbubble population for contrast imaging in medical ultrasound, *Ultrasound Med. Biol.*, 2000, **26**, 8, 1293-1300.

Chong, W. K., Intravascular ultrasound, Invasive Ultrasound, Rees, W. R. and Lyons, E. A., Martin Dunitz, London, UK, 1996

Chung, B. J., Robertson, A. M., and Peters, D. G., The numerical design of a parallel plate flow chamber for investigation of endothelial cell response to shear stress, *Computers & Structures*, 2003, **81**, 8-11, 535-546.

Church, C. C., The effects of an elastic solid surface layer on the radial pulsations of gas bubbles, *The Journal of the Acoustical Society of America*, 1995, **97**, 3, 1510-1521.

Cosgrove, D. O. and Blomley, M. J. K., Evaluation of tumors using echo-enhancing agents, Ultrasound Contrast Agents, Goldberg, B. B, Martin Duntiz, London, 1997

Dayton, P. and Ferrara, K., Targeted imaging using ultrasound, *Journal of Magnetic Resonance Imaging*, 2002, **16**, 362-377.

Dayton, P., Klibanov, A., Brandenburger, G., and Ferrara, K., Acoustic radiation force in vivo: A mechanism to assist targeting of microbubbles, *Ultrasound in Medicine and Biology*, 1999a, **25**, 8, 1195-1201.

Dayton, P., Morgan, K., Allietta, M., Klibanov, A., Brandenburger, G., and Ferrara, K., Simultaneous optical and acoustical observations of contrast agents, *IEEE Ultrasonics Symposium*, 1997, 1583-1591.

Dayton, P. A., Morgan, K. E., Klibanov, A. L., Brandenburger, G. H., and Ferrara, K. W., Optical and acoustical observations of the effects of ultrasound on contrast agents, *IEEE Transactions on Ultrasonics, Ferroelectrics, and Frequency Control*, 1999b, **46**, 1, 220-232.

de Jong, N., Bouakaz, A., and Frinking, P., Basic acoustic properties of microbubbles, *Echocardiography*, 2002, **19**, 3, 229-240.

de Jong, N., Cornet, R., and Lancée, C. T., Higher harmonics of vibrating gas-filled microspheres. Part one: simulations, *Ultrasonics*, 1994, **32**, 6, 447-453.

de Jong, N., Frinking, P. J. A., Bouakaz, A., Goorden, M., Schourmans, T., Xu, J. P., and Mastik, F., Optical imaging of contrast agent microbubbles in an ultrasound field with a 100-MHz camera, *Ultrasound in Medicine and Biology*, 2000, **26**, 3, 487-492.

de Korte, C. L. and van der Steen, A. F. W., Intravascular ultrasound elastography: an overview, *Ultrasonics*, 2002, **40**, 1-8, 859-865.

Demos, S. M., Alkan-Onyuksel, H., Kane, B. J., Ramani, K., Nagaraj, A., Greene, R., Klegerman, M., and McPherson, D. D., In vivo targeting of acoustically reflective liposomes for intravascular and transvascular ultrasonic enhancement, *Journal of the American College of Cardiology*, 1999, **33**, 3, 867-875.

Deng, C. X. and Lizzi, F. L., A review of physical phenomena associated with ultrasonic contrast agents and illustrative clinical applications, *Ultrasound Med Biol*, 2002, **28**, 3, 277-286.

Dijkmans, P. A., Juffermans, L. J. M., Musters, R. J. P., van Wamel, A., Ten Cate, F. J., van Gilst, W., Visser, C. A., de Jong, N., and Kamp, O., Microbubbles and ultrasound: from diagnosis to therapy, *European Journal Of Echocardiography: The Journal Of The Working Group On Echocardiography Of The European Society Of Cardiology*, 2004, **5**, 4, 245-256.

Ellegala, D. B., Leong-Poi, H., Carpenter, J. E., Klibanov, A. L., Kaul, S., Shaffrey, M. E., Sklenar, J., and Lindner, J. R., Imaging tumor angiogenesis with contrast ultrasound and microbubbles targeted to {alpha}v{beta}3, *Circulation*, 2003, **108**, 3, 336-341.

Elzo, D., Schmitz, P., Houi, D., and Joscelyne, S., Measurement of particle/membrane interactions by a hydrodynamic method, *Journal of Membrane Science*, 1996, **109**, 43-53.

Fatemi, R. S. and Rittgers, S. E., Derivation of shear rates from near-wall LDA measurements under steady and pulsatile flow conditions, *J Biomech Eng*, 1994, **116**, 361-368.

Feinstein, S. B., Ten Cate, F. J., Werner, Z., Ong, K., Maurer, G., Tei, C., Shah, P. M., Meerbaum, S., and Corday, E., Two-dimensional contrast echocardiography. 1. In-vito development and quantitative analysis of echo contrast agents, *J Am Coll Cardiol*, 1984, **3**, 14-20.

Forsberg, F., Physics of ultrasound contrast agents, Ultrasound Contrast Agents, Goldberg, B. B, Martin Dunitz, London, 1997

Foster, F. S., Zhang, M. Y., Zhou, Y. Q., Liu, G., Mehi, J., Cherin, E., Harasiewicz, K. A., Starkoski, B. G., Zan, L., Knapik, D. A., and Adamson, S. L., A new ultrasound instrument for in vivo microimaging of mice, *Ultrasound Med Biol*, 2002, **28**, 9, 1165-1172.

Frinking, P. J., Bouakaz, A., Kirkhorn, J., Ten Cate, F. J., and de Jong, N., Ultrasound contrast imaging: current and new potential methods, *Ultrasound in Medicine and Biology*, 2000, **26**, 6, 965-975.

Gatzoulis, L., Ramnarine, K. V., Pye, S. D., Anderson, T., Newby, D. E., Hoskins, P. R., and McDicken, W. N., Doppler colour flow imaging and flow quantification with a novel forward-viewing intravascular ultrasound system, *Ultrasound Med Biol*, 2003, **29**, 1, 53-64.

Goertz, D. E., Cherin, E., Needles, A., Karshafian, R., Brown, A. S., Burns, P. N., and Foster, F. S., High frequency nonlinear B-scan imaging of microbubbles contrast agents, *IEEE Transactions on Ultrasonics, Ferroelectrics, and Frequency Control*, 2005a, **52**, 1, 65-79.

Goertz, D. E., van Wamel, A., Frijlink, M. E., de Jong, N., and van der Steen, A. F. W., Nonlinear imaging of targeted microbubbles with intravascular ultrasound, *IEEE Proceedings on Ultrasonics Symposium*, 2005b, 2003-2005.

Goss, S. A., Johnston, R. L., and Dunn, F., Comprehensive compilation of empirical ultrasonic properties of mammalian tissues, *The Journal of the Acoustical Society of America*, 1978, **64**, 2, 423-457.

Gramiak, R., The beginnings of ultrasound contrast, Ultrasound Contrast Agents, Goldberg, B. B, Martin Dunitz, London, 1997

Gramiak, R. and Shah, P. M., Echocardiography of the aortic root, *Investigative Radiology*, 1968, **3**, 356-366.

Gramiak, R., Shah, P. M., and Kramer, D. H., Ultrasound cardiography: contrast studies in anatomy and function, *Radiology*, 1969, **92**, 939-948.

Hall, T. J., Bilgen, M., Insana, M. F., and Krouskop, T. A., Phantom materials for elastography, *IEEE Transactions on Ultrasonics, Ferroelectrics, and Frequency Control*, 1997, **44**, 6, 1355-1365.

Hamilton, A., Huang, S. L., Warnick, D., Stein, A., Rabbat, M., Madhav, T., Kane, B., Nagaraj, A., Klegerman, M., MacDonald, R., and McPherson, D., Left ventricular thrombus enhancement after intravenous injection of echogenic immunoliposomes: studies in a new experimental model, *Circulation*, 2002, **105**, 23, 2772-2778.

Hamilton, A. J., Huang, S. L., Warnick, D., Rabbat, M., Kane, B., Nagaraj, A., Klegerman, M., and McPherson, D. D., Intravascular ultrasound molecular imaging of atheroma components in vivo, *Journal of the American College of Cardiology*, 2004, **43**, 3, 453-460.

Harvey, C. J., Blomley, M., Eckersley, R. J., Heckemann, R. A., Butler-Barnes, J., and Cosgrove, D. O., Pulse-inversion mode imaging of liver specific microbubbles: improved detection of subcentimetre metastases, *The Lancet*, 2000, **355**, 9206, 807-808.

Hauff, P., Reinhardt, M., Briel, A., Debus, N., and Schirner, M., Molecular targeting of lymph nodes with L-selectin ligand-specific US contrast agent: a feasibility study in mice and dogs, *Radiology*, 2004, **231**, 3, 667-673.

Hilgenfeldt, S., Lohse, D., and Zomack, M., Response of bubbles to diagnostic ultrasound: a unifying theoretical approach, *The European Physical Journal B*, 1998, **4**, 247-255.

Hoeks, A. P. G., Samijo, S. K., Brands, P. J., and Reneman, R. S., Noninvasive determination of shear-rate distribution across the arterial lumen, *Hypertension*, 1995, **26**, 1, 26-33.

Hoff, L., Sontum, P. C., and Hovem, J. M., Oscillations of polymeric microbubbles: Effect of the encapsulating shell, *The Journal of the Acoustical Society of America*, 2000, **107**, 4, 2272-2280.

Hubbe, M. A., Theory of detachment of colloidal particles from flat surfaces exposed to flow, *Colloids and Surfaces*, 1984, **12**, 151-178.

Hughes, P. E. and How, T. V., Quantitative measurement of wall shear rate by pulsed Doppler ultrasound, *Journal of Medical Engineering and Technology*, 1993, **17**, 2, 58-64.

Inglis, Scott, User manual for the SAM analysis and display toolbox 1, Internal Report, Medical Physics, University of Edinburgh, 1999

Kaul, S., Myocardial contrast echocardiography: Basic principles*1, *Prog Cardiovasc Dis*, 2001, **44**, 1, 1-11.

Klibanov, A. L., Hughes, M. S., Marsh, J. N., Hall, C. S., Miller, J. G., Wible, J. H., and Brandenburger, G. H., Targeting of ultrasound contrast material. An in vitro feasibility study, *Acta Radiol Suppl*, 1997, **412**, 113-120.

Klibanov, A. L., Targeted delivery of gas-filled microspheres, contrast agents for ultrasound imaging, *Advanced Drug Delivery Reviews*, 1999, **37**, 1-3, 139-157.

Klibanov, A. L., Hughes, M. S., Villanueva, F. S., Jankowski, R. J., Wagner, W. R., Wojdyla, J. K., Wible, J. H., and Brandenburger, G. H., Targeting and ultrasound imaging of microbubble-based contrast agents, *MAGMA*, 1999, **8**, 3, 177-184.

Krams, R., Wentzel, J. J., Oomen, J. A. F., Vinke, R., Schuurbiers, J. C. H., de Feyter, P. J., Serruys, P. W., and Slager, C. J., Evaluation of endothelial shear stress and 3D geometry as factors determining the development of atherosclerosis and remodeling in human coronary arteries in vivo : combining 3D reconstruction from angiography and IVUS (ANGUS) with computational fluid dynamics, *Arterioscler Thromb Vasc Biol*, 1997, **17**, 10, 2061-2065.

Lanza, G., Hall, C., Scott, M., Fuhrhop, R., Marsh, J., and Wickline, S., Molecular imaging with targeted ultrasound contrast agents, *IEEE Ultrasonics Symposium*, 2000, 1917-1926.

Lanza, G. M., A novel site-targeted ultrasonic contrast agent with broad biomedical application, *Circulation*, 1996, **94**, 3334-3340.

Lanza, G. M., Wallace, K. D., Fischer, S. E., Christy, D. H., Scott, M. J., Trousil, R. L., Cacheris, W. P., Miller, J. G., Gaffney, P. J., and Wickline, S. A., High-frequency ultrasonic detection of thrombi with a targeted contrast system, *Ultrasound Med Biol*, 1997, **23**, 6, 863-870.

Lanza, G. M. and Wickline, S. A., Targeted ultrasonic contrast agents for molecular imaging and therapy, *Current Problems in Cardiology*, 2003, **28**, 12, 625-653.

Lauterborn, W., Numerical investigation of nonlinear oscillations of gas bubbles in liquids, *Journal of the Acoustical Society of America*, 1976, **59**, 2, 283-293.

Leong-Poi, H., Ellegala, D., Carpenter, J., Klibanov, A. L., Duong, V., Kaul, S., Shaffrey, M. E., and Lindner, J. R., Site-specific imaging of tumor angiogenesis using contrast-enhanced ultrasound imaging with microbubbles targeted to alpha-V beta-3, *Journal of the American College of Cardiology*, 2003, **41**, 6, Supplement 2, 431-431.

Levick, J. R., An introduction to cardiovascular physiology, Arnold, London, 2003

Libby, P., Molecular bases of the acute coronary syndromes, *Circulation*, 1995, **91**, 11, 2844-2850.

Libby, P., What happens inside an atherosclerotic plaque?, *International Congress Series*, 2004, **1262**, 253-256.

Libby, P., Ridker, P. M., and Maseri, A., Inflammation and atherosclerosis, *Circulation*, 2002, **105**, 9, 1135-1143.

Lindner, J. R. and Kaul, S., Delivery of drugs with ultrasound, *Echocardiography*, 2001, **18**, 4, 329-338.

Lindner, J. R., Detection of inflamed plaques with contrast ultrasound, *The American Journal of Cardiology*, 2002, **90**, 10, Supplement 3, L32-L35.

Lindner, J. R., Coggins, M. P., Kaul, S., Klibanov, A. L., Brandenburger, G. H., and Ley, K., Microbubble persistence in the microcirculation during ischemia/reperfusion and inflammation is caused by integrin- and complement-mediated adherence to activated leukocytes, *Circulation*, 2000a, **101**, 6, 668-675.

Lindner, J. R., Dayton, P. A., Coggins, M. P., Ley, K., Song, J., Ferrara, K., and Kaul, S., Noninvasive imaging of inflammation by ultrasound detection of phagocytosed microbubbles, *Circulation*, 2000b, **102**, 5, 531-538.

Lindner, J. R., Song, J., Xu, F., Klibanov, A. L., Singbartl, K., Ley, K., and Kaul, S., Noninvasive ultrasound imaging of inflammation using microbubbles targeted to activated leukocytes, *Circulation*, 2000c, **102**, 22, 2745-2750.

Lupotti, F., Quantitative blood flow as assessed by intravascular ultrasound, 2002, 17-

Malek, A. M., Alper, S. L., and Izumo, S., Hemodynamic shear stress and its role in atherosclerosis, *JAMA*, 1999, **282**, 21, 2035-2042.

McLeod, A. L., Watson, R. J., Anderson, T., Inglis, S., Newby, D. E., Northridge, D. B., Uren, N. G., and McDicken, W. N., Classification of arterial plaque by spectral analysis in remodelled human atherosclerotic coronary arteries, *Ultrasound Med Biol*, 2004, **30**, 2, 155-159.

Miller, A. P. and Nanda, N. C., Contrast echocardiography: new agents, *Ultrasound Med Biol*, 2004, **30**, 4, 425-434.

Miller, D. L., Frequency relationship for ultrasonic activation of free microbubbles, encapsulated microbubbles, and gas-filled micropores, *Journal of the Acoustical Society of America*, 1998, **104**, 4, 2498-2505.

Moraes, R. and Evans, D. H., Effects of nonuniform insonation by catheter-tipped Doppler transducers on velocity estimation, *Ultrasound Med Biol*, 1995, **21**, 6, 779-791.

Moran, C. M., Ross, J., Ansell, I., Oliver, C., Butler, M., Williamson, J., and Anderson, T., Characterisation of a newly developed ultrasonic contrast agent., *Heart*, 2003a, **89**, 3,

Moran, C. M., Ross, J., Cunningham, C., Butler, M., Anderson, T., Newby, D., Fox, K. A. A., and McDicken, W. N., Manufacture and acoustical characterisation of a high frequency contrast agent for targeting applications, *Ultrasound Med Biol*, 2006, **in press**,

Moran, C. M., Ross, J., Oliver, C., Butler, M., McDicken, W., and Fox, K., Ultrasonic characterisation of a newly developed targeted ultrasonic contrast agent., *Eur J Echocardiogr*, 2003b, **4**, S19-

Moran, C. M., Ross, J. A., Oliver, C., Butler, M., and McDicken, W. N., In vitro 40 MHz characterisation of in-house liposomal microbubble dispersions developed for targeting atherosclerotic plaque, *IEEE Ultrasonics Symposium*, 2004, 1395, 1397-

Moran, C. M., Watson, R. J., Fox, K. A. A., and McDicken, W. N., In vitro acoustic characterisation of four intravenous ultrasonic contrast agents at 30 MHz, *Ultrasound in Medicine and Biology*, 2002, **28**, 6, 785-791.

Morgan, K., Dayton, P., Klibanov, A., Brandenburger, G., Kaul, S., Wei, K., and Ferrara, K., Properties of contrast agents insonified at frequencies above 10 MHz, *IEEE Proceedings on Ultrasonics Symposium*, 1996, **2**, 1127-1130.

Newman, C. M., Lawrie, A., Brisken, A. F., and Cumberland, D. C., Ultrasound gene therapy: on the road from concept to reality, *Echocardiography*, 2001, **18**, 4, 339-347.

NHS report, Myocardial perfusion scintigraphy for the diagnosis and management of angina and myocardial infarction, NHS Technology appraisal 73, 2003

Nichols, W. W. and O'Rourke, M. F., McDonald's Blood Flow in Arteries, Edward Arnold, London, 1990

Nissen, S. E., Cinical images from intravascular ultrasound: coronary disease, plaque rupture, and intervention - the inside view, *The American Journal of Cardiology*, 2001, **88**, (8A), 16K-18K.

Nissen, S. E., Application of intravascular ultrasound to characterize coronary artery disease and assess the progression or regression of atherosclerosis, *American Journal of Cardiology*, 2002, **89**, 4A, 24B-31B.

Nissen, S. E., Identifying patients at risk: novel diagnostic techniques, *European Heart Journal Supplements*, 2004, **6**, Supplement 3, C15-C20.

O'Brian, K. D., McDonald, T. O., Chait, A., Allen, M. D., and Alpers, C. E., Neovascular expression of E-selectin, intercellular adhesion molecule-1 in human atherosclerosis and their relation to intimal leukocyte content, *Circulation*, 1996, **93**, 672-682.

O'Neil, M. E., A sphere in contact with a plane wall in a slow linear shear flow, *Chemical Engineering Science*, 1968, **23**, 1293-1298.

Ophir, J. and Parker, K. J., Contrast agents in diagnostic ultrasound, *Ultrasound in Medicine and Biology*, 1989, **15**, 4, 319-333.

Petersen, S, Peto, V, and Rayner, M, 12th Edition of coronary heart disease statistics, 2004

Porenta, G., Schima, H., Pentaris, A., Tsangaris, S., Moertl, D., Probst, P., Maurer, G., and Baumgartner, H., Assessment of coronary stenoses by Doppler wires: a validation study using in vitro modeling and computer simulations, *Ultrasound Med Biol*, 1999, **25**, 5, 793-801.

Prasad, A. K., Particle image velocimetry, *Current Science*, 2000, **79**, 1, 51-60.

Preston, R. C., Output measurements for medical ultrasound, Springer-Verlag, London, 1991

Prosperetti, A., Crum, L. A., and Commander, K. W., Nonlinear bubble dynamics, *The Journal of the Acoustical Society of America*, 1988, **83**, 502-514.

Rainger, G. E., Stone, P., Morland, C. M., and Nash, G. B., A novel system for investigating the ability of smooth muscle cells and fibroblasts to regulate adhesion of flowing leukocytes to endothelial cells, *Journal of Immunological Methods*, 2001, **255**, 1-2, 73-82.

Ramnarine, K. V. and Browne, J., User manual for the scanning acoustic macroscope (SAM), Internal Report, Medical Physics, University of Edinburgh, 1999

Rayleigh, J. W., On the pressure developed in a liquid during the collapse of a spherical cavity, *Phil Mag*, 1917, **34**, 94-98.

Regar, E., Schaar, J. A., Mont, E., Virmani, R., and Serruys, P. W., Optical coherence tomography, *Cardiovascular Radiation Medicine*, 2003, **4**, 198-204.

Roelandt, J., Contrast Echocardiography, *Ultrasound in Medicine and Biology*, 1982, **8**, 5, 471-&.

Rudd, J. N., Davies, J. R., and Weissberg.P.L, Imaging of atherosclerosis - can we predict plaque rupture, *Trends in Cardiovascular Medicine*, 2005, **15**, 1, 17-24.

Rychak, J. J., Klibanov, A. L., and Hossack, J., Acoustic radiation force enhances adhesion of microbubbles targeted to P-selectin, *IEEE Proceedings on Ultrasonics Ferroelectrics and Frequency Control*, 2004,

Rychak, J. J., Klibanov, A. L., and Hossack, J. A., Acoustic radiation force enhances targeted delivery of ultrasound contrast microbubbles: in vitro varification, *IEEE Transactions on Ultrasonics, Ferroelectrics, and Frequency Control*, 2005, **52**, 3, 421-433.

Sboros, V., MacDonald, C. A., Pye, S. D., Moran, C. M., Gomatam, J., and McDicken, W. N., The dependence of ultrasound contrast agents backscatter on acoustic pressure: theory versus experiment, *Ultrasonics*, 2002, **40**, 1-8, 579-583.

Sboros, V., Moran, C. M., Pye, S. D., and McDicken, W. N., The behaviour of individual contrast agent microbubbles, *Ultrasound Med Biol*, 2003, **29**, 5, 687-694.

Scheirner, M., Menrad, A., Stephens, A., Freznel, T., Hauff, P., and Licha, K., Molecular imaging of tumor angiogenesis, *Ann NY Acad Sci*, 2004, **1014**, 1, 67-75.

Schirner, M., Menrad, A., Stephens, A., Freznel, T., Hauff, P., and Licha, K., Molecular imaging of tumor angiogenesis, *Ann NY Acad Sci*, 2004, **1014**, 1, 67-75.

Schroeder, A. P. and Falk, E., Vulnerable and dangerous coronary plaques, *Atherosclerosis*, 1995, **118**, Supplement 1, S141-S149.

Seeley, R., Stephens, T., and Tate, P., Essentials of anatomy and physiology, Wm. C. Brown Publishers, UK, 1996

Shaaban, A. M. and Duerinckx, A. J., Wall shear stress and early atherosclerosis: A review, *American Journal of Roentgenology*, 2000, **174**, 6, 1657-1665.

Shohet, R. V., Chen, S., Zhou, Y. T., Wang, Z., Meidell, R. S., Under, R. H., and Grayburn, P. A., Echocardiographic destruction of albumin microbubbles directs gene delivery to the myocardium, *Circulation*, 2000, **101**, 22, 2554-2556.

Stride, E. and Saffari, N., Microbubble ultrasound contrast agents:a review, *Proc Inst Mech Eng [H]*, 2003, **217**, 429-447.

Takalkar, A. M., Klibanov, A. L., Rychak, J. J., Lindner, J. R., and Ley, K., Binding and detachment dynamics of microbubbles targeted to P-selectin under controlled shear flow, *J Control Release*, 2004, **96**, 3, 473-482.

Teirlinck, C. J. P. M., Bezemer, R. A., Kollmann, C., Lubbers, J., Hoskins, P. R., Fish, P., Fredfeldt, K. E., and Schaarschmidt, U. G., Development of an example flow test object and comparison of five of these test objects, constructed in various laboratories, *Ultrasonics*, 1998, **36**, 1-5, 653-660.

Unger, E. C., Hersh, E., Vannan, M., and McCreery, T., Gene delivery using ultrasound contrast agents, *Echocardiography*, 2001a, **18**, 4, 355-361.

Unger, E. C., Matsunaga, T. O., McCreery, T., Schumann, P., Sweitzer, R., and Quigley, R., Therapeutic applications of microbubbles, *Eur. J. Radiol.*, 2002, **42**, 2, 160-168.

Unger, E. C., McCreery, T. P., Sweitzer, R. H., Shen, D. K., and Wu, G. L., In vitro studies of a new thrombus-specific ultrasound contrast agent, *American Journal of Cardiology*, 1998, **81**, 12A, 58G-61G.

Unger, E. C. and Sweitzer, R., Ultrasound-targeted gene and drug therapy, *Ultrasound Med Biol*, 2003, **29**, 5, Supplement 1, S41-S41.

Unger, E. C., Hersh, E., Vannan, M., Matsunaga, T. O., and McCreery, T., Local drug and gene delivery through microbubbles, *Prog Cardiovasc Dis*, 2001b, **44**, 1, 45-54.

Unger, E. C., Porter, T., Culp, W., Labell, R., Matsunaga, T., and Zutshi, R., Therapeutic applications of lipid-coated microbubbles, *Advanced Drug Delivery Reviews*, 2004, **56**, 9, 1291-1314.

van Kooten, T. G., Schakenraad, J. M., van der Mei, H. C., and Busscher, H. J., Development and use of a parallel-plate flow chamber for studying cellular adhesion to solid surfaces, *Journal of Biomedical Materials Research*, 1992, **26**, 725-738.

Villanueva, F., Jankowski MS, R. J., Manaugh BS, C., and Wagner PhD, W. R., Albumin microbubble adherence to human coronary endothelium: implications for assessment of endothelial function using myocardial contrast echocardiography, *Journal of the American College of Cardiology*, 1997, **30**, 3, 689-693.

Villanueva, F. S., Jankowski, R. J., Klibanov, S., Pina, M. L., Alber, S. M., Watkins, S. C., Brandenburger, G. H., and Wagner, W. R., Microbubbles targeted to intercellular adhesion molecule-1 bind to activated coronary artery endothelial cells, *Circulation*, 1998, **98**, 1, 1-5.

Vokurka, K., Comparison of Rayleigh's, Herring's, and Gilmore's models of gas bubbles, *Acustica*, 1986, **56**, 214-219.

Walsh, M., McGloughlin, T., Liepsch, D. W., O'Brien, T., Morris, L., and Ansari, A. R., On using experimentally estimated wall shear stresses to validate numerically predicted results, *Proc Inst Mech Eng [H]*, 2003, **217**, 2, 77-90.

Watrasiewicz, B. M. and Rudd, M. J., Laser Doppler measurements, The Butterworth Group, London, 1976

Watson, R. J., McLean, C. C., Moore, M. P., Spencer, T., Salter, D. M., Anderson, T., Fox, K. A. A., and McDicken, W. N., Classification of arterial plaque by spectral analysis of in vitro radio frequency intravascular ultrasound data, *Ultrasound Med Biol*, 2000, **26**, 1, 73-80.

Weast, R. C., Astle, M. J., and Beyer, W. H., Handbook of chemistry and physics 69th edition, Weast, Robert C, Astle, Melvin J, and Beyer, William H, CRC Press, Florida, 1988

Weller, G. E. R., Villanueva, F. S., Klibanov, A. L., and Wagner, W. R., Modulating targeted adhesion of an ultrasound contrast agent to dysfunctional endothelium, *Ann Biomed Eng*, 2002, **30**, 1012-1019.

Yeh, Y. and Cummins, H. Z., Localised fluid flow measurement with an He-Ne laser spectrometer, *Applied Physics Letters*, 1964, **4**, 10, 176-178.